OPEN ACCESS
IOP Publishing | IMMT
International Journal of Extreme Manufacturing
Int. J. Extrem. Manuf. 6 (2024) 022007 (82pp)
https://doi.org/10.1088/2631-7990/ad16d6

Topical Review

Nontraditional energy-assisted mechanical machining of difficult-to-cut materials and components in aerospace community: a comparative analysis

Guolong Zhao, Biao Zhao, Wenfeng Ding*, Lianjia Xin, Zhiwen Nian, Jianhao Peng, Ning He and Jiuhua Xu

College of Mechanical and Electrical Engineering, Nanjing University of Aeronautics and Astronautics, Nanjing 210016, People's Republic of China

E-mail: dingwf2000@vip.163.com

Received 13 July 2023, revised 29 August 2023
Accepted for publication 12 December 2023
Published 29 January 2024

Abstract

The aerospace community widely uses difficult-to-cut materials, such as titanium alloys, high-temperature alloys, metal/ceramic/polymer matrix composites, hard and brittle materials, and geometrically complex components, such as thin-walled structures, microchannels, and complex surfaces. Mechanical machining is the main material removal process for the vast majority of aerospace components. However, many problems exist, including severe and rapid tool wear, low machining efficiency, and poor surface integrity. Nontraditional energy-assisted mechanical machining is a hybrid process that uses nontraditional energies (vibration, laser, electricity, etc) to improve the machinability of local materials and decrease the burden of mechanical machining. This provides a feasible and promising method to improve the material removal rate and surface quality, reduce process forces, and prolong tool life. However, systematic reviews of this technology are lacking with respect to the current research status and development direction. This paper reviews the recent progress in the nontraditional energy-assisted mechanical machining of difficult-to-cut materials and components in the aerospace community. In addition, this paper focuses on the processing principles, material responses under nontraditional energy, resultant forces and temperatures, material removal mechanisms, and applications of these processes, including vibration-, laser-, electric-, magnetic-, chemical-, advanced coolant-, and hybrid nontraditional energy-assisted mechanical machining. Finally, a comprehensive summary of the principles, advantages, and limitations of each hybrid process is provided, and future perspectives on forward design, device

* Author to whom any correspondence should be addressed.

2631-7990/24/022007+82$33.00

development, and sustainability of nontraditional energy-assisted mechanical machining processes are discussed.

Keywords: difficult-to-cut materials, geometrically complex components, nontraditional energy, mechanical machining, aerospace community

Nomenclature

BUE	Built-up edge
LAM	Laser-assisted machining
CAMM	Chemical-assisted mechanical machining
LAT	Laser-assisted turning
CAP	Chemical-assisted polishing
LIAAG	Laser-induced ablation-assisted grinding
CCAM	Cryogenic cooling-assisted mechanical machining
LN_2	Liquid nitrogen
CCAG	Cryogenic cooling-assisted grinding
MAB	Magnetic field-assisted burnishing
CFRP	Carbon fiber-reinforced plastic
MAF	Magnetic abrasive finishing
C_f/SiC	Carbon fiber-reinforced silicon carbide
MAMP	Magnetic field-assisted mass polishing
CM	Conventional milling
MAP	Magnetic field-assisted polishing
CMC	Ceramic matrix composite
MEAP	Magnetic energy-assisted polishing
CMP	Chemical mechanical polishing
MEAT	Magnetic energy-assisted turning
CNMQL	Cryogenic nanofluid minimum quantity lubrication
MEAMM	Magnetic energy-assisted mechanical machining
CRUM	Chemical-assisted rotary ultrasonic machining
MECM	Mechanoelectrochemical milling
DS-CMP	Double-sided chemical mechanical polishing
MMC	Metal matrix composite
EAMM	Energy-assisted mechanical machining
MQL	Minimum quantity lubrication
EBSD	Electron backscatter diffraction
MR	Magnetorheological
ECM	Electrochemical machining
MRF	Magnetorheological fluid
ECMP	Electrochemical mechanical polishing
MRR	Material removal rate
EDAG	Electric discharge-assisted grinding
MWF	Metal working fluid
EDAM	Electric discharge-assisted milling
nMQL	Nanofluid minimal quantity lubrication
EDAMM	Electric discharge-assisted mechanical machining
PCBN	Polycrystalline cubic boron nitride
EDG	Electrical discharge grinding
PCD	Polycrystalline diamond
EDM	Electric discharge machining
PEEK	Polyether ether ketone
EFAP	Electric field-assisted polishing
SiC_f/SiC	Silicon carbide fiber-reinforced silicon carbide
EFAMM	Electric field-assisted mechanical machining
SiC_f/Ti	Silicon carbide fiber-reinforced titanium
ER	Electrorheological
SiC_p/Al	Silicon carbide particle-reinforced aluminum
FRCMC	Fiber-reinforced ceramic matrix composite
SPDT	Single-point diamond turning
FRP	Fiber-reinforced plastic
SS-CMP	Single-sided chemical mechanical polishing
GFRP	Glass fiber-reinforced plastic
SSD	Subsurface damage
HAZ	Heat-affected zone
TEM	Transmission electron microscopy
HE-LAT	High effective laser-assisted turning
TPS	Thermal protection system
HF	Hydrofluoric
UAECMP	Ultrasonic vibration-assisted electrochemical mechanical polishing
HPPT	High-pressure phase transformation
UAMP	Ultrasound-assisted magnetorheological polishing
HF-EDAM	High-frequency electrical discharge-assisted milling
UVAG	Ultrasonic vibration-assisted grinding
LAG	Laser-assisted grinding
UVAM	Ultrasonic vibration-assisted milling
LAMM	Laser-assisted micro-milling
UVAT	Ultrasonic vibration-assisted turning

1. Introduction

Aerospace equipment has always been at the forefront of scientific and technological innovation chains because of its great significance for national economic and defense development. High performance, light weight, reliability, and long service life are essential themes in the design and manufacture of aerospace equipment, such as aircraft, rockets, aeroengines, satellites, and spacecraft [1–3]. These requirements have promoted the wide application of difficult-to-cut materials and geometrically complex components with excellent mechanical, thermal, and tribological properties, as shown in figure 1. Difficult-to-cut materials in the aerospace community can be classified into three categories according to the main properties that determine the performance of the parts or components. Materials in the first category are characterized by excellent strength and high toughness, such as titanium alloys, high-temperature alloys, high- and ultrahigh-strength steels, and stainless steels [4–8]. These materials are used in aerospace parts or components operated under high stress or high temperature, including aeroengine blisks and turbine blades [9–12]. The second category of materials, such as advanced ceramics (Al_2O_3, Si_3N_4, SiC, ZrO_2, etc) and glasses, is mainly utilized in tribological or optical applications [13–15]. The typical properties of these materials are their high hardness and

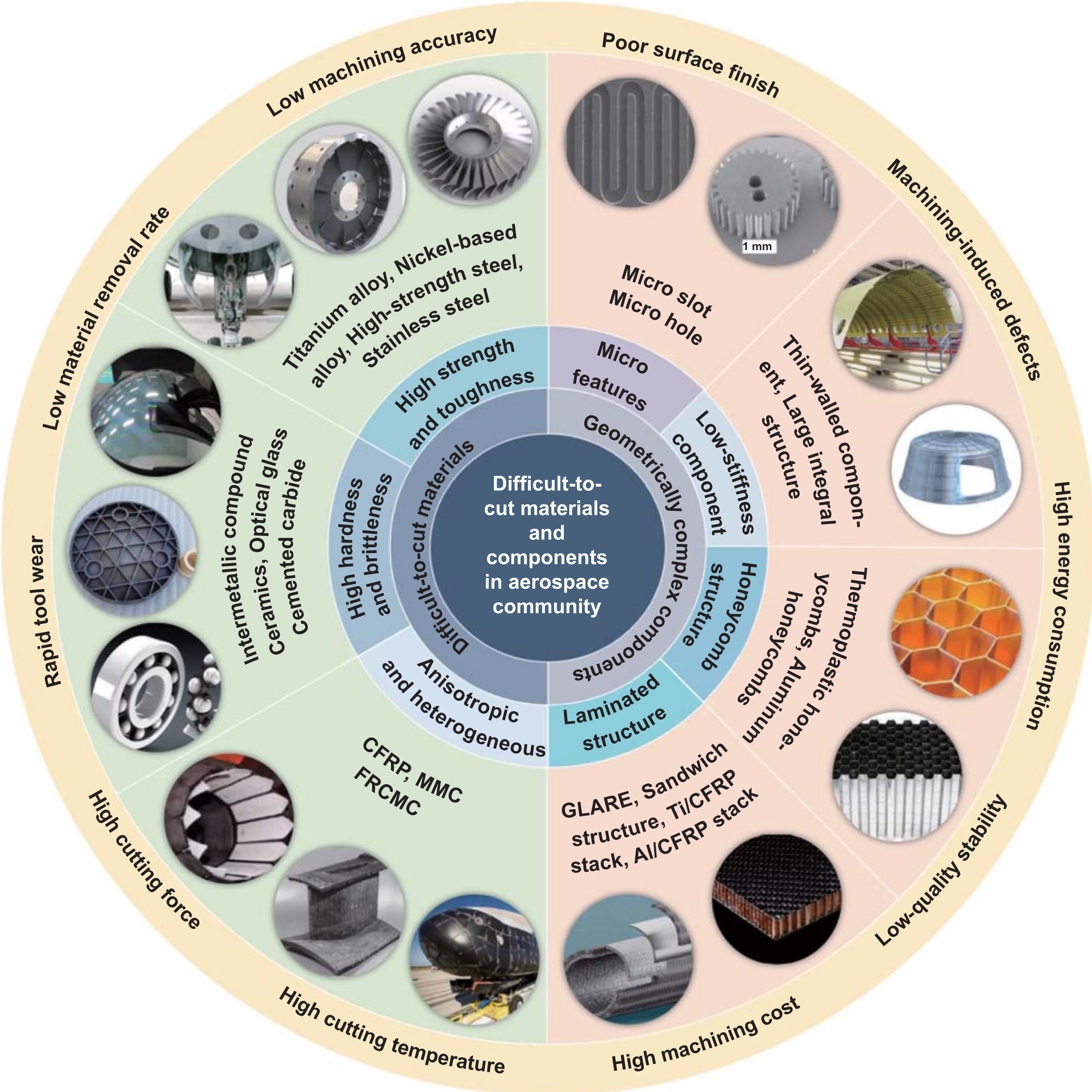

Figure 1. Difficult-to-cut materials and geometrically complex components in the aerospace community. (GLARE: Glass Laminate Aluminum Reinforced Epoxy)

brittleness. The microstructural characteristics of materials in the third category are anisotropy and heterogeneity. Typical materials in this category are FRPs (such as CFRP and GFRP), FRCMCs (such as C_f/SiC and SiC_f/SiC), and MMCs (such as SiC_p/Al and SiC_f/Ti) [16–20]. The geometrically complex components in the aerospace community mainly include micro-features (e.g. *S*-shaped micro-slots in terahertz radar and film-cooling micro-holes in turbine blades), low-stiffness components (such as aircraft wing panels and aeroengine casings), honeycomb structures (e.g. aluminum honeycombs and Nomex honeycombs), and laminated structures (e.g. glass fiber-reinforced aluminum laminates and composite/metal stacks) [21–24]. The mechanical machining of difficult-to-cut materials and geometrically complex components is usually accompanied by high cutting force and temperature, rapid tool wear, low MRR, low machining accuracy, poor surface finish, and machining-induced defects [25–29]. These issues can further result in a reduced machining efficiency, inconsistent quality, increased energy consumption, and higher machining cost.

The improvement of service performance requires key materials and components of aerospace equipment to work in extremely harsh environments, such as ultrahigh or ultralow temperatures, complex stresses, and strong mechanical and thermal shocks. As a result, advanced materials and components with extreme performance are constantly emerging. For example, the TPS of a spacecraft must withstand extremely high temperatures of up to 1800 °C and high aerodynamic force during the reentry phase into Earth's atmosphere [30]. Conventional high-temperature materials, such as high-temperature alloys, are no longer suitable due to their insufficient mechanical and thermal properties under such harsh environmental conditions. FRCMCs, including carbon fiber or silicon carbide fiber-reinforced silicon carbide matrix (C_f/SiC or SiC_f/SiC) composites, display high thermal stability and mass specific properties [31, 32]. This makes them appropriate materials for hot-end applications, such as the TPS of Boeing's X-37B space plane and the nose cap of NASA's X-38 space vehicle. However, the mechanical machining of FRCMCs is an extremely difficult task, which is ascribed to their high hardness and brittleness, anisotropy, and heterogeneity. The machining process of FRCMCs is characterized by a high cutting force, rapid tool wear, deteriorated surface quality, and machining-induced defects, such as cavities, debonding, edge collapse, and delamination [33, 34]. CFRP–titanium alloy (CFRP/Ti) stacks are increasingly becoming the most commonly used laminated structures in the aerospace community because they combine the unique properties of both CFRP and titanium alloy, such as high specific strength and stiffness, great corrosion resistance, and low density. They are widely used for skin segments, fuselages, and wing segments of commercial aircraft. A large number of holes are drilled on stacks during assembly. However, because of the significant differences in the mechanical and thermal properties between CFRP and titanium alloy, their machining characteristics differ in terms of cutting force and temperature. As a result, the drilling of CFRP/Ti stacks has problems of low accuracy, poor hole quality, and even defects, which further affect the strength and fatigue life of the components [35–38].

Machining processes for these materials and components are of great significance and versatility for the aerospace community because they affect the service performance, stability, and reliability of the aerospace equipment. The main machining processes are divided into traditional mechanical machining and nontraditional machining processes [39, 40]. Traditional mechanical machining consists mainly of cutting processes (e.g. turning, milling, drilling, and boring) and abrasive machining processes (grinding, honing, lapping, and polishing), in which edged tools, wheels, discs, or abrasives are employed to remove materials. According to the source energy used to remove the material, nontraditional machining is divided into thermal energy-based processes (e.g. laser machining), electric energy-based processes (e.g. EDM), acoustic energy-based processes (e.g. ultrasonic machining), and chemical and electrochemical energy-based processes (e.g. chemical milling and electrochemical machining). Traditional mechanical machining is the main

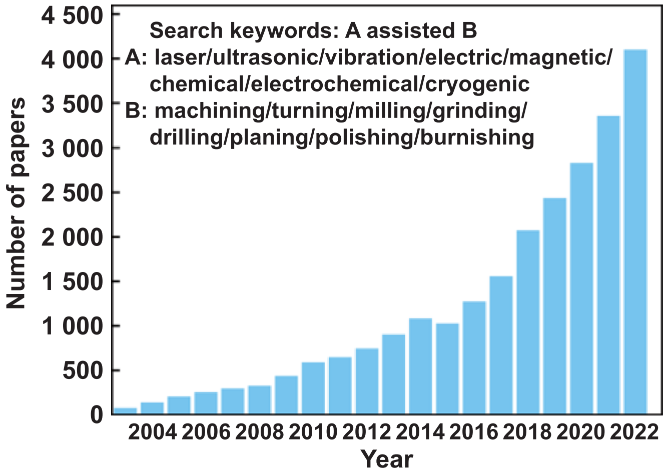

Figure 2. Evolution of published papers in reference to nontraditional EAMM over the past two decades [source: Scopus].

material removal process for the vast majority of aerospace components. It can achieve the most conceivable geometrical contours, surface topographies, dimensional tolerances, and positional accuracies. In addition, traditional mechanical machining can be applied to most available materials and has a minimal influence on the original properties of materials [41, 42]. For the aerospace community, the most significant advantage of traditional mechanical machining is that it is the most favorable way to generate prototypes or a limited number production-run components. However, traditional mechanical machining has certain limitations for constantly emerging difficult-to-cut materials and geometrically complex components, such as extremely low MRR, poor machined surface integrity, and inability to remove materials. Therefore, it is necessary and urgent to develop innovative traditional mechanical machining processes to overcome the aforementioned problems and respond to challenges in the aerospace community.

The challenges in machining of difficult-to-cut materials and components, as well as the difficulties in achieving the desired geometric shape and surface integrity at low costs, limit the application of mechanical machining in the aerospace community [43, 44]. Nontraditional EAMM, as a hybrid manufacturing method, has been proposed and developed to address these challenges. In this process, mechanical machining is the main technique for material removal, which is assisted by nontraditional energies that have significant positive effects on the material removal process. Nontraditional energies, such as thermal, acoustic, electric, magnetic, and chemical energies, are responsible for enhancing the machinability of the local workpiece material, resulting in the reduction of material properties or modification of material microstructures [45–47]. In the past two decades, a number of papers have reported the process principles, material removal mechanisms, tool performance, and surface integrity of various nontraditional EAMM processes. As shown in figure 2,

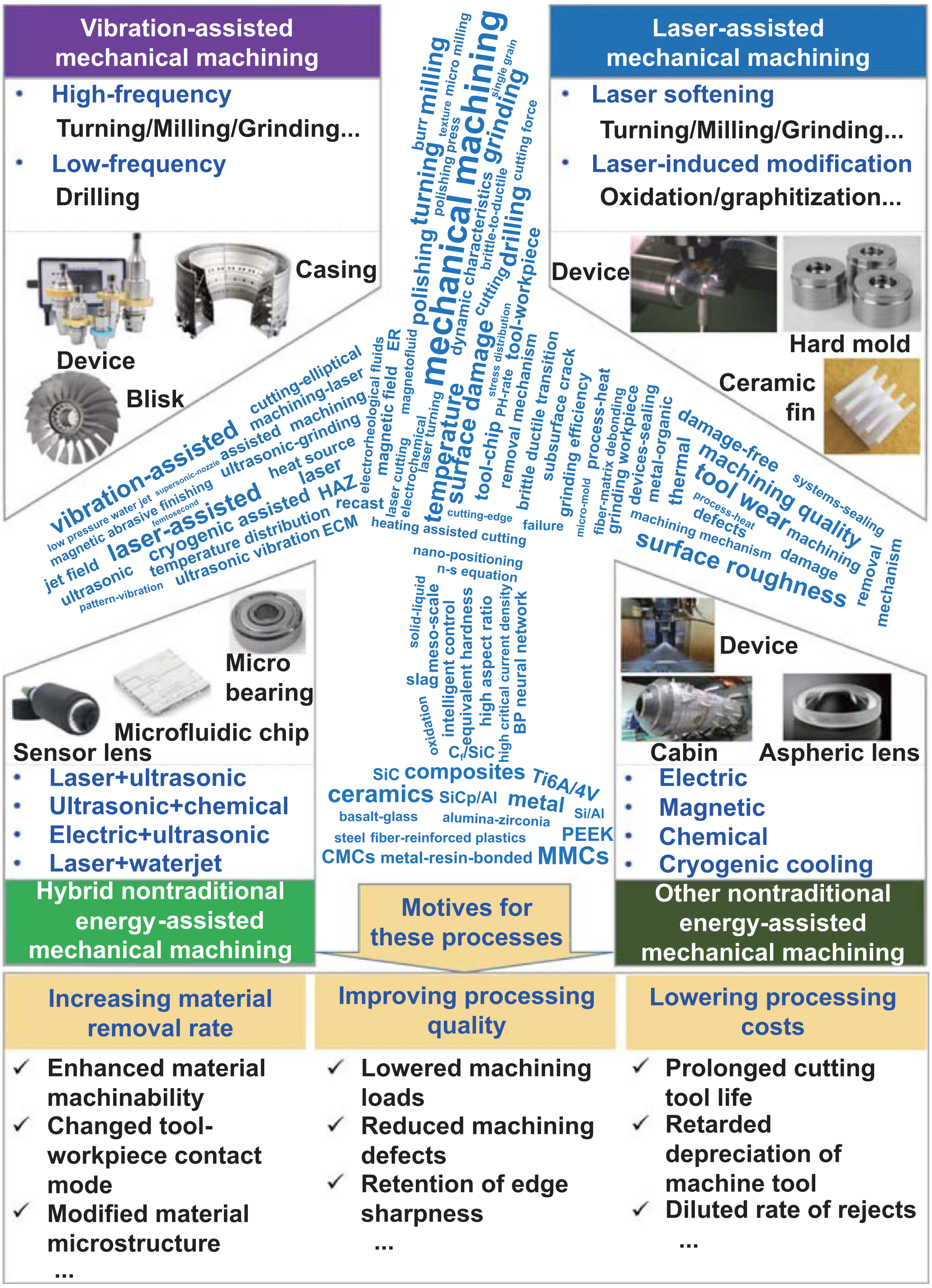

Figure 3. Nontraditional EAMM processes and their advantages and applications in the aerospace community.

the number of published papers in this scope is increasing year by year, indicating that nontraditional EAMM technique has become a global research hotspot.

Nontraditional EAMM provides a novel path for the efficient and precise machining of difficult-to-cut materials and components in the aerospace community. The motives for developing nontraditional EAMM processes are driven by various aspects from the aerospace community, as shown in figure 3. From the perspective of increasing MRR, nontraditional energies reduce the physical and mechanical properties of the material (such as laser-induced-softening-assisted machining), change the tool–workpiece contact mode (e.g. vibration-assisted machining), modify the material microstructure (e.g. laser-induced-oxidation-assisted machining), or even remove part of the material directly (e.g. laser ablation-assisted machining). As a result, the cutting force and temperature are reduced, tool life is prolonged, and larger machining parameters can be adopted. Therefore, the

MRR is improved. From the perspective of improving the processing quality, owing to the reduced mechanical, thermal, tribological, and chemical loads on the workpiece material when assisted by nontraditional energies, the grades of work hardening, residual stresses, brittle fracture, lamination, and burr formation are significantly decreased. In addition, a substantial decrease in the tool wear rate and retention of edge sharpness are achieved. As a result, the machined surface quality and dimensional accuracy are improved. From the perspective of lowering processing costs, the tool usage costs are decreased because of the prolonged life in nontraditional EAMM processes. Moreover, the reduced mechanical and thermal loads also retard depreciation and prolong the life of machine tools. Additionally, the rate of rejection is reduced due to the improved processing stability, thus lowering the processing costs.

The rapid development of the aerospace community has significantly promoted the constant advent of novel difficult-to-cut materials and components with excellent properties [48–50]. Moreover, the demands for enhanced dimensional/geometrical accuracies, improved workpiece surface integrity, and expanded production capacities are becoming increasingly high and urgent. Nontraditional EAMM has become a vital and indispensable machining process that provides an advanced technique for meeting these challenges and demands. Therefore, this paper presents a systematic review of recent research progress on techniques for machining difficult-to-cut materials and components in the aerospace community. The process principles, key features, outcomes, advantages, and limitations are comprehensively discussed.

The remainder of this paper is organized as follows. Section 2 describes vibration-assisted mechanical machining processes. Section 3 introduces the laser-assisted mechanical machining processes. Section 4 introduces hybrid nontraditional energy-assisted mechanical machining processes (i.e. a combination of two or more of the aforementioned nontraditional energies). Sections 5–7 describe electric energy, magnetic energy, and CAMM, respectively. Section 8 presents a review of the advanced coolant-assisted mechanical machining. Finally, a summary of process characteristics, advantages, limitations, and future development trends is presented at the end of this paper.

2. Vibration-assisted mechanical machining

Vibration-assisted mechanical machining technology is based on conventional machining by applying regular vibrations to tools or workpieces. This technology has attracted increasing attention from researchers worldwide, with the aim of obtaining the desired machining quality and excellent machining efficiency. Vibration-assisted mechanical machining technology plays a crucial role in dynamically changing the instantaneous motion relationship between the workpiece and tool. Ultrasound (high frequency; $>$20 kHz), a major form of vibration, is combined with traditional mechanical machining techniques to change the tool and workpiece trajectories, material removal, and surface formation mechanisms [51]. Currently, ultrasonic vibrations can be utilized in various mechanical machining processes for difficult-to-cut materials (e.g. titanium alloys and nickel-based superalloys), including turning, milling, and grinding operations to achieve a higher MRR and improved machined surface quality [52].

Studies on the preparation of ultrasonic vibration-assisted systems (e.g. vibrating spindle, vibrating toolholder, and vibrating clamp), relative trajectories between tools and workpiece, material removal mechanism, and tool wear mechanism are discussed in the following sections. In addition, the research challenges, status, and progress of each ultrasonic vibration-assisted technology are summarized. The detailed framework of ultrasonic vibration-assisted mechanical machining technology is illustrated in figure 4.

2.1. Ultrasonic vibration-assisted turning

The UVAT process utilizes ultrasonic vibrations to alter the state of material removal from continuous to intermittent cutting, thereby enhancing the machining efficiency and quality of difficult-to-cut materials. Recent domestic and international research has focused on understanding the material removal mechanism, optimizing the process, and developing vibrating equipment or systems.

In terms of material removal mechanism and process optimization, Jamshidi and Nategh [56] studied the tool chip contact behavior during UVAT of Al 6061 workpiece and concluded that the reduction in cutting force was caused by the decrease in the friction coefficient. Peng *et al* [57] found that ultrasonic vibration transformed the material removal mode into intermittent cutting, reducing the main cutting force by 40%. The external turning precision of thin-walled titanium cylinders was greatly increased by the effective suppression of flutter by ultrasonic vibration. Liu *et al* [58] constructed a one-dimensional UVAT system for PCD tools. By optimizing the process parameters, a regular micro-texture morphology was manufactured, which exhibited a good friction performance. To explore the variations in cutting force during material removal, Duan *et al* [59] developed a cutting force simulation model that considered the effects of vibration amplitude and other cutting parameters on cutting force.

In terms of vibrating equipment or systems, Wang *et al* [60] connected an ultrasonic generator to a turning tool through a piezoelectric ceramic transducer and then machined 304 stainless steel. They discovered that UVAT altered both the surface profile of the substrate and the path taken by the tool tip. Traditional 3D ultrasonic vibration-assisted machining systems often require two or more ultrasonic actuators [61, 62], which are complex and lead to a slow response. Wei *et al* [63] developed a new ultrasonic vibration actuator through simulation and experimental design and prepared a new 3D UVAT system with a single ultrasonic actuator (figure 5). A vibration-carrying rod with spiral grooves represented a significant innovation of this device, enabling the transmission of the vibration signals to the turning tool. Consequently, it facilitated the attainment of 3D curved motion for the tool. This novel 3D UVAT system effectively reduced the friction coefficient, resulting in a significantly smaller peak to valley on the

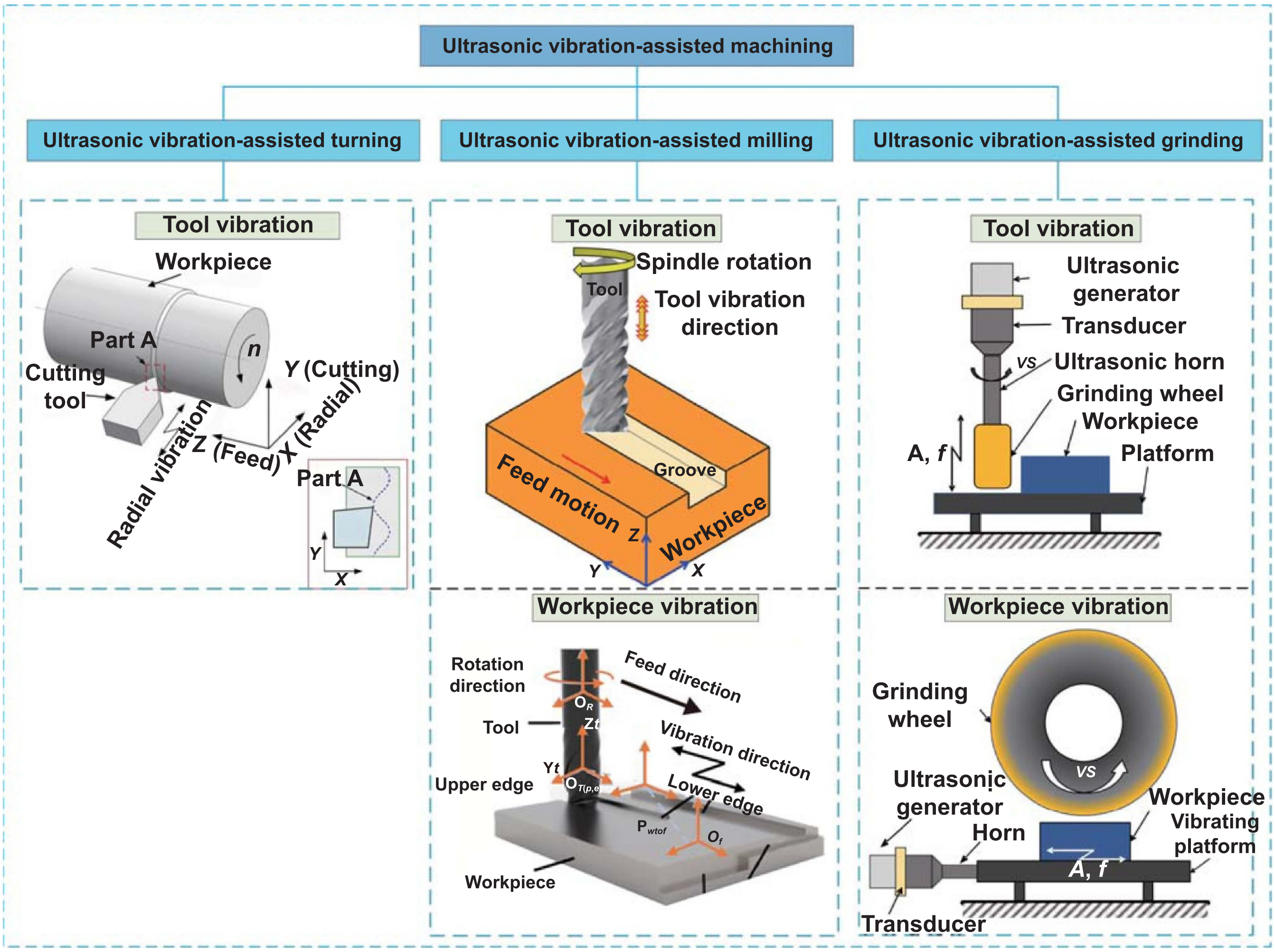

Figure 4. Classification diagram of ultrasonic vibration-assisted mechanical machining [53–55]. Reprinted from [53],© 2018 Elsevier B.V. All rights reserved. Reproduced from [54], with permission from Springer Nature. Reprinted from [55], © 2021 Elsevier Ltd. All rights reserved.

machined surface, measuring only 5.7 μm. This is far lower than that of the traditional processing method, which yields a height of 15.1 μm. Júnior *et al* [64] designed a unique ultrasonic vibration turning device using flexible hinges. The vibration of the cutting tool acted as a 'vibrating screen', thereby achieving the self-cleaning effect of the tool.

The implementation of workpiece UVAT is constrained and challenging due to the impact of workpiece geometry, mass variability, and machine configuration. Furthermore, most studies on UVAT have primarily concentrated on ultrasonic devices and processes, with little attention paid to cutting tools. The direct application of high-frequency ultrasonic vibration and high cutting loads to the tool necessitates a high level of tool performance [52, 65, 66]. Therefore, the development of turning tools suitable for ultrasonic machining may become a prominent research direction in the future. In addition, achieving UVAT for workpieces faces numerous limitations and challenges due to factors, such as workpiece shape, mass variability, and machine tool structure. Currently, no relevant research on workpiece vibration-assisted turning has been identified.

2.2. *Ultrasonic vibration-assisted milling*

The UVAM technology combines ultrasonic machining with traditional milling, applying ultrasonic vibration to the milling cutter or workpiece. Compared to traditional machining, this technique enables periodic high-frequency separation of tool parts, resulting in superior machining performance.

2.2.1. Tool ultrasonic vibration-assisted milling. Research on UVAM technology started relatively late, and published studies are mainly from the early 21st century. Many scholars [67–69] have investigated the impact of process parameters, including spindle speed, depth of cut, feed rate, vibration amplitude, and vibration frequency, on outcome performance indicators (e.g. machined surface roughness, surface topography, cutting edge, and tool wear).

Considering the impact of UVAM on machining performance, a number of investigations have demonstrated that UVAM, particularly longitudinal tool vibration-based ultrasonic milling, can significantly enhance machining performance by reducing the cutting force and improving

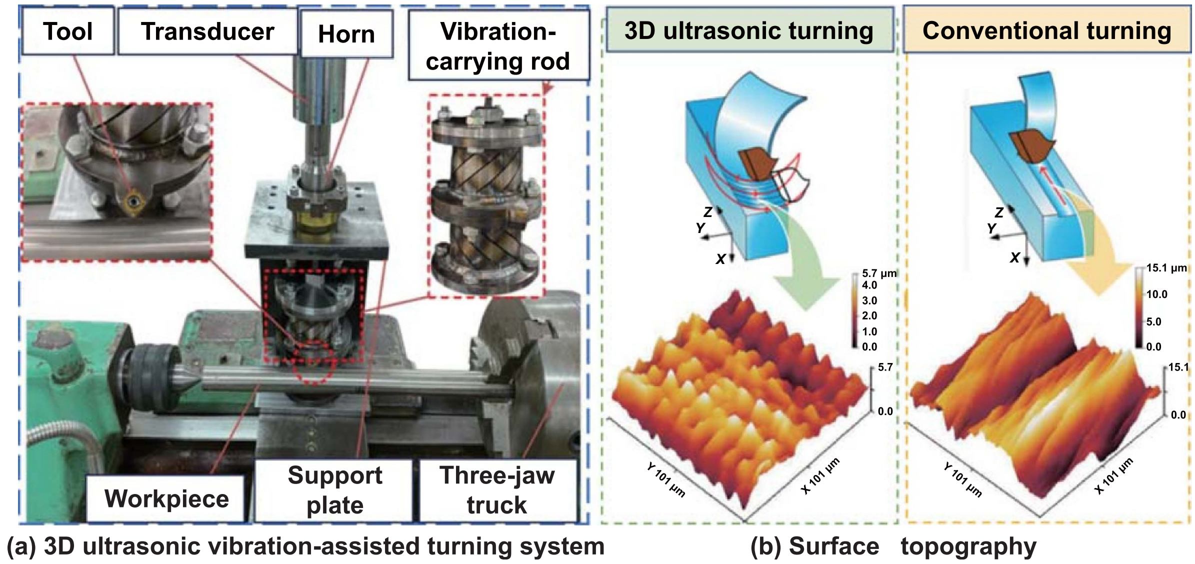

Figure 5. 3DThree-dimensional ultrasonic vibration-assisted turningUVAT and generated surface. (a) 3D UVAT system [63]. (b) Surfaces generated with 3D UVAT and conventional turning processes [63]. Reproduced from [63], with permission from Springer Nature.

tool durability. Tong *et al* [70] simulated milling with high-frequency periodic vibrations applied simultaneously into the circumferential and axial axes of cutting tools. It was found that various cutting forces frequently returned to zero, and the average cutting force decreased significantly. Hence, the deformation of the thin-walled items was substantially reduced throughout the machining process. Gao *et al* [71] realized high-frequency longitudinal torsional compound motion of AlTiN coated tool using a self-designed ultrasonic system. They carried out machining experiments on Ti–6Al–4V alloys and studied the milling cutter wear mechanism. Their results demonstrated the significant advantages of UVAM in terms of both milling forces and machined morphology. Xiong *et al* [72] used an ultrasonic vibration tool holder and PCD composite tool for milling SiC_f/SiC composite materials. Combined with UVAM, the tool service life was over four times longer than that of the traditional machining method. Ultrasonic vibration also exhibited a significant strengthening effect on the machined surface. Yin *et al* [73] found that ultrasonic vibration milling caused high-frequency squeezing of Inconel 718 workpiece by the tool, resulting in a surface hardness increase of 79.93%. In addition, ultrasonic vibration also refined the subsurface grains, and a single treatment could increase the thickness of the plastic deformation layer by nearly 80%, contributing to the improved fatigue life of the workpiece. Similarly, Xu *et al* [74] used the longitudinal UVAM method to machine Inconel 718. They found that ultrasonic high-speed impact extrusion increased the microhardness by 13.8%, while the plastic deformation thickness increased from 3.1 to 8.2 μm.

In recent years, an increasing number of researchers have focused on the effects of ultrasonic vibration on the interior of workpieces because the vibration results in residual stress inside the machined surface, which affects the machining performance of the workpiece [75, 76]. Xie *et al* [77] examined the machining pattern of longitudinal torsional UVAM of TC18 titanium alloys by applying vertical ultrasonic vibration on an end mill. The continuous machining surface impact changed the grain morphology and microstructure inside the workpiece. Under higher amplitude conditions, longitudinal torsional UVAM generated over 20% larger residual stresses and thicker (up to 5.4 μm) subsurface deformation layers than CM. Chang *et al* [78] investigated an ultrasonic vibration-assisted side milling process by clamping an ultrasonic vibration system on the tool spindle, with the goal of decreasing machining flaws during side milling of Inconel 718 superalloy. A schematic of the UVAM system and surface formation is shown in figure 6. The constant intervention of ultrasonic high-frequency energy impact not only suppressed tool clatter and surface defects but also led to subsurface grain refinement.

The aforementioned research indicates that UVAM causes milling forces to fluctuate with vibration, and thus reduces the average milling force, due to the fast separation cutting mechanism and influence of the dynamic cutting thickness. At the same time, the workpiece achieves better processing quality and has a broad application space, owing to the constant effect of ultrasonic energy.

2.2.2. Workpiece vibration-assisted milling. Workpiece vibration-assisted milling is a machining technique that enhances the performance of traditional milling by applying auxiliary ultrasonic vibrations to the workpiece [79, 80]. In recent years, researchers have primarily concentrated on investigating the effects of various machining and vibration parameters on milling outcomes as well as exploring the impact of ultrasonic vibrations on workpiece surface morphology and tool wear mechanisms.

In recent years, many academics have examined the influence of machining settings and vibration parameters on milling performance. Fang *et al* [81] investigated the effects

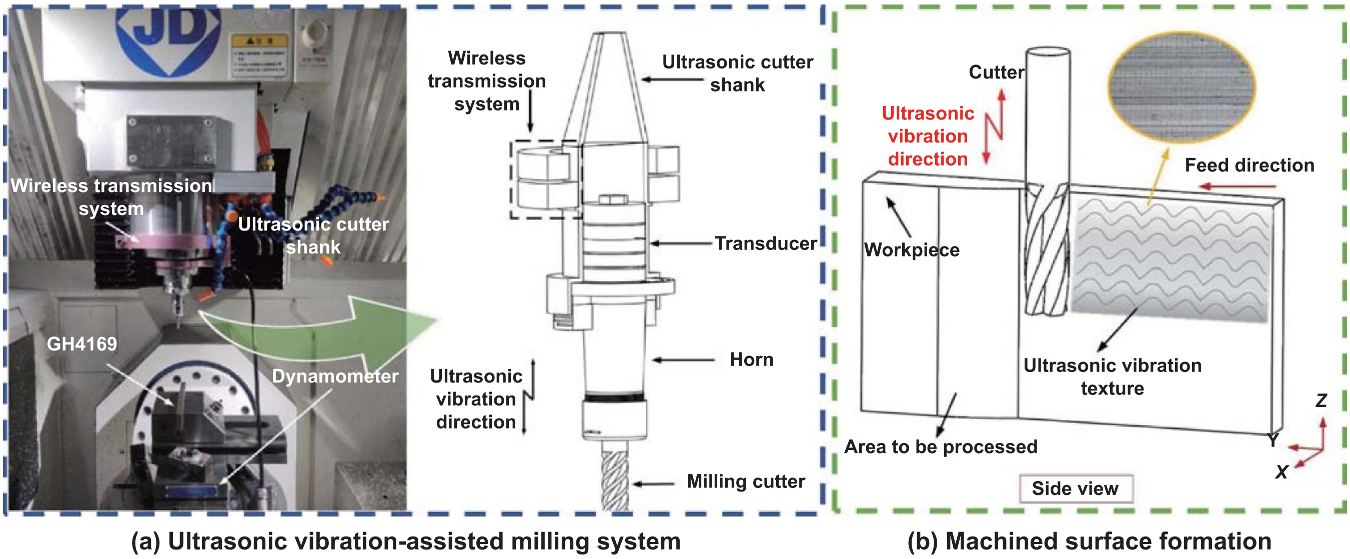

Figure 6. Schematic diagram of the UVAM system and surface formation. (a) UVAM system [78]. (b) Formation of ultrasonic vibration texture on the machined surface [78]. Reprinted from [78],

of feed per tooth on milling force and surface morphology of a high-temperature nickel-based alloy. Properly increasing the feed per tooth effectively suppressed the formation of stacked edges and reduced defects, such as pits, protrusions, and grooves, caused by traditional micro-milling processes. Shen and Xu [82] used vibration to guide a workpiece along the tool feed direction and investigated the influence of vibration amplitude on milling performance. It was found that a larger ultrasonic amplitude leads to excessive mechanical shock and tool instability.

In addition, some studies have focused on the role of ultrasonic milling in the functionalization and texturing of a machined surface. Börner *et al* [83] added ultrasonic vibrations to a workpiece during surface milling to achieve functionalization of the sample surface. Lu *et al* [55] investigated the mechanism of ultrasonic vibration-assisted surface texture generation and achieved quantitative design of surface textures. Ni *et al* [84] designed a workpiece UVAM system consisting of four parts (i.e. the ultrasonic vibration system, CNC machining center, online monitoring system, and data acquisition system), as shown in figure 7. Traditional cutting produced obvious tool marks, protrusions, and jumps, whereas ultrasonic milling resulted in homogeneous vibration textures on the machined surface due to the constant separation and contact between the cutting edge and the workpiece.

Regarding the wear mechanism of cutting tools in UVAM, Maurotto and Wickramarachchi [85] investigated the effect of ultrasonic vibration frequency on milling cutter damage characteristics. They discovered that the ultrasonic vibration frequency had a significant influence on tool wear. Ni *et al* [65] discovered that during the ultrasonic vibration cycle, the rapid change of friction and friction direction easily generated microcracks at the tool tip, and the effect of high-frequency pulse cutting forces and alternating stiffness aggravated tool wear, eventually causing tool fatigue failure.

In summary, both tool and workpiece vibration-assisted milling processes have the potential to enhance the machining performance. However, the relatively simple structure of tool ultrasonic vibration system exerts a greater influence on work hardening and residual stress. The application of ultrasonic vibration to workpieces offers significant advantages in enhancing machining quality and surface morphology. However, varying the processing conditions requires distinct process optimizations to avoid negative processing effects.

2.3. *Ultrasonic vibration-assisted grinding*

UVAG applies ultrasonic frequency vibrations to a grinding wheel or workpiece during conventional grinding, resulting in a surface finish that is processed through a combination of ultrasonic frequency vibrations and the grinding wheel. In the past few years, ultrasonic-assisted machining has gained increasing popularity in the grinding of difficult-to-cut materials because it effectively addresses a range of issues, such as high grinding forces, poor surface quality, severe wheel wear, and limited lifespan associated with traditional machining processes.

2.3.1. Tool ultrasonic vibration-assisted grinding. Tool UVAG is a process in which an ultrasonic transducer is tightly connected to the grinding wheel through a spring chuck or other connection methods, forming a resonant system that generates ultrasonic vibration in a fixed direction and frequency within the grinding wheel. Recent research includes exploration of the impact of vibration parameters on machining quality, material removal processes, and wear reduction mechanisms.

Several studies have confirmed the benefits of utilizing ultrasonic-assisted grinding tools to achieve high-quality

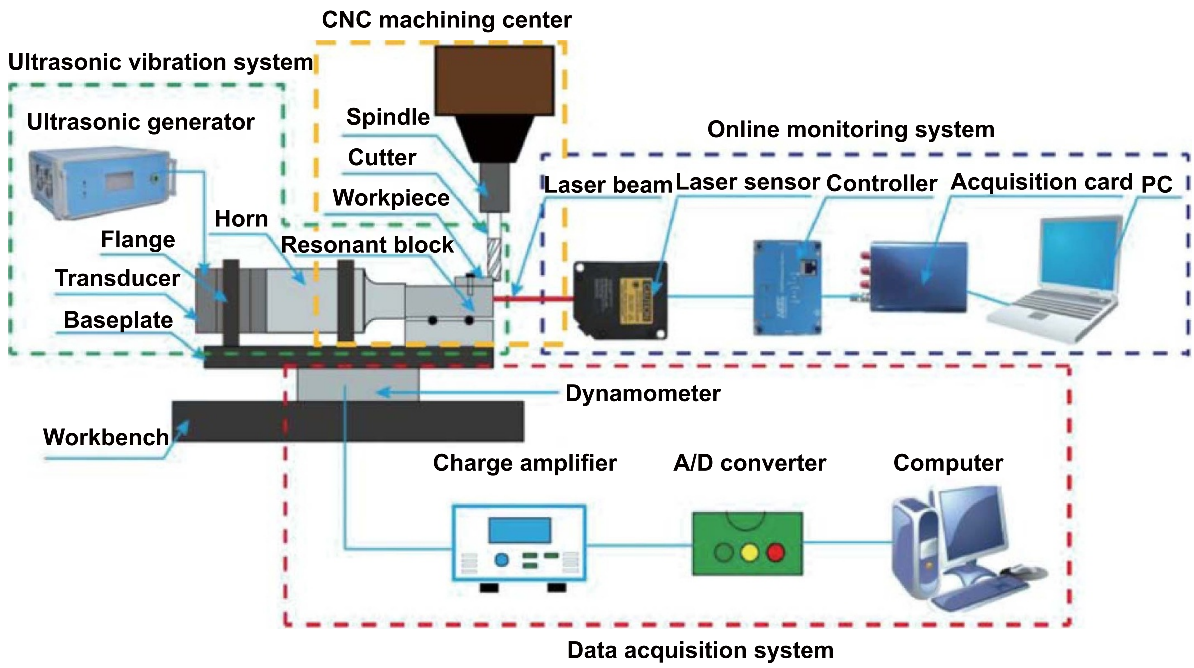

Figure 7. Schematic of a workpiece UVAM system [84]. Reprinted from [84], © 2018 Elsevier Ltd. All rights reserved.

material removal across various machining and vibration parameters [86]. Li *et al* [87] combined vibration-assisted machining technology with abrasive belt grinding, as shown in figure 8. They experimentally analyzed the impact of linear speed and feed rate on the machined surface and simulated the material removal mode of sand belts with flexible characteristics under vibration assistance. Compared with traditional belt grinding, this technology reduced surface roughness by 25% and generated a peak-like intermittent texture surface morphology of Inconel 718 superalloys. At the same time, the impact strengthening of abrasive particles increased the residual compressive stress on the surface more than twice. Qin *et al* [88] developed a new theoretical model to predict the machined surface morphology after studying the surface characteristics of UVAG of hard brittle materials. Smaller feed rates and larger ultrasonic amplitudes were found to be more suitable for UVAG processes.

Ultrasonic vibration is widely used in grinding because of reduced friction. Although many attempts have been made to analyze it from the perspective of kinematics in the literature, the friction mechanism of the tool–workpiece contact remains unknown. Because of the Poisson effect, when ultrasonic vibration is applied in the spindle direction, the tool can generate an additional amplitude of 0.4 μm along the radial direction. Zhou *et al* [89] proposed a new predictive model for calculating the plowing friction coefficient with the assistance of two-dimensional ultrasonic vibration and attempted to explain the friction reduction mechanism of ultrasonic vibration in view of the tool–workpiece contact deformation process. Ultrasonic waves drive the grinding wheel in both radial and circumferential directions to generate high-frequency vibrations. Feng *et al* [90] applied ultrasonic vibration to diamond grinding wheels for machining blind holes in hard alloys. The UVAG process, characterized by a high overlap rate of motion trajectories, reduced the grinding forces. The high-frequency vibration changed the contact state between the abrasive grains and workpiece, reducing friction and improving the cooling and lubrication properties of cutting fluids.

The tool ultrasonic vibration machining process does not have strict requirements for the shape and size of the workpiece and can be used to process complex-shaped parts. Therefore, it has received widespread attention from scholars and industries. However, the size of the grinding wheel is limited, which in turn limits the grinding speed and material removal efficiency because ultrasonic vibrations must meet system resonance conditions.

2.3.2. Workpiece ultrasonic vibration-assisted grinding. The UVAG process for workpieces involves the utilization of an ultrasonic vibration platform to achieve workpiece vibration during the grinding process. Currently, researchers are primarily focused on developing workpiece vibration platforms and studying the complex machining processes that involve auxiliary procedures.

Compared with tool ultrasonic vibration, workpiece ultrasonic vibration requires specific equipment designs based on the characteristics of part structure, material, size, and ultrasonic vibration direction [91, 92]. Therefore, equipment structures for workpiece ultrasonic vibration vary widely [93]. Paknejad *et al* [94] created a special ultrasonic vibration device for workpiece to achieve low-temperature slow feed deep grinding. Cao *et al* [95] investigated the influences of two-dimensional vibration coupling on workpiece UVAG. Compared with conventional grinding, the optimized

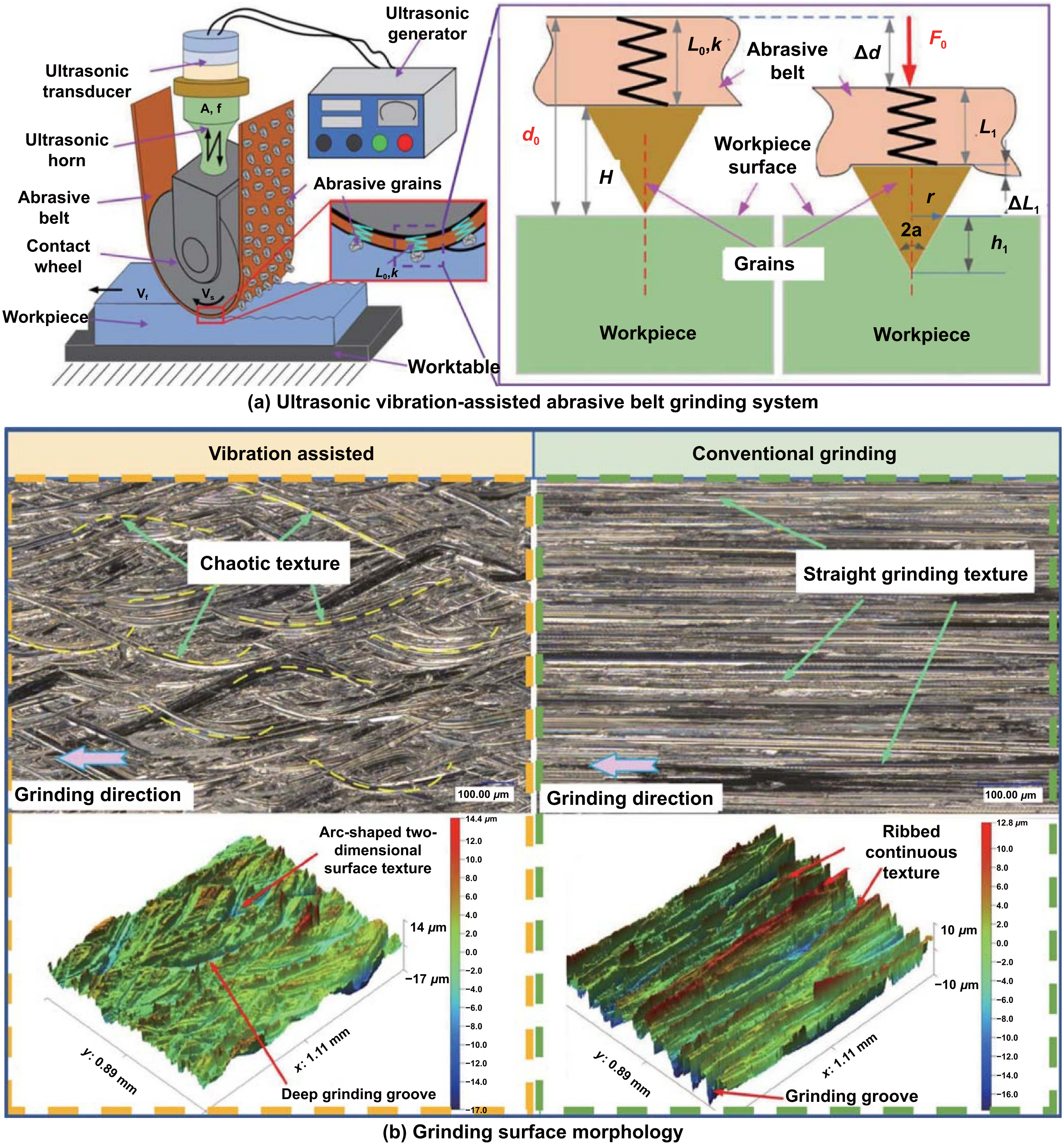

Figure 8. Ultrasonic vibration-assisted abrasive belt grinding and generated surface morphology. (a) Schematic of the process [87]. (b) Comparison of surface morphology generated with and without vibration assistance [87]. Reprinted from [87], © 2022 The Society of Manufacturing Engineers. Published by Elsevier Ltd. All rights reserved.

two-dimensional workpiece UVAG reduced the cutting force and surface roughness by more than 10%. Zhao *et al* [96] created an innovative radial UVAG device, as illustrated in figure 9. The vibration converter designed with a special cross structure can achieve better vibration uniformity. The intermittent cutting action of UVAG minimized the proportion of sliding and plowing, as depicted in figure 9(b). MRR was increased by 2.8 times, whereas the grinding temperature was reduced by more than 20%.

Combining UVAG with other auxiliary processes can further improve the MRR. Singh and Sharma [97] introduced ultrasonic vibration with an actual amplitude of 9.2 μm into a workpiece, supplemented by atomized cutting fluids to achieve double-assisted vibratory grinding of nickel-based

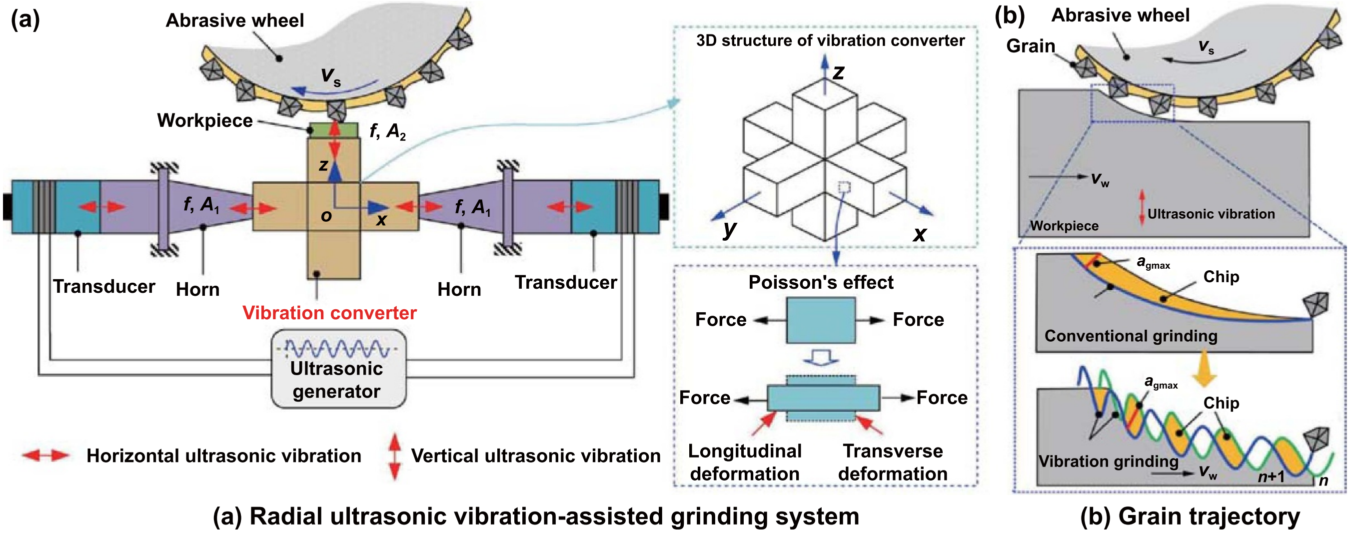

Figure 9. Schematic of (a) radial UVAG system and (b) grain trajectory [96]. Reproduced with permission from [96]. © 2023 Production and hosting by Elsevier Ltd on behalf of the Chinese Society of Aeronautics and Astronautics.

superalloys. Ultrasonic vibration softened the material and reduced the cutting force by more than 50%. Simultaneously, the intermittent cutting effect of ultrasonic vibrations facilitated the entry of tiny lubricating droplets into the grinding area, thus allowing the wetting and spreading properties of the cutting fluid to be fully utilized and reducing the optimal surface roughness by 46.48%.

When ultrasonic vibration is applied to the tool, the effective tool diameter becomes smaller, resulting in a low grinding speed and, consequently, a reduced MRR. The workpiece UVAG process applies vibrations to the workpiece platform, and the grinding wheel is not affected. Therefore, the workpiece UVAG can be carried out using large-diameter grinding wheels, achieving slow near-deep grinding, high-speed grinding, and efficient deep grinding. It is especially suitable for working conditions with a high grinding load and high MRR. However, the quality, material, and shape of the workpiece can all have an impact on the effectiveness of ultrasonic vibration. Existing ultrasonic vibration processing devices are limited by power and other factors, making it difficult to achieve ultrasonic vibration on large, heavy, and complex materials and workpiece shapes, which affects their industrial application. Wang *et al* [98, 99] used both workpiece vibration and tool vibration to achieve three-dimensional rotational ultrasonic vibration for machining CFRP materials. Two ultrasonic power sources were used to drive the workpiece horizontal ultrasonic vibration and tool vertical vibration, which were superimposed with the grinding rotational motion to form a special three-dimensional abrasive grain motion trajectory, as shown in figure 10. The grinding force and ground surface roughness were lower in 3D rotary UVAG than in conventional rotary UVAG. However, compared with tool ultrasonic vibrations, the workpiece ultrasonic vibration system is more specific according to the particular material properties and structures of components. Therefore, the module cannot be universally applied to machine different components.

The UVAG technique is well suited for processing small and medium-sized workpieces, while also being capable of accommodating large-diameter grinding wheels. This makes it particularly suitable for working conditions characterized by high grinding loads and MRRs. Moreover, there is no universally fixed equipment structure for workpiece ultrasonic vibration, and specific designs must be tailored based on the characteristics of the part structure, material, size, and ultrasonic vibration direction. Consequently, the equipment structure for ultrasonic vibration of workpieces exhibits a greater degree of diversity.

Because of the sensitivity of the ultrasonic vibration system to the load, excessive loading can disrupt its stability and alter the resonant frequency. Therefore, ultrasonic vibration-assisted drilling is primarily suitable for machining conditions with low or uniform loads. Compared with high-frequency vibration machining, low-frequency vibration is typically generated by a mechanical vibration device with a higher loading capacity and larger amplitude, resulting in the ability to achieve a higher MRR [100]. Many studies [101–104] have demonstrated the efficacy of high-frequency vibration-assisted drilling in enhancing hole quality. However, low-frequency vibration-assisted drilling is hampered by challenges, such as the intricate development of vibration equipment and suboptimal stability. To address these issues, it is recommended to conduct further analysis on the specific impact patterns of vibration on tool–workpiece interaction, including tool trajectory, cutting angle, and chip breaking mechanism.

Overall, the integration of ultrasonic vibration with traditional machining techniques is a highly effective approach for enhancing the machining performance. Table 1 presents a comparison of the output parameters of various ultrasonic

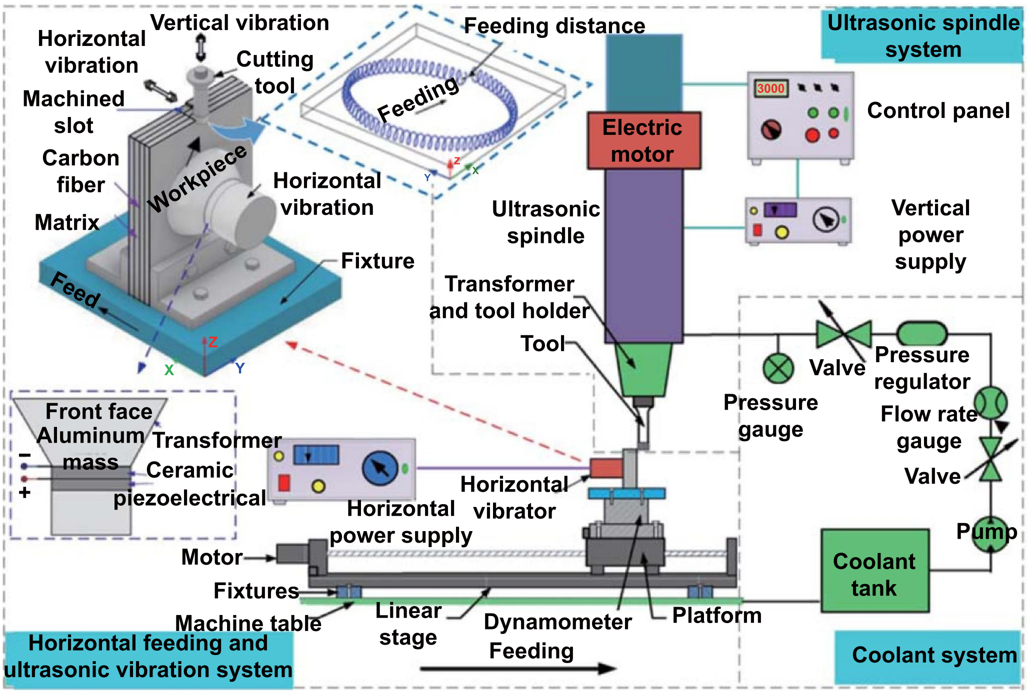

Figure 10. Schematic of 3D rotating ultrasonic vibration machining [99]. Reprinted from [99],

vibration-assisted machining processes and conventional mechanical machining processes. However, the current vibration-assisted machining systems often possess intricate configurations and large footprints that are frequently added to or modified from existing machine tools, rendering their implementation challenging. Novel ultrasonic vibration-assisted machining systems can be designed using professional-grade machine tools and other equipment tailored to match. During ultrasonic vibration-assisted machining, the tools, as the primary object of high-frequency vibration, often endure prolonged dynamic impact loads, thereby imposing new and elevated demands on machining tools. This necessitates the development of novel tools that are suitable for ultrasonic vibration to meet increasingly exacting machining requirements. The technology of ultrasonic vibration-assisted machining tools has undergone rapid development and boasts broad application prospects, yet its MRR remains relatively low. Conversely, the system of workpiece ultrasonic vibration-assisted machining is comparatively simple and yields a high MRR. However, the promotion and application of this method are hindered by severe restrictions on the size, weight, and shape of the processed workpiece. Further development is necessary to fulfill the ultrasonic equipment requirements for power, workpiece shape, and size. Although there is currently some research on the mechanism of ultrasonic vibration-assisted machining, most of it is based on analyzing experimental results and process characteristics, lacking a unified and scientifically quantitative description. Therefore, it is critical to increase the use of finite-element technology and develop new mathematical models and characterization techniques.

3. Laser-assisted mechanical machining

It is well known that the strength and hardness of most materials tend to decrease upon heating. In addition, the microstructure or phase of these materials may be altered at elevated temperatures. This phenomenon is behind the development and innovation of heat-assisted machining [112–114]. In heat-assisted mechanical machining, an external heating source is utilized to heat the local workpiece material prior to mechanical machining, resulting in softening or modification of the material. As a result, a reduced cutting force and prolonged tool life are achieved. For hard materials, such as ceramics and cemented carbides, their deformation behavior at elevated temperatures is transformed from brittle to ductile, which is beneficial for improving the quality of the machined surface. According to the type of heating source, heat-assisted mechanical machining can be classified into laser-assisted mechanical machining, induction-assisted mechanical machining (using an induction coil as the heating source), flame-assisted mechanical machining (using acetylene gas as the heating source), and plasma-assisted mechanical machining.

Owing to the advantages of lasers in terms of energy concentration, fast processing, good controllability, and high accuracy, laser-assisted mechanical machining has become a research hotspot [115–121]. Laser-assisted mechanical machining is a hybrid process that uses a laser to reduce the physical/mechanical properties of materials or to modify the phase/microstructure of local materials to improve machinability. According to the output waveforms, lasers can be divided into two categories: continuous-wave lasers and

Table 1. Ultrasonic vibration-assisted mechanical machining processes and output parameters. (↑: increased by.↓: decreased by)

Reference	Workpiece material	Hybrid process	Process parameters	Output parameters (compared with conventional)
Jamshidi and Nategh [56]	Al 6061	UVAT	Cutting speed: 27 m min^{-1} Frequency: 20 kHz Amplitude: 4–10 μm	Normal force: ↓19%–82% Friction force: ↓24%–76%
Peng *et al* [57]	Ti–6Al–4V	High-speed ultrasonic vibration cutting	Frequency: 22 kHz Amplitude: 20 μm Cutting speed: 200 m min^{-1} Feed: 0.05 mm rev^{-1} Depth of cut: 0.1 mm	Cutting force: ↓40% Surface roughness: ↓1.7%–20.4%
Duan *et al* [59]	AISI 304	3D UVAT	Frequency: 20/30 kHz Cutting speed: >320 rpm Depth of cut: 0.05 mm Feed: 0.08 mm rev^{-1}	Cutting force: ↓63.5%
Zhou *et al* [105]	SiC_p/Al	Ultrasonic elliptical vibration-assisted turning	Frequency: 43.194 kHz Amplitude: 3.9/3.59 μm Cutting speed: 200 mm min^{-1} Feed: 0.2 mm rev^{-1} Depth of cut: 0.025 mm	Surface roughness: ↓20%
Kang *et al* [106]	GH4068 super alloy	UVAT	Frequency: 18 kHz Amplitude: 3–12 μm Cutting speed: 14–66 m min^{-1} Feed: 0.08–0.24 mm rev^{-1} Depth of cut: 0.05–0.25 mm	Cutting force F_x: ↓44% Cutting force F_y: ↓63% Surface roughness: ↓31%
Bertolini *et al* [107]	SiC/Al	UVAT	Frequency: 30 kHz Amplitude: 5 μm Cutting speed: 60/120 m min^{-1} Feed: 0.02/0.06/0.1 mm rev^{-1} Depth of cut: 0.05 mm	Tool wear: ↓51% Surface roughness: ↓21%
Tong *et al* [70]	TC4 titanium alloy	Longitudinal–torsional composite UVAM	Frequency: 35 kHz Amplitude of the longitudinal wave: 8 μm Spindle speed: 1000 rpm Feed per tooth: 0.09 mm z^{-1}	Radial cutting force: ↓17.4%–31.3% Feed cutting force: ↓5.4%–38.7%
Xie *et al* [77]	TC18 titanium alloy	Longitudinal–torsional UVAM	Feed per tooth: 0.01–0.04 mm z^{-1} Cutting speed: 15–45 m min^{-1} Depth of cut: 0.5 mm Amplitude: 2–5 μm	Surface roughness: ↑29.82%–42.63% Residual stress: ↑20.62%–35.88% Depth of the plastic deformation layer: ↑134.78%
Shen and Xu [82]	2A12 aluminum alloy	UVAM	Feed per tooth: 3 μm z^{-1} Spindle speed: 3000 rpm Depth of cut: 0.2 mm Frequency: 19.58 kHz Amplitude: 7 μm	Maximum milling force: ↓21.7%
Yin *et al* [73]	Inconel 718	Ultrasonic vibration ball end mill	Feed per tooth: 0.025 mm z^{-1} Spindle speed: 4000 rpm Depth of cut: 0.05 mm Frequency: 21 kHz Amplitude: 6 μm	Surface hardness: ↑79.93% Surface residual compressive stress: ↑29.4% Thickness of the plastic deformation layer: ↑79.5% Fatigue life of the workpiece: ↑210%
Xu *et al* [108]	Inconel 718	Cryogenic UVAM	Feed rates: 30–70 mm min^{-1} Spindle speed: 80–3000 rpm Radial depth: 0.1 mm Axial depth: 1.5 mm Frequency: 43.26 kHz Amplitude: 3.07 μm	Cutting force: ↓36.5% Surface roughness: ↓39.1%

(Continued.)

Table 1. (Continued.)

Reference	Workpiece material	Hybrid process	Process parameters	Output parameters (compared with conventional)
Li *et al* [109]	TC18 titanium alloy	Ultrasonic-assisted milling	Feed rates: 4–28 μm rev^{-1} Cutting speed: 15–45 m min^{-1} Depth of cut: 0.1–0.4 mm Amplitude: 0–3.5 μm	Cutting force: ↓15% Peak temperature: ↓42% Residual compressive stress: ↑40% Surface roughness: ↓44%
Xu *et al* [74]	Inconel 718	Longitudinal UVAM	Spindle speed: 3000 rpm Feed rates: 50–150 mm min^{-1} Depth of cut: 0.05–0.11 mm Frequency: 30.8 kHz Amplitude: 3.12 μm	Cutting force: ↓23.3% Average cutting temperature: ↓19.8% Microhardness: ↑13.8
Li *et al* [87]	Inconel 718	Ultrasonic-assisted abrasive belt grinding	Depth of cut: 0.05 mm Line speed: 2–4 m s^{-1} Feed speed: 2–8 mm s^{-1} Frequency: 24.62 kHz Amplitude: 10 μm	Surface roughness: ↓25% Surface residual compressive stress: ↑110%
Cao *et al* [95]	Inconel 718	UVAG	Grinding speed: 10–30 m s^{-1} Workpiece infeed speed: 100–400 mm min^{-1} Depth of cut: 0.1–0.4 mm Frequency: 20 kHz	Normal grinding force: ↓15% Tangential grinding force: ↓11% Surface roughness R_a: ↓10%
Zhao *et al* [96]	Particle-reinforced titanium matrix composites	Radial UVAG	Amplitude: 5 μm Frequency: 19.5 kHz Amplitude: 5 μm Depth of cut: 20–80 μm Grinding speed: 90–120 m s^{-1}	Tangential grinding force: ↓5.0%–17.2% Normal grinding force: ↑6.5%–14.9% Grinding temperature: ↓24.2%–51.8% Removal rate: ↑280%
Wang *et al* [110]	γ-TiAl	Ultrasonic vibration-assisted high-efficiency deep grinding	Grinding speed: 80–140 m s^{-1} Workpiece speed: 1.5–6 m min^{-1} Depth of cut: 0.15–0.6 mm Ultrasonic frequency: 19.56 kHz Ultrasonic amplitude: 8 μm	Normal grinding force: ↓38.69% Grinding temperature: ↓39.05% Specific grinding energy: ↓23.95 Surface roughness: ↓19.53%
Huang *et al* [111]	Hardened GCr15 steel	UVAG	Grinding speed: 15–30 m s^{-1} Feed speed: 4–10 m min^{-1} Depth of cut: 10–25 mm Ultrasonic frequency: 19.6 kHz Ultrasonic amplitude: 6 μm	Normal grinding force: ↓18.91% Tangential grinding force: ↓20.51% Surface roughness: ↓9.47%

pulsed lasers. Continuous-wave lasers with relatively high power are employed to heat and soften the local workpiece material, resulting in decreased properties and increased machinability. Pulsed lasers can be classified into millisecond, microsecond, nanosecond, picosecond, and femtosecond lasers according to the range of the pulse width. Generally, the effects of millisecond, microsecond, and nanosecond lasers on materials are the same as those of continuous-wave lasers. On the contrary, due to the ultrashort pulse width, picosecond and femtosecond lasers possess ultrahigh instantaneous energy density, resulting in direct material removal.

The physical process of laser–material interaction is essentially the interaction between the electromagnetic field (optical field) and material microstructure, involving resonance interaction and energy conversion. It is a cross-coupling process of disciplines, such as optics, thermodynamics, and mechanics. When a laser beam is irradiated onto a material, several physical and chemical changes occur on both the surface and subsurface. Under the irradiation of continuous-wave or long-pulse laser, energy is absorbed by the material through the conversion of incident photons, stimulated electrons, and phonons. As a result, a three-phase thermal melting process of solid–liquid–gas takes place, and material processing is achieved. However, thermal energy also diffuses to the adjacent zones of the irradiated area due to heat conduction, resulting in undesired thermal effects or severe thermal damage.

As the laser pulse width decreases, the area and degree of thermal effects and damage also decrease. The pulse widths of ultrafast pulsed lasers are much smaller than both the thermal diffusion time and the electron–phonon coupling time in the

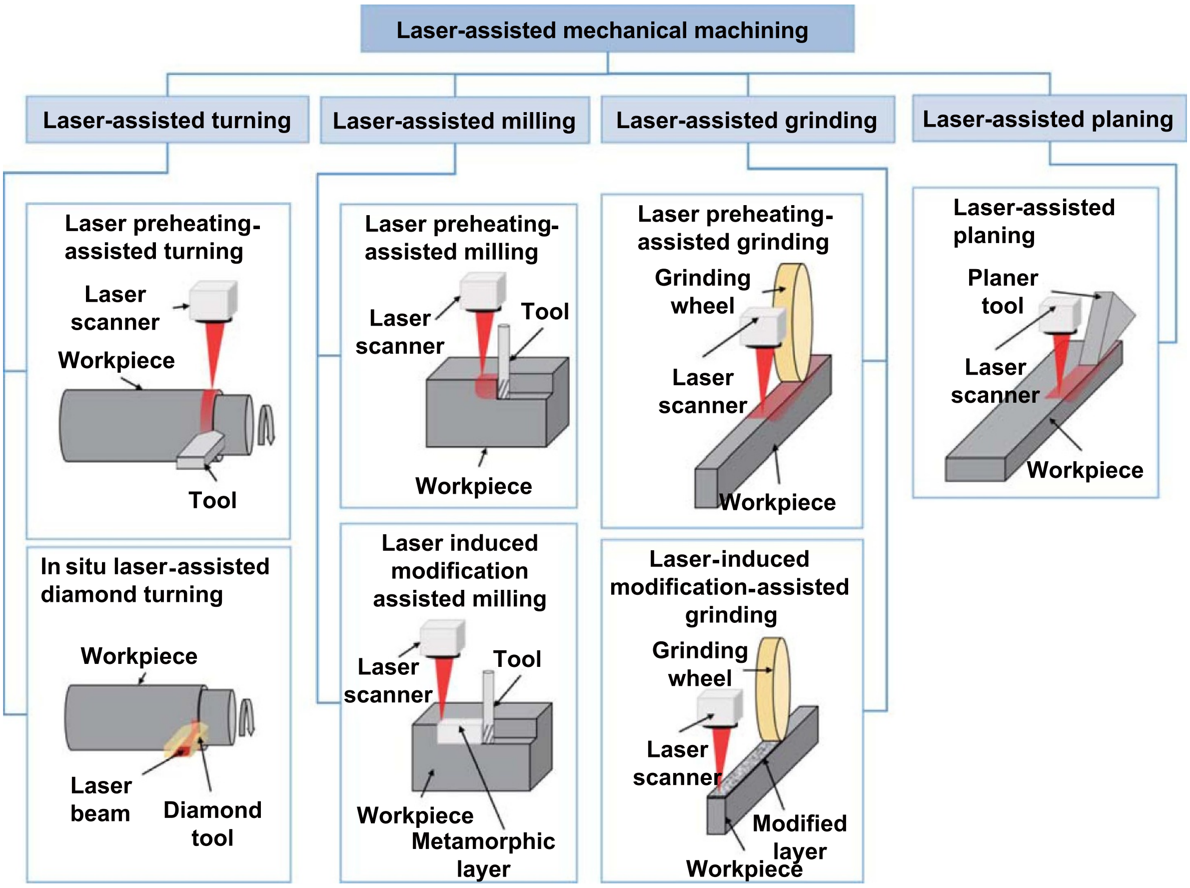

Figure 11. Classification diagram of laser-assisted mechanical machining.

material. Therefore, it is necessary to consider only the excitation and energy storage processes of electron absorption of incident photons during laser irradiation, while the electron temperature resulting from the cooling of radiative phonons and thermal diffusion processes can be completely ignored. The interaction between the laser and the material mainly manifests as the process of stimulated absorption and energy storage by electrons, fundamentally avoiding the transfer, conversion, and existence of energy, as well as the effects caused by thermal energy and thermal diffusion, achieving nonthermal melting processing with lasers [122–124].

To date, research on laser-assisted mechanical machining has mainly focused on LAT, milling, grinding, and planing. The detailed framework of laser-assisted mechanical machining technologies is illustrated in figure 11.

3.1. Laser-assisted turning

LAT is a popular research interest in the field of LAM. The current research on LAT is mainly focused on two aspects: laser preheating-assisted turning and *in situ* laser-assisted diamond turning.

3.1.1. Laser preheating-assisted turning. Laser preheating-assisted turning mainly uses laser-induced thermal effects to soften the irradiated local material in advance, thereby enhancing its machinability and reducing the cutting force during subsequent turning. A schematic illustrating its principle is depicted in figure 12(a). During the machining process, the temperature of the material to be removed can be controlled by manipulating the laser parameters, such as varying the laser power or adjusting the distance between the laser spot and the tool tip. Research has indicated that the strength of materials undergoes changes at different temperatures. At elevated temperatures, materials tend to soften, resulting in a decrease in strength, as illustrated in figure 12(b). This softening effect makes them more amenable to the machining processes. Therefore, scholars have conducted extensive research on laser preheating-assisted turning [125–130]. Attia *et al* [131] investigated the processing characteristics of Inconel 718 in laser-assisted high-speed turning, and a comparison with dry turning process was performed. The results demonstrated that under optimal LAT conditions, a significant reduction in cutting forces and improvement in surface finish were achieved in the hybrid process, as shown in figures 12(c) and (d), respectively. Moreover, the MRR of the hybrid process increased by approximately 800%. Wei *et al* [132, 133] reported a new LAT approach to process silicon carbide particle-reinforced aluminum matrix composite (SiC_p/Al composite), employing a high-speed and high-density continuous-wave

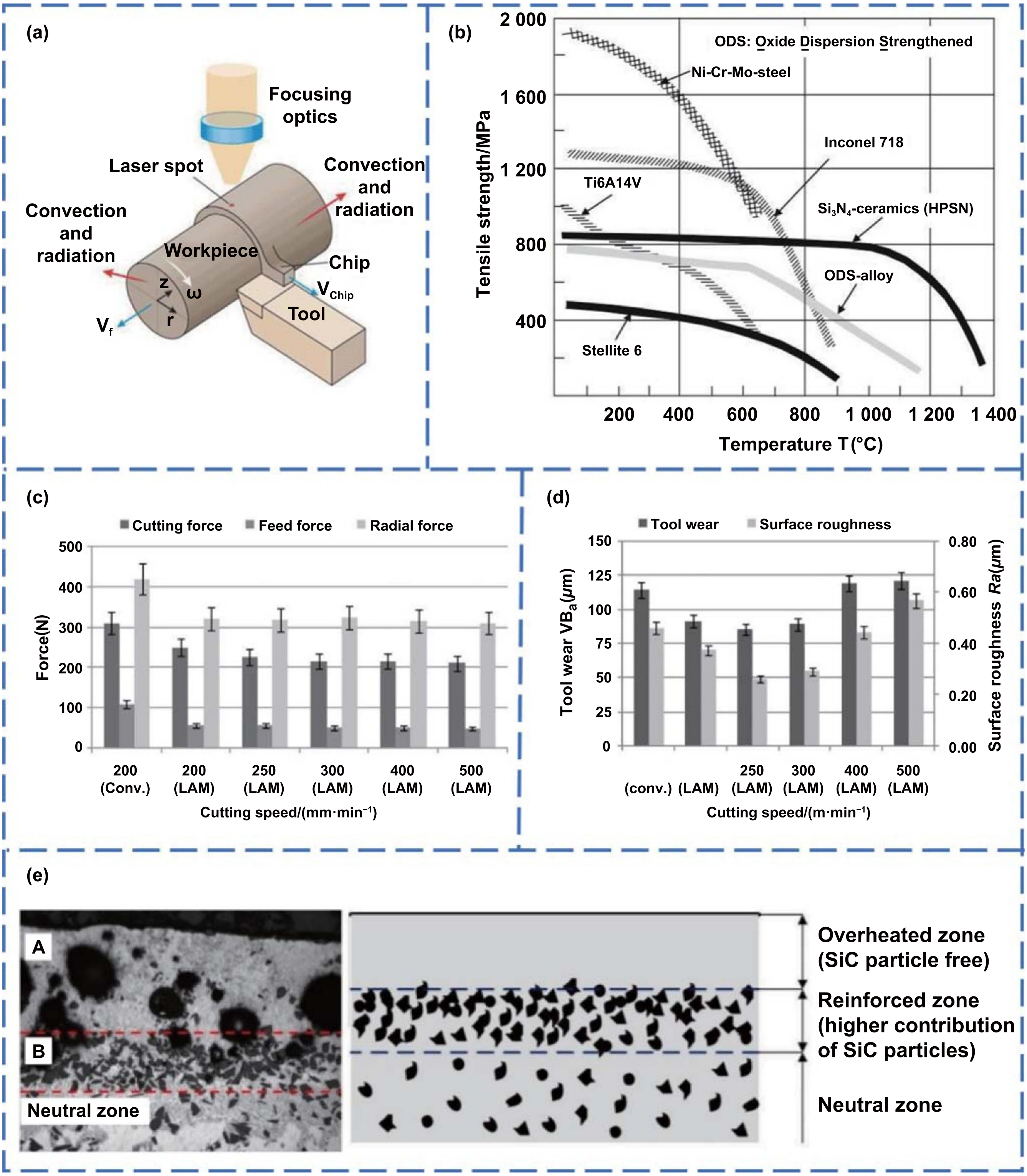

Figure 12. Laser preheating-assisted turning process and outcomes. (a) Schematic of LAT [43]. (b) Strength of various materials at elevated temperatures [43]. (c) Comparison of resultant forces between conventional turning and LAT under various cutting speeds [131]. (d) Comparison of tool wear between conventional turning and LAT under various cutting speeds [131]. (e) Cross-sectional morphology showing particle deposition that resulted from laser heating [135].

laser. A high cutting speed was used to ensure the timely removal of the locally heated material, thereby reducing heat conduction from the heated material to adjacent areas. The experimental results demonstrated that compared to conventional machining, LAT reduced the cutting force by 62.5% and decreased tool wear by 65%. Moreover, the machined surface exhibited superior quality, with a reduction in surface roughness of 75.4%. Xu *et al* [134] carried out a fully coupled thermomechanical simulation of LAT Ti–6Al–4V alloy to study the formation mechanism and morphological evolution of serrated chips. Their results indicated that the chip morphology was mainly influenced by the thermoplastic instability caused by laser heating. Przestacki *et al* [135, 136] found that two distinct layers were formed on the workpiece surface of an A359/20SiC$_p$ composite after laser heating, as shown in figure 12(e). The top layer was an overheated zone free of SiC particles or possessing a small amount of them. The second layer was a reinforced zone with a higher contribution of SiC particles. The formation mechanism of the layer structure was the sedimentation of SiC particles in the liquid aluminum matrix resulting from laser overheating. The unique phenomenon of enhanced particle deposition resulting from laser heating can yield numerous beneficial effects on machining. Because of the deposition of the reinforced phase particles, there were fewer SiC particles in the upper layer of the material, making it easier to remove. As a result, the cutting forces in LAT were significantly reduced, tool wear was reduced by approximately 50%, and surface roughness was decreased by 32%. Furthermore, the post-machining surface acquired more reinforced phase particles through deposition, leading to a 27% improvement in surface wear resistance.

3.1.2. In situ laser-assisted turning. The high-efficiency and ultraprecision machining of hard and brittle materials, such as ceramics, cemented carbides, and sapphire, has always been a hot topic. Studies have demonstrated that the brittle-to-ductile transition mechanism plays an important role in achieving a super surface finish of brittle materials. *In situ* LAT is a hybrid process in which a laser beam is delivered through a cutting tool, focusing on the material. Diamond cutting tools are mostly used in this process because of their good transparency and low absorptivity to lasers. The *in situ* laser increases the ductility and machinability of the local material. Dong [137] incorporated a laser heating system into the SPDT process, forming an *in situ* LAT platform. Experiments on the hybrid processing of silicon wafer showed that the cutting force and tool wear were reduced, which can be ascribed to thermally softened high-pressure phase transformation of silicon (covalent to metallic crystalline structure). You *et al* [138–140] proposed an HE-LAT method and conducted experiments on binderless tungsten carbide (WC). A schematic of the HE-LAT process is shown in figure 13(a). The laser beam passes through a diamond tool, refracts at the tool rake face and cutting edge, and then totally reflects at tool flank face, as shown in figure 13(b). In this process, surface fluctuation was effectively eliminated, and a great surface finish with S_a of 0.92 nm was achieved. In addition, local graphitization of the diamond tool was suppressed, and chip adhesion on tool cutting edge was inhibited effectively, which can be attributed to the relatively low laser power. Zhang *et al* [141, 142] studied the brittle-to-ductile transition behavior of reaction-bonded silicon carbide (RB SiC). Grooving experiments were performed under both conventional and *in situ* laser-assisted diamond cutting conditions. The results showed that the critical depth of cut for the brittle-to-ductile transition of RB SiC was increased from 52.2 nm in conventional cutting to 106.7 nm in *in situ* laser-assisted diamond cutting. The increment of critical depth of cut allows higher cutting parameters to be used in the hybrid process, thus improving the MRR. By employing *in situ* LAT, a significant reduction in surface defects can be achieved. Compared to turning without laser assistance, the surface roughness was reduced by 84.3%, and tool wear was greatly diminished, as shown in figures 13(c) and (d), respectively. Park *et al* [143] also observed a reduction in cutting force (by approximately 30%) and surface roughness (by approximately 68%) in *in situ* laser-assisted cutting of Zr bulk metallic glasses, compared to those in conventional cutting.

3.2. Laser-assisted milling

Current research on laser-assisted milling is mainly focused on laser preheating-assisted milling. Laser heating can effectively reduce the milling force and improve the machinability of materials [144]. Scholars have primarily studied the effects of laser parameters and laser scanning paths on machining.

3.2.1. Laser preheating-assisted milling. Yang *et al* [145] studied the effect of laser preheating on tool edge chipping during laser-assisted milling of silicon nitride (Si_3N_4) ceramics. When the temperature of a laser preheated material was between 1300 °C and 1400 °C, a substantial decrease in edge chipping was achieved. This resulted from the reduced cutting force in the laser preheating-assisted milling process. To predict the temperature near the edge of zinc oxide (ZnO) ceramics irradiated by a laser, Muženič *et al* [146] established a novel transient analytical thermal model and carried out a theoretical analysis and experimental verification. Their results revealed that the propagation of intergranular fracture of ZnO material was prevented at elevated temperatures. The surface damage could be controlled by adjusting the process parameters, and the minimum damage was realized at a temperature of 380 °C and a feed per tooth of 0.18 mm. Ding *et al* [147] performed thermal and mechanical modeling analysis of LAMM of difficult-to-cut materials, including Ti–6Al–4V alloy, Inconel 718 alloy, and stainless steel AISI 422. They found that proper heating of the local material in front of the cutting tool reduced or eliminated the formation of BUE.

Lasers can be easily controlled spatially and temporally by adjusting parameters, such as laser power, frequency, scanning speed, and scanning path. Shang *et al* [148] proposed a novel

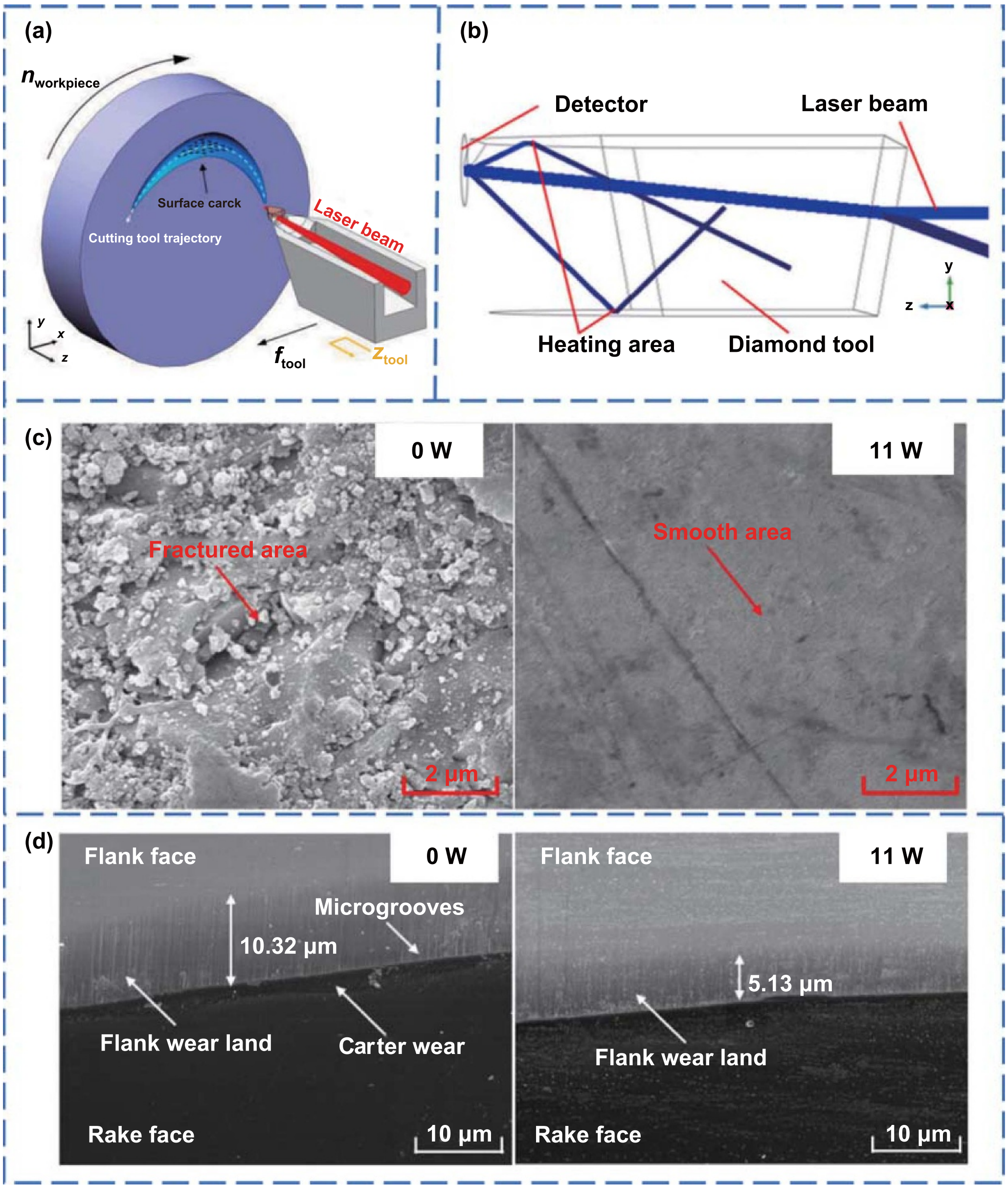

Figure 13. *In situ* LAT and process characteristics. (a) Schematic of the process [138]. (b) Laser beam path in the diamond tool [142]. (c) Morphologies of the surfaces machined without and with *in situ* LAT [142]. (d) Tool cutting edges after turning without and with *in situ* LAT [142]. Reprinted from [138], © 2021 Published by Elsevier Ltd. Reprinted from [142], © 2022 The Society of Manufacturing Engineers. Published by Elsevier Ltd. All rights reserved.

laser heating approach, in which a small laser spot was used to heat up a large workpiece area, as shown schematically in figure 14(a). In a conventional laser-assisted milling setup, the laser spot is focused at a fixed position ahead of the cutting tool, resulting in some problems in terms of small heating area and uneven heat distribution. This novel approach solves these problems. The experimental results indicated a 55% reduction in the cutting force during the processing of the Inconel 718 alloy using the novel approach, as shown in figure 14(b). By comparing the surfaces machined using conventional laser-assisted milling, path-optimized laser-assisted milling, and dry milling, it was found that the surface roughness of the path-optimized laser-assisted milling decreased by approximately 10.8%. Furthermore, unlike conventional laser-assisted milling, no surface burn was observed in path-optimized laser-assisted milling, as illustrated in figure 14(c). Kang and Lee [149] introduced a novel back-and-forth laser preheating method to obtain the desired material temperature at the laser spot. Through finite-element analyses, the researchers determined the appropriate laser power and feed for cutting Si_3N_4 ceramics and successfully conducted experiments using these parameters. The results showed good agreement between the finite-element analyses and experiments, and the material temperature was within a 10% margin of error.

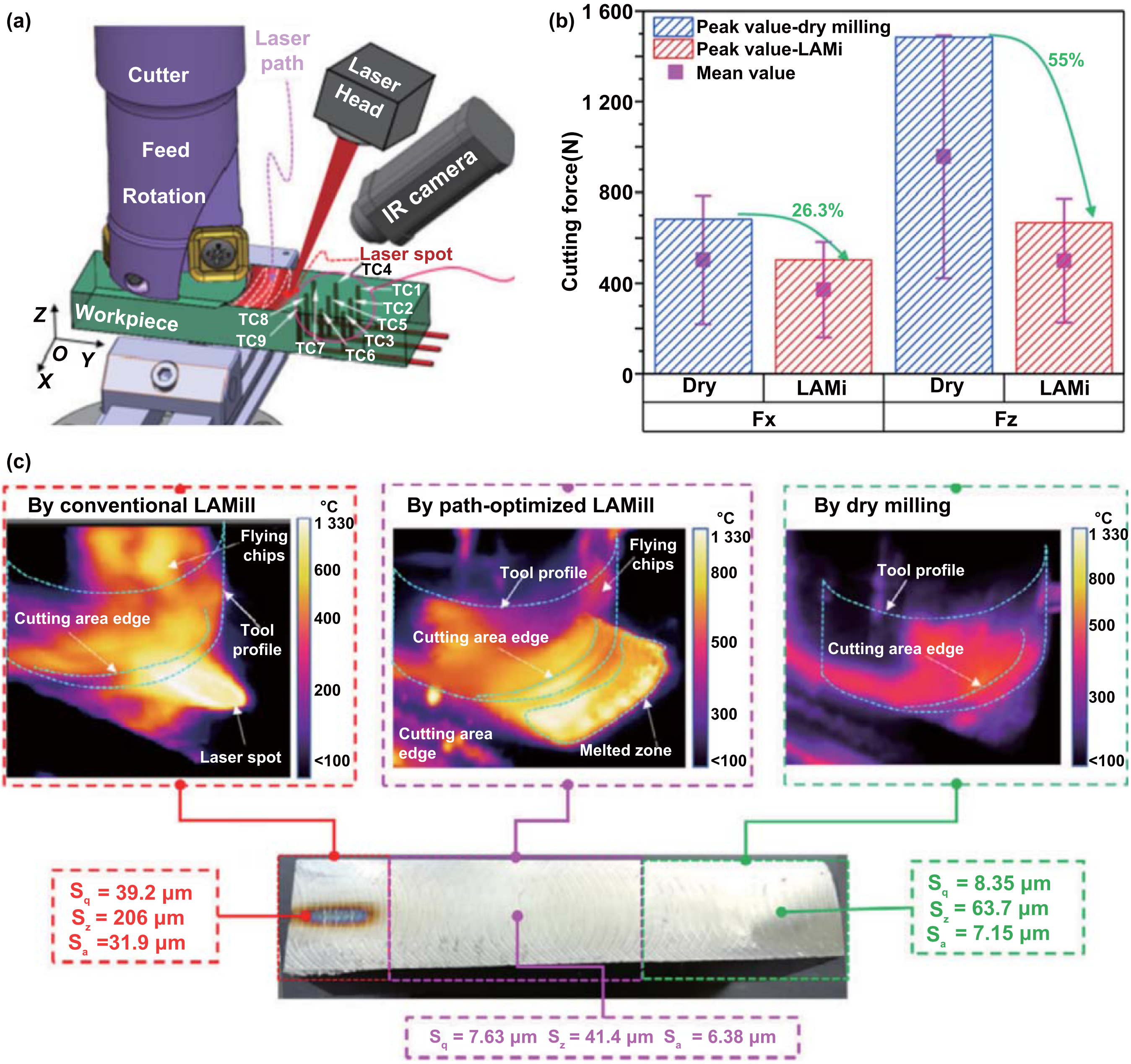

Figure 14. Laser preheating-assisted milling process and outcomes. (a) Schematic of the spatially and temporally controlled laser-assisted milling [148]. (b) Comparison of cutting forces in dry and laser-assisted milling [148]. (c) Surface roughness generated using three processes [148]. Reprinted from [148], © 2018 Elsevier Ltd. All rights reserved.

3.2.2. Laser-induced modification-assisted milling. Some researchers have used lasers to induce material surface modifications to assist milling. Xia *et al* [150–161] proposed a novel hybrid machining process of laser-induced oxidation-assisted milling (LOAM) to enhance the machinability of difficult-to-cut materials. By utilizing a pulsed laser, an oxidation reaction was induced between the irradiated workpiece material and oxygen, as shown in figure 15(a). This resulted in the formation of loose and porous oxides, which could be easily removed with the milling tool (figure 15(b)). The outcomes were improved MRR and extended tool life. Experimental research has been conducted on difficult-to-cut materials, such as Inconel 718, Ti–6Al–4V, WC-Co cemented carbide, SiC_p/Al composites, TiB_2–TiC composites, and C_f/SiC composites. The results indicated that compared with CM, LOAM can significantly reduce the milling force, effectively extend tool life, and decrease surface damages, thereby obtaining high-quality machined surfaces, as shown in figures 15(c)–(e). In a separate study by Chen *et al* [162], the mechanism of laser-induced ablation in SiC_f/SiC composites was explored, along with the correlation between laser parameters and ablation depth. The results highlighted the influential role of laser scanning speed and scanning spacing in determining the ablation depth. Notably, the continuous-wave mode resulted in a greater ablation depth due to the continuous input of energy. Consequently, the continuous-wave laser proved to be more

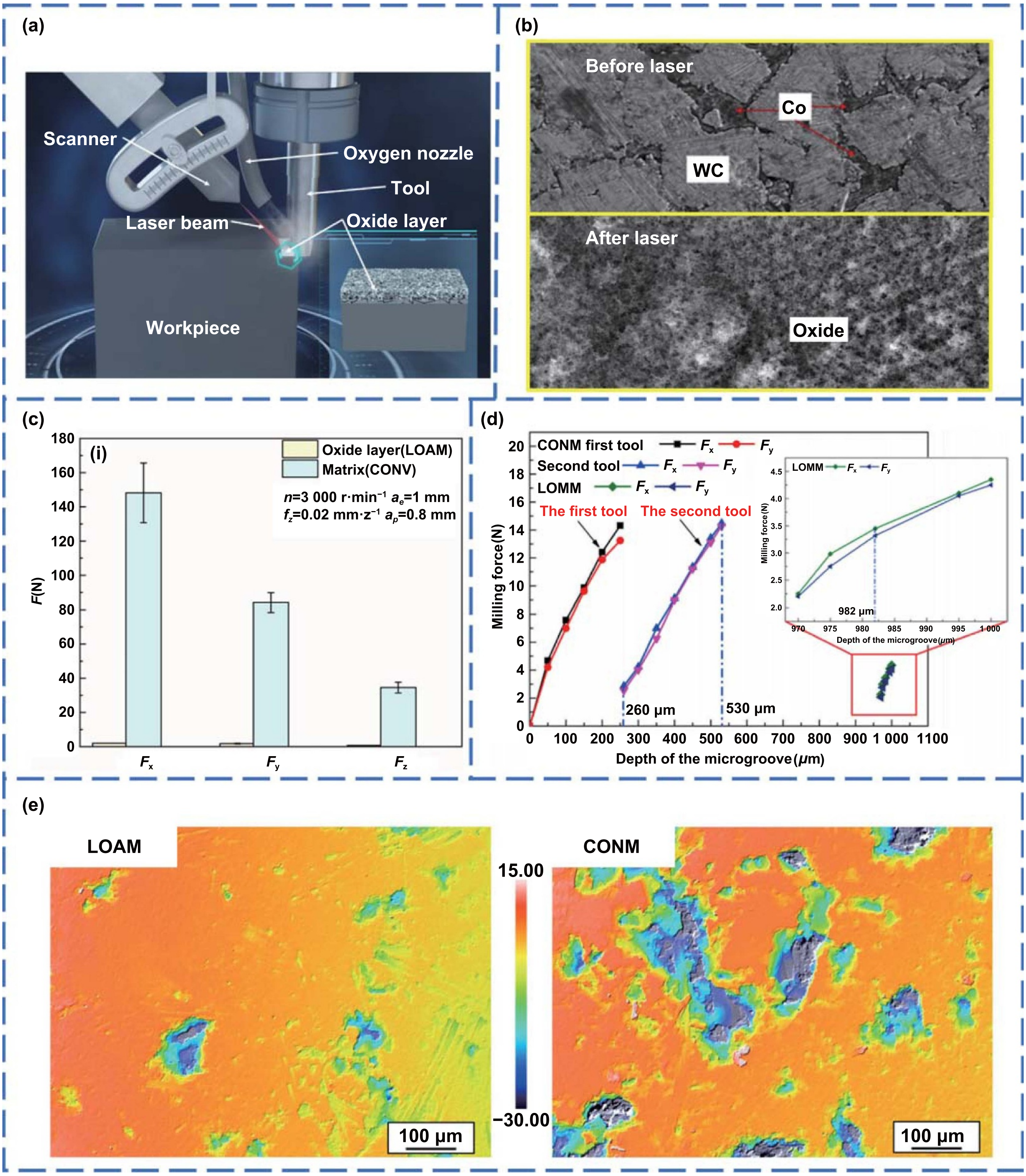

Figure 15. LOAM process and outcomes. (a) Process principle. (b) Surface microstructure before and after laser irradiation [157]. (c) Comparison of cutting forces in milling oxide layer and matrix [161]. (d) Comparisons of milling force and tool life in CM and LOAM [152]. (e) 3D confocal images of the surfaces machined with and without LOAM [161]. Reprinted from [157], © 2019 Elsevier Ltd and Techna Group S.r.l. All rights reserved. Reprinted from [152], © 2020 Elsevier Ltd and Techna Group S.r.l. All rights reserved. Reprinted from [161], © 2022 The Author(s). Published by Elsevier B.V.

suitable for generating varying and larger ablation depths, thereby accommodating different cutting allowances.

Currently, research on laser-assisted milling is only applicable to unidirectional plane milling or groove structure machining. For laser-assisted milling of complex parts, it is necessary to develop specialized LAM equipment. In addition, during continuous machining, the temperature of the cutting zone may continue to increase considering the inability to use a coolant. Realizing the precise control of the workpiece and tool temperatures in real time during LAM can also be a focus of future research.

3.3. Laser-assisted grinding

The purpose of LAG is to generate a temperature increase through laser beam irradiation, thereby reducing the temperature gradient during the grinding process or reducing the hardness of local materials [163, 164]. Consequently, LAG is highly effective for enhancing both the efficiency and grinding quality of hard and brittle materials.

3.3.1. Laser preheating-assisted grinding. Ma *et al* [165, 166] proposed a model for predicting the grinding force in the LAG process of zirconia ceramic, which comprehensively considered the material temperature-dependent mechanical properties, interactions between the grit and the material, and the stochastic shapes and random distributions of abrasive grits. The LAG experimental setup is shown in figure 16(a). The simulated results are in good agreement with the experimental measurements, with error rates within 12%. Furthermore, by optimizing the machining parameters, the grinding force can be effectively reduced by 29.4%–60.1%, as shown in figure 16(b). Fortunato *et al* [167] introduced a novel hybrid process for grinding Si_3N_4 ceramics, which incorporated a laser treatment phase for weakening the material to assist the subsequent diamond grinding. By leveraging laser-induced cracking, the grinding force was reduced by 30%, thereby reducing wheel wear when operating with identical cutting parameters or improving machining efficiency, maintaining the same wear rate. He *et al* [168] investigated the surface formation process during LAG of high-strength alloys. A laser-assisted scratching experiment and a molecular dynamics simulation were conducted on TC17 titanium alloy. The findings revealed that the scratch force decreased with the increment in laser power, whereas MRR initially increased and then decreased. Through TEM and EBSD mapping, it was observed that laser-assisted scratching resulted in a reduction in SSD compared to conventional scratching, owing to the reduced force (figure 16(c)). Molecular dynamics simulations indicated that heat accumulation led to an annealing effect that promoted the growth of refined grains. The LAG experiments further demonstrated less damage during the grinding process, highlighting the superiority of LAM.

3.3.2. Laser-induced modification-assisted grinding. Kumar *et al* [169] investigated a two-step laser-assisted micro-grinding technique. With this innovative approach, they utilized laser irradiation to selectively weaken the Si_3N_4 ceramic material, followed by micro-grinding of the debilitated material to achieve a refined microscale feature. Compared with conventional micro-grinding, up to 43.2% reduction in grinding forces was achieved with laser assistance. Moreover, the integration of laser assistance exhibited a notable advantage in terms of reducing tool wear (figure 17).

A novel two-step LAG technique was proposed by Azarhoushang *et al* [170] to enhance the MRR in the processing of Si_3N_4 ceramics. In this method, they employed lasers to create microstructures on the surface of the material prior to grinding, which aided in the subsequent step of grinding. The findings indicated that the proposed approach reduced the specific grinding energy by up to 55% and led to a slight improvement in ground surface quality. Zhou *et al* [171] proposed a novel method of LIAAG to machine C_f/SiC composites, in which the workpiece was ablated by lasers before grinding. At elevated temperatures, C_f/SiC composites underwent a remarkable chemical metamorphosis, transforming into loose products consisting of SiO_2 and recrystallized SiC. This transformation rendered them easier to remove during the grinding process. Under ideal conditions, the application of optimal parameters resulted in a 47% reduction in the grinding force, 40% reduction in the grinding temperature, and 26% reduction in the surface roughness, as illustrated in figure 18.

3.4. Laser-assisted planing

Chang and Kuo [172, 173] conducted an investigation on laser-assisted planing (LAP) of Al_2O_3 ceramics. A schematic of the LAP setup is shown in figure 19. The experimental findings demonstrated that LAP effectively reduced the feed force by 22% and the thrust force by 20% while simultaneously achieving superior workpiece surface quality compared with conventional planing. Zhai *et al* [174] investigated the characteristics and underlying mechanism for LAP of C/SiC composites with varying fiber orientations. The results revealed that the degree of surface roughness reduction varied and was dependent on fiber orientation. The largest reduction in roughness was observed at a 90° fiber orientation, followed by 0° and 45°, whereas the smallest reduction was obtained at a 135° fiber orientation (figure 20).

In summary, the primary application of LAM currently lies in the realm of laser heating-assisted machining. Table 2 lists various laser-assisted mechanical machining processes and output parameters compared with conventional mechanical machining. By utilizing laser-induced material softening and removing the material during the softening phase, the cutting-zone temperature increases significantly. However, when employing diamond or similar cutting tools, the elevated temperature can accelerate tool failure. Thus, further research is necessary to thoroughly investigate the impact of LAM on cutting tool performance, particularly the influence of cutting-zone temperature on tool performance. To address this concern, it is imperative to establish a comprehensive mapping model that correlates the process parameters with cutting-zone temperature. In laser-assisted milling, the coordination and

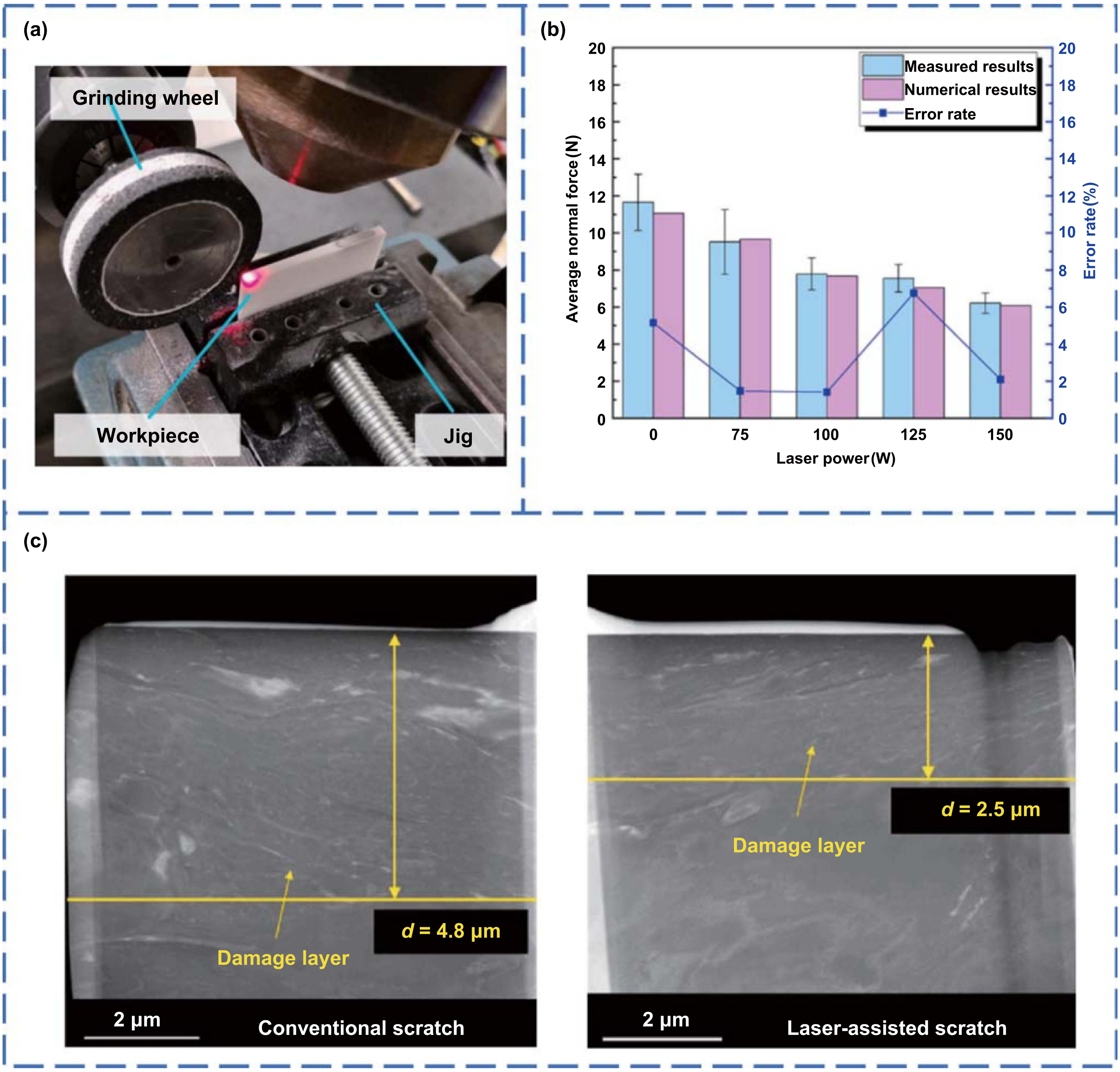

Figure 16. Laser preheating-assisted grinding process, resultant force, and damage. (a) Experimental setup of LAG [165]. (b) Grinding forces under various laser powers [165]. (c) Thicknesses of the damage layer generated in conventional and laser-assisted scratches [168].

control of laser scanning and tool feed remain relatively understudied. Therefore, additional research is needed to explore the synergistic collaboration between laser scanning parameters, scanning paths, and cutting feed parameters in laser-assisted milling processes. In current studies, the employed laser beam energy distribution predominantly follows a Gaussian distribution, resulting in nonuniform energy distribution that hampers temperature control. Future investigations may be considered by adopting laser beam shaping techniques to transform the Gaussian beam into a flat-top beam with a uniform energy distribution. Furthermore, it is worth noting that the current LAM technique is only suitable for unidirectional cutting and is not effective for machining parts with complex surfaces. Consequently, the development of advanced LAM equipment is crucial for meeting the processing requirements associated with complex surfaces.

4. Hybrid nontraditional energy-assisted mechanical machining

Hybrid nontraditional energy-assisted mechanical machining is a technique that employs two or more nontraditional energies to improve the machinability of the workpiece material

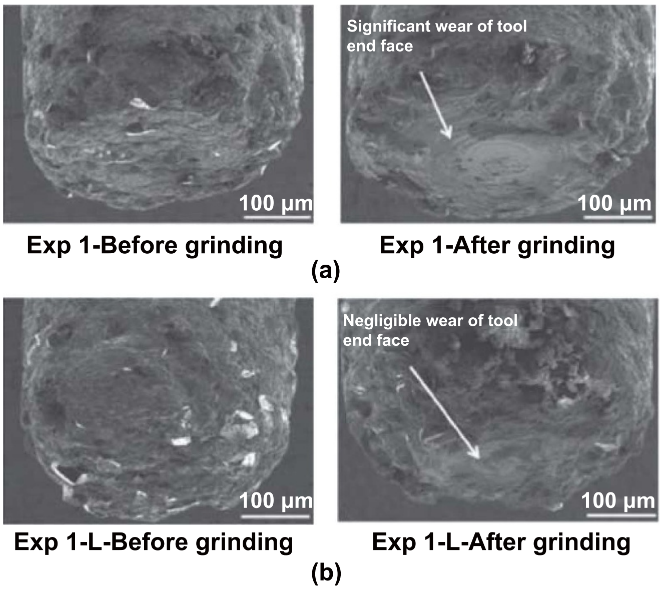

Figure 17. SEM images of tool before and after cutting (a) with and (b) without laser assistance [169]. Reprinted from [169], Copyright © 2011 CIRP. Published by Elsevier Ltd. All rights reserved.

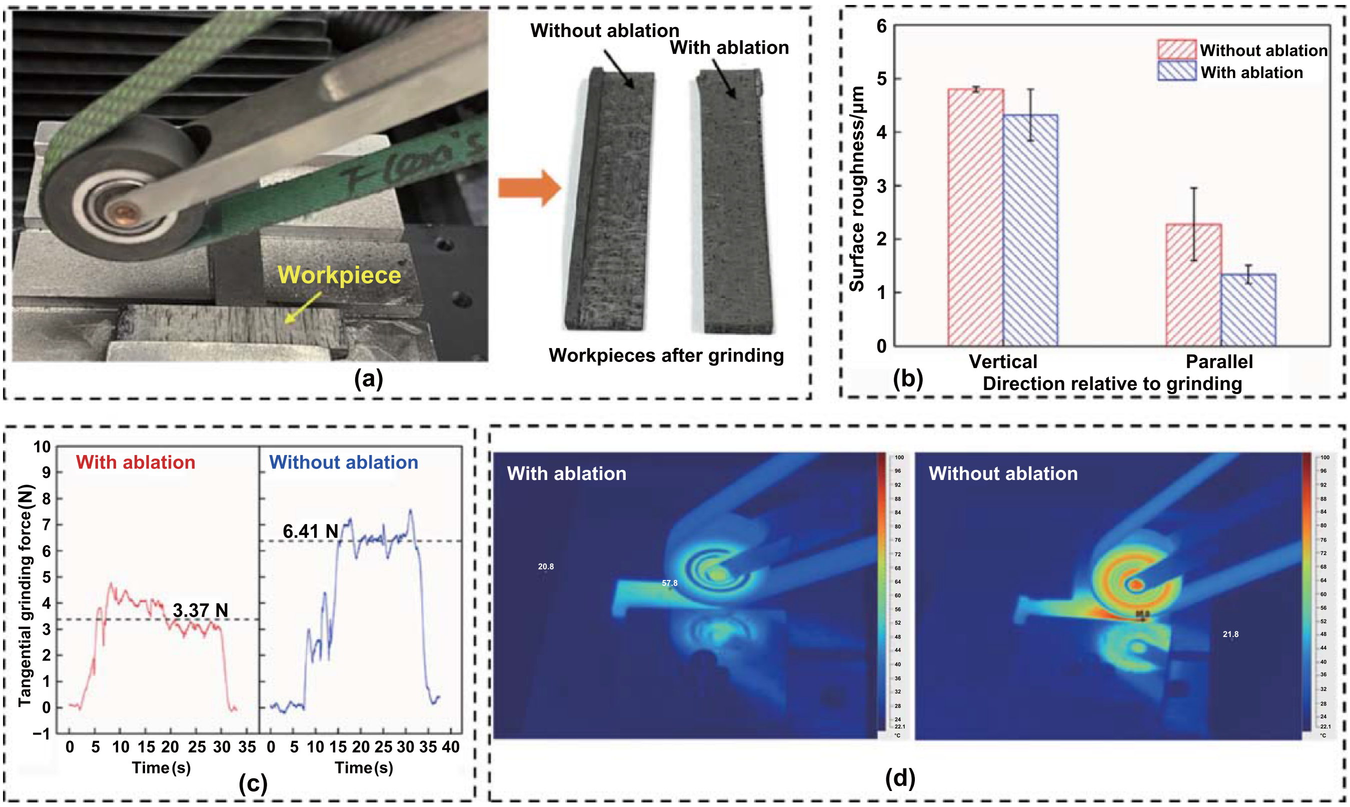

Figure 18. Laser-induced ablation-assisted belt grinding process and outcomes. (a) Experimental setup [171]. (b) Surface roughness generated with and without laser ablation assistance [171]. (c) Comparison of tangential grinding force [171]. (d) Comparison of temperature field [171]. Reprinted from [171], © 2022 Elsevier B.V. All rights reserved.

prior to mechanical machining. The combination of hybrid nontraditional energies has multiple positive effects on the mechanical machining process, which mainly includes changing the properties or deformation behavior of workpiece materials, inducing phase transition or structural modification, altering tool/workpiece interaction, and improving the chipping process. The hybrid nontraditional energy-assisted mechanical machining process can effectively leverage the unique benefits of each nontraditional energy while mitigating the limitations of individual nontraditional EAMM. This process

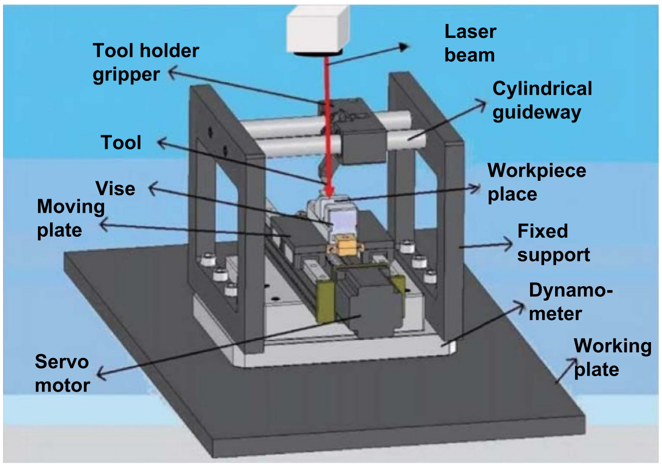

Figure 19. Schematic of the LAP process [172]. Reprinted from [172], Copyright © 2006 Elsevier Ltd. All rights reserved.

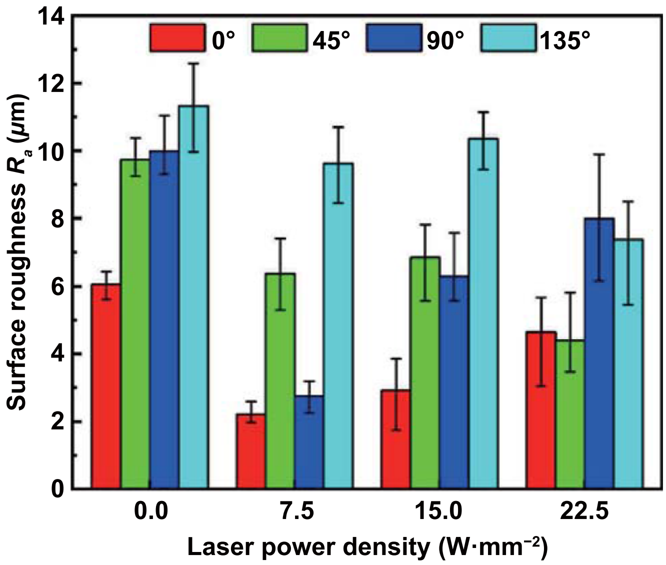

Figure 20. Surface roughness of different fiber orientations of C/SiC composites machined at various laser power densities [174]. Reprinted from [174], © 2021 Elsevier Ltd and Techna Group S.r.l. All rights reserved.

has tremendous potential for enhancing material machinability, thereby further improving processing efficiency, tool service life, and machining quality. An example of hybrid nontraditional energy-assisted mechanical machining is the combination of laser and ultrasonic vibration-assisted mechanical machining. In laser-assisted mechanical machining, the elevated temperatures resulting from laser irradiation may exacerbate tool wear. When mechanical machining is assisted only by ultrasonic vibration, further improvement in machining efficiency is required. However, through the combination of laser and ultrasonic vibration energies into a hybrid nontraditional energy, the process performance of '$1 + 1 > 2$' is realized. The machining temperature is effectively reduced by the discontinuous cutting effect generated by ultrasonic vibration. Because of the laser-induced material modification, material machinability is significantly enhanced. In addition, tool wear is greatly reduced, and machining efficiency is markedly increased. The detailed framework of the hybrid nontraditional energy-assisted mechanical machining technologies is illustrated in figure 21.

4.1. Hybrid nontraditional energy-assisted turning

In current research on hybrid nontraditional energy-assisted turning, ultrasonic vibration and laser are two prominent forms of energy fields. The focus of investigation is to understand the material removal process and mechanisms when subjected to the combined action of ultrasonic vibration, laser, and mechanical machining. Temperature control and chip formation during the machining process are areas that require close attention. In most studies, tool life is extended, but improvement in surface quality after machining has only been observed in certain research endeavors. Kim *et al* [176, 179] and Li *et al* [180] studied a distinct and unique machining process named laser and ultrasonic vibration-assisted machining (LUVAM), and its schematic is shown in figure 22(a). This

Table 2. Laser-assisted mechanical machining processes and output parameters. (↑: increased by.↓: decreased by)

Reference	Workpiece material	Hybrid process	Process parameters	Output parameters (compared with conventional)
Germain *et al* [116]	42CrMo4	Laser preheating-assisted turning	Laser power: 1000 W Cutting speed: 1, 2, and 4 m s^{-1} Feed: 0.1 mm rev^{-1}	Cutting force: ↓ up to 40% Residual stress: ↓ 35% of compressive stresses
Bejjani *et al* [118]	TiC/Ti–6Al–4V	Laser preheating-assisted turning	Laser power: 840–1875 W Cutting speed: 100 and 170 m min^{-1} Feed: 0.2 mm rev^{-1} Depth of cut: 0.15 mm	Cutting force: ↓ maximum 25% Total cut volume: ↑ 180% Surface roughness: ↑ 15%
Navas *et al* [125]	Inconel 718	Laser preheating-assisted turning	Laser power: 2000 W Cutting speed: 50 and 70 m min^{-1} Feed: 0.1–0.25 mm rev^{-1} Depth of cut: 0.25–0.8 mm	Cutting force: ↓ up to 36% Surface roughness: ↓ more than 50% Surface hardness: ↓ 41% Tool life: shortened for carbide insert, decreased notching, and chipping
Wang *et al* [126]	Al_2O_3/Al	Laser preheating-assisted turning	Laser power: 150 W Cutting speed: 25.12 m min^{-1} Feed: 0.1 mm rev^{-1} Depth of cut: 0.38 mm	Cutting force: ↓ 30%–50% Tool wear: ↓ 20%–30% Residual stress: ↑ 200% of compressive stresses
Rashid *et al* [127]	Ti–6Cr–5Mo–5V–4Al	Laser preheating-assisted turning	Laser power: 1200 W Cutting speed: 9.5–200 m min^{-1} Feed: 0.054–0.28 mm rev^{-1} Depth of cut: 1 mm	Cutting force: ↓ maximum 15%
Attia *et al* [131]	Inconel 718	Laser preheating-assisted turning	Laser power: 2.5–3 kW Laser spot diameter: 0.3–3 mm Cutting speed: 200–500 m min^{-1} Feed: 0.25–0.50 mm rev^{-1} Depth of cut: 0.25 mm	Cutting force: ↓ maximum 38.3% Surface hardness: $-13.5\% \sim +8.4\%$ MRR: ↑ 800% Tool life: ↑ 40% Surface roughness: ↓ maximum 29.5%
Wei *et al* [132, 133]	SiC_p/Al composite	Laser preheating-assisted turning	Laser power: 7.5–13 kW Cutting speed: 188 and 565 m min^{-1} Feed: 0.1 mm rev^{-1} Depth of cut: 0.75 mm	Cutting force: ↓ maximum 62.5% Tool wear: ↓ maximum 65% Surface roughness: ↓ maximum 75.4%
Przestacki *et al* [135, 136]	A359/20SiC_p	Laser preheating-assisted turning	Laser power: 300–1400 W Cutting speed: 10 m min^{-1} Feed: 0.04 mm rev^{-1} Depth of cut: 0.1 mm	Tool wear: ↓ maximum 50% Surface roughness: ↓ maximum 32% Surface wear resistance: ↑ maximum 27%
You *et al* [139, 140]	Binderless WC	*In situ* LAT	Laser power: 5–20 W Cutting speed: 100 m s^{-1} Depth of cut: 5 nm	Surface roughness S_a: optimal 0.97 nm Tool wear: no chip adhesion Residual stress: ↓ 40% of compressive stresses
Zhang *et al* [141, 142]	RB SiC	*In situ* LAT	Laser power: 2 and 4 W Cutting speed: 500 and 1000 mm min^{-1} Depth of cut: 52.2 and 106.7 nm	Surface defects significantly decreased Surface roughness S_a: ↓ maximum 84.3%
Park *et al* [143]	Zr bulk metallic glasses	*In situ* LAT	Laser power: 2.8 and 7.9 W Cutting speed: 50–150 mm min^{-1} Depth of cut: 15 μm	Cutting force: ↓ 40% Surface roughness S_a: ↓ maximum 68%
Muženič *et al* [146]	ZnO ceramics	Laser preheating-assisted milling	Laser power: 400 W Cutting speed: 75.4 m min^{-1} Depth of cut: 0.1 mm Width of cut: 2.2 mm	Surface damage: ↓ 55% Edge chipping: similar
Ding *et al* [147]	Inconel 718	Laser preheating-assisted micro-milling	Laser power: 17.4 and 20.6 W Cutting speed: 58.8 m min^{-1} Depth of cut: 200 μm Width of cut: 10 μm	Tool wear rate: ↓ 72% BUE formation was eliminated

(Continued.)

Table 2. (Continued.)

Reference	Workpiece material	Hybrid process	Process parameters	Output parameters (compared with conventional)
Shang *et al* [148]	Inconel 718	Laser preheating-assisted milling	Laser power: 4800 W Laser scanning speed: 1.5 m s^{-1} Cutting speed: 41 m min^{-1} Feed: 0.5 mm/tooth Depth of cut: 0.26 mm Width of cut: 19 mm	Cutting force: ↓ maximum 55% Surface roughness S_a: ↓ 10.8%
Xin *et al* [151]	Inconel 718	Laser-induced modification-assisted micro-milling	Laser power: 3.5–6.5 W Feed speed: 80 mm min^{-1} Depth of cut: 4 μm Width of cut: 500 μm	Cutting force: ↓ maximum 79% Surface roughness S_a: ↓ maximum 49% Tool life: ↑ 50%
Xia *et al* [152]	TiB2–TiC ceramic	Laser-induced modification-assisted micro-milling	Laser power: 3.5–6.5 W Feed speed: 60–240 mm min^{-1} Depth of cut: 1 and 2 μm Width of cut: 400 μm	Cutting force: ↓ maximum 70% Surface roughness S_a: optimal 146 nm Tool life: ↑ at least 400% Machining efficiency: ↑ 106%
Zhao *et al* [155]	SiC_p/Al composites	Laser-induced modification-assisted milling	Laser power: 10 W Feed rate: 5, 10, 15, and 20 μm z^{-1} Depth of cut: 0.1 and 0.2 mm Width of cut: 10 mm	Cutting force: ↓ maximum 55% Surface roughness S_a: ↓ maximum 12% Tool wear: ↓ 25%
Zhao *et al* [157]	WC-Co cemented carbide	Laser-induced modification-assisted micro-milling	Laser power: 4–7 W Feed speed: 6, 20, 30, and 40 mm min^{-1} Depth of cut: 2 and 4 μm Width of cut: 700 μm	Cutting force: ↓ maximum 58% Surface roughness S_a: optimal 57 nm Cutting length: ↑ 45%
Zhao *et al* [161]	C_f/SiC composite	Laser-induced modification-assisted milling	Laser power: 60–90 W Feed speed: 120 mm min^{-1} Depth of cut: 0.8 mm Width of cut: 1 mm	Cutting force: ↓ maximum 97% Surface roughness S_a: optimal 9.5 μm Tool wear: ↓ maximum 90%
Ma *et al* [165]	Zirconia ceramic	Laser preheating-assisted grinding	Laser power: 75–175 W Wheel speed: 8–14 m s^{-1} Feed speed: 1–4 mm s^{-1} Depth of grinding: 25–100 μm	Grinding force: ↓ maximum 60.1% Surface roughness S_a: ↓ maximum 69.4%
Fortunato *et al* [167]	Si_3N_4 ceramics	Laser preheating-assisted grinding	Laser power: 20–560 W Wheel speed: 28.7 m s^{-1} Feed speed: 130 mm s^{-1} Depth of grinding: 12.7 μm	Grinding force: ↓ maximum 30% Surface hardness: similar
Kumar *et al* [169]	Si_3N_4 ceramics	Laser-induced modification-assisted grinding	Laser power: 15 W Wheel speed: 3.3 m s^{-1} Feed speed: 50 mm s^{-1} Depth of grinding: 5 and 10 μm	Grinding force: ↓ maximum 43.2% Surface roughness: similar Tool wear: ↓
Zhou *et al* [171]	C_f/SiC composites	Laser-induced modification-assisted grinding	Laser power: 10–70 W Wheel speed: 62.5 m s^{-1} Depth of grinding: 200 μm	Grinding force: ↓ maximum 47% Grinding temperature: ↓ maximum 40% Surface roughness R_a: ↓ maximum 41% Tool wear: ↓
Chang and Kuo [172, 173]	Al_2O_3 ceramics	LAP	Laser power: 25 W Cutting speed: 0.5 and 1 m min^{-1} Depth of cutting: 50 μm	Cutting force: ↓ maximum 16% Surface roughness R_a: ↓ maximum 74%
Zhai *et al* [174]	C/SiC composites	LAP	Laser power density: 7.5–22.5 W mm^{-2} Cutting speed: 200 mm s^{-1} Depth of cutting: 35 μm	Surface roughness R_a: ↓ maximum 72.4%
Ding and Shin [175]	AISI 4130	Laser preheating-assisted turning	Laser power: 1500 W Cutting speed: 150–300 m min^{-1} Feed: 0.075–0.1 mm rev^{-1} Depth of cut: 0.36 mm	Cutting force: ↓ 20% Residual stress: ↑ 150 MPa of compressive stresses Surface hardness: similar

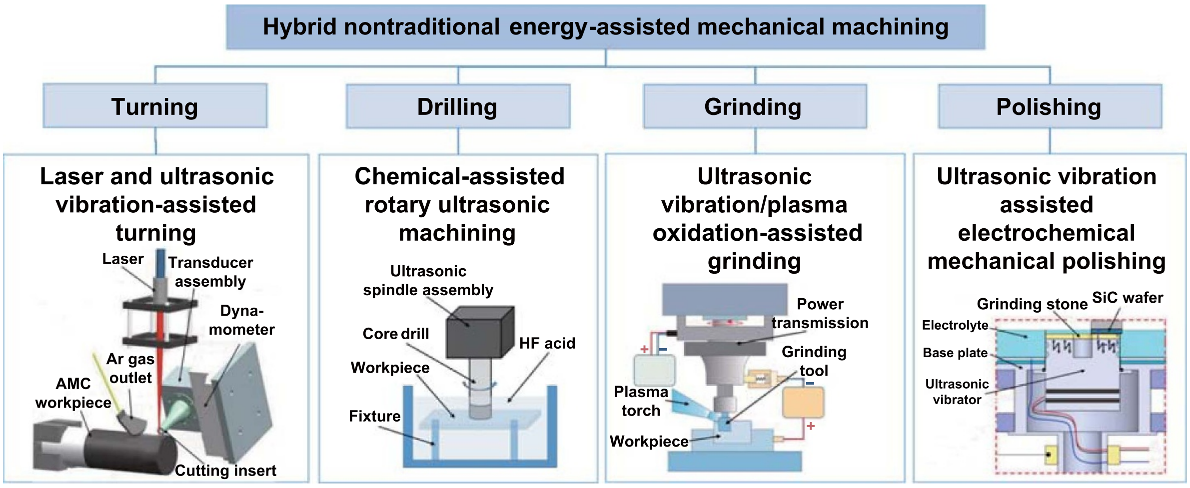

Figure 21. Classification diagram of hybrid nontraditional energy-assisted mechanical machining [176–178]. Reproduced from [176]. CC BY 4.0. Reprinted from [177], © 2023 The Society of Manufacturing Engineers. Published by Elsevier Ltd. All rights reserved. Reprinted from [178], © 2021 Elsevier Ltd and Techna Group S.r.l. All rights reserved.

process aims to enhance the machining performance of three types of micro-SiC/AA2124 composites. During this novel process, the material is first heated and softened using a laser before it is removed. The softened material is then removed with ultrasonic vibration cutting edge. As a result of the periodic separation and contact between the tool and workpiece, the machining process experiences notable reductions in temperature, defects, and cutting force. The results showed that optimizing the laser power was crucial for machined surface roughness and machining efficiency, as shown in figure 22(b). Dominguez-Caballero *et al* [181] and Deswal and Kant [182] introduced a hybrid LUVAM technique to enhance the machinability of Ti–6Al–4V alloy in a turning process. The combined effect of the laser and ultrasonic assistance was particularly noticeable at the lowest cutting speed of 20 m min^{-1}, resulting in significant reductions in cutting forces in the tangential, radial, and feed directions, as shown in figure 22(c). Specifically, the cutting forces were reduced by 70.1%, 59%, and 43%, respectively. Peng *et al* [183] proposed a novel machining method that combines ultrasonic elliptical vibration with laser heating to assist turning of 70% SiCp/Al composites. The results of their study demonstrated that this hybrid process effectively reduced the cutting forces and surface roughness, improved the plastic removal capacity, and decreased the surface damage and SSD. In a separate investigation, Jiao *et al* [184, 185] conducted a study on the behavior of PCD tools during the turning of tungsten carbides. In their research, they applied ultrasonic vibration to the tools and utilized laser-induced heating on the workpieces. A comparison with conventional turning revealed a significant reduction in cutting forces by 67.5% in LAT and UVAT. In addition, this process exhibited a substantial enhancement in tool life, with an improvement of 95.3%, as shown in figure 22(d).

In addition, Wang *et al* [186] conducted a comprehensive analysis of the combination of turning with cryogenic cooling and plasma-enhanced machining. A cryogenic cooling technique was utilized to reduce the machining temperature, and plasma was employed to soften the workpiece. In comparison to conventional turning, the novel process demonstrated a significant improvement in the machining of Inconel 718. The cutting force was reduced by 30%–50%, whereas the surface roughness showed a remarkable reduction of 250%. Additionally, the tool life experienced a substantial improvement of up to 170%.

4.2. Hybrid nontraditional energy-assisted drilling

There is relatively limited research on hybrid nontraditional energy-assisted drilling. This is primarily because of the fact that during drilling, the tool penetrates deep into the workpiece, and many specialized energy field generation devices cannot be integrated or directly applied to the drilling tool. As a result, ultrasonic vibration and chemical methods are currently among the few energy fields that can be effectively employed as auxiliary techniques in drilling processes. Sharma *et al* [187] introduced a novel machining technology named chemical-assisted rotary ultrasonic machining, and its schematic is shown in figure 23(a). Brazed diamond core drills with abrasive grits of 100–150 meshes were used in the experiment. Microscopic images of the fresh and used tools are displayed in figures 23(b) and (c), respectively. HF acid was used to weaken the intermolecular structure of the glass. The corrosive properties of HF acid stem from its strong acidity and the action of fluoride ions. HF acid is capable of breaking the silicon–oxygen bonds present on the surface of the glass, leading to the release of free silicon and oxygen atoms. Simultaneously, fluoride ions can react with these free silicon and oxygen atoms to form compounds, such as silicon fluoride and aluminum fluoride. These compounds possess high solubility and can be further dissolved by HF acid, thereby accelerating the corrosion process of the glass. The results showed that this novel process resulted in the smallest chipping size (0.32 mm); however, the strong corrosion of the HF acid resulted in rapid tool wear.

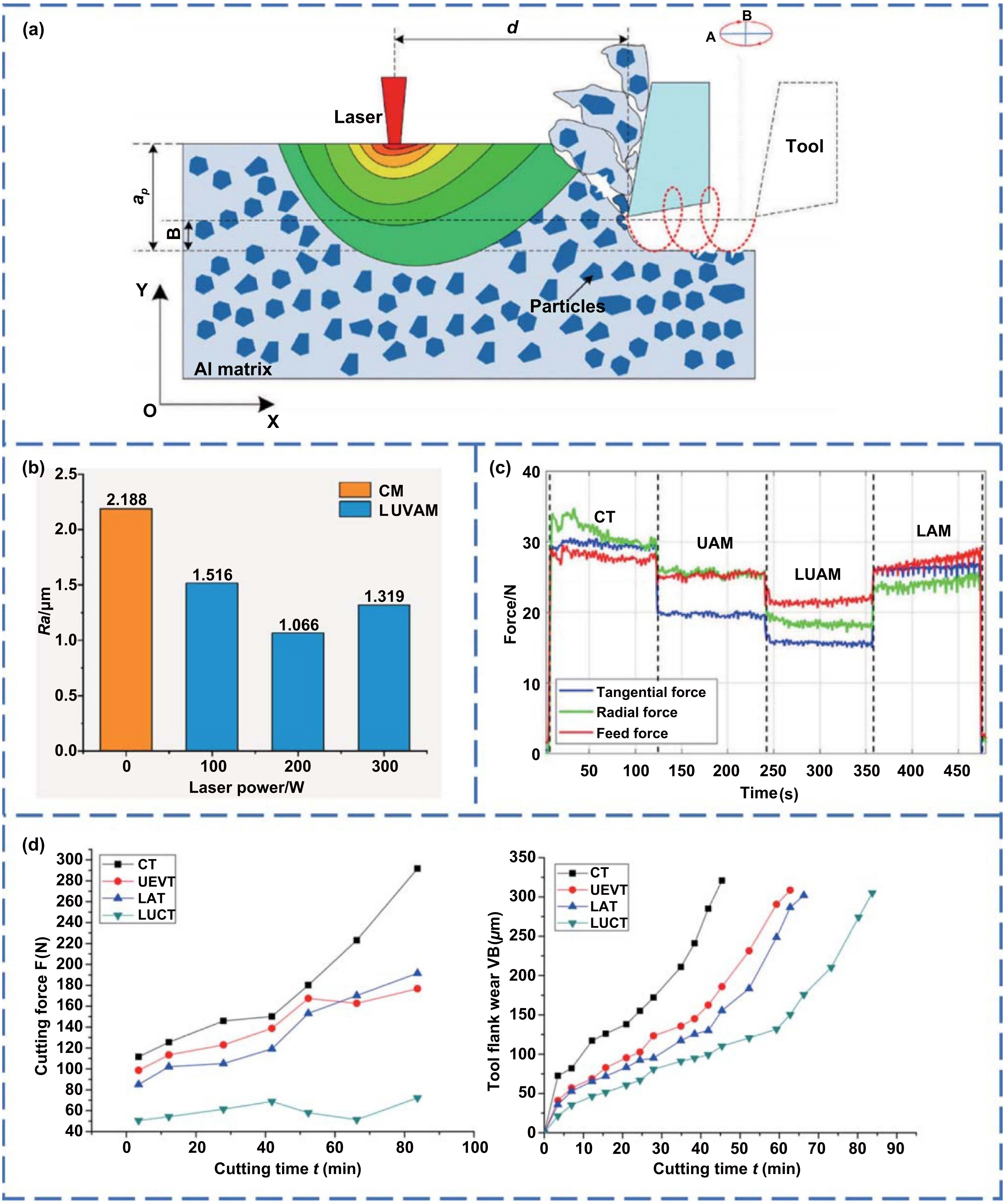

Figure 22. Laser andLUVAM process and comparisons with conventional machining, ultrasonic vibration-assisted machining, and LAM. (a) Process principle of LUVAM [180]. (b) Surface roughness generated at various laser powers [180]. (c) Comparison of cutting forces in a single run [181]. (d) Comparison of cutting force and tool wear progression [184]. Reprinted from [180], © 2022 Elsevier Ltd and Techna Group S.r.l. All rights reserved. Reproduced from [181]. CC BY 4.0. Reproduced from [184]. CC BY 4.0.

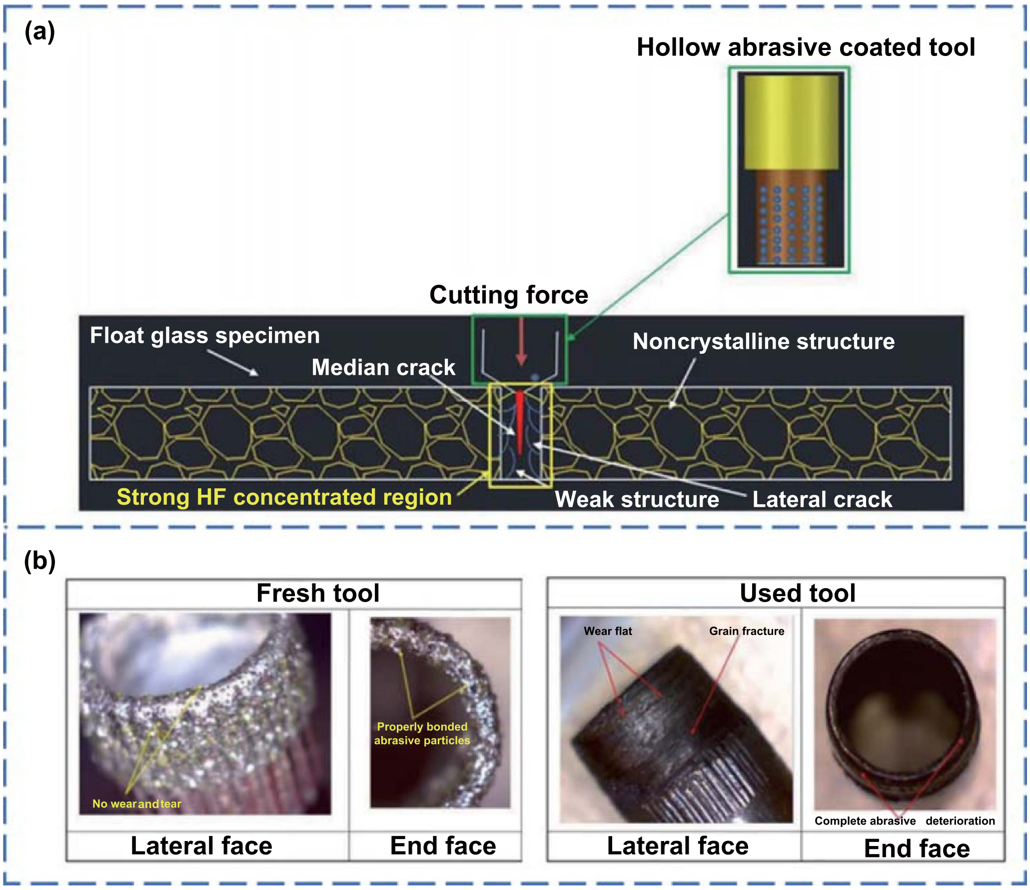

Figure 23. CRUM process and tool wear. (a) Principle of the hybrid process [187]. (b) Lateral and end faces of the fresh and used tools [187]. Reprinted from [187], © 2019 Elsevier Ltd. All rights reserved. Selection and peer review under responsibility of the scientific committee of the 10th International Conference on Materials Processing and Characterization.

4.3. Hybrid nontraditional energy-assisted grinding

Similarly, there is limited research on hybrid nontraditional energy-assisted grinding techniques. Current studies have primarily focused on utilizing ultrasonic vibration and surface treatments to assist grinding processes. Emphasis is placed on investigating the material removal mechanisms during grinding. Wu *et al* [177] conducted a study on a hybrid machining process involving ultrasonic vibration and plasma oxidation-assisted grinding (UPOAG) of Ti–6Al–4V titanium alloy. Researchers have focused on investigating the effects of ultrasonic vibration on the machining characteristics. A schematic of the chip formation process is shown in figure 24(a). The findings revealed that as the vibration amplitude increased, the value of removal ratio η exhibited a linear increase, regardless of the presence or absence of plasma oxidation. However, the rate of increase was significantly higher when plasma oxidation was applied, as shown in figure 24(b). The intensity of the plasma discharge also increased with the increment in vibration amplitude. This increment in intensity reduced the microhardness of the plasma-oxidized layer on the Ti–6Al–4V specimens (figure 24(c)). The combination of the 'overlapped ironing effect' of ultrasonic vibration and the lubrication effect of the plasma-oxidized layer resulted in a reduction in the redeposition of the work material on the ground surface. Consequently, this led to an improvement in machined surface quality. With an increase in vibration amplitude, the machined surface quality was improved. The surface roughness (R_a) was reduced by approximately 60%. The minimum R_a achieved in the study was 0.6 μm.

4.4. Hybrid nontraditional energy-assisted polishing

In contrast to the fields of drilling and grinding, scholars have conducted extensive research on hybrid nontraditional energy-assisted polishing techniques. The combined effect of ultrasonic vibration with magnetic or electric fields has attracted significant attention because of the remarkable improvement in MRRs during polishing. An ER fluid is a functional fluid that exhibits variable viscosity in response to an applied electric field strength. Zhang *et al* [188–190] conducted research on a polishing method called ER fluid-assisted polishing, in which an effective area was created between the tool and the workpiece by applying an electric field. Within this area, the abrasives effectively removed the material from the workpiece. The researchers developed a specialized five-axis ER fluid-assisted polishing equipment specifically designed for finishing curved surfaces. The results of their study indicated that the minimum surface roughness achieved after polishing

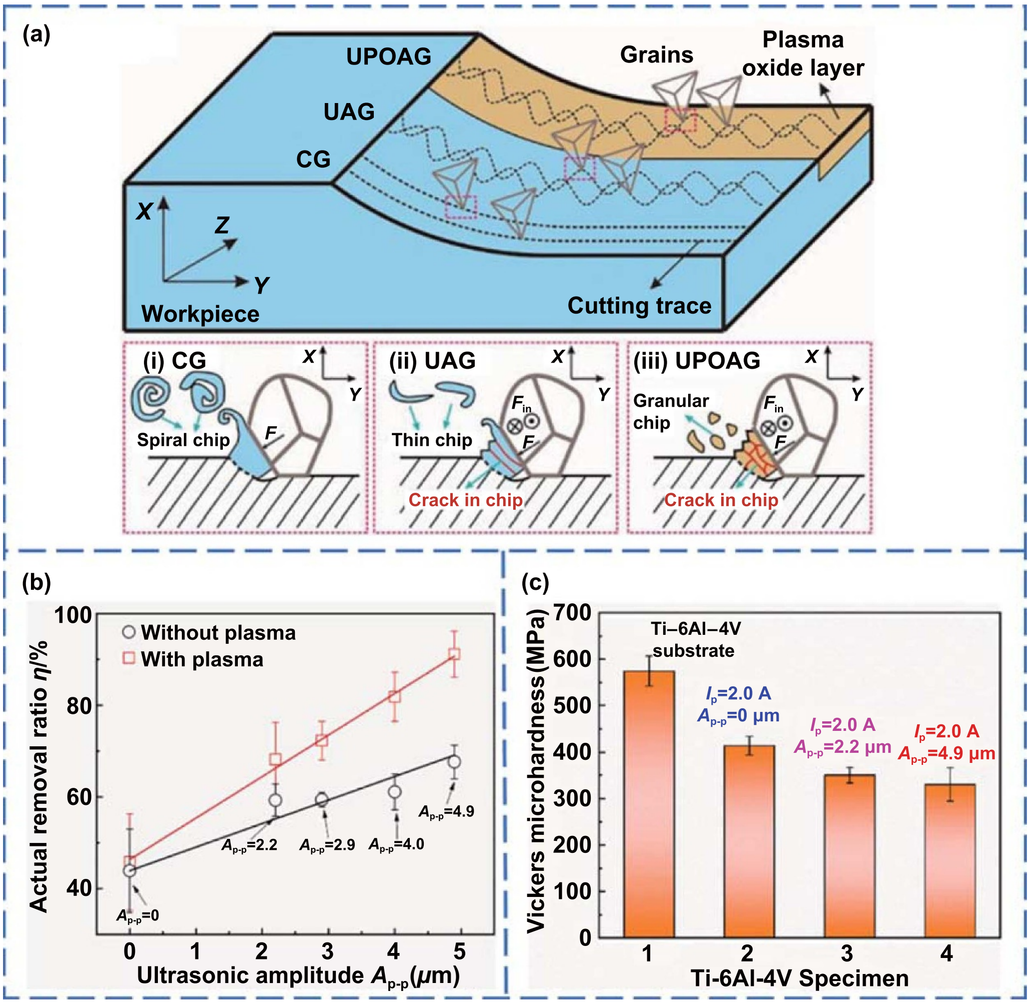

Figure 24. UltrasonicUPOAG and process characteristics. (a) Schematic of chip formation [177]. (b) MRRs under various ultrasonic amplitudes with and without plasma oxidation-assisted grinding [177]. (c) Microhardness of the plasma-oxidized surfaces under different conditions [177]. Reprinted from [177], © 2023 The Society of Manufacturing Engineers. Published by Elsevier Ltd. All rights reserved. (UAG: ultrasonic vibration-assisted grinding. CG: conventional grinding)

optical glass was 7 nm, whereas it was 40 nm for tungsten carbide.

An innovative approach combining megasonic vibration and CMP was developed by Zhai *et al* [191], as shown in figure 25, which improved the process performance of global planarization of silicon wafer. Under megasonic vibration, the slurry is well dispersed. The adhesive force of abrasive particles is detached efficiently. The megasonic acoustic streaming generated by the vibration promotes slurry exchange. In addition, the chemical reaction is accelerated due to the megasonic vibration. Therefore, both MRR and machining quality are enhanced in megasonic vibration-assisted CMP. In this process, the surface roughness R_a reached 0.387 nm (vs. 0.509 nm in conventional CMP).

Yang *et al* [178] introduced UAECMP, which exhibited a remarkable polishing efficiency that was 4.5 times higher than that of conventional ECMP in polishing 4H-SiC wafers. As depicted in figures 26(a)–(d), the enhanced efficiency is attributed to the intensified contact force between the abrasive and the SiC surface, which is facilitated by the impact of ultrasonic vibrations. The average MRRs of MP, ECMP, and UAECMP are shown in figure 26(e). MP and ECMP showed average MRRs of 0.05 and 3.20 μm h^{-1}, respectively, whereas UAECMP had an average MRR of 14.54 μm h^{-1}. This impact induces a substantial local strain on the SiC surface, thereby promoting anodic oxidation. Additionally, the heat generated by the ultrasonic vibrations further augments the anodic oxidation. However, the surface roughness of UAECMP is increased by the vibration; thus, the machined surface needs a subsequent finishing with ECMP.

Ultrasonic vibration-assisted magnetorheological polishing (UAMP) technology was used to polish a sapphire substrate using an Fe_3O_4/SiO_2 core–shell abrasive [192]. Figures 27(a)–(d) illustrate the experimental setup employed in this study. By applying ultrasonic vibrations to the sapphire wafer, MRR was significantly enhanced, reaching approximately 3.4 times higher than that achieved through conventional magnetorheological polishing. Through the application of UAMP, the ultimate MRR of 1.974 μm h^{-1} was achieved, accompanied by a comparatively low surface roughness of 0.442 nm, as shown in figure 27(e).

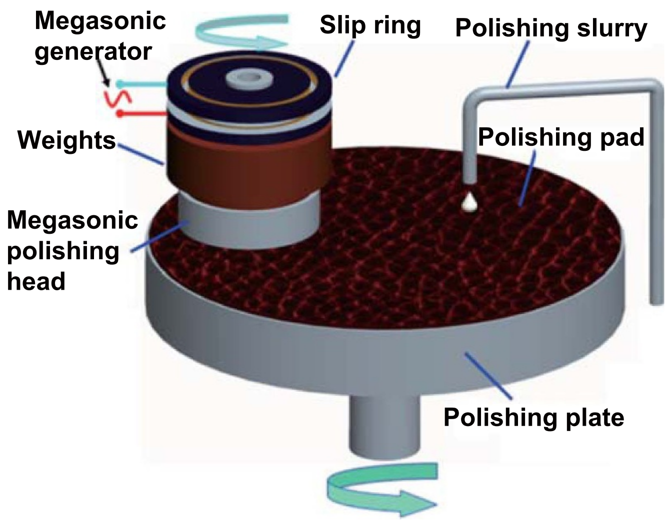

Figure 25. Schematic of megasonic vibration-assisted CMP system [191]. Reprinted from [191],

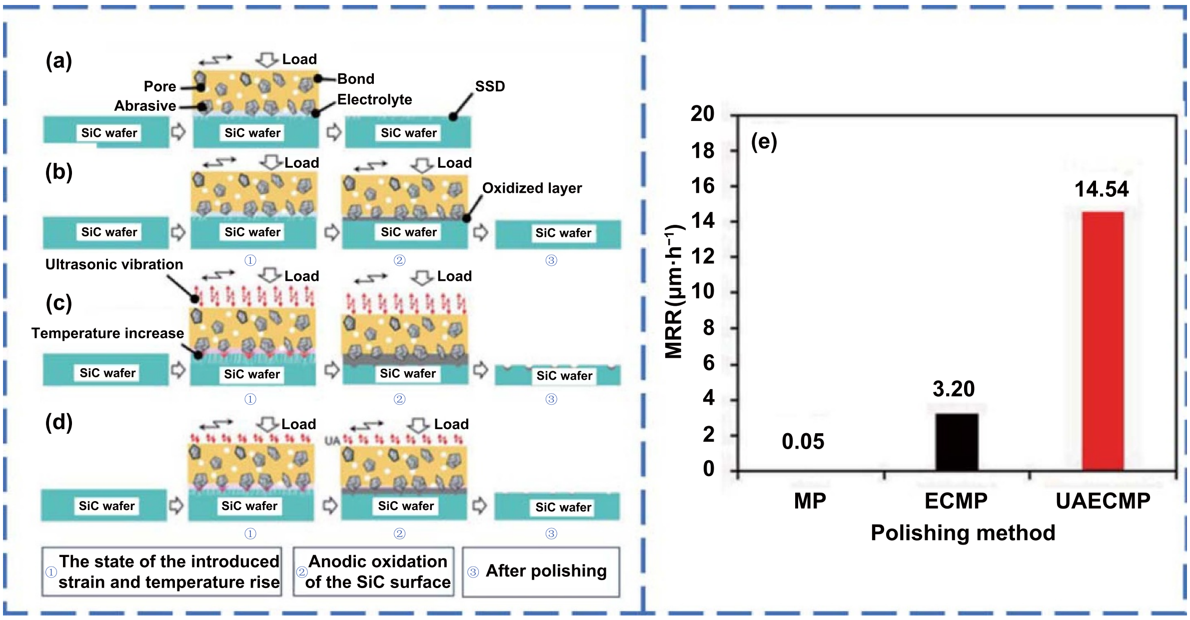

Figure 26. Mechanical polishing (MP), ECMP, and UAECMP processes and their MRRs. (a)–(d) Material removal mechanisms of MP, ECMP, UAECMP with a large vibration amplitude, and UAECMP with a small vibration amplitude [178]. (e) Comparison of average MRRs between these processes [178]. Reprinted from [178],

Guo *et al* [193] investigated the refinement of rectangular microfeatures through utilization of a localized vibration-assisted magnetic abrasive polishing technique. Their findings verified the efficacy of the method in treating curved rectangular microfeatures, irrespective of the magnetic properties of the material. The surface integrity exhibited a notable enhancement, as depicted in figures 28(a) and (b), wherein the elimination of burrs and tool marks was achieved while preserving the form of the microfeatures. The surface roughness of both the top and side microfeatures decreased as the polishing time increased (figures 28(c) and (d)).

Hybrid nontraditional energy-assisted mechanical machining techniques effectively combine the unique advantages of each nontraditional energy while mitigating the limitations of individual nontraditional energy-assisted machining process. This approach has tremendous potential for enhancing material machinability, thereby further improving machining efficiency, tool life, and overall machining quality. Table 3 presents a comparison of hybrid nontraditional energy-assisted mechanical machining processes and their output parameters with conventional mechanical machining processes. Current research on hybrid nontraditional energy-assisted mechanical machining is primarily focused on the areas of polishing and turning. The exploration of new machining processes in this domain is limited by the increased complexity and difficulty of integrating and applying two or more nontraditional energy fields concurrently. Additionally, the research interest of scholars can only be aroused when

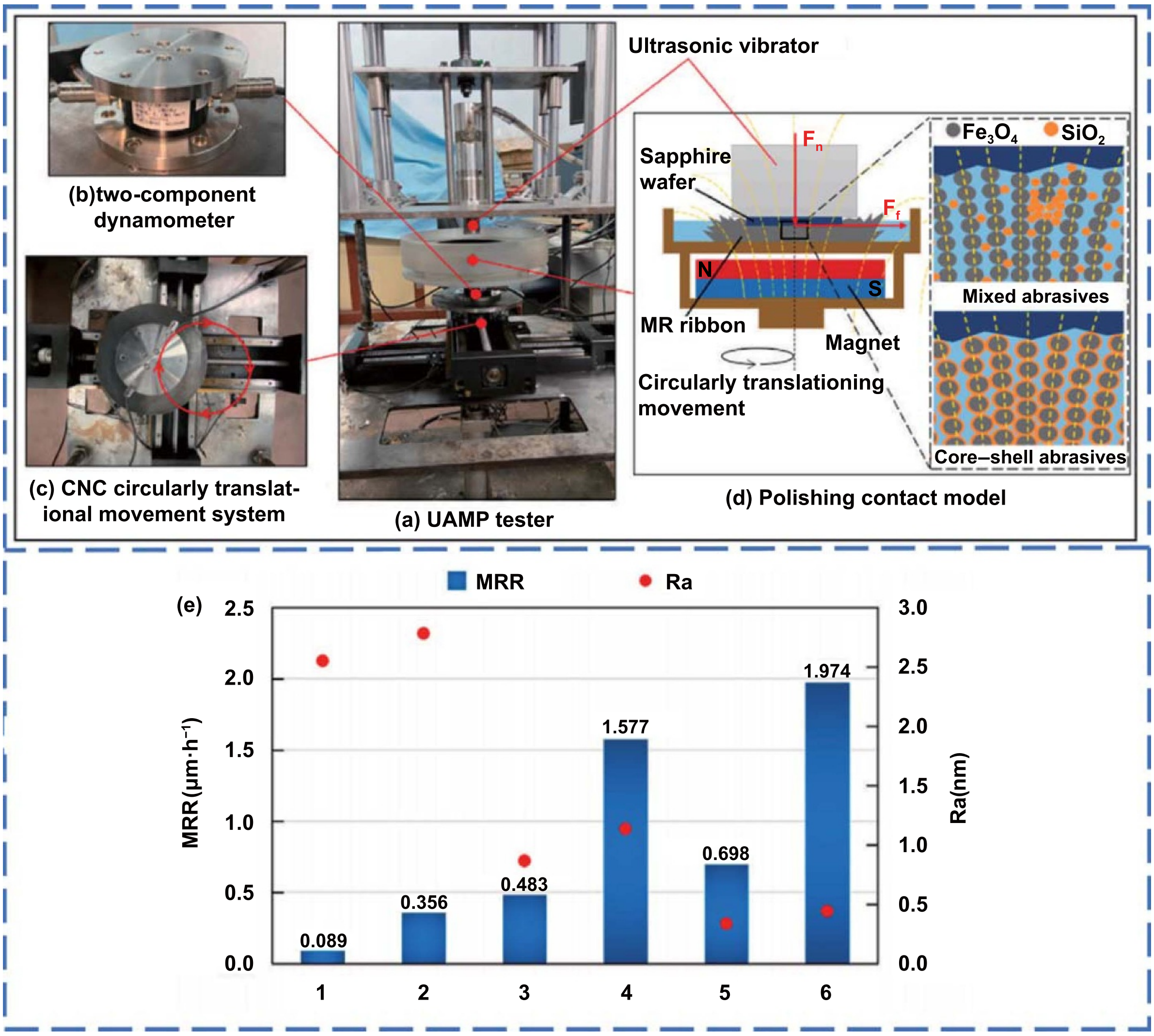

Figure 27. UAMP process and outcomes when various abrasives are used. (a) Experimental setup [192]. (b) Two-component dynamometer for force testing [192]. (c) The developed CNC circularly translational movement system [192]. (d) Schematic of polishing contact model [192]. (e) MRRs and surface roughness with different abrasives (1 and 2 are pure Fe_3O_4 particles, 3 and 4 are mixed compounds of Fe_3O_4 and SiO_2, and 5 and 6 are Fe_3O_4/SiO_2 core–shell abrasives) [192]. Reprinted from [192],

the positive effect achieved by the combination of hybrid energy fields is greater than the cost required by adopting them. In future research, it is crucial for scholars to focus on determining the combination of energy fields that should be employed in auxiliary machining processes based on specific requirements and demands in different processes and materials. Furthermore, understanding the coupling mechanisms between different energy fields should be a key area of investigation.

5. Electric energy-assisted mechanical machining

EAMM can be categorized into two main techniques: EDAMM and EFAMM. EDAMM, a type of heating-assisted mechanical machining technique, involves the sequential and cyclic occurrence of discharge heating, cooling, and mechanical machining. The EDAMM process combines the advantages of both EDM and mechanical machining. During EDAMM, the maximum workpiece surface temperature can reach 7000 K or even higher when high electric discharge energy is utilized [194–196]. This extreme temperature causes the complete melting and vaporization of materials. Additionally, a well-known by-product called recast layer is formed [197–199]. The modified layer is removed using a subsequent mechanical machining process. It should be noted that the machinability of the subsurface material (material beneath the modified layer) is also enhanced, which is attributed to the softening effect of elevated temperature caused by electric discharge. EFAMM utilizes electric field to control the behavior of abrasive particles, which are mixed with an ER fluid to remove material from the raw workpiece. The viscosity of the ER fluid varies with the applied electric field intensity, leading to an enhanced stabilization of the abrasive particles surrounding the tool tip. EFAP represents a prototypical EFAMM process. By adjusting the electric field intensity, the shear strength

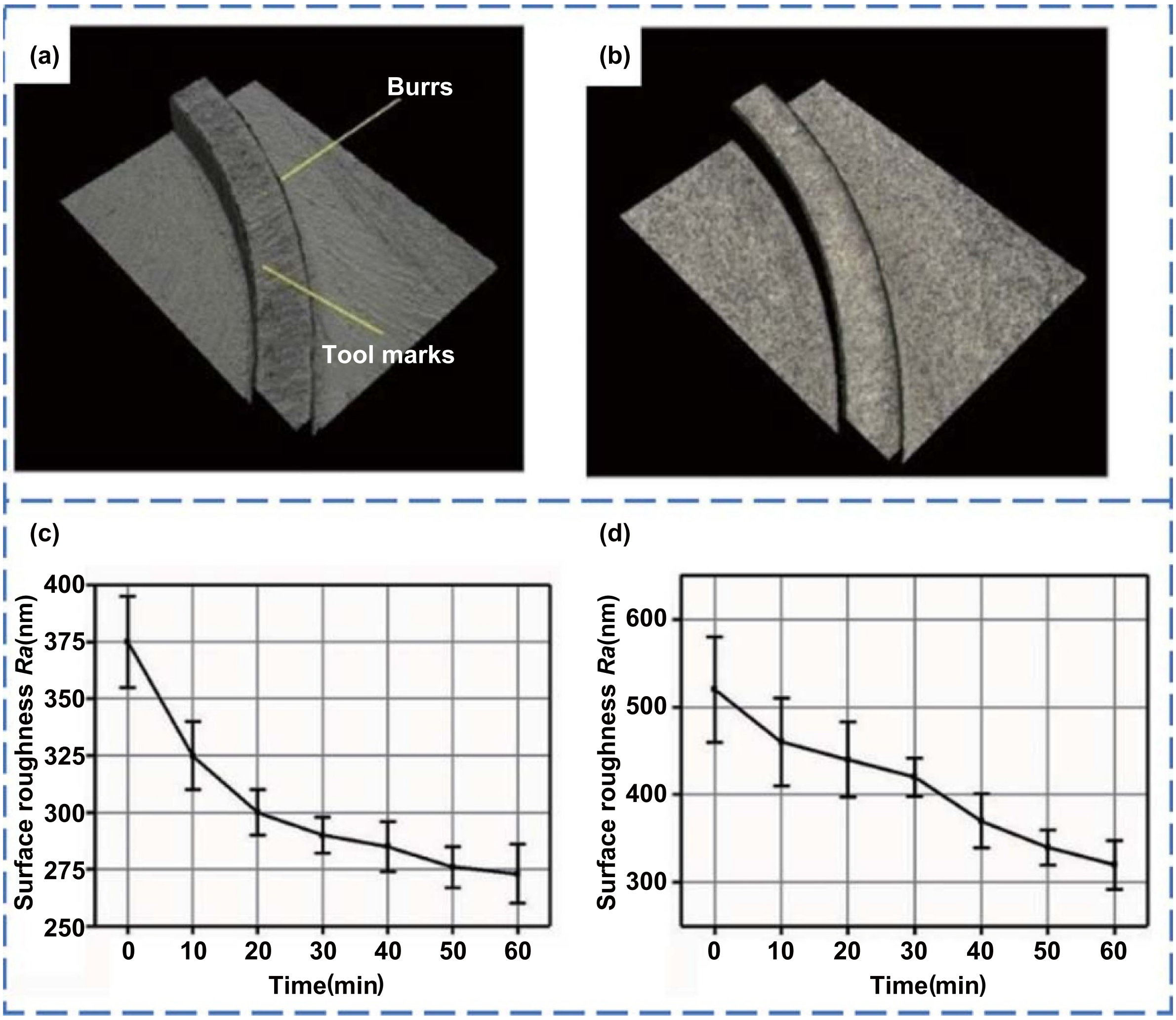

Figure 28. Morphologies of curved microfeatures (a) before and (b) after 40 min polishing, and surface roughness with respect to polishing time on (c) top and (d) side of microfeatures [193]. Reprinted from [193],

of the ER polishing liquid can be controlled. The ER components in the polishing fluid form a chain or columnar structure. The abrasive particles are retained within the microstructure, thereby forming a flexible polishing head. This process facilitates precise machining control and enables polishing of complex structures [200, 201]. Figure 29 illustrates the research framework of EAMM.

5.1. Electric discharge-assisted milling

EDAM is a hybrid technology that combines EDM with CM, utilizing sharp cutting edges to effectively remove metamorphic material through the generation of electric sparks [206]. This method reduces tool wear, improves machining quality, and enhances machining efficiency. Li *et al* [202, 207–210] extensively investigated the process mechanisms, specific tool design, process simulation, output parameters, and effects of process parameters on them. A schematic of the material removal process is presented in figure 30(a). Following EDM of the local material to be processed, an easily machinable layer consisting of a recast layer and a heat-affected layer is generated. Subsequently, mechanical milling is performed to eliminate this layer. To ensure that the microstructure and phase of the machined surface remain consistent with those of the raw material, a small amount of matrix material is also removed through mechanical milling. The capacitance exerts a significant influence on the process performance. As the capacitance increases, both the maximum temperature of the workpiece surface and the EDM-induced crater size increase, whereas the cutting force and stress decrease. Experimental results on EDAM of Ti–6Al–4V titanium alloy demonstrated that the cutting force in EDAM was reduced by more than 50% compared to CM, as depicted in figure 30(b). Furthermore, the surface roughness and tool wear rate exhibited a remarkable reduction of five times and three times, respectively, compared to CM, as evidenced in figures 30(c) and (d). Additionally, an investigation was conducted to compare the surface integrity parameters, including surface hardness, residual stress,

Table 3. Hybrid nontraditional energy-assisted mechanical machining processes and output parameters. (↑: increased by.↓: decreased by)

Reference	Workpiece material	Hybrid process	Process parameters	Output parameters (compared with conventional)
Wu *et al* [177]	Ti–6Al–4V	UPOAG	Plasma current: 2.0 A Frequency: 40 kHz Duty ratio: 50% Vibration frequency: 25 kHz Amplitude: 0, 2.2, 2.9, 4.0, and 4.9 μm Grinding speed: 94.2 m min^{-1} Feed: 60 mm min^{-1} Depth of cut: 0.01 mm	MRR: ↑ maximum 210% Surface roughness R_a: ↓ maximum 60%
Yang *et al* [178]	4H-SiC	UAECMP	Wafer speed: 50 rpm Grinding stone speed: 200 rpm Oscillation rate: 2 mm s^{-1} Oscillation distance: 3 mm Polishing pressure: 30 kPa Ultrasonic frequency: 35 kHz Ultrasonic power: 500 W Abrasive particle size: 0.5–2.0 μm	MRR: ↑ maximum 450%
Kim *et al* [179]	SiCp/AA2124 composites	LAT and UVAT	Laser power: 529, 476, and 582 W Frequency: 20.33 kHz with WC tool and 20.23 kHz with PCD tool Amplitude: 28, 1, and 1.7 μm with WC tool and 28, 0.9, and 1.5 μm with PCD tool Cutting speed: 30 m min^{-1} Feed: 0.14 mm rev^{-1} Depth of cut: 0.15 mm	Cutting force: ↓ maximum 43.6% Surface roughness S_a: ↓ maximum 19.3% Surface roughness R_a: optimal 765.3 nm
Dominguez-Caballero *et al* [181]	Ti–6Al–4V	LAT and UVAT	Laser power: 60–750 W Frequency: 20.33 kHz Amplitude: 28.8, 7.2, and 8.1 μm Cutting speed: 20, 45, and 70 m min^{-1} Feed: 0.04 mm rev^{-1} Depth of cut: 0.15, 0.2, and 0.25 mm	Cutting force: ↓ maximum 70.1% Surface roughness R_a: optimal 0.7 μm
Deswal and Kant [182]	Ti–6Al–4V	LAT and UVAT	Laser power: 100, 200, and 300 W Frequency: 20 kHz Amplitude: 20 μm Cutting speed: 11 and 21 m min^{-1} Feed: 0.1 mm rev^{-1} Depth of cut: 0.1 mm	Cutting force: ↓ maximum 79% Surface roughness R_a: ↓ maximum 45%
Zhang and Jiao [184]	WC	LAT and UVAT	Laser power: 350 W Frequency: 35 kHz Amplitude: 1.4 and 2.1 μm Cutting speed: 30 m min^{-1} Feed: 0.014 mm rev^{-1} Depth of cut: 15 μm	Cutting force: ↓ maximum 67.5% Tool life: ↑ maximum 95.3% Surface roughness R_a: ↓ maximum 91%
Wang *et al* [186]	Inconel 718	Cryogenic cooling and plasma-assisted turning	Plasma gas flow rate: 1.7 l min^{-1} Shield gas flow rate: 14 l min^{-1} Arc current: 265 Amp Cutting speed: 5.2 m min^{-1} Feed: 0.127 mm rev^{-1} Depth of cut: 0.76 mm LN_2 pressure: 160 psi	Cutting force: ↓ maximum 50% Tool life: ↑ maximum 156% Surface roughness R_a: ↓ maximum 51%
Zhai *et al* [191]	Silicon	Megasonic vibration and chemical assisted-polishing	Megasonic frequency: 1.7 MHz Pressure: 2 psi Platen speed: 55 and 35 rpm Carrier speed: 50 rpm Time: 20 and 30 min Flow rate of polishing slurry: 20 ml min^{-1}	MRR: ↑ maximum 25% Surface roughness R_a: ↓ maximum 24%
Zhai *et al* [192]	Sapphire	UAMP	Polishing pressure: 25 kPa Relative velocity: 0.1 m s^{-1} Polishing time: 2 h Ultrasonic frequency: 20 kHz Ultrasonic amplitude: 50 μm	Surface roughness R_a was slightly deteriorated. MRR: ↑ maximum 340%

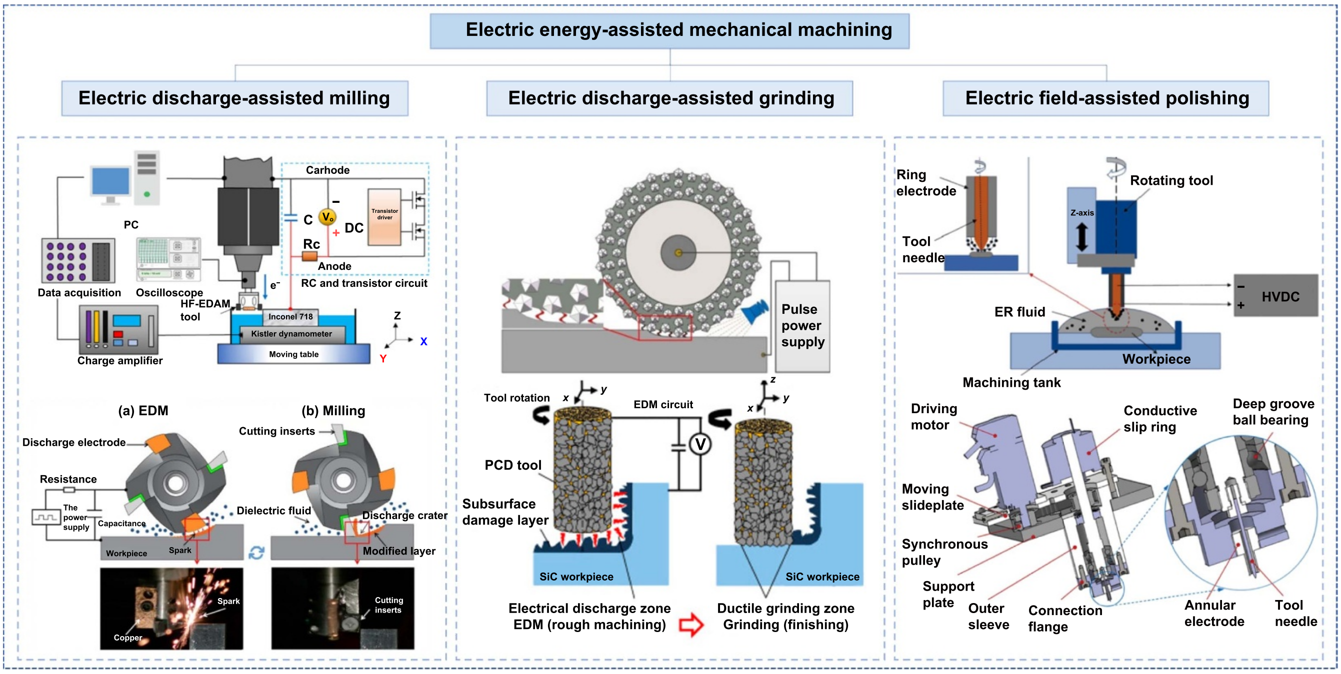

Figure 29. Classification diagram of electric EAMM [200, 202–205]. Reprinted from [200], © 2022 Elsevier B.V. All rights reserved. Reprinted from [202], © 2022 Published by Elsevier Ltd on behalf of The Society of Manufacturing Engineers. Reprinted from [203], © 2022 The Society of Manufacturing Engineers. Published by Elsevier Ltd. All rights reserved. Reprinted from [204], Copyright © 2015 CIRP. Published by Elsevier Ltd. All rights reserved. Reproduced from [205], with permission from Springer Nature. (HVDC: High Voltage Direct Current. DC: Direct Current)

and surface defects, between EDAM and CM. The residual stress generated in EDAM, mainly compressive stress, is much lower than that generated in CM. The two processes exhibit similar surface hardness, suggesting that electric energy has a minor influence on work hardening. The predominant surface defects in EDAM are chips, pits, and pitting corrosion. As a result of the elevated temperature during the EDM and milling processes, chips adhere to the tool surface following EDAM. The occurrence of tool edge fracture after CM, as depicted in figure 30(e), is a common phenomenon observed during the machining of Ti–6Al–4V titanium alloy. The enhancement in surface integrity and tool performance can be attributed to the softening effect resulting from the heat generated by electric discharge.

Additionally, Xu *et al* [203] developed an improved processing technique, known as HF-EDAM, for the machining of Inconel 718. A specifically designed electrode using a copper–beryllium bundle is shown in figure 31(a). In HF-EDAM, the copper–beryllium bundle not only serves as an electrode during the EDM stage but also effectively eliminates chips at the milling stage, thereby improving both discharge efficiency and process performance. The results demonstrated that the application of this process led to a significant reduction in cutting forces (up to 32.55%) compared to CM. Furthermore, the surface roughness in HF-EDAM was considerably decreased, with a measured R_a value of 1.09 μm. Moreover, the issue of chip adhesion commonly observed on the machined surface during CM of Inconel 718 was significantly mitigated in HF-EDAM because of the effective cleaning action facilitated by the copper–beryllium bundle, as illustrated in figure 31(b).

Kim *et al* [211] investigated the mechanisms of burr reduction in EDAM of AISI 1045 alloy steel. Owing to the thermal effect of EDAM, burr adhesion was greatly weakened, and the burr was easy to fracture. Compared with CM, the generation of burrs in EDAM was suppressed effectively. The increase in discharge capacitance resulted in a minimized burr height.

5.2. Electric discharge-assisted grinding

EDAG is a hybrid process that combines the interactions of EDM and mechanical grinding to machine electrically conductive materials. Electric discharge occurs when the distance between the grinding wheel and the workpiece surface is appropriate, causing localized thermal softening in the grinding zone. This results in an improved machinability. In addition, electric discharges are utilized for dressing and declogging the grinding wheel, thereby enhancing the process performance. The schematic in figure 32(a) illustrates the process principle of EDAG. Current research on the EDAG process primarily focuses on investigating the impact of EDM parameters (e.g. voltage, current, pulse width, and pulse interval) and grinding parameters (e.g. wheel speed, radial depth of cut, and feed speed) on various process outcomes, including force generation, surface integrity, and wheel performance.

The process characteristics of high-speed steel with a hardness of 1200 HV in EDAG were investigated by Koshy *et al* [214]. They also examined the influence of machining parameters on these characteristics. The experimental results showed that MRR was improved with an increase in current, whereas the normal grinding force and specific grinding

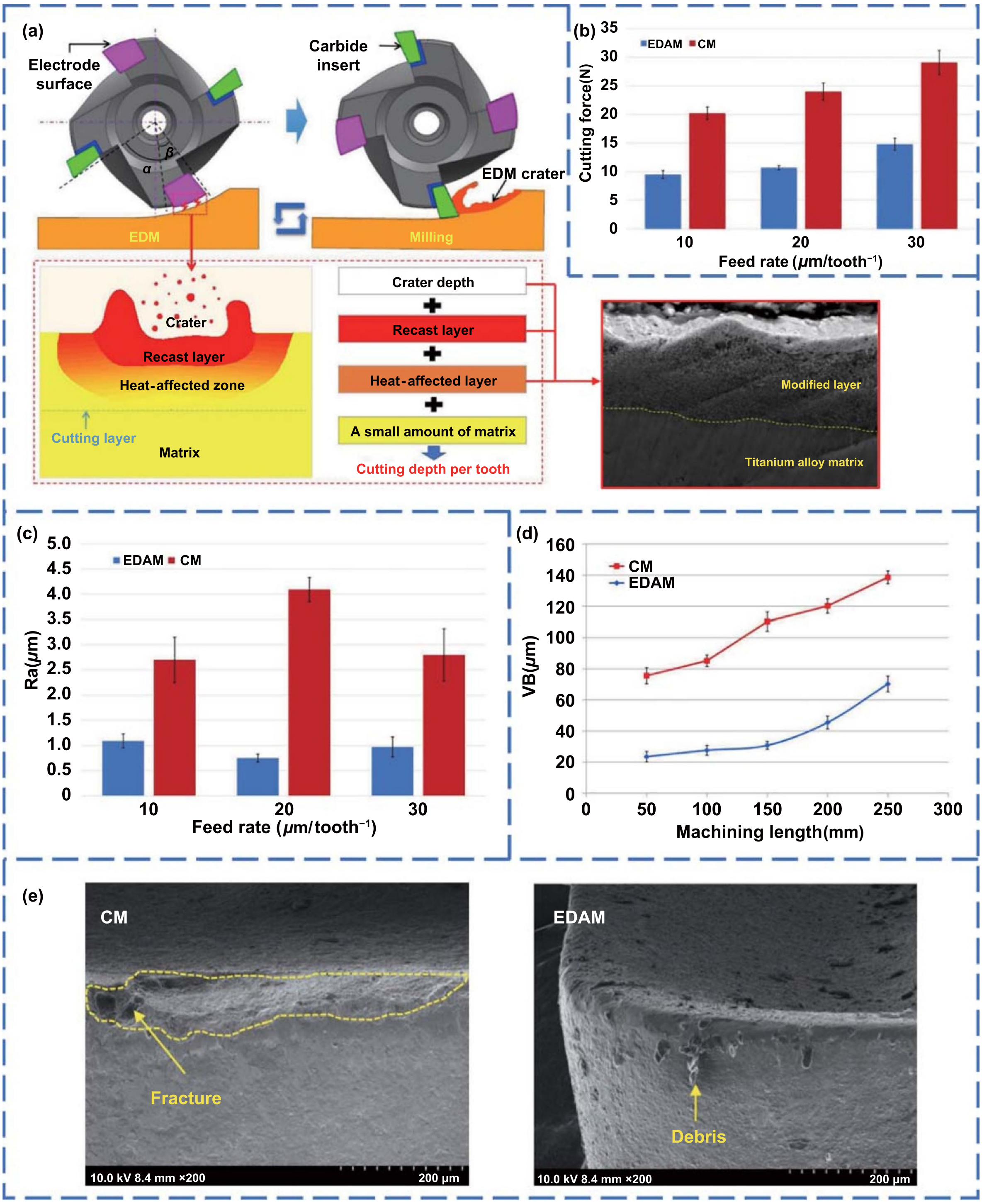

Figure 30. EDAM process and outcomes. (a) Process principle and electric discharge-induced modified layer [202]. Comparisons of (b) cutting force, (c) surface roughness, and (d) tool wear between EDAM and CM [210]. (e) Tool wear morphologies in CM and EDAM [202]. Reprinted from [202], © 2022 Published by Elsevier Ltd on behalf of The Society of Manufacturing Engineers. Reprinted from [210], © 2020 Elsevier B.V. All rights reserved.

energy displayed the opposite trend. Compared to pure grinding, EDAG showed a significant improvement in both MRR (eight times higher) and specific grinding energy (86% lower). However, the radial wheel wear rate exhibited a substantial increase with an increase in current, reaching approximately five times higher than that observed in pure grinding. Wei *et al* [213] compared the surface integrity of Inconel 718 in EDAG with that in CM. They found that the microhardness and modulus of the machined surface in EDAG were much lower than those in CM (figures 32(a) and (b)). The softened layer can be removed easily during the finishing stage. Moreover, the local misorientations in the EDG zone were significantly lower

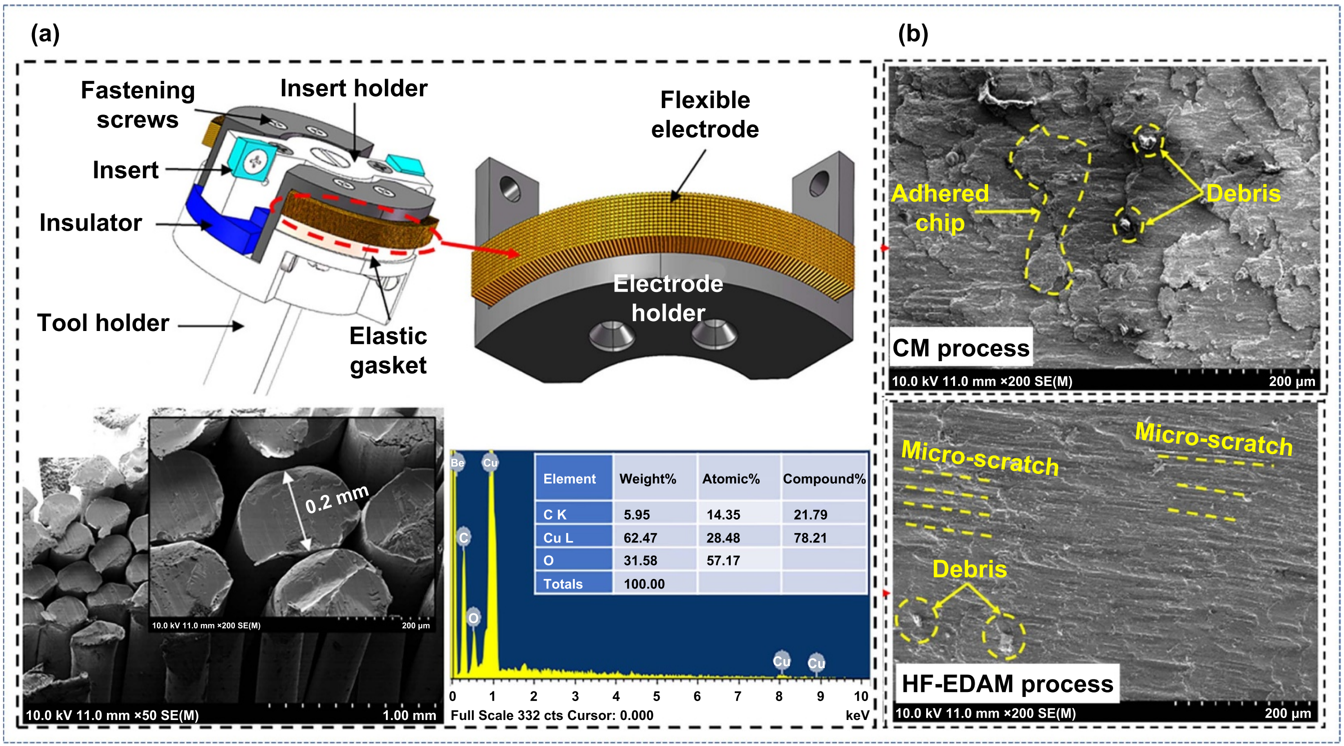

Figure 31. HF-EDAM process and resultant surface defects. (a) Schematic of the developed specific tool using copper–beryllium bundle electrodes [203]. (b) Resultant surface defects in CM and HF-EDAM processes [203]. Reprinted from [203],

than those in the pure grinding zone. However, the corrosion resistance of the EDG zone was considerably inferior to that of the pure grinding zone. Shu and Tu [215] found that the MRR in EDAG of HPM50 mold steel using a metal matrix (Cu/SiC_p) grinding wheel was up to seven times higher compared to pure EDM. Yan and Tan [204] demonstrated the formation of a recast layer consisting of SiC, Si, and C in the EDAG process of single-crystal SiC. As voltage increased from 70 to 110 V, the thickness of the recast layer increased from 2 to 3 μm (figure 32(d)). The hardness of the recast layer was lower than that of the bulk because of the material decomposition. An extremely smooth surface with a roughness R_a of 1.85 nm was achieved. Because of the interdependence and interaction of EDM and mechanical grinding, the material removal mechanism in EDAG is complicated. Satyarthi and Pandey [212] established a mathematical model to investigate the influence of the two processes on material removal. This model can be used to predict the MRR of EDAG and analyze the effects of the input process parameters on MRR. They found that the electric discharge energy was the main factor influencing the material removal. The corresponding experimental results for the Al_2O_3–SiC_w–TiC ceramic composite indicated that the accuracy of the mathematical model was more than 97%. Similarly, a prediction model of MRR was established by Shrivastava and Dubey [216] by applying a hybrid approach of neural network and genetic algorithm. This model was used to optimize the process parameters of EDAG, and a significant improvement of 48.24% was realized for the MRR of copper–iron–carbide MMC.

The defects generated in EDAG are significantly distinct from those produced in conventional machining processes because of the coupling effect of discharge sparks and abrasive grains. For this reason, Rao *et al* [205, 217] analyzed the subsurface defects in EDAG of RB SiC. Different material removal mechanisms and distinctive morphologies of the machined surface were exhibited in the EDM and grinding zones. When pure grinding was used, a thick SSD layer with many voids was produced (figure 33(a)), resulting from the brittle fracture of the material under grinding action. The increase in discharge energy promoted the brittle–ductile transition and workpiece decomposition while initially reducing and subsequently increasing the thickness of the SSD layer (figures 33(b)–(d)). The damages mainly consisted of voids, microcracks, and stacking faults. In addition, considering the limitation of EDAG, Ji *et al* [218] proposed a new electric discharge method using synchronous servo double electrodes. The utilization of this method effectively enhanced tool longevity, enabled in-process wheel dressing, improved surface quality, and facilitated machining of nonconductive materials.

5.3. Electric field-assisted polishing

EFAP is an advanced machining method that selectively polishes surfaces using the ER effect. The polishing compound used in EFAP contains an ER material that can be classified into two types: particle and liquid crystal polymer. As a remarkable class of intelligent functional materials, ER fluids

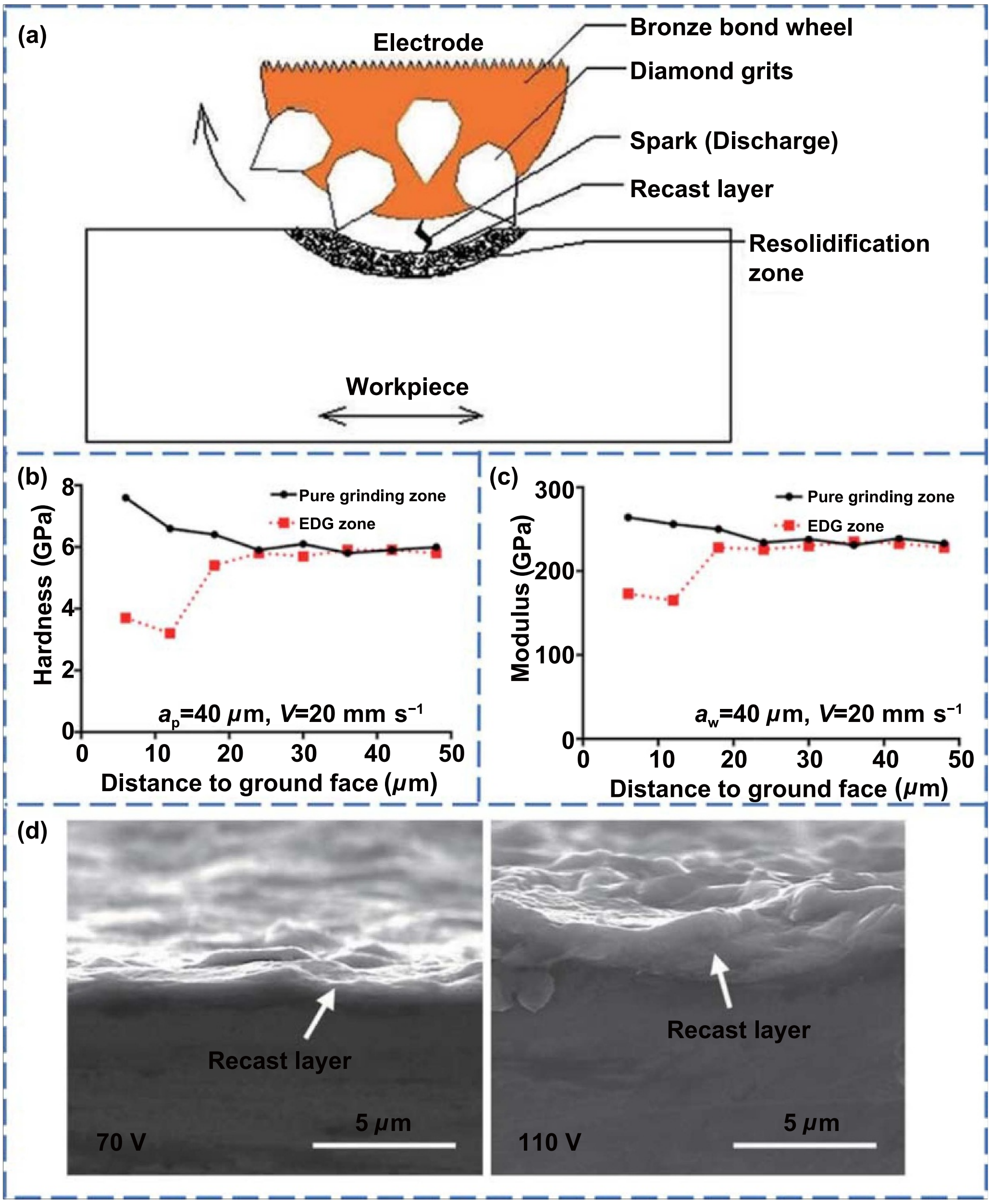

Figure 32. EDAG process and comparisons with pure grinding. (a) Schematic of process principle [212]. (b) Surface hardness and (c) modulus of the materials in the EDAG and pure grinding zones [213]. (d) Morphologies of recast layers showing thickness evolution with input voltage [204]. Reprinted from [212], Copyright © 2013 Elsevier Ltd. All rights reserved. Reproduced from [213], with permission from Springer Nature. Reprinted from [204], Copyright © 2015 CIRP. Published by Elsevier Ltd. All rights reserved.

demonstrate a distinctive rheological behavior triggered by an electric field. When subjected to an electric field, ER fluids exhibit a rapid increase in apparent viscosity and yield strength, resembling the characteristics of solids. After the removal of the external electric field, ER fluids return to their original fluidic properties. Current studies on EFAP primarily focus on optimizing the machining parameters and investigating the material removal mechanisms.

Kuriyagawa *et al* [219] proposed a novel ER fluid-assisted polishing method for miniaturized components. The effects of polishing parameters, including electrode shape, electric field strength, and abrasive particle type, on the machining quality of BK7 glass were investigated. The dielectric constant of the abrasive surpassed that of the ER fluid to ensure a high-quality polishing process. Feng *et al* [220] conducted a study on the machining influence of different electrode materials and various ER fluids on glass. The utilization of quenched steel and stainless-steel electrodes yielded larger and deeper machining regions with uniform material removal, whereas graphite electrodes exhibited a lower MRR and nonuniform material elimination. Furthermore, the machining trace of zeolite ER fluid demonstrated enhanced integration and depth compared with the SiO_2 ER fluid. Fan *et al* [221] investigated the possible factors affecting the ER polishing of aluminum. They found that tool spindle speed, polishing time, and applied voltage had a significant influence on the roughness of the machined

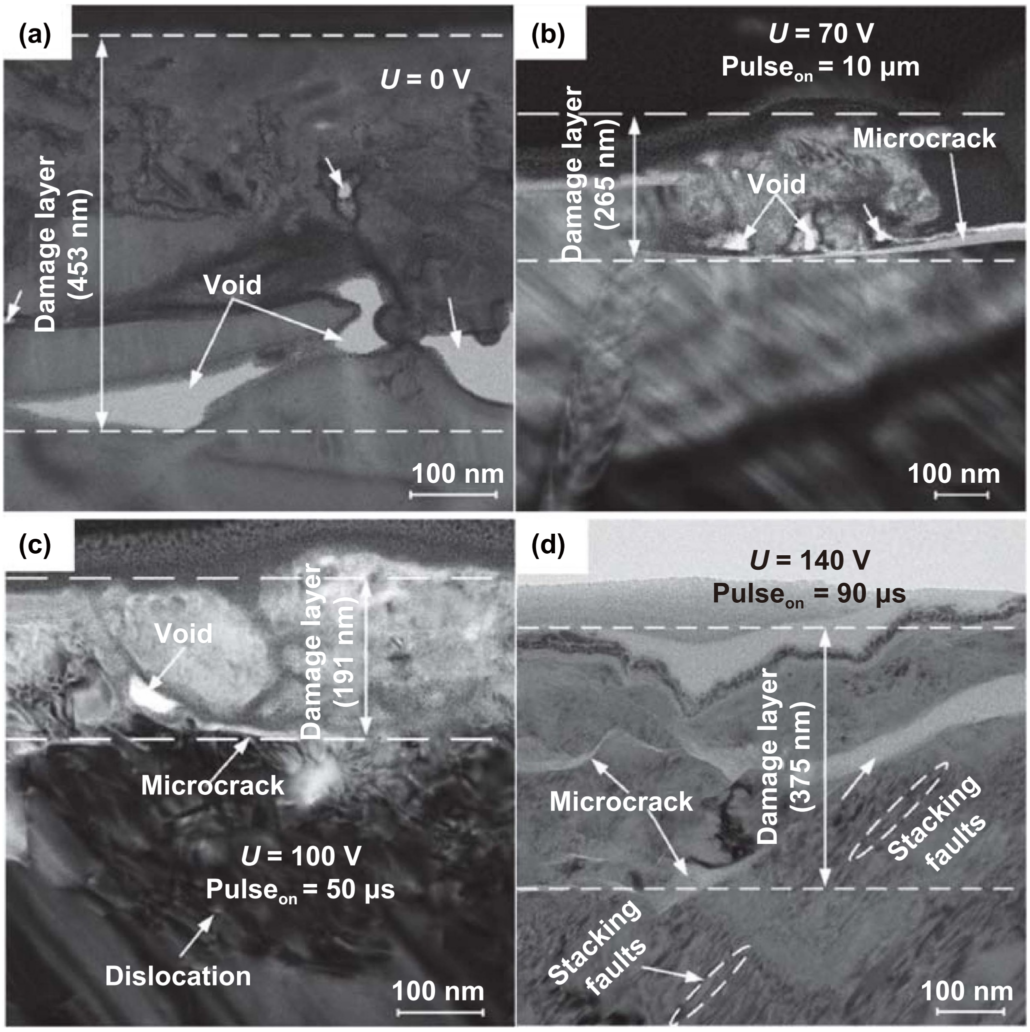

Figure 33. SSDs generated in (a) pure grinding, and (b)–(d) EDAG using various open-circuit voltages and pulse-on times [217]. Reprinted from [217], © 2020 Elsevier Ltd. All rights reserved.

surface. Subsequently, they established a material removal model to describe the material removal process, providing a technical basis for predicting the ER polishing surface quality [200]. Su *et al* [222] analyzed the interaction force of different microparticles (including starch and ceria particles) in the polishing compound based on a body-centered tetragonal lattice model (figure 34(a)). As shown in figures 34(b)–(d), the influence of machining parameters, such as supply voltage and working distance, on particle force and footprint depth was evident. A significant correlation between the particle force and the material removal capability was observed. When the supply voltage increased from 3000 to 5000 V, the particle size and the polishing footprint depth increased by more than one and three times, respectively. On the contrary, the depth of the footprint and the particle size were reduced with an increase in the working distance. An ultrasmooth polished spot with a surface roughness of 1.04 nm was achieved.

EAMM has great advantages in terms of reducing process force and tool wear rate, as well as enhancing surface integrity and process efficiency. EDAG allows the in-process dressing of the grinding wheel, thereby enhancing the overall performance of the process. EFAP can realize ultraprecision polishing of freeform components and microparts due to the high abrasive concentration. However, only electrically conductive materials can be processed using either EDAM or EDAG. Novel techniques to address this limitation need to be developed in the future, such as pretreating the workpiece surface to make it locally conductive. Further theoretical investigations into the synergistic mechanisms between electric discharge and mechanical machining are required. Table 4 presents a comparison of the output parameters of the various EAMM processes and conventional mechanical machining.

6. Magnetic energy-assisted mechanical machining

MEAMM is a novel technology in which an external magnetic field is applied to control the properties of MRF. When an external magnetic field is applied, the magnetic particles in MRF condense rapidly, and the viscosity of the fluid increases [223, 224]. The surface of the workpiece is processed using a 'small polishing head' formed within the MRF

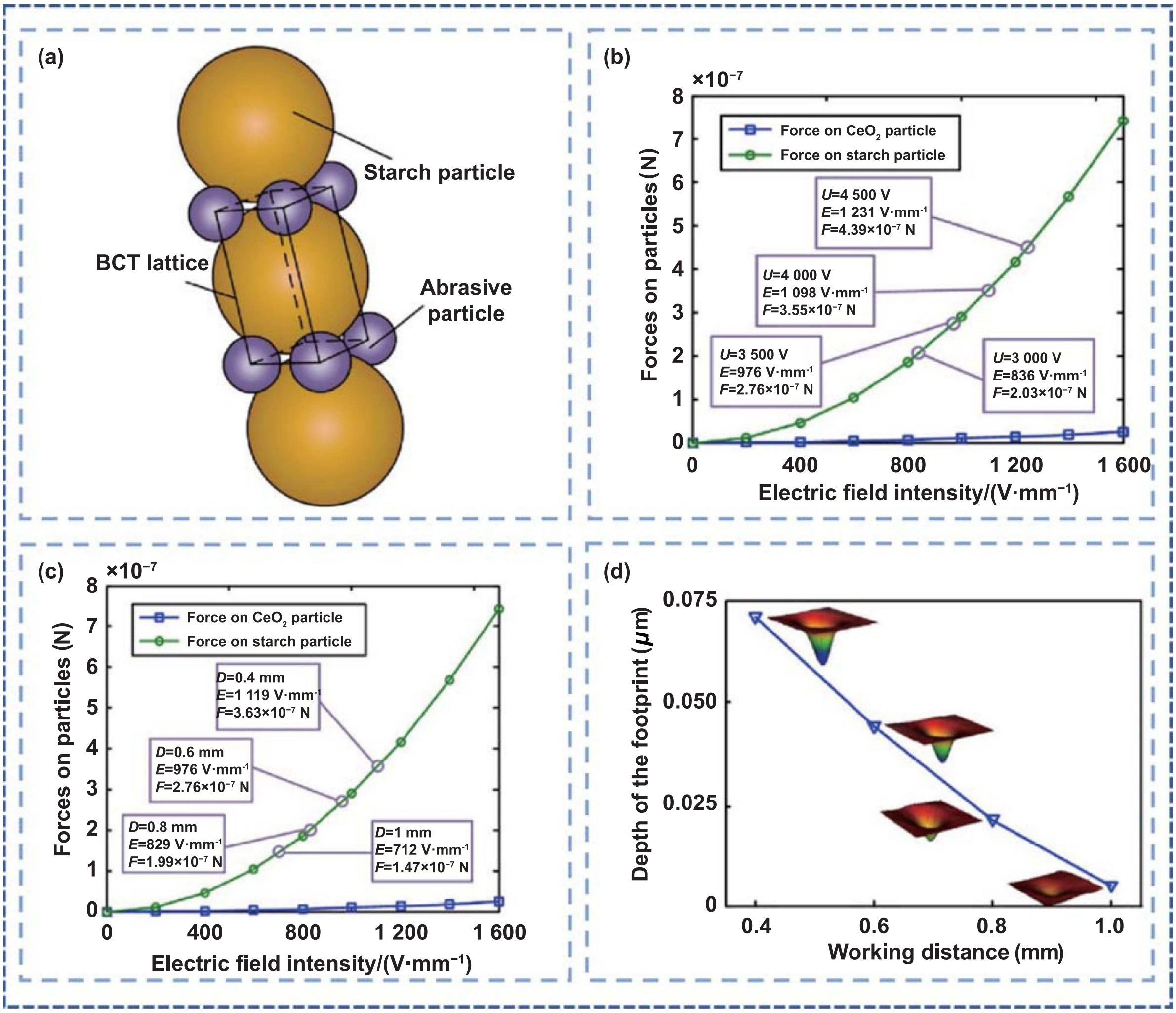

Figure 34. Characteristics of EFAP with different particles and process parameters. (a) Body-centered tetragonal (BCT) lattice model of particles [222]. (b), (c) Evolution of forces on particles with electric field intensity and working distance [222]. (d) Evolution of footprint depth with working distance [222]. Reprinted from [222], © 2016 Elsevier B.V. All rights reserved.

in the polishing area. Because of the real-time control of the shape and hardness of the small polishing head, the MEAP technology not only controls the size and shape of the polishing area but also ensures the stability, contact stiffness, and toughness of the polishing fluid [225]. These advantages are incomparable to those of the conventional mechanical polishing. In addition, MEAT, milling, and boring processes have been investigated. Damping is implemented by utilizing an external magnetic field on either the tool or workpiece, effectively reducing vibration during the cutting process and enhancing the machining quality [226–228]. The research framework of MEAMM is shown in figure 35.

6.1. Magnetic energy-assisted polishing

MEAP utilizes a flexible MRF as a polishing medium, enabling the removal of surface material from the workpiece through shear force. A schematic of the MEAP process is shown in figure 36(a). During the polishing process, the MRF entering the polishing area is constantly renewed. The polishing head is barely worn, thus ensuring the stability of the material removal efficiency. The polishing head size is small, which is suitable for machining complex structures, and can effectively control the edge effect. Compared with conventional polishing, MEAP has the advantages of high efficiency, less SSD, adjustable hardness of the polishing head, and no tool wear during machining [231]. MEAP is a research hotspot at home and abroad, which ranges from simple plane polishing to freeform surface polishing and from hard and brittle material polishing to hard metal surface polishing. Suzuki *et al* [223] proposed a MAP method for finishing synthetic silica diffractive optical element (DOE) lenses. To reduce the surface sagging of the DOE lens step, a brush-type polisher was used (figure 36(b)). These brushes could equally press the peak and valley of the lens surface, thus improving the form accuracy. During the MEAP process, the structured surface of lens can be finished without compromising the form accuracy or causing surface sagging, and a form accuracy of 1.1 μm *P–V* was achieved. Yamaguchi *et al* [224] studied the surface roughness and residual stress of selective laser melting-manufactured 316L stainless steel in MEAP. The results showed that the roughness underwent significant modifications over a wide

Table 4. Electric EAMM processes and output parameters. (↑: increased by.↓: decreased by)

Reference	Workpiece material	Hybrid process	Process parameters	Output parameters (compared with conventional)
Li *et al* [202]	Ti–6Al–4V	EDAM	Discharge voltage: 220 V Capacitance: 1000, 10 000, and 100 000 pF Spindle speed: 3000 rpm Feed rate: 0.01 mm z^{-1} Radial cutting depth: 0.08 mm Axial cutting depth: 0.2 and 1.5 mm	Cutting force: ↓ maximum 43.98% Cutting stress: ↓ 17.27%
Xu *et al* [203]	Inconel 718	EDAM	Discharge voltage: 200 V Capacitance: 10 000, 100 000, and 1 000 000 pF Dielectric: EDM oil Spindle speed: 3000 rpm Feed rate: 1, 5, and 10 mm z^{-1} Radial cutting depth: 0.1 mm Axial cutting depth: 1 mm	Cutting force: ↓ maximum 32.55% Surface roughness: ↓ maximum 56.8%
Yan and Tan [204]	Single-crystal SiC	EDAG	Voltage: 70 and 110 V Capacitance: 100–3000 pF Wheel speed: 3000 rpm	Surface roughness R_a: optimal 1.85 nm
Li *et al* [207]	STD 11 alloy steel	EDAM	Discharge voltage: 220 V Capacitance: 100 pF Spindle speed: 3000 rpm Feed speed: 1 mm min^{-1} Radial cutting depth: 0–1 mm Axial cutting depth: 0.3 mm	Tool life: ↑ more than five times Surface roughness: ↓ 140.1% Process efficiency: 14.4 times faster
Xu *et al* [208]	Ti–6Al–4V	EDAM	Discharge voltage: 220 V Capacitance: 1000, 10 000, and 100 000 pF Spindle speed: 2000–5000 rpm Feed rate: 10–70 mm min^{-1} Radial cutting depth: 0.15 mm Axial cutting depth: 1.5 mm	Surface roughness: ↓ 193% Surface hardness: ↓ 3.91% Burr free Lower compressive residual stress
Xu *et al* [209]	Ti–6Al–4V	EDAM	Discharge voltage: 220 V Capacitance: 1000, 10 000, and 100 000 pF Dielectric: kerosene, EDM oil, and DI water Spindle speed: 3000 rpm Feed speed: 30, 60, and 90 mm min^{-1}	Surface roughness: ↓ maximum 121.68%
Li *et al* [210]	Ti–6Al–4V	EDAM	Discharge voltage: 220 V Capacitance: 100 000 pF Discharge gap: 20 μm Spindle speed: 3000 rpm Feed rate: 10, 20, and 30 μm z^{-1} Radial cutting depth: 0.05 mm Axial cutting depth: 1.5 mm	Cutting force: ↓ more than 50% Surface roughness: five times lower Tool wear rate: three times lower
Kim *et al* [211]	AISI 1045 alloy steel	EDAM	Discharge voltage: 220 V Capacitance: 10, 100, 1000, and 10 000 pF Dielectric: EDM oil Spindle speed: 3000 rpm Feed speed: 2 mm min^{-1} Radial cutting depth: 0.25 mm Axial cutting depth: 0.1, 0.3, 0.5, and 0.7 mm	Cutting force: ↓ maximum 50% Burr height: ↓ maximum 84%
Koshy *et al* [214]	High-speed steel	EDAG	Voltage: 40 V Pulse width: 100 μs Duty factor: 0.5 Wheel speed: 60 m min^{-1}	MRR: ↑ more than eight times Specific grinding energy: ↓ maximum 86% Radial wheel wear rate: ↑ about five times

(Continued.)

Table 4. (Continued.)

Reference	Workpiece material	Hybrid process	Process parameters	Output parameters (compared with conventional)
Wei *et al* [213]	Inconel 718	EDAG	Voltage: 70, 100, and 140 V Current: 2, 4, and 6 A Pulse width: 50 μs Pulse interval: 50 μs Wheel speed: 30 m s^{-1} Feed speed: 20, 40, and 60 mm s^{-1} Depth of cut: 10, 40, and 100 μm	Surface hardness: ↓ approximately 50% Modulus: ↓ approximately 35%
Kuriyagawa *et al* [219]	BK 7 glass	EFAP	Tool rotational speed: 5000 rpm Workpiece rotational speed: 200 rpm Abrasive: SiC Gap between wheel and workpiece: 3 μm Polishing time: 10 min	Efficiency: ↑ 5.6 times
Su *et al* [222]	—	Electric field-assisted polishing	Voltage: 3, 3.5, 4, and 4.5 kV Working distance: 0.4, 0.6, 0.8, and 1 mm Wheel speed: 600 rpm	Surface roughness: optimal 1.04 nm

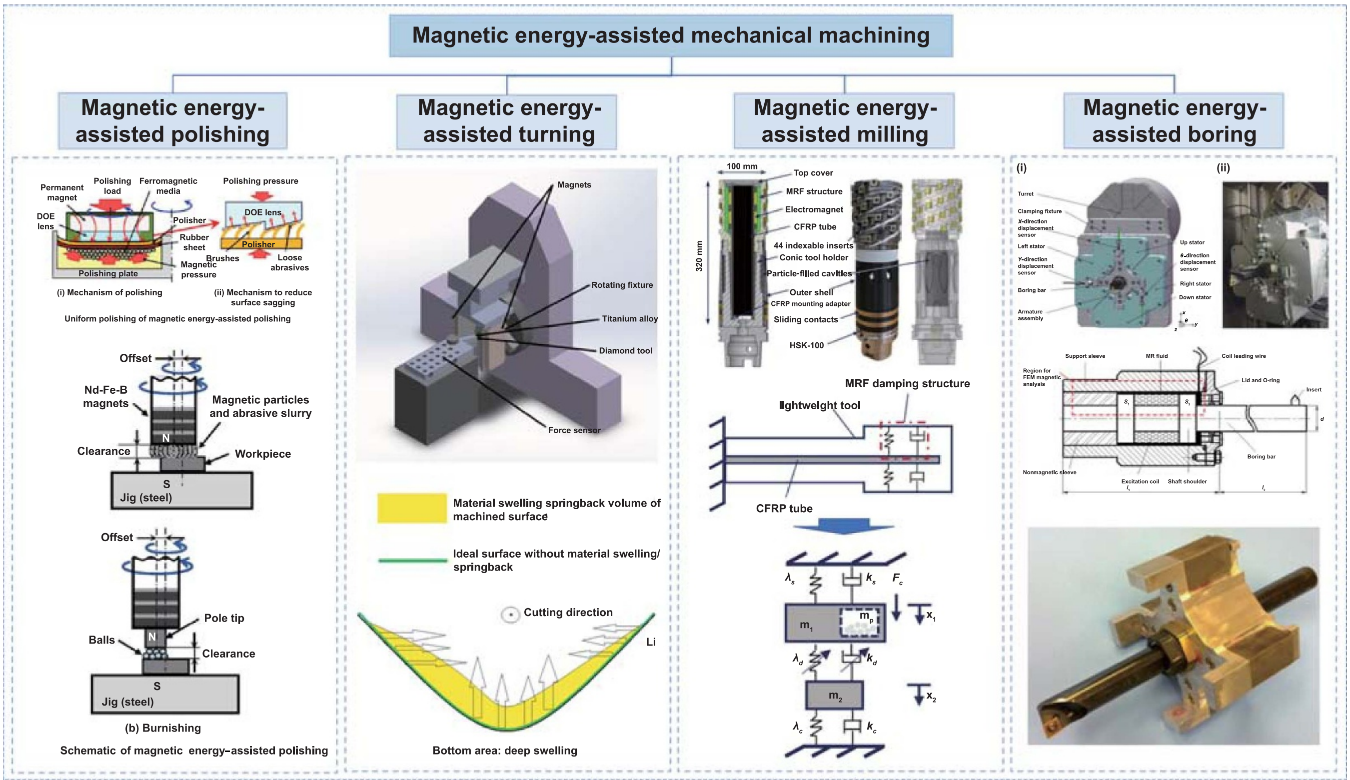

Figure 35. Classification diagram of MEAMM [223, 224, 226–230]. Reprinted from [223], Copyright © 2014 CIRP. Published by Elsevier Ltd. All rights reserved. Reprinted from [224], © 2017 Published by Elsevier Ltd on behalf of CIRP. Reproduced from [226]. CC BY 4.0. Reprinted from [227], © 2017 Elsevier B.V. All rights reserved. Reprinted from [228], Copyright © 2008 Elsevier B.V. All rights reserved. Reproduced from [229]. © IOP Publishing Ltd. All rights reserved. Reprinted from [230], Copyright © 2014 Elsevier Ltd. All rights reserved.

range, ranging from over 100 μm (initial roughness) to 0.1 μm. The roughness S_a of the MEAP surface decreased by approximately 65% compared with that of the sanded surface, as shown in figures 36(c) and (d). The residual stress generated with MEAP was tensile stress, and the residual stress in the laser scanning direction was lower than that of the raw workpiece.

Wu *et al* [233] proposed a novel ultraprecision MAF technique, utilizing a low-frequency alternating magnetic field. The process principle is shown in figure 37(a). The magnetic cluster experienced vertical oscillations under the influence of the alternating magnetic force. The movement not only enhanced the dispersion of magnetic particles but also improved the cross-cutting and stirring effects of the abrasives.

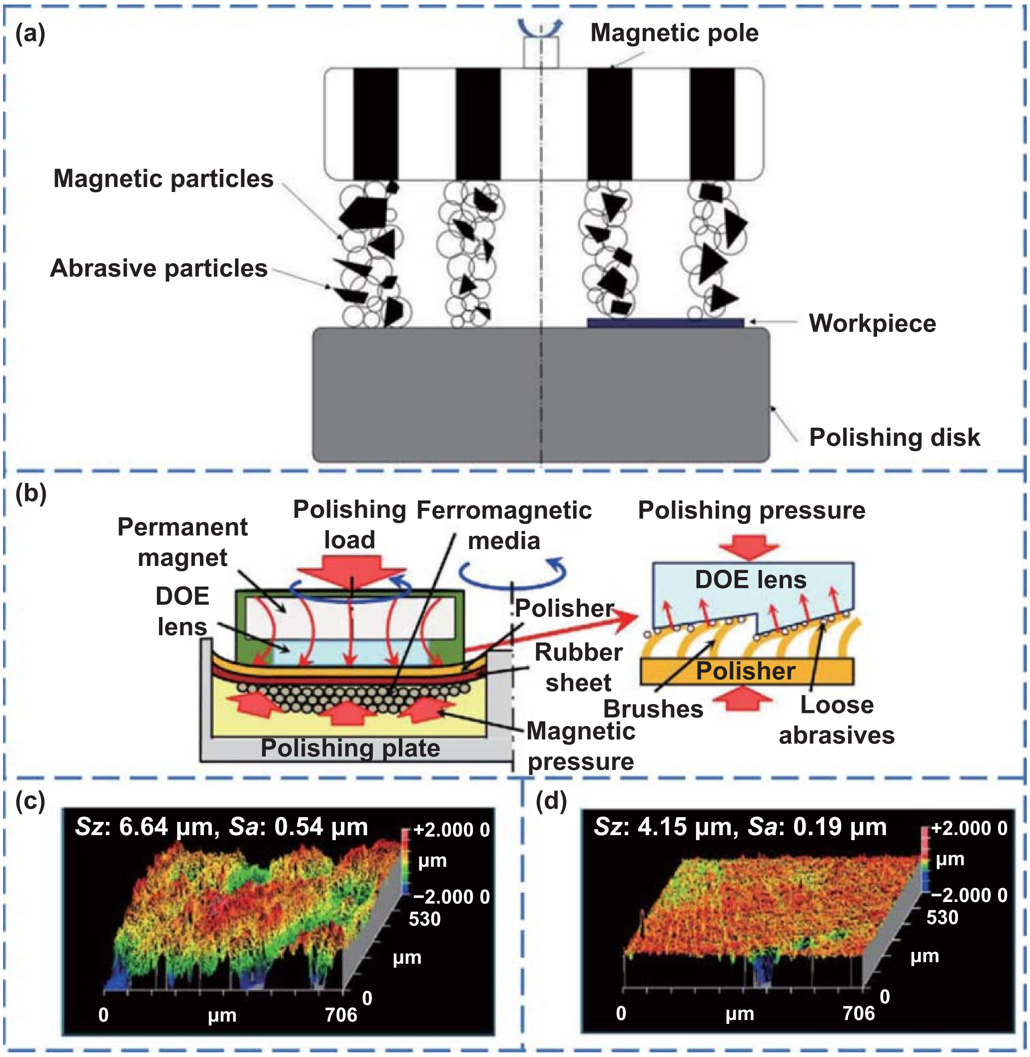

Figure 36. MEAP process and resultant surface roughness. (a) Schematic of the MEAP process [232]. (b) Principle of uniform polishing of DOE lens [223]. Surface geometries obtained with (c) sand polishing and (d) MEAP [224]. Reprinted from [232], © 2020 Elsevier B.V. All rights reserved. Reprinted from [223], Copyright © 2014 CIRP. Published by Elsevier Ltd. All rights reserved. Reprinted from [224], © 2017 Published by Elsevier Ltd on behalf of CIRP.

As a result, circulation and updating were achieved, ensuring grinding stability. The results demonstrated that this novel process enabled the ultraprecision finishing of flat surfaces. The surface roughness of the machined SUS304 stainless steel was decreased from 240 to 30 nm, as shown in figure 37(b). In addition, MRR was improved by applying this novel technique. After processing for 60 min, the material removal amount of MAF was twice as high as that of the direct polishing process. Murata *et al* [234] prepared a unique core–shell abrasive for polishing soda-lime glass with the assistance of magnetic field. They achieved a significantly higher MRR when using the magnetic field compared to conventional abrasives. In addition, this process had superior surface quality and higher polishing efficiency than conventional polishing methods.

Wang *et al* [235] put forward an innovative MAMP technique for achieving high-efficiency polishing of multiple freeform components. The process principle is shown in figure 38(a). A rotational magnetic field was applied to an annular chamber with six pieces of workpiece mounted inside. Simultaneously, the magnetic abrasives inside the annular chamber are driven to work on the workpiece surface and remove the material. Two types of abrasives, i.e. large bonded magnetic abrasives and loose magnetic abrasives, were applied in rough polishing and fine polishing, respectively. The morphologies, surface roughness, and microstructures of the unpolished and polished surfaces are shown in figure 38(b). The experimental findings validated the effectiveness of MAMP in machining freeform surfaces, resulting in nanometric surface roughness. The surface roughness was reduced by up to 96.97% with MAMP, as demonstrated in figure 38(c). The surface roughness rapidly decreased initially and then showed only a slight change with an increase in the polishing time. Furthermore, the rotational speed had a significant impact on the MRR. As shown in figure 38(d), the MRR at a rotational speed of 2000 rpm was ten times that at 100 rpm.

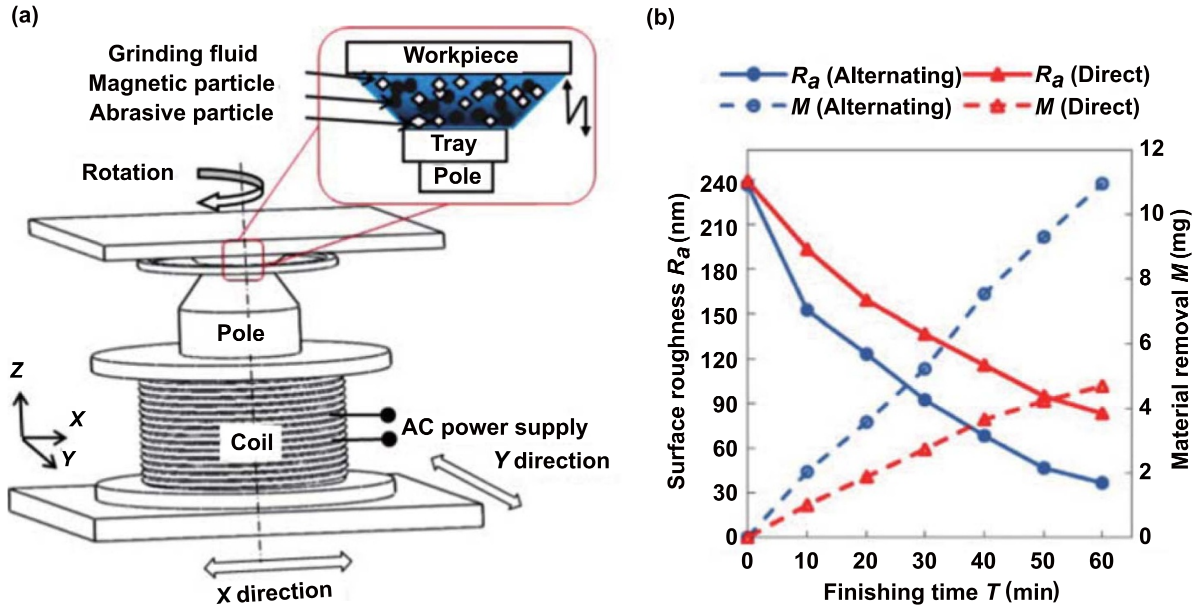

Figure 37. MAF) and comparison with direct polishing. (a) Process setup of MAF [233]. (b) Comparisons of surface roughness and material removal amount between MAF and direct polishing [233]. Reprinted from [233], Copyright © 2015 Elsevier B.V. All rights reserved.

6.2. Magnetic energy-assisted turning

MEAT differs from MEAP in terms of process principles. MEAT is a machining technique that utilizes a magnetic field to produce damping on the workpiece, thereby reducing machining vibration and improving machining stability. As a result, the tool life, generated geometrical accuracy, and surface integrity are improved. Vibration suppression in the MEAT process is due to the eddy damping effect. When an external magnetic field is applied to a rotational conductive workpiece, an eddy current is generated through a stationary magnetic field inside the workpiece. As a result, another magnetic field is formed due to the eddy current, and the direction of this magnetic field is opposite to that of the external magnetic field. Consequently, a repulsive force (i.e. Lorentz force) is induced, which is proportional to the workpiece rotational speed and external magnetic field intensity. The external magnet and rotational workpiece act as a viscous damper system, enabling the suppression of machining vibration.

The process performance of the magnetic energy-assisted SPDT of Ti–6Al–4V titanium alloy was investigated by Yip *et al* [227, 229, 236]. The repulsive force due to the eddy damping effect compensated for the machining vibration induced by the turning process. Consequently, the machinability of the titanium alloy was improved, adhesive tool wear was reduced significantly, and cutting force variation was improved remarkably. The surface roughness and coefficient of force variation were reduced by up to 55% and 65.88%, respectively. In addition, chip formation was improved in the hybrid process, as shown in figure 39(a). When no magnetic field was applied (intensity of 0 T), discontinuous chips were formed, indicating the formation of defects on the machined surface due to tool vibrations. In contrast, when a magnetic field with an intensity of 0.2 T was applied, long and continuous chips were formed. Moreover, the chip surface was flat and smooth without sawtooth tips, indicating a continuous turning and stable cutting mode. The presence of a magnetic field during turning also prevented material swelling/recovery on the machined surface (figure 39(b)), reducing adhesive wear and flank wear, as well as BUE in processing Ti–6Al–4V titanium alloy. The form error of the samples processed with MEAT was less than 4%, whereas it was 25%–37% for those processed with conventional turning. The maximum flank wear width in MEAT decreased by approximately 58% compared with that in conventional turning, as shown in figure 39(c). The improved process performance is attributed to the suppression of vibration in MEAT.

Magnetic field intensity is a key factor of MEAMM that influences the viscosity of MRF, further affecting the machinability, tool wear, chip formation, and surface quality of the workpiece material. Khalil *et al* [237] studied the influence of magnetic field intensity on the machining performance in magnetic energy-assisted ultraprecision single-point turning of Ti–6Al–4V titanium alloy. The results demonstrated that for the investigated range of magnetic field intensities, the machined surface roughness decreased with an increase in the magnetic field intensity. The minimum value of surface roughness (13.33 nm at magnetic field intensity of 0.02 T) achieved with MEAT was 33% lower than that achieved without MEAT. In addition, magnetic energy improved the chipping process and led to continuous chip formation. Moreover, lower tool wear rate was achieved in MEAT due to the reduction in BUE formation. Magnetic energy was also applied to facilitate the penetration of cutting fluids into the cutting zone, which had a beneficial effect on cooling and lubrication. Zhang *et al* [238] carried out a very interesting study on the MEAT of Ti–6Al–4V

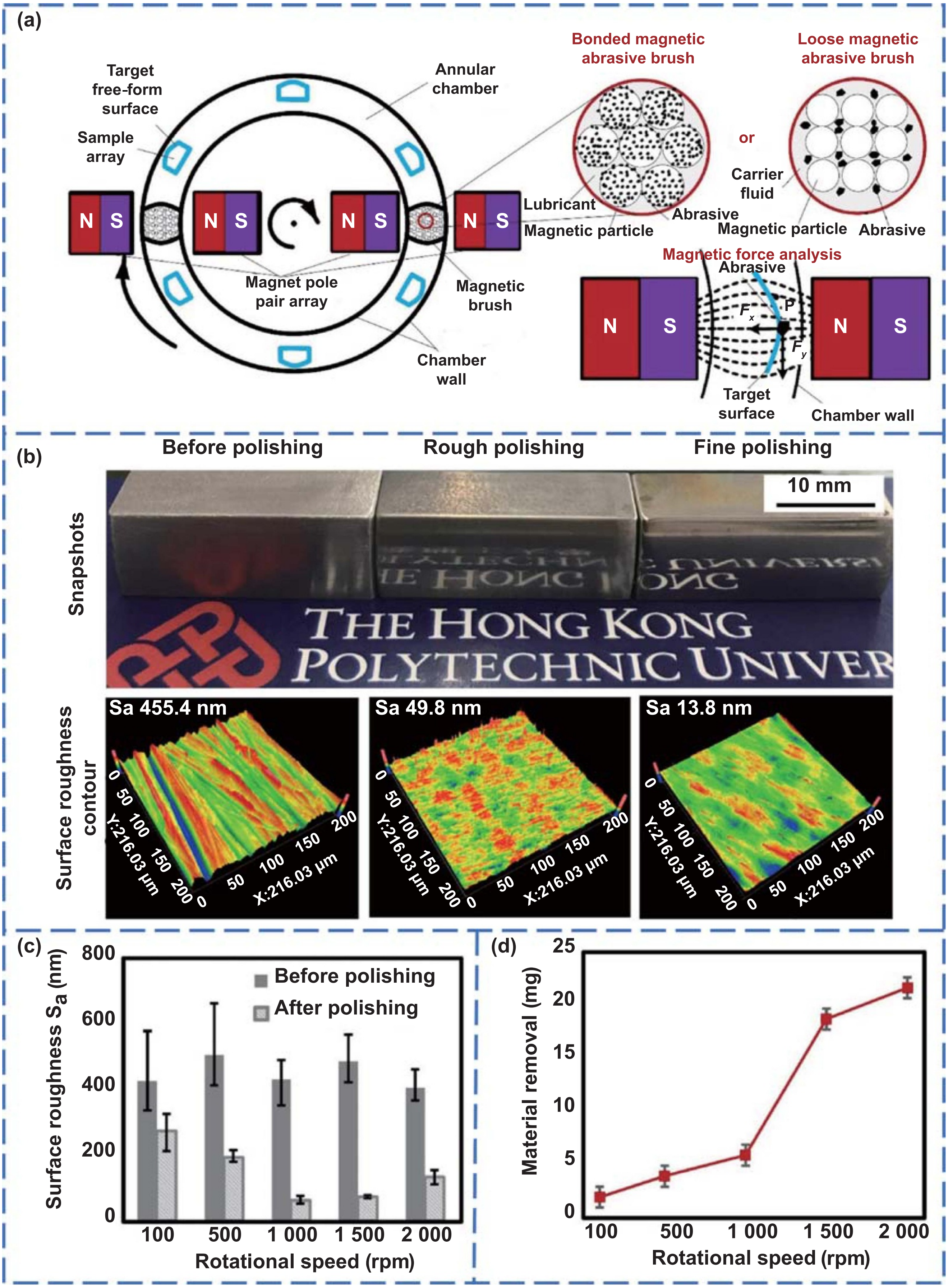

Figure 38. MAMP and process characteristics. (a) Schematic of process principle [235]. (b) Surface geometries at different polishing stages [235]. Evolution of (c) surface roughness and (d) material removal amount with rotational speed [235]. Reprinted from [235], © 2019 Elsevier B.V. All rights reserved.

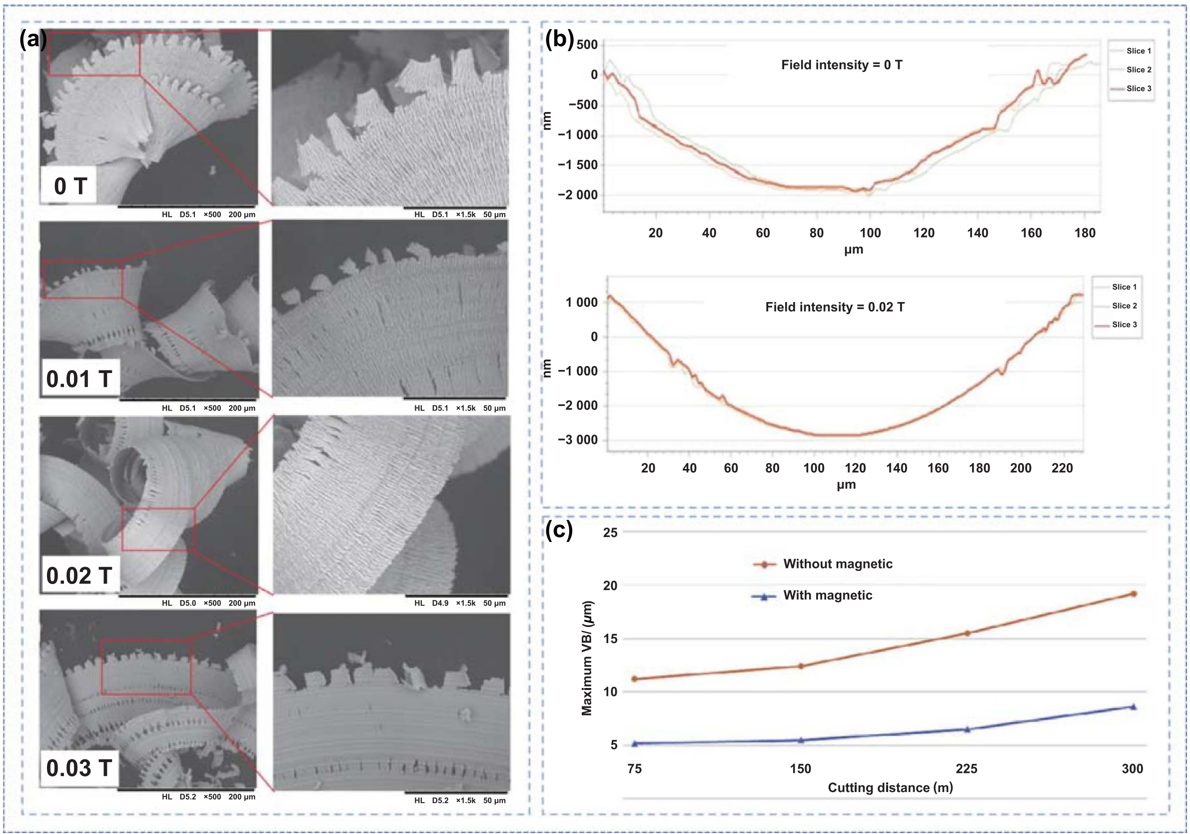

Figure 39. Comparisons of chip formation, form accuracy, and tool wear between conventional turning and MEAT. (a) Morphologies of chips when using various magnetic field intensities [229]. (b) Cutting curves and (c) evolution of the maximum tool flank wear width with and without magnetic energy assistance [227, 236]. Reprinted from [227], © 2017 Elsevier B.V. All rights reserved. Reproduced from [229]. © IOP Publishing Ltd. All rights reserved. Reprinted from [236], © 2017 Elsevier Ltd. All rights reserved.

titanium alloy with micro-textured tool and Fe_3O_4@CNTs nanofluid. By applying magnetic energy in the direction parallel to the tool micro-texture, the nanofluid was transported to the tool/chip interface in a directional manner, forming a long-chain structure. This was advantageous for forming a more stable lubrication layer and preventing direct contact between the tool and chip, as shown in figure 40. As a result, the cutting forces and tool wear of the textured tool were alleviated. With an increase in the magnetic field intensity, the cutting performance improved. Under the highest intensity of 1200 Gs, micro-textured tools achieved a 36.9% reduction in cutting force and 28.15% reduction in surface roughness compared to non-textured tools.

6.3. Magnetic energy-assisted milling

During the mechanical machining operation, long cantilevered high-performance milling tools often experience vibrations caused by process excitation. These vibrations can negatively impact the surface quality and limit the MRR. Optimizing the dynamic properties of the milling process can greatly improve the machining performance, which can be achieved with the assistance of a magnetic field. Möhring and Werkle [226] introduced an end mill with an internal damping system based on MRFs. The structure of the end mill is shown in figure 41(a). By implementing a CFRP structure and an MRF damper, the dynamic stiffness of the tool was increased, whereas its mass was reduced. The investigations demonstrated that this approach enabled adjustment of the dynamic behavior of the tool. In the presence of the magnetic field the settling time was only 0.005 s, whereas it was 0.04 s in the absence of the magnetic field. Because of the improvement in dynamic properties, a higher cutting depth can be adopted, and the MRR can be improved substantially. The comparison experiments indicated that the MRR increased by a factor of 4, which was eight times that of the conventional tool in processing AISI 1024. As shown in figure 41(b), the surface roughness decreased by approximately 90% when the damped tool was used.

6.4. Magnetic energy-assisted boring

Similar to the milling process, a long and cantilevered boring tool used in deep-hole boring also has inherently low stiffness. As a result, chatter is prone to be induced even when adopting a very low depth of cut, leading to a reduction in the dimensional and form accuracy, surface integrity, MRR, and tool life. To suppress the chatter of the boring tool, Mei *et al* [228] proposed a novel method using an MRF-controlled boring bar during the boring of AISI 1020 low-carbon steel. The structure of the boring bar is shown in figure 42(a). By applying a magnetic field to the MR fluid, a phase transformation

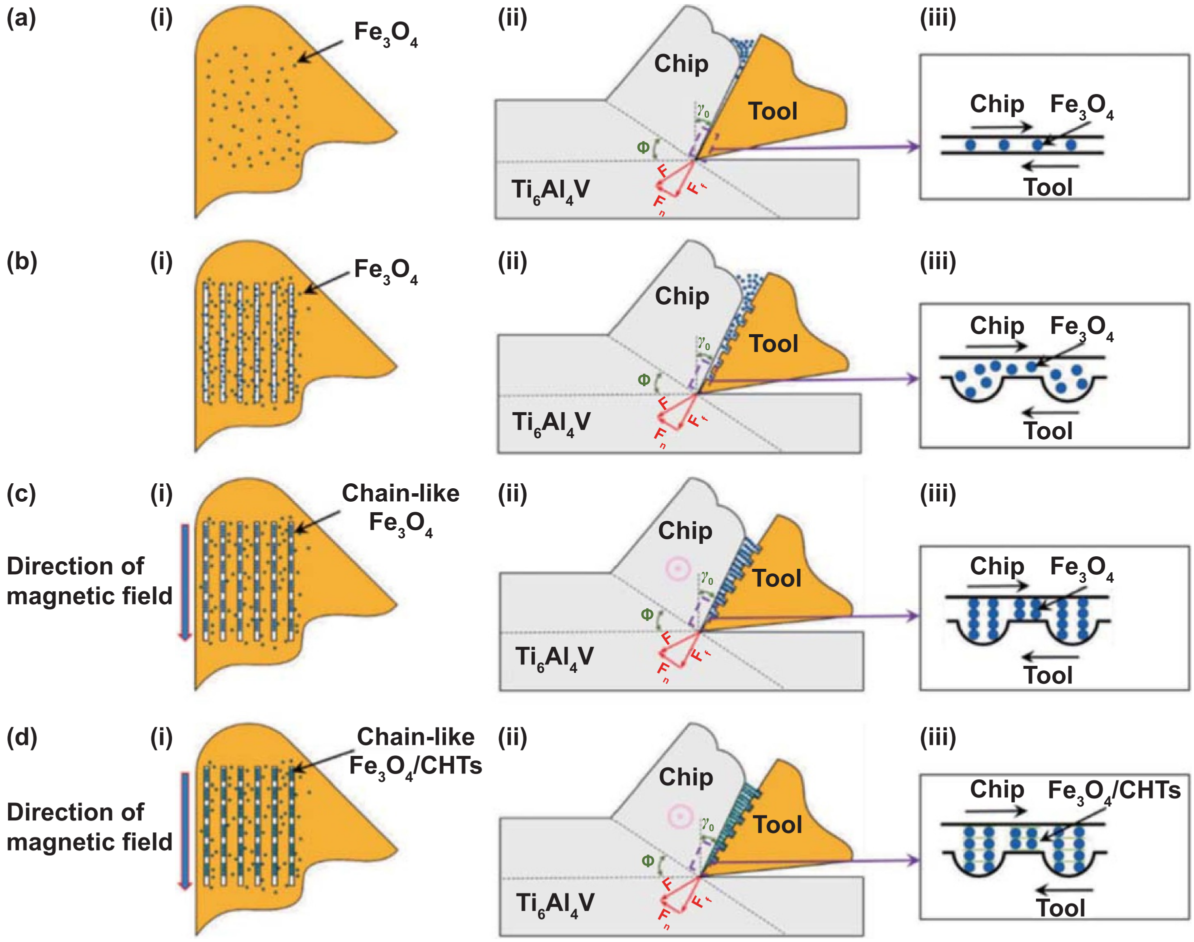

Figure 40. Distribution of nanofluids at the tool/chip contact zone under various conditions. (a) Non-textured tool + Fe_3O_4 nanofluid without magnetic field [238]. (b) Textured tool + Fe_3O_4 nanofluid without magnetic field [238]. (c) Textured tool + Fe_3O_4 nanofluid under magnetic field [238]. (d) Textured tool + Fe_3O_4@CNTs nanofluid under magnetic field [238]. Reprinted from [238], © 2022 The Society of Manufacturing Engineers. Published by Elsevier Ltd. All rights reserved.

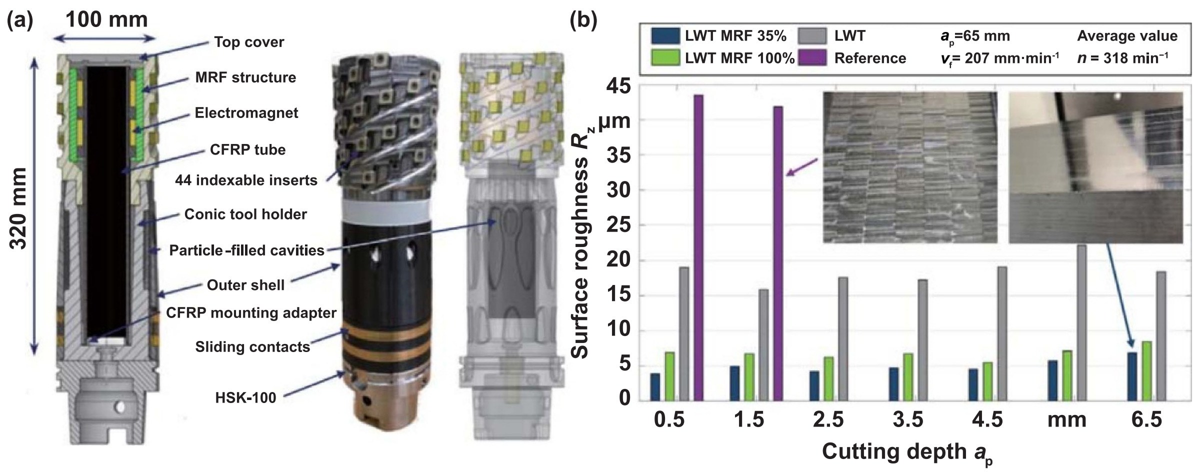

Figure 41. Milling tool with an internal damping system and its performance. (a) Structure of the tool [226]. (b) Surface roughness generated with different magnetic field intensities [226]. Reproduced from [226]. CC BY 4.0.

occurred, resulting in changes in its viscosity and shear stress. The stiffness of the boring tool increased, and the chatter was suppressed. The FEM analysis of the MR fluid-controlled boring tool indicated that the regenerative chatter was suppressed effectively. The experimental results also showed that the chatter marks, which were formed in conventional boring, disappeared with the MR fluid-controlled boring tool (figure 42(b)). The maximum vibration acceleration amplitude was reduced

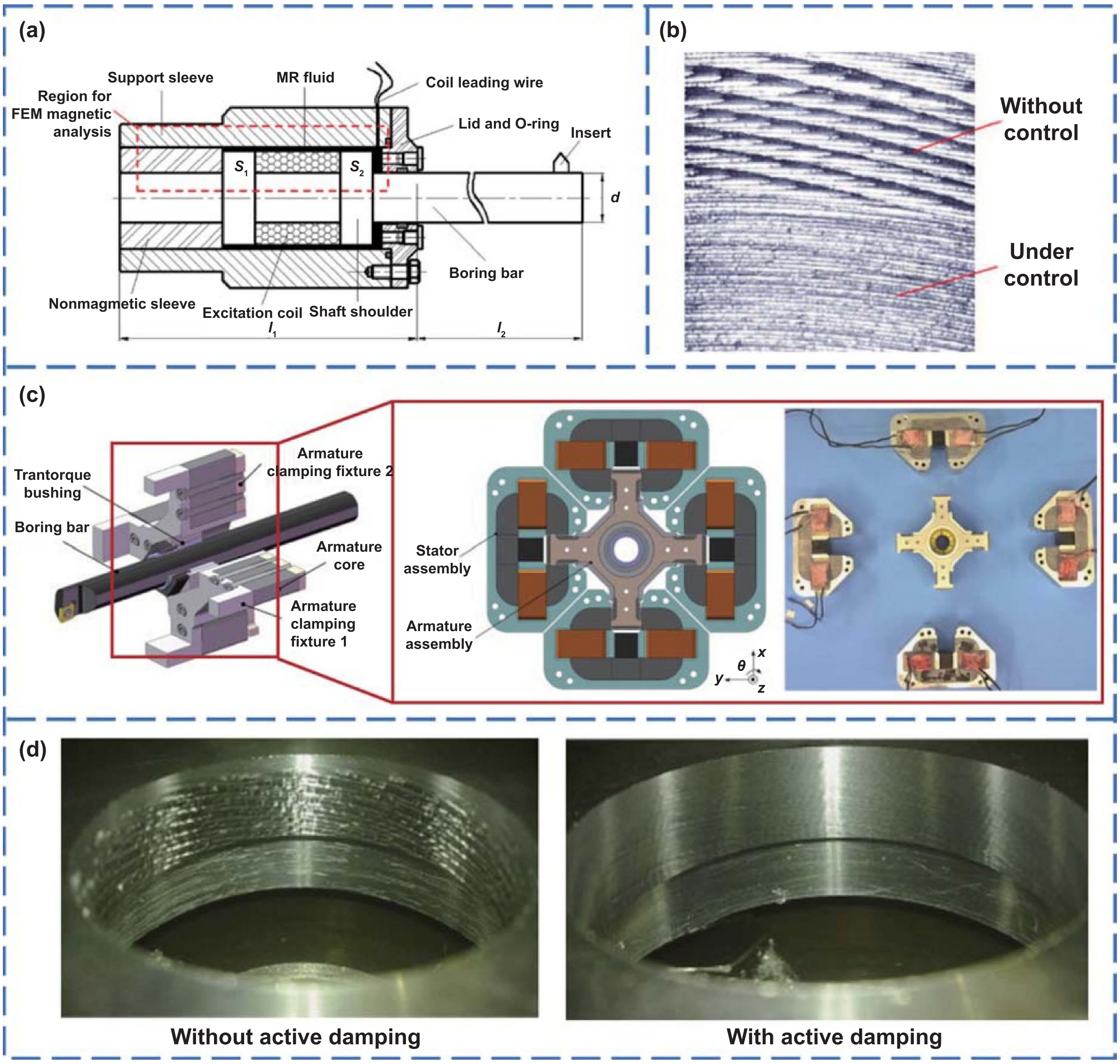

Figure 42. MRF-controlled boring bar and its performance. (a) Structure of the boring bar [228]. (b) Chatter marks generated with and without control [228]. (c) Components of the active damped boring bar [230]. (d) Comparison of surface morphology with and without active damping [230]. Reprinted from [228], Copyright © 2008 Elsevier B.V. All rights reserved. Reprinted from [230], Copyright © 2014 Elsevier Ltd. All rights reserved.

by 100%, and the values of accelerations in the frequency domain were approximately 50 times lower than those in conventional boring. In addition, the surface roughness R_a decreased from 5 μm when using a conventional tool to 1 μm when using the MR fluid-controlled tool. Chen *et al* [230, 239, 240] proposed a novel noncontact linear magnetic actuator with two radial and one rotational degrees of freedom. The structure and components are shown in figure 42(c). The magnetic actuator was able to damp both lateral and torsional vibrations, thereby increasing both the damping and static stiffness of the boring bar. The experiments on boring of 6061 T6 aluminum demonstrated that chatter occurred when no active damping was applied due to the high flexibility of the boring bar. In contrast, when active damping was applied, no chatter was observed, and a stable boring process was achieved. The enhanced machining stability improved the surface quality (figure 42(d)). Except for long boring bars, the proposed novel magnetic actuator can also be applied to other rotation shafts.

Studies on MEAMM have mainly focused on magnetic energy-assisted polishing and material removal mechanisms. In addition, the introduced magnetic field was proved to be helpful in enhancing the stiffness of flexible parts and stability of the machining process. Table 5 presents a comparison of the output parameters of the various MEAMM processes and conventional mechanical machining.

7. Chemical-assisted mechanical machining

CAMM is a hybrid machining technique in which a chemical reaction is introduced to enhance the machinability of the

Table 5. MEAMM processes and output parameters. (↑: increased by.↓: decreased by)

Reference	Workpiece material	Hybrid process	Process parameters	Output parameters (compared with conventional)
Yamaguchi *et al* [224]	316L steel	MEAP	Magnet revolution: 600 rpm Diamond abrasive: 120 mm mean size	Surface roughness S_a: ↓ 65% Residual stress: ↓ (tensile stress)
Mohring and Werkle [226]	AISI 1024	Magnetic energy-assisted milling	Magnetic field strength: 57.6 kA m^{-1} Spindle speed: 318 rpm Feed speed: 411 mm min^{-1} Cutting depth: 6.5 mm Cutting width: 65 mm	Settling time: ↓ 87.5% MRR: ↑ seven times Surface roughness R_z: ↓ 90%
Yip and To [227]	Ti–6Al–4V	MEAT	Magnetic field intensity: 0.02 T Feed rate: 200 mm min^{-1} Depth of cut: 3 μm	Form errors: under 4%, whereas 25%–37% in conventional
Mei *et al* [228]	AISI 1020	Magnetic energy-assisted boring	Current: 0–2 A Frequency: 1 Hz Spindle speed: 200 rpm Feed rate: 0.1 mm rev^{-1} Depth of cut: 0.2 mm	Maximum vibration acceleration amplitude: ↓ 100% acceleration in the frequency domain: ↓ 50 times Surface roughness R_a: ↓ 80%
Yip and To [229]	Ti–6Al–4V	Magnetic energy-assisted turning	Magnetic field intensity: 0.01, 0.02, and 0.03 T Spindle speed: 1500 rpm Feed rate: 8 mm min^{-1} Depth of cut: 4 μm	Coefficient of force variation: ↓ maximum 65.88%
Wu *et al* [233]		MEAP	Direct current: 1.9 A Current frequency: 1, 3, 5, and 7 Hz Rotation speed: 200, 250, 300, and 350 rpm Feed speed of mobile stage: 260 mm min^{-1}	Surface roughness: ↓ 87.5% MRR: ↑ two times
Wang *et al* [235]	304 stainless steel	MEAP	Rotational speed: 100–2000 rpm Gap between the magnet and chamber: 1, 5, and 9 mm Polishing time: 5–30 min	Surface roughness: ↓ 96.97%
Yip and To [236]	Ti–6Al–4V	MEAT	Magnetic field intensity: 0.02 T Spindle speed: 1500 rpm Feed rate: 8 mm min^{-1} Depth of cut: 5 μm	Flank wear width: ↓ 57.2%–68.99%

material. Currently, the primary focus of CAMM research is on CAP and milling, as shown in figure 43.

7.1. Chemical-assisted polishing

The CAP technology, also known as CMP, emerged in the late 1980s. It was first developed by IBM for the production of a 64 MB DRAM. It then progressed rapidly and was widely applied in the manufacture of the first generation of semiconductor single-crystal silicon [244, 245]. This technology was originally called chemical mechanical planarization because that was the purpose why it was invented. CAP is a hybrid method that takes into account both chemical corrosion and mechanical removal. Figure 44 shows the basic setup and pad/workpiece interaction in the CAP process. The principle of CAP is to realize the flat processing of hard-to-machine material by chemical corrosion effect on the polishing compound and the mechanical removal of abrasive particles to achieve an excellent machining quality [246]. Generally, there are two chemical reaction modes in the CAP process: solid–solid and solid–liquid modes. In the first mode, a chemical reaction takes place between the solid abrasive particles and the solid workpiece, forming a soft layer that can be easily removed by the abrasive particles. In the second mode, a chemical reaction takes place between the liquid reagent and solid workpiece, forming a soft layer. Nowadays, CAP is widely used in processing not only silicon wafer but also sapphire, diamond film, and metals. It is generally believed that the reaction process of CAP involves the self-dissolution process of the metal in an electrolyte solution. Therefore, CAP is an electrochemical process. Although there is no external power supply, CAP has different electrode potentials due to the uneven microstructure and different surface finishes of different materials [247]. Once the metal materials are immersed in a chemical polishing solution, a

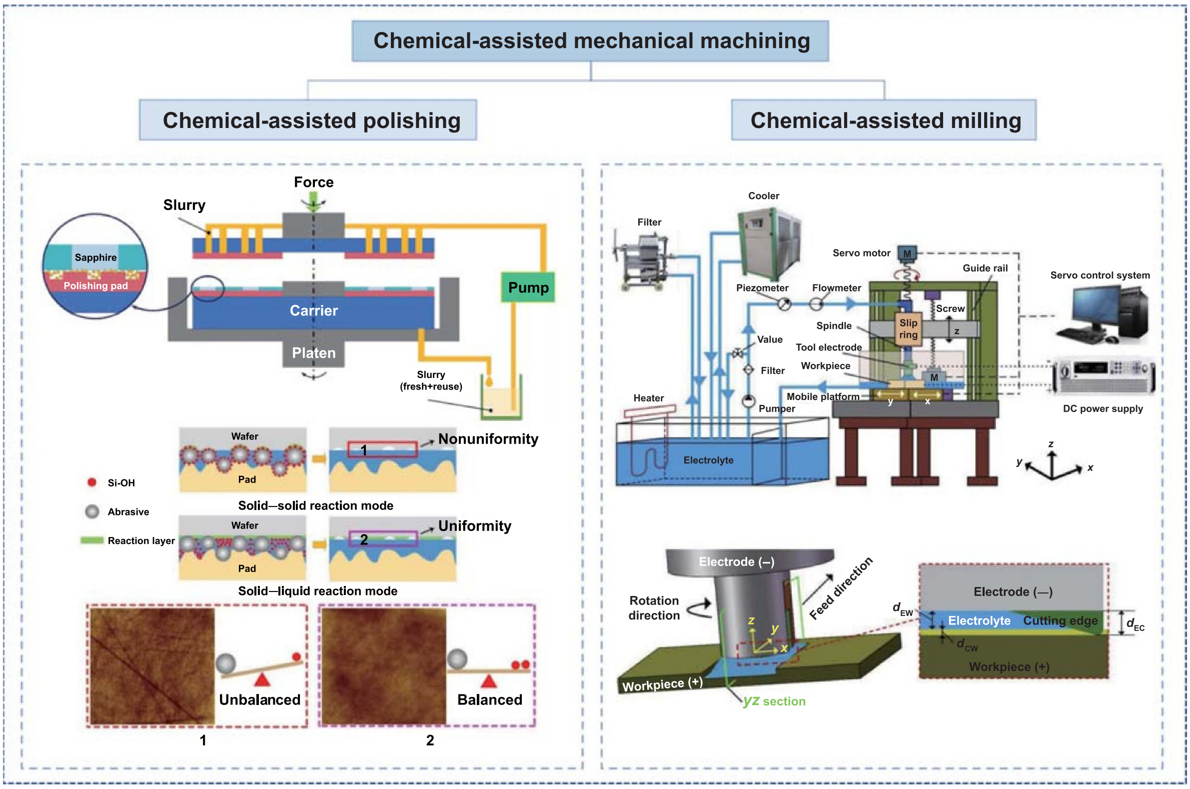

Figure 43. Classification diagram of CAMM [241–243]. Reprinted from [241], © 2020 CIRP. Reproduced from [242], with permission from Springer Nature. Reprinted from [243], © 2021 Elsevier B.V. All rights reserved.

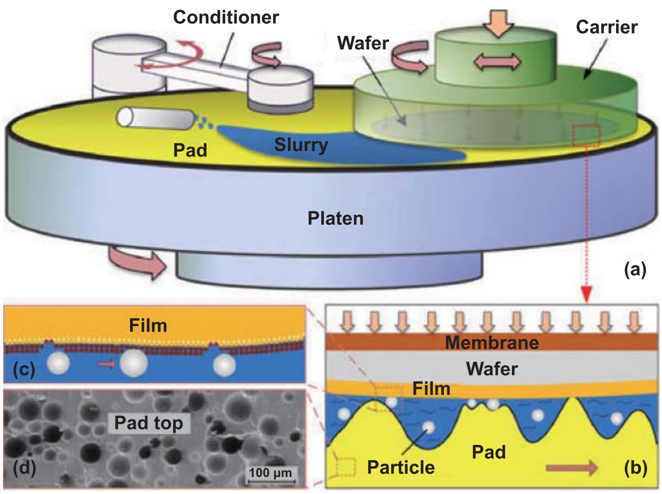

Figure 44. Schematic of (a) CAP process, (b) pad–workpiece interaction, (c) particle–film interaction, and (d) surface morphology of pad [250]. Reproduced from [250]. CC BY 2.0.

complex hybrid micro-battery system is formed [248, 249]. As a result, the parts with negative electrode potential lose electrons and enter the solution to dissolve continuously. Thus, the thickness of the workpiece is reduced, and the convex peaks are removed.

The slurry plays an important role and impacts the process performance of CAP significantly because the chemical reaction and machinability of the produced layer are predominantly affected by it. Zhang *et al* [241] studied the effects of slurry on the chemical reaction mode and polishing performance in the CAP of yttrium aluminum garnet (YAG) and sapphire. Two slurries, colloidal SiO_2 (slurry 1) and ZrO_2 + 5 wt% $Na_2SiO_3{\cdot}5H_2O$ (slurry 2), with the same abrasive size and concentration were employed. The chemical reaction mode when using slurry 1 was a solid–solid mode, whereas it was a solid–liquid mode when using slurry 2. For both modes, the same chemical reaction was generated on the polishing interface. However, the forms of Si–OH were different, i.e. solid state in slurry 1 and ion state in slurry 2. The formation mechanism of the soft layer (consisting of yttrium silicate and andalusite) is shown in figure 45(a). The experimental results showed that the solid–liquid mode can achieve better surface quality (figure 45(b)) and uniform material removal. Takaya *et al* [251, 252] developed a novel slurry of water-soluble fullerenol for polishing a patterned Cu wafer. An *in situ* surface analysis method based on surface-enhanced Raman scattering was also developed to reveal the material removal mechanism. During the CAP process with the novel slurry, a chemical reaction occurred between fullerenol and copper, producing a complex Cu–fullerenol brittle layer. Figures 45(c) and (d) demonstrate the formation mechanism and morphology of the brittle layer, respectively. The brittle layer can be easily removed by the friction force between the polishing pad and the workpiece surface. A higher MRR and low dishing performance were achieved. When using the water-soluble fullerenol slurry, the MRR was approximately twice as high as when using conventional colloidal SiO_2 slurry (particle size of 20 nm). The surface roughness

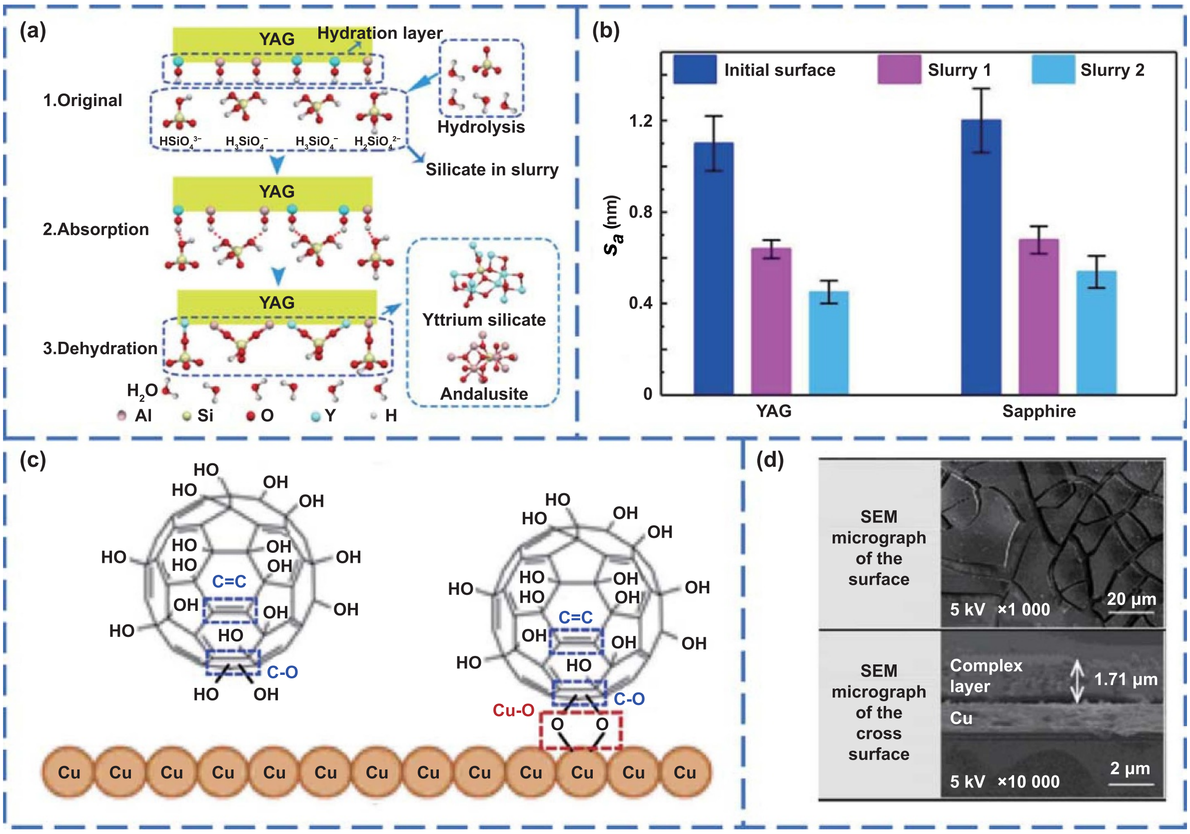

Figure 45. Performance of the CAP process. (a) Chemical reaction on the polishing interface and formation mechanism of soft layer [255]. (b) Surface roughness obtained when using colloidal SiO_2 (slurry 1) and ZrO_2+ 5 wt% $Na_2SiO_3{\cdot}5H_2O$ (slurry 2) [241]. (c) Chemical reaction between fullerenol and copper, producing a complex Cu–fullerenol brittle layer [252]. (d) Morphology of the complex Cu–fullerenol brittle layer [251]. Reprinted from [241], © 2020 CIRP. Reprinted from [251], Copyright © 2011 CIRP. Published by Elsevier Ltd. All rights reserved. Reprinted from [252], Copyright © 2013 CIRP. Published by Elsevier Ltd. All rights reserved. Reprinted from [255], © 2021 Elsevier B.V. All rights reserved.

decreased by 18%. To obtain a copper surface roughness of less than 1 nm, Zhang *et al* [253] developed an environmentally friendly slurry consisting of silica, hydrogen peroxide, and chitosan oligosaccharide. The chemical reaction between hydrogen peroxide and copper produced CuO and $Cu(OH)_2$, which can be dissolved by the ionization of the chitosan oligosaccharide. As a result, Cu^{2+} ions were chelated by chitosan oligosaccharide molecules, and the absorbed layer was subsequently removed by abrasive silica. A surface roughness S_a of 0.444 nm was achieved. Guo *et al* [254] proposed a novel slurry of KOH-based silica slurry containing graphite oxide nanosheets to achieve close-to-atomic polishing of $LiNbO_3$ crystal, which is widely used in advanced photonics and nonlinear optics. An ultrasmooth surface with roughness S_a of 0.15 nm was obtained. Compared to polishing with the SiO_2 abrasive slurry, the surface roughness decreased by 52%, and MRR increased by 125% when polishing with the novel slurry.

The polishing pad is a key factor that influences the planarity and surface quality in the CAP process because the pad surface is responsible for delivering forces to abrasives by physical contact of surface peaks. Byrne *et al* [256] investigated the effect of pad wear on wafer planarity by analyzing the process of new and worn pads. The FEM analysis indicated that pad wear resulted in increased stress at the outer regions of the wafer and a reduction in stress at its center. The polishing process shifted toward a 'center slow' approach when the pad was worn. Generally, the surface of a polishing pad is geometrically rough and mechanically soft, which can suppress the hydroplaning phenomenon and prevent stretching of the workpiece surface. Ryu *et al* [257] established a contact mechanics model in the CAP process to reveal the effects of pad roughness on polishing performance. They found that a high MRR could be obtained when the polishing pad possessed both a mechanically compliant material and a hard surface. However, compliant materials are usually soft with low surface hardness, resulting in a large contact width but small indentation depth on the wafer, as shown in figure 46(a). On the contrary, materials with high hardness are usually rigid, resulting in a large indentation depth but small contact width. Based on this conclusion, they proposed a bilayered pad using compliant and rigid materials as the base and coating surface, respectively (figure 46(b)). Consequently, both mechanical compliance and surface hardness were achieved, which was beneficial for obtaining a large contact width and indentation depth on the wafer.

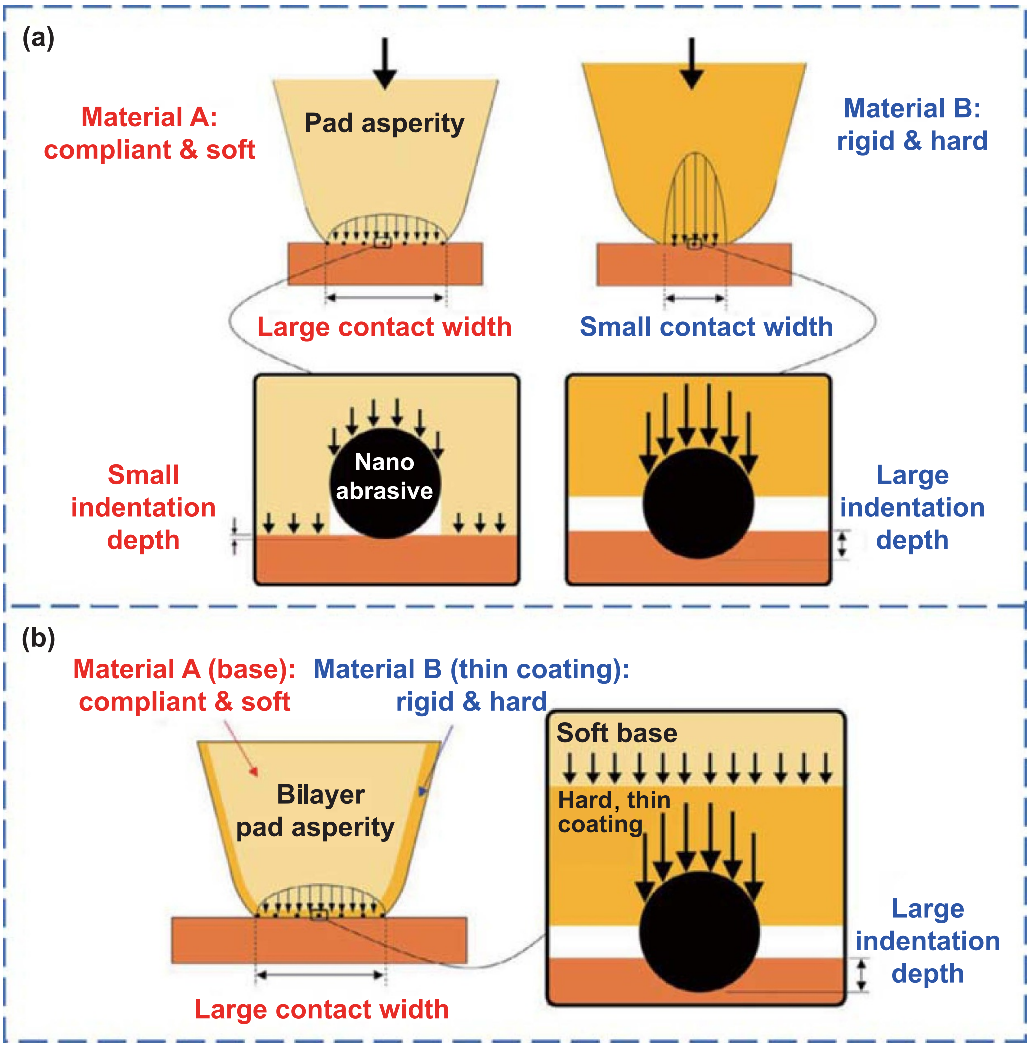

Figure 46. Schematic of contact width and indentation depth of (a) a pad made of compliant and rigid materials and (b) a bilayered pad [257]. Reprinted from [257], © 2021 CIRP. Published by Elsevier Ltd. All rights reserved.

The effects of process parameters, such as pressure, relative rotational speed, and polishing time, on the output parameters were investigated by Li *et al* [242]. SS-CMP and DS-CMP experiments on sapphire wafers were performed. The results demonstrated that both the surface quality and MRR improved with an increase in the polishing pressure within a certain range, which was due to the strengthening of mechanical action. However, excessively high pressure prevented the contribution of chemical reaction and caused defects, such as mechanical scratches on the wafer surface. The polishing performance of DS-CMP was significantly better than that of SS-CMP under identical process parameters. Polishing of narrow channels is challenging. Wang *et al* [258] proposed a novel CMP motion pattern and built a track polishing device for polishing narrow channels on single-crystal silicon. The effects of the motion cycle ratio between the workpiece and the polishing pad on surface roughness were investigated. An inappropriate motion cycle ratio would result in insufficient coverage of the workpiece surface by the trajectory of the abrasive particles. The optimal motion cycle ratio was 4.77 under which a minimum surface roughness of 0.864 nm was achieved.

7.2. Chemical-assisted milling

Chemical-assisted milling is a novel processing method in which chemical reactions are introduced into the CM process to deteriorate the material in the cutting zone, thereby reducing the mechanical properties of the material and making it easier to remove. The material removal mechanisms of the MECM of TC4 titanium alloy have been investigated in depth by Qu *et al* [243, 259]. A schematic of the material removal process is shown in figure 47(a). A specific structured electrode tool (figure 47(b)) was designed and used in the experiments. In addition, the contributions of CM and electrochemical machining (ECM) during MECM were analyzed. The material removal behavior in the MECM process was dependent on the tool feed speed. Two critical feed speeds related to the processing parameters were proposed to generalize the material removal process. When the tool feed speed was lower than the first critical feed speed, the material removal process of MECM was pure ECM. When the tool feed speed was higher than the second critical feed speed, the material removal process was CM $\rightarrow$ ECM. When the tool feed speed was

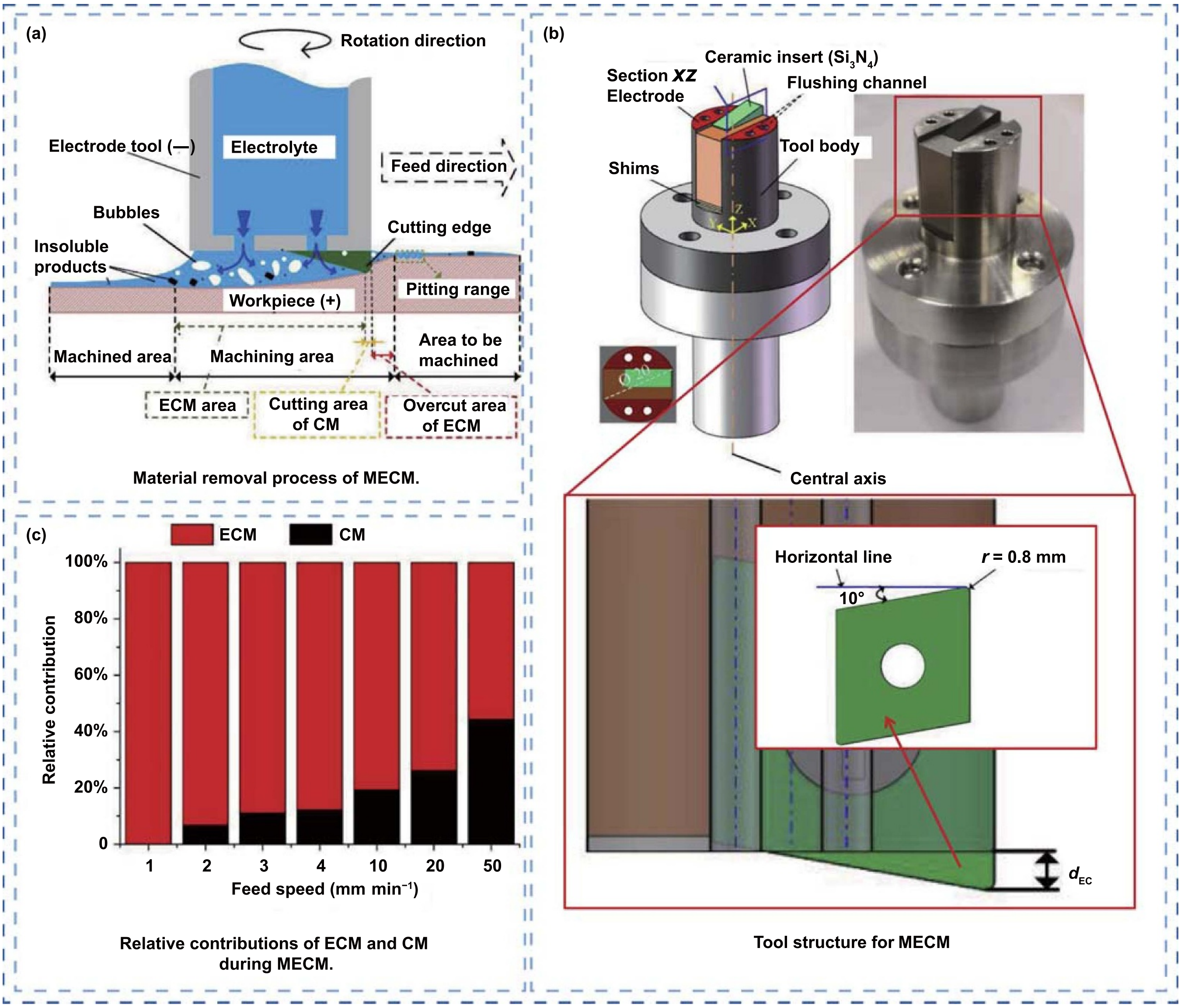

Figure 47. MECM of TC4 titanium alloy. (a) Schematic of the material removal mechanism [243]. (b) Specific structured electrode tool for MECM [243]. (c) Relative contribution of ECM and CM in the MECM process [243]. Reprinted from [243],

between the two critical values, the material removal process was ECM → CM → ECM. The relative contributions of ECM and CM under various feed speeds, as shown in figure 47(c), verified the analysis.

For an in-depth understanding of the material removal mechanisms in the MECM process, the interaction between the ECM and CM processes has also been studied [259]. The electrochemical dissolution behavior of the initial CM surface of TC4 titanium alloy is shown in figure 48. During the CM process with the milling tool, numerous tooth marks were generated on the surface. The electrochemical dissolution of the initial CM surface occurred first at the junction of the adjacent tooth marks, shown as 'first dissolution stage' in figure 48. Subsequently, the area of dissolution expanded gradually, leading to large-scale local dissolution during the 'second dissolution stage'. Finally, all the tooth marks on the intimal CM surface were completely dissolved and removed. The experimental results indicated that the microhardness of the initial ECM surface was lower than that of the initial CM surface. Therefore, the milling force in the CM process decreased, resulting in reduced tool wear and improved tool life.

Overall, CAMM is known for its high-precision and efficient machining capabilities. Table 6 presents a comparison of the output parameters of CAMM and conventional mechanical machining. The precise control of the chemical reaction process and balancing the contributions of chemical reactions and mechanical polishing in the CAMM process are challenging tasks. Further research on chemical reaction kinetics and development of novel and sustainable slurries and polishing pads is needed. Moreover, to obtain higher form accuracy and better planarity, techniques for in-process monitoring of pad wear and controlling of pad surface need to be proposed, and advanced pad design should be explored.

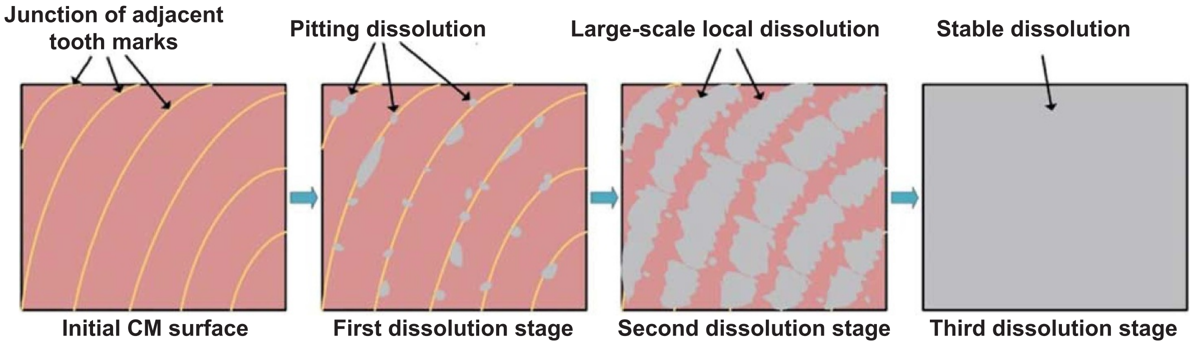

Figure 48. Schematic showing the three stages of the electrochemical dissolution behavior of the initial CM surface of TC4 titanium alloy [259]. Reproduced from [259].

Table 6. CAMM processes and output parameters. (↑: increased by.↓: decreased by)

Reference	Workpiece material	Hybrid process	Process parameters	Output parameters (compared with conventional)
Zhang *et al* [241]	YAG and sapphire	CAP	Conventional abrasive: 2.5 mm Al_2O_3 Slurry 1: colloidal SiO_2 Slurry 2: ZrO_2 + 5 wt% $Na_2SiO_3 \cdot 5H_2O$	Surface roughness: ↓ 45% (slurry 1) and 63% (slurry 2)
Takaya *et al* [251]	Cu	CAP	Conventional slurry: colloidal SiO_2 Novel slurry: fullerenol	Surface roughness: ↓ 18% MRR: ↑ two times
Zhang *et al* [253]	Cu	CAP	Novel slurry: mixture of silica, hydrogen peroxide, and chitosan oligosaccharide	Surface roughness of 0.444 nm
Guo *et al* [254]	$LiNbO_3$	CAP	Conventional slurry: colloidal SiO_2 Novel slurry: graphite oxide nanosheet added KOH-based silica	Surface roughness: ↓ 52% MRR: ↑ 125%
Zhang *et al* [255]	YAG	CAP	Conventional slurry: colloidal SiO_2 Novel slurry: ZrO_2 + 5 wt% $Na_2SiO_3 \cdot 5H_2O$	Surface roughness: ↓ 47% MRR: ↑ 240%

8. Advanced coolant-assisted mechanical machining

The energy expended during a typical mechanical machining operation is predominantly transformed into thermal energy. The majority of issues encountered during machining arise from the generation of heat during the deformation process and the friction at the interfaces between the tool and chip as well as the tool and workpiece. Consequently, elevated temperatures are associated with machining issues [260]. When dealing with difficult-to-cut alloys, the cutting zone experiences even more pronounced heat generation, as the machining process demands greater energy compared to working with materials of lower strength. Advanced coolant-assisted mechanical machining encompasses three main techniques: CCAM, minimum quantity lubrication (MQL)-assisted mechanical machining, and high-pressure coolant-assisted mechanical machining. The research framework for advanced coolant-assisted mechanical machining is shown in figure 49.

Cryogenic cooling-assisted technology uses strong cooling media, such as liquid ammonia, to lower the machining temperature through the mechanisms of heat conduction and heat convection, resulting in a reduction in the temperature of the cutting zone [266]. In addition, some scholars have demonstrated the significant impact of cryogenic cooling-assisted technologies on the properties of the workpiece (for example, reducing ductility), ultimately enhancing its machinability [260, 267]. CCAM technology also has distinct advantages in terms of improving the surface quality and efficiency of machining, prolonging tool life, and reducing the overall costs [268].

The MQL-assisted technique mixes compressed air with a small amount of lubricating fluid and precisely delivers a millimeter- or micron-level gas mist into the cutting zone at high pressure [269]. This method effectively accomplishes the cooling and lubrication of the tool–workpiece interface. Furthermore, it has exceptional environmental friendliness and economic efficiency [270–272].

High-pressure coolant-assisted technology involves precise and rapid injection of pressurized cutting fluid into the cutting zone [273, 274]. This enhances the cooling and lubrication performance in the cutting area, leading to an improved heat transfer efficiency within the cutting zone. Additionally, it reduces the contact stress between the tool and workpiece and between the tool and chip contact surfaces [275]. Furthermore, by altering the chip morphology, the technique reduces the size

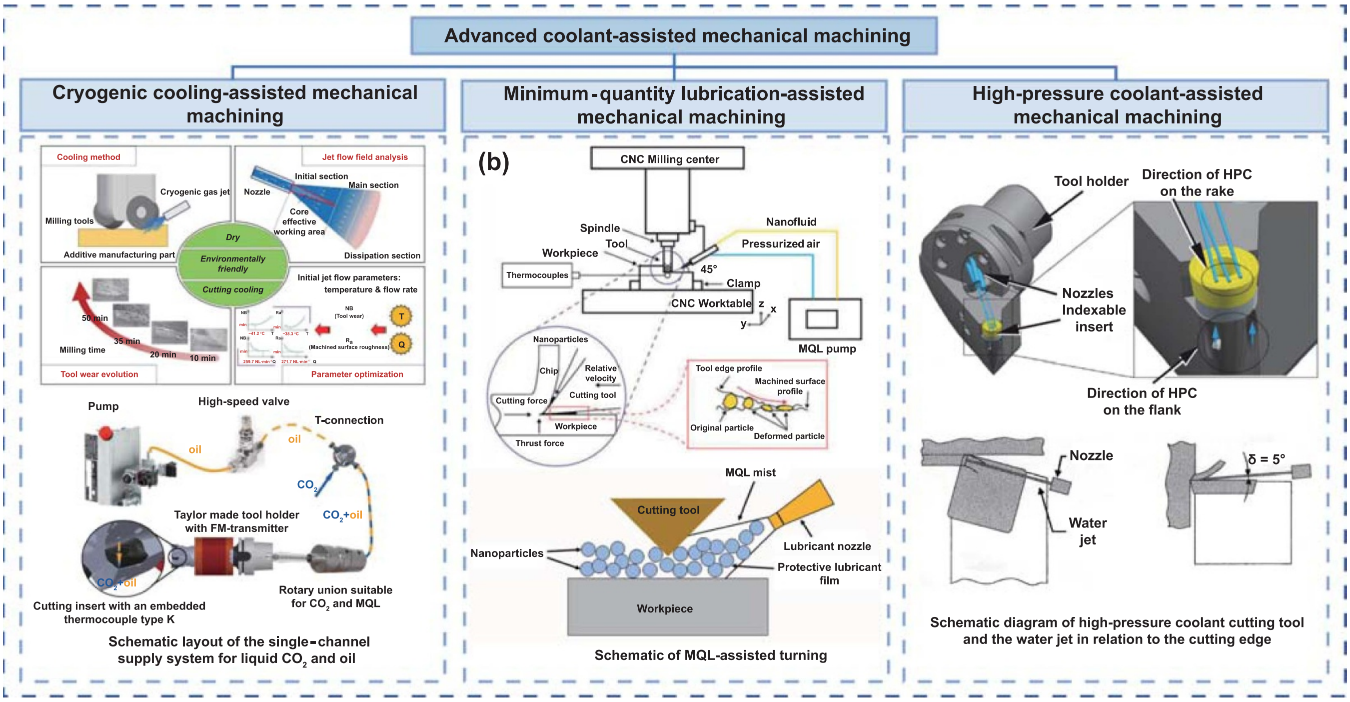

Figure 49. Classification diagram of advanced coolant-assisted mechanical machining [260–265]. Reprinted from [260], © 2023 The Society of Manufacturing Engineers. Published by Elsevier Ltd. All rights reserved. Reprinted from [261], © 2021 CIRP. Reprinted from [262], © 2022 CIRP. Reprinted from [263], Crown Copyright © 2021 Published by Elsevier Ltd. All rights reserved. Reprinted from [264], Copyright © 2000 Elsevier Science B.V. All rights reserved. Reproduced from [265]. CC BY 4.0. (HPC: high-pressure coolant)

of the tool–chip contact area and subsequently diminishes friction at the tool–chip interface [276, 277]. This achieves wear reduction and temperature moderation, thereby enhancing tool durability and refining workpiece quality.

8.1. Cryogenic cooling-assisted mechanical machining

8.1.1. Cryogenic cooling-assisted turning. Cryogenic cooling-assisted turning has been widely studied because of its simple experimental device and considerable outcome improvements. Klocke *et al* [278] investigated the influences of high-pressure lubricoolant supply and cryogenic cooling on thermomechanical tool load during turning of Ti–6Al–4V alloy. Their results revealed that the enhanced cooling provided by the high-pressure lubricoolant supply and cryogenic cooling had a positive effect on tool life, as shown in figure 50(a). Wang and Rajurkar [279] reported consistent improvements in surface quality and extended tool life when utilizing LN_2 for turning Ti- and Ni-based alloys. Moreover, cryogenic turning has been employed in the machining of Si_3N_4 ceramics using PCBN tools [280]. Notably, a significant reduction in R_a from 7.8 to 1.5 μm (with a machining length of 60 mm) was observed in the machining of Inconel 718. Pusavec *et al* [281] found that cryogenic machining of Inconel 718 resulted in a thicker compressive zone beneath the surface, expanding it from 40 to 70 μm. The lower temperatures led to reduced tool wear and improved surface quality. Paul *et al* [282] investigated the impact of cryogenic cooling using a LN_2 jet on tool wear and surface finish in plain turning of AISI 1060. Cryogenic cooling resulted in a better tool lifespan and surface finish compared to dry machining and machining with soluble oil as a coolant.

8.1.2. Cryogenic cooling-assisted milling. Pei *et al* [260] analyzed the jet flow characteristics of cryogenic gas in milling of GH4169. They investigated the core length of the jet flow with a single nozzle and the envelope effect of the jet flow field on the cooling heat transfer process with multiple nozzles. The results demonstrated that cryogenic gas jet cooling significantly improved the tool life and surface quality. The changes in tool wear and surface roughness with varying initial jet flow temperatures across different milling durations are shown in figures 50(b) and (c), respectively. As the cutting temperature decreased, the width of the flank wear region narrowed, whereas the surface roughness experienced an initial reduction followed by an eventual increase. The continuous cutting time with optimal processing parameters reached approximately 50 min. Augspurger *et al* [261] proposed a novel methodology to decouple the mechanical effects from thermal effects in machining, which allowed for the calculation of heat flow and heat partitions in milling of 42CrMo4 and Ti–6Al–4V. This study revealed the combined influence of cooling and process parameters, tool wear, and material properties. The results indicated that the cutting forces were influenced by the temperature in the cutting zone and thermal softening of the workpiece material. Additionally, the cutting forces were higher with high-pressure cutting fluid supply than with cryogenic cooling lubrication.

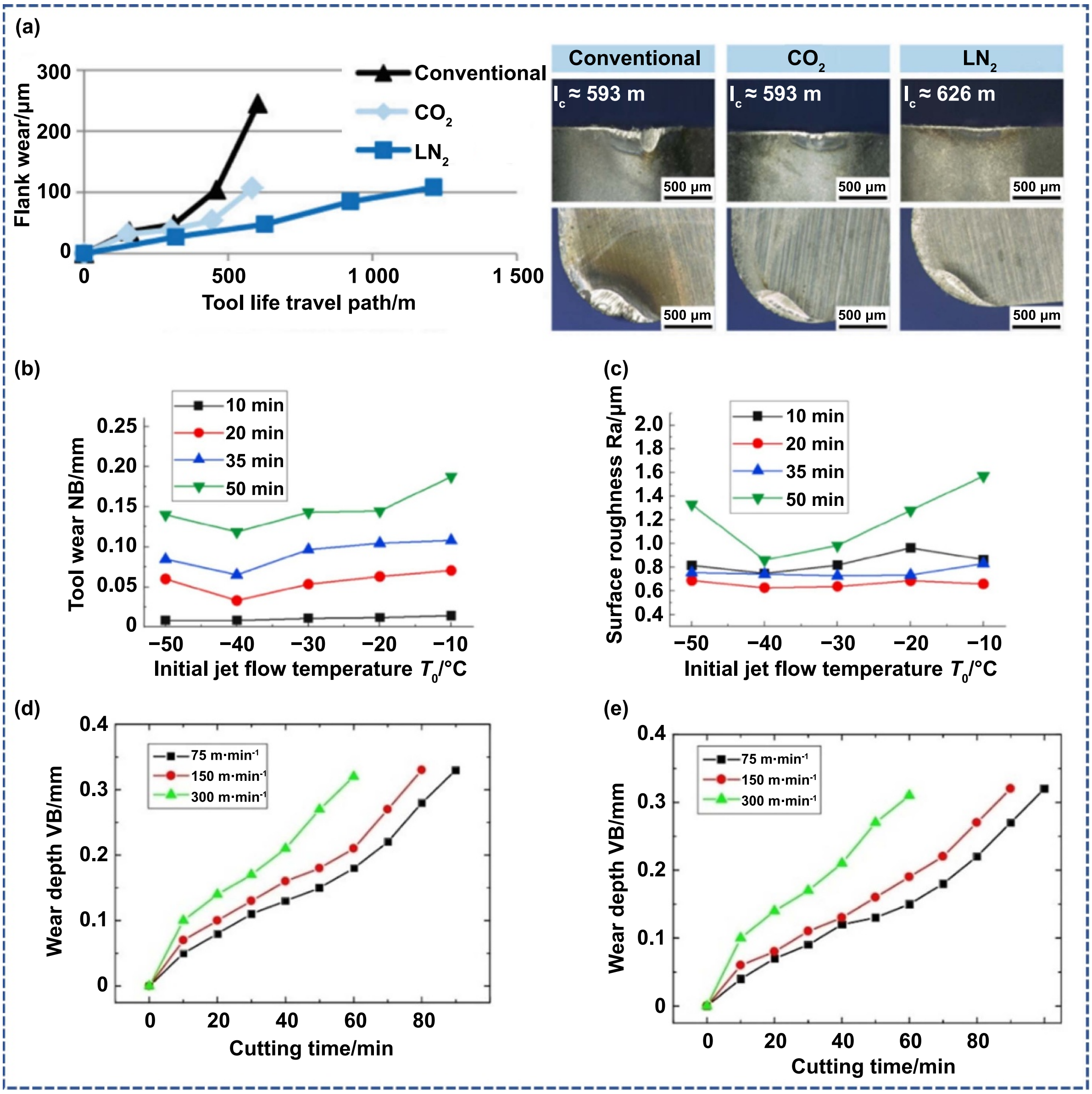

Figure 50. Performance of cryogenic cooling-assisted turning and milling. (a) Tool wear progression in turning Ti–6Al–4V alloy with conventional flood, CO_2, and LN_2 as coolants [278]. Evolution of (b) tool wear and (c) surface roughness with initial jet flow temperature at different cutting times [260]. Evolution of tool wear when using (d) external and (e) inner LN_2 injection cooling methods in milling of nickel-based alloy [283]. Reprinted from [260], © 2023 The Society of Manufacturing Engineers. Published by Elsevier Ltd. All rights reserved. Reprinted from [278], Copyright © 2012 Alexander Krämer. Published by Elsevier B.V. Reprinted from [283], © 2021 The Society of Manufacturing Engineers. Published by Elsevier Ltd. All rights reserved. (Conv.: Conventional)

Some scholars have studied the machining quality and tool wear progression in cryogenic cooling-assisted milling. Wang and Wang [283] investigated the distinctive impact of various cooling methods on machining precision, LN_2 flow requirements, and tool wear. Their findings revealed that flood cooling resulted in cutting temperatures of over 400 °C, whereas LN_2 cooling maintained temperatures below 0 °C, particularly at high speeds. The tool life of LN_2 cooling increased by approximately 100% (figures 50(d) and (e)) compared to that of conventional flood cooling. Furthermore, the utilization of an inner injection strategy proved to be more economical in terms of LN_2 consumption than external spray methods. In addition, Huang *et al* [284] found that LN_2 cooling surpassed the stability limit of the CM processes. The utilization of LN_2 in the machining environment significantly enhanced the cutting stability by 50%–100%.

8.1.3. Cryogenic cooling-assisted drilling. Rodríguez *et al* [285] researched the drilling mechanism of CFRP–Ti–6Al–4V stacks with the assistance of CO_2 cryogenic cooling. The findings revealed that when CO_2 was applied during drilling operations, the divergence of the hole-diameter values from their nominal counterparts was limited to a mere 0.5% (figure 51(a)). Moreover, the utilization of CO_2 as a coolant led to a substantial reduction in tool-tip temperature, thereby

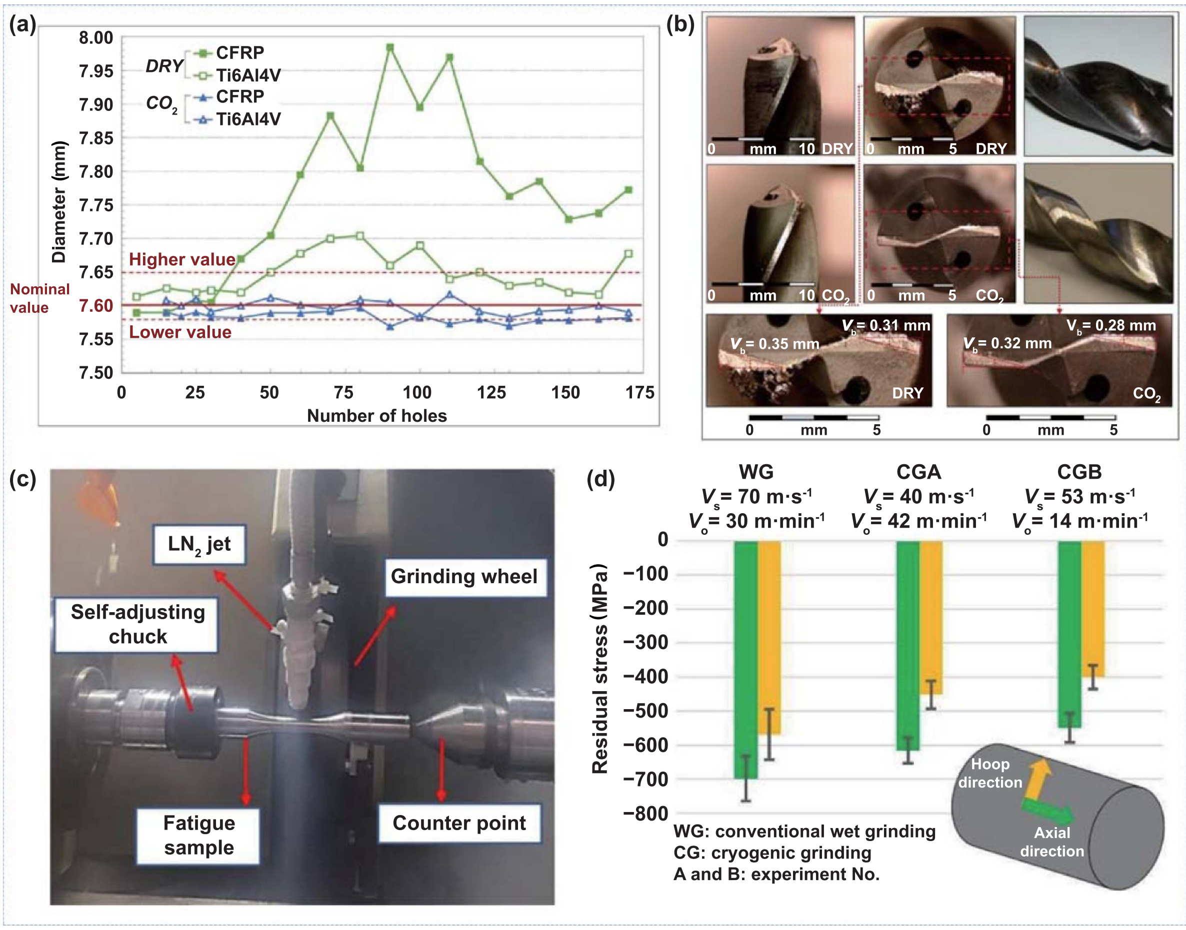

Figure 51. Performance of cryogenic cooling-assisted drilling and grinding. (a) Hole diameters obtained by dry and cryogenic CO_2-assisted drilling of CFRP–Ti–6Al–4V stacks [285]. (b) Tool wear morphologies during dry and cryogenic CO_2-assisted drilling [285]. (c) Experimental setup of CCAG [289]. (d) Generated surface residual stresses in conventional wet grinding and CCAG [289]. Reprinted from [285], © 2021 The Authors. Published by Elsevier Ltd on behalf of The Society of Manufacturing Engineers. Reprinted from [289], © 2023 The Author(s). Published by Elsevier B.V.

ensuring the preservation of the pristine surface integrity of the CFRP layers. The tool wear morphologies, shown in figure 51(b), demonstrate that BUE was avoided by cryogenic CO_2. The machinability of CFRP was improved by the cryogenic cooling. Mura and Dini [286] compared the hole-making quality under dry and precooled conditions. Although the thrust force was higher in cryogenic drilling than in dry drilling, delamination was significantly reduced using a cryogenic coolant. However, because of the large thrust force, the tool wear was accelerated under cryogenic conditions. Kumar *et al* [287] studied the cutting temperature with LN_2 coolant supply during drilling of titanium. Their findings showed that the cryogenic conditions led to a remarkable reduction in the machining temperature by 33%–50%. Attanasio *et al* [288] proposed a tool wear model to describe the tool wear progression during drilling of Inconel 718 under conventional MWF and LN_2 cooling. The tool life under the LN_2 cooling condition was only two-fifths that under the MWF condition.

8.1.4. Cryogenic cooling-assisted grinding. CCAG can significantly lower the temperature within the grinding zone, thereby relieving the surface burning and excessive residual stress. Cryogenic cooling, with its exceptionally low temperature, has garnered considerable attention as a nonpolluting cooling method. Paul and Chattopadhyay [290, 291] extensively explored the outcomes achieved when employing cryogenic cooling in terms of grinding forces, specific energy, and grinding zone temperature, as well as surface residual stress. These findings were compared with those obtained from dry grinding and grinding with soluble oil. Cryogenic cooling exhibited a distinct advantage over other coolants in terms of temperature control, residual stress management, and forces. Fredj and Sidhom [292] further investigated the advantageous effects of LN_2 on the ground surface integrity of AISI 304 stainless steel. The investigation revealed that cryogenic cooling during grinding yielded surfaces with reduced roughness, fewer defects, enhanced work hardening, and diminished tensile residual stresses compared to surfaces ground with an oil-based grinding fluid. Moreover, a notable increase of nearly 15% in the endurance limit at 2×10^6 cycles was observed. Fatigue cracks on the ground surfaces of the specimens under cryogenic cooling were also shorter, measuring 30–50 μm, in contrast to those formed under oil-based cooling

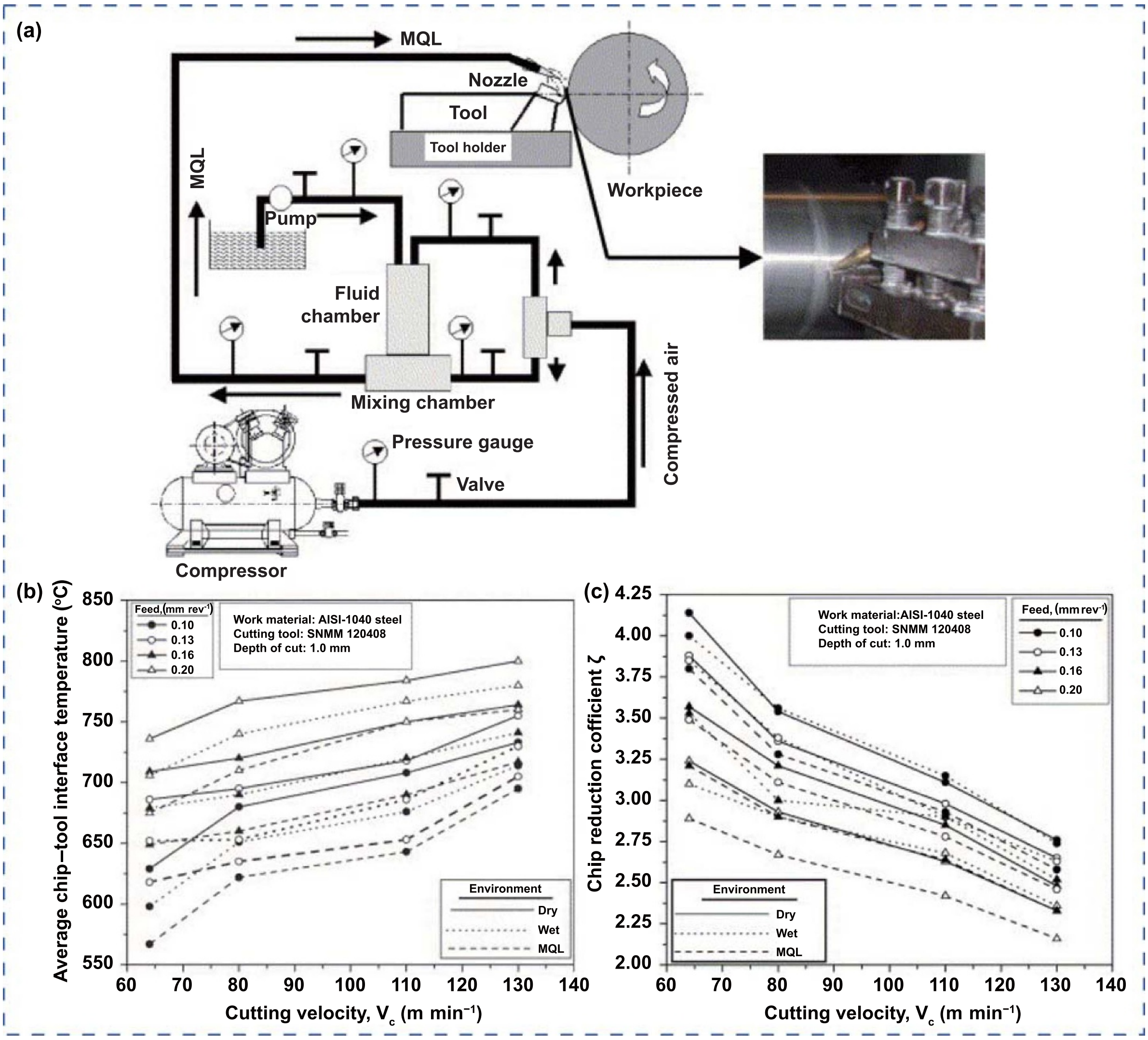

Figure 52. MQL-assisted turning and process performance. (a) Preparation and application of MQL [296]. Variations in (b) average chip–tool interface temperature and (c) chip reduction coefficient with cutting velocity and feed rate during turning under dry, wet, and MQL conditions [296]. Reprinted from [296], Copyright © 2005 Elsevier B.V. All rights reserved.

(150–200 μm). These improvements in surface integrity and fatigue behavior can be attributed to the reduction in the grinding zone temperature. During the grinding process, the excessive machining load applied to the machined surface was mainly responsible for inducing defects in the polymer materials. According to Khoran *et al* [293], the implementation of cryogenic cooling effectively enhanced the machinability of PEEK. This approach yielded significant reductions in both the grinding load and surface quality. Abedrabbo *et al* [289] investigated the surface integrity and fatigue performance of cryogenically ground surfaces of 27MnCr5 steel. The experimental setup is shown in figure 51(c). The findings revealed that the compressive residual stresses resulting from cryogenic grinding were 10%–20% lower than those obtained by traditional wet grinding, as shown in figure 51(d). This investigation demonstrated the potential of replacing traditional lubricating fluids in grinding operations.

8.2. Minimum quantity lubrication-assisted mechanical machining

MQL-assisted technology is an effective machining approach in which the cutting fluid performs the roles of cooling, lubrication, and chip transport. This technology was applied in the American aerospace industry during the 1970s, specifically tailored for difficult-to-machine materials [294]. This technique, also known as near-dry machining, involves dispensing cutting fluids at meticulously calibrated (typically minimal) flow rates, wherein minute volumes of cutting fluid are carefully directed to the cutting zone [295].

8.2.1. Minimum quantity lubrication-assisted turning. Dhar *et al* [296] investigated the role of MQL on cutting temperature, chip formation, and product quality in turning of AISI-1040 steel. The MQL principle is displayed in figure 52(a).

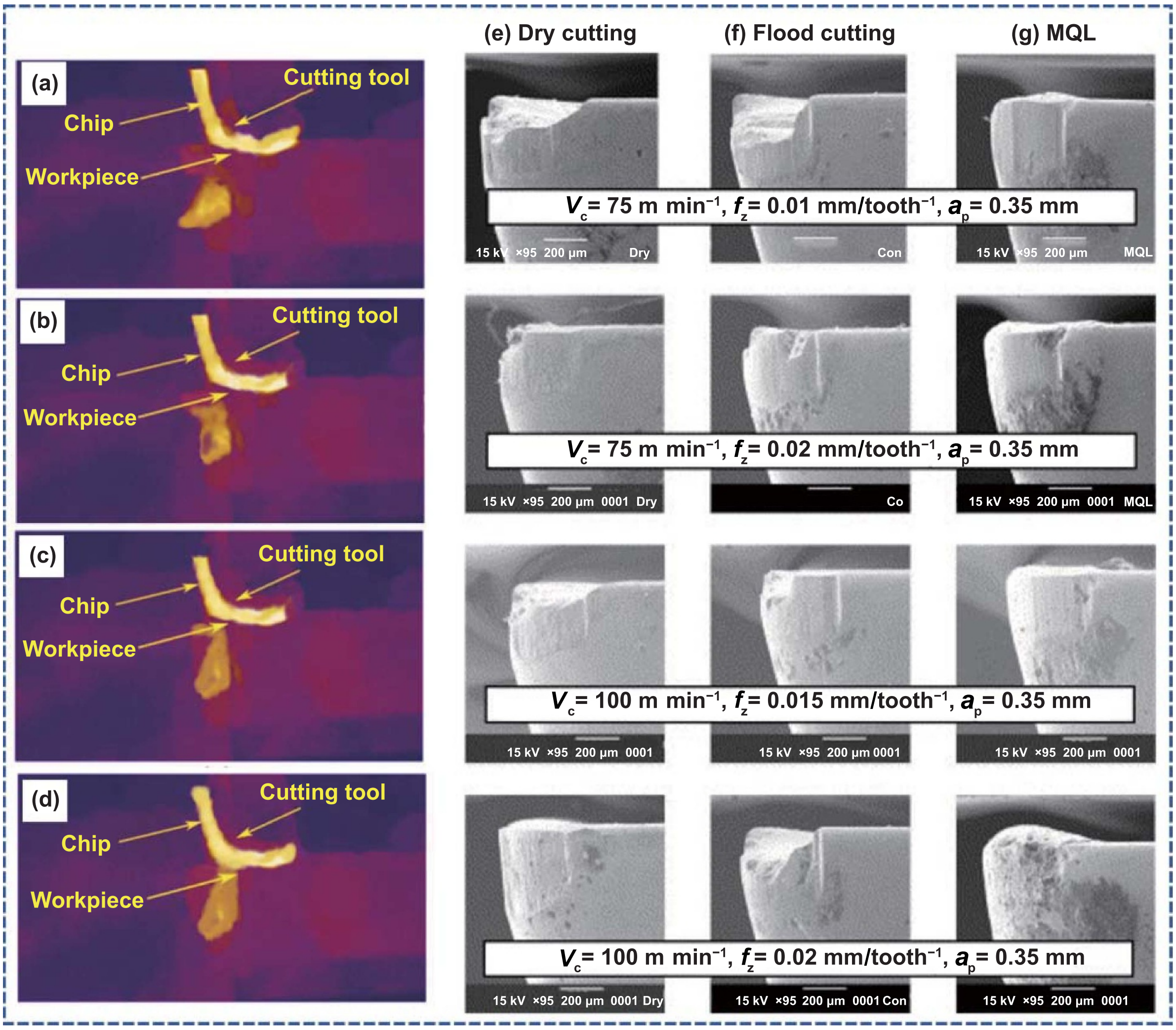

Figure 53. Process characteristics of MQL-assisted milling. (a)–(d) Thermal images acquired under dry, MQL, nMQL (MoS_2), nMQL (graphite) conditions, respectively [262]. (e)–(g) Tool wear morphologies under dry, flood cooling, and MQL conditions, respectively [299]. Reprinted from [262], © 2022 CIRP. Reprinted from [299], Copyright © 2002 Published by Elsevier Ltd.

The experimental results indicated that MQL enabled a substantial reduction in the cutting temperature. The MQL jet demonstrated a notable reduction in cutting temperature, albeit to varying extents, for different combinations of cutting velocity and feed, as depicted in figure 52(b). Furthermore, it was observed that the chip formation and the interaction between the chip and tool exhibited a more advantageous behavior under MQL conditions, as exemplified in figure 52(c). Wang *et al* [297] examined the impact of LN_2 and MQL + CO_2 cooling on tool wear mechanisms and chip formation while milling Ta-2.5W. The transition from adhesive wear to notch wear in tool failure occurred as a result of the changes in the mechanical properties of the workpiece caused by cryogenic cooling. In a separate study, Das *et al* [298] discovered that the concurrent utilization of LN_2 and vegetable oil-based MQL in a hybrid cooling approach improved the machining quality and extended tool life during the micro-turning of lead-free brass.

Makhesana *et al* [262] investigated the cutting performance during the turning of Inconel 625 using dry, MQL, and nanofluid-based MQL (nMQL). It was found that nMQL incorporating graphite and MoS_2 effectively showed the progression of tool wear. This enhanced performance of nMQL was attributed to its superior ability to penetrate machining interfaces. The application of MQL with compressed air facilitated the efficient chip evacuation and heat dissipation during the machining process. As depicted in figures 53(a) and (d), MQL, nMQL with MoS_2, and nMQL (graphite) lowered the cutting temperatures by 18%, 35%, and 25%, respectively, in comparison with dry turning.

8.2.2. Minimum quantity lubrication-assisted milling. Rahman *et al* [299] carried out milling experiments to investigate the influence of MQL technique on milling of ASSAB 718 HH steel by utilizing carbide inserts. In contrast to the fracture observed during flood cooling or flaking in dry cutting, the carbide inserts used with MQL exhibited continued usability despite displaying a greater width of flank wear. The MQL technique is an economically and environmentally sustainable lubrication method that is particularly suitable for

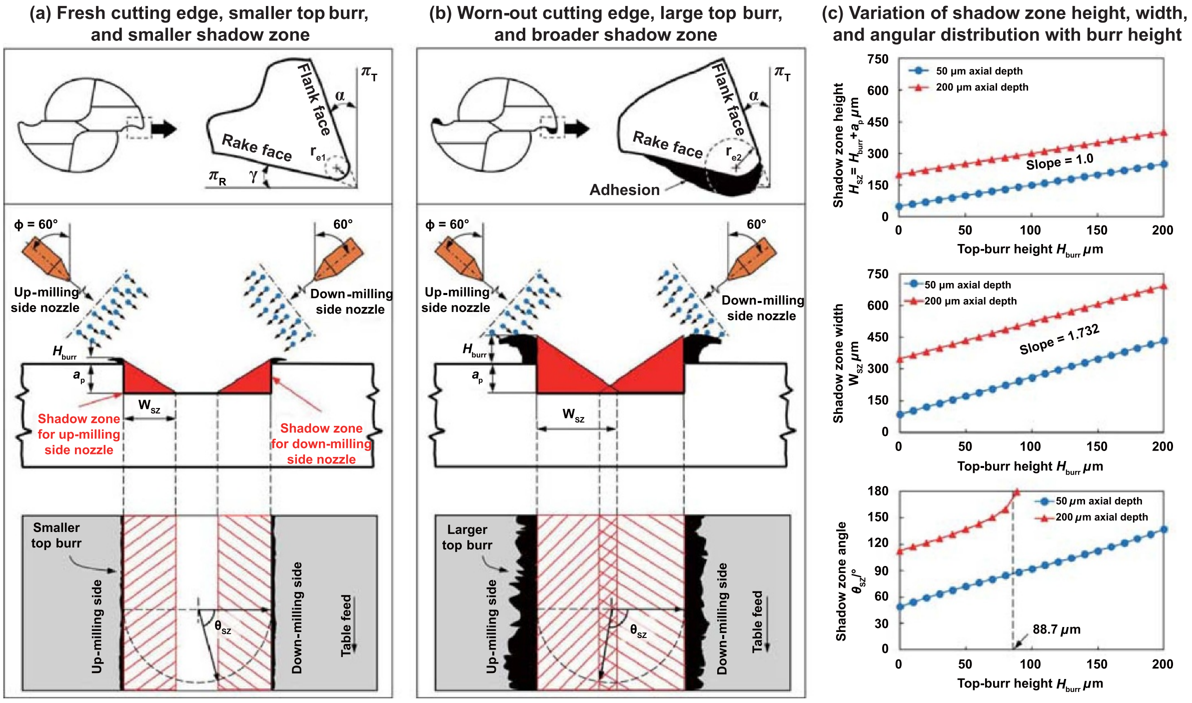

Figure 54. Impact of top-burr height on MQL performance. (a) Schematic of a smaller shadow zone that resulted from a smaller top burr [302]. (b) Schematic of the broader shadow zone that resulted from a large top burr [302]. (c) Evolution of shadow zone dimensions with top-burr height in MQL-assisted micro-milling of Ti–6Al–4V with axial depths of cut of 50 and 200 μm [302]. Reprinted from [302],

operations characterized by low speed, feed rate, and depth of cut.

Duan *et al* [300] explored the influence of Al_2O_3 nanofluid derived from cottonseed oil on the milling of 45 steel. The outcomes revealed that the lowest milling force was achieved at a concentration of 0.2 wt% ($F_x = 58$ N; $F_y = 12$ N). The minimum surface roughness ($R_a = 1.009$ μm; $RS_m = 0.136$ mm) was attained with a mass concentration of 0.5 wt%.

Laghari *et al* [301] investigated the effect of lubricooling technique on the machining process of SiC_p/Al (SiC_p 65%). Both MQL and CO_2 cooled cutting environments were employed. The investigation revealed that the combination of lubrication and cooling effectively mitigated tool wear and enhanced tool life by up to 29% for SiC_p and 65% under moderate cutting conditions. While subzero cooling conditions and dry cutting led to the formation of a build-up edge on the rake face of the cutting tool, MQL-assisted machining proved advantageous in preventing material adhesion to the cutting tool. Haq *et al* [263] investigated the manufacturing process of face milling Inconel 718, employing two distinct lubrication conditions: MQL and nanofluid-based MQL (nMQL). The findings underscored the significance of the depth of cut as the primary process parameter for both lubrication environments. Notably, the results indicated that nMQL is a superior alternative, yielding reductions of 20.1%, 14.7%, and 13.3% in surface roughness, temperature, and power consumption, respectively. Furthermore, the study revealed that nMQL exhibited a higher desirability achievement score (71.3%) than that of MQL (70.1%).

In addition, Saha *et al* [302] investigated the reachability of MQL oil droplets and the subsequent decline in the wetting efficiency at a constant MQL oil flow rate, attributed to the enlargement of top burrs due to tool wear during micro-milling of Ti–6Al–4V at varying aspect ratios. At an axial depth of 200 μm, the height of the burr increased from 21 to 190 μm over a cutting length of 125 mm, resulting in a decrease in the wetted area from 1036 to 3776 μm^2. Inadequate wetting led to the cutting edge operating under partially dry conditions, subsequently lowering the effectiveness of MQL in improving the machinability as the machining process progressed. In the milling process, some of the oil droplets were obstructed by the sidewalls of the milled feature before they reached the tool–workpiece interaction zone. The occurrence of this phenomenon led to the formation of a region devoid of droplets adjacent to the slot wall, as illustrated in figure 54. Introducing this concept for the first time, Saha *et al* [303] termed these regions ‘shadow zones’. Notably, the shadow zone on the up-milling side was exclusively linked to the up-milling side nozzle. Within this shadow zone, the oil droplets discharged by the down-milling nozzle were capable of reaching. Similarly, the shadow zone on the down-milling wall occurred exclusively in the context of the down-milling nozzle.

Khosravi *et al* [304] investigated the effects of supercritical CO_2 cooling (Sc-CO_2) on the high-speed milling of Ti–6Al–4V with an Sc-CO_2 + MQL delivery system. The side milling experiments under Sc-CO_2 + MQL and flood cooling are shown in figure 55(a). The experimental findings

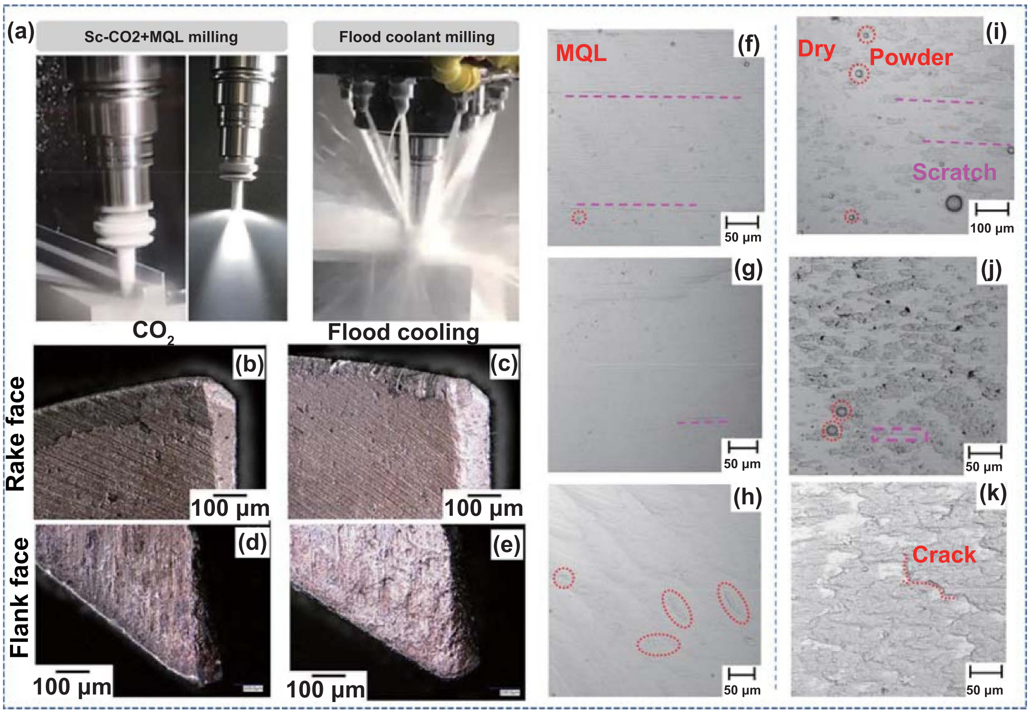

Figure 55. Comparisons of MQL-assisted, conventional flood coolant, and dry milling. (a) Experimental setups of Sc-CO_2 cooling + MQL-assisted milling and conventional flood coolant milling [304]. (b)–(e) Tool wear morphologies under two cooling–lubricating conditions [304]. (f)–(k) Surface defects induced in MQL-assisted and dry milling processes [305]. Reprinted from [304], Reprinted from [305],

highlighted that Sc-CO_2 milling led to diminished tool wear (figures 55(b)–(e)), reduced cutting forces (by up to 50%), elevated surface microhardness (up to 30%), and lower surface roughness (by up to 50%) in comparison to milling processes with flood coolants.

Li *et al* [305] compared the cutting mechanisms between MQL and dry milling in the fabrication of titanium alloy holes. The hole wall morphologies of the specimens under different processes are shown in figures 55(f)–(k). It was found that the MQL process with a feed rate of 20 mm min^{-1} had the best hole wall quality and the least chip–hole wall adhesion and tool scratch defects. The MQL process involved the utilization of relatively small chip sizes and increased intercalation of metal powder. A small chip size is more conducive to discharge, as the lubricant encapsulates the chips. Similarly, effective discharge of the residual metal powder occurred during the MQL process. Kim *et al* [306] explored the influence of nozzle spray angles and cooling media in milling of Ti–6Al–4V. As illustrated in figure 56, numerical models were established to analyze the impact of different nozzle spray angles and fluid volumes on machining performance. The results demonstrated that LN_2 spraying provided highly effective cooling for both the Ti–6Al–4V workpiece and the tungsten carbide tool during milling. The 0° nMQL spray angle was the most favorable for enhancing cooling and lubrication performance, regardless of whether N_2 or LN_2 spraying conditions were employed.

8.2.3. Minimum quantity lubrication-assisted drilling. The impact of liquid carbon dioxide (LCO_2) cooling combined with MQL in the drilling of 42CrMo4 steel was examined by Sterle *et al* [307]. The experimental setup is shown in figure 57(a). The utilization of the MQL technique led to a noteworthy decrease and stabilization in the drilling torque and machining temperature. Under the optimal processing condition, the torque exhibited a reduction of 0.56%, and the drilling temperature showed a substantial decrease of 71%, as illustrated in figure 57(b).

Khunt *et al* [308] assessed the efficacy of vegetable oil-based MQL during drilling of aluminum alloys. They examined the impact of various processing parameters on surface roughness and cutting force. The findings demonstrated that the utilization of sunflower oil-based MQL led to a reduction in surface roughness of as much as 44%, accompanied by up to 52% decrease in torque. Pal *et al* [309] introduced aluminum oxide nanoparticles into sunflower vegetable oil during MQL drilling of AISI 321 stainless steel and analyzed the performance of this technique. Their findings revealed that employing MQL drilling with Al_2O_3–mixed vegetable oil-based cutting fluid yielded superior results compared with dry, wet, and pure MQL drilling processes. Specifically, when utilizing nMQL drilling with a composition of 1.5 wt% Al_2O_3 nanoparticles, thrust force, torque, surface roughness, and drill tip temperature exhibited reductions of approximately 44%, 67%, 56%, and 26%, respectively, in contrast to conventional flood conditions.

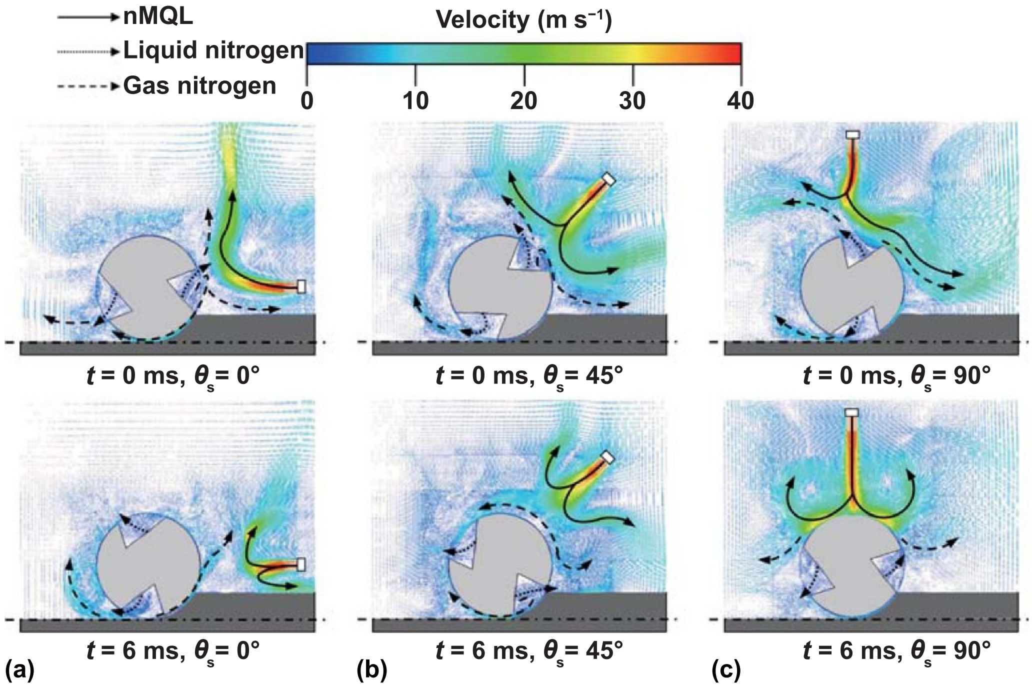

Figure 56. Modeling of the velocity vector field for nozzle spray angles of (a) 0°, (b) 45°, and (c) 90° in latent cooling system at 0 and 6 ms [306]. Reprinted from [306], © 2021 Elsevier Ltd. All rights reserved.

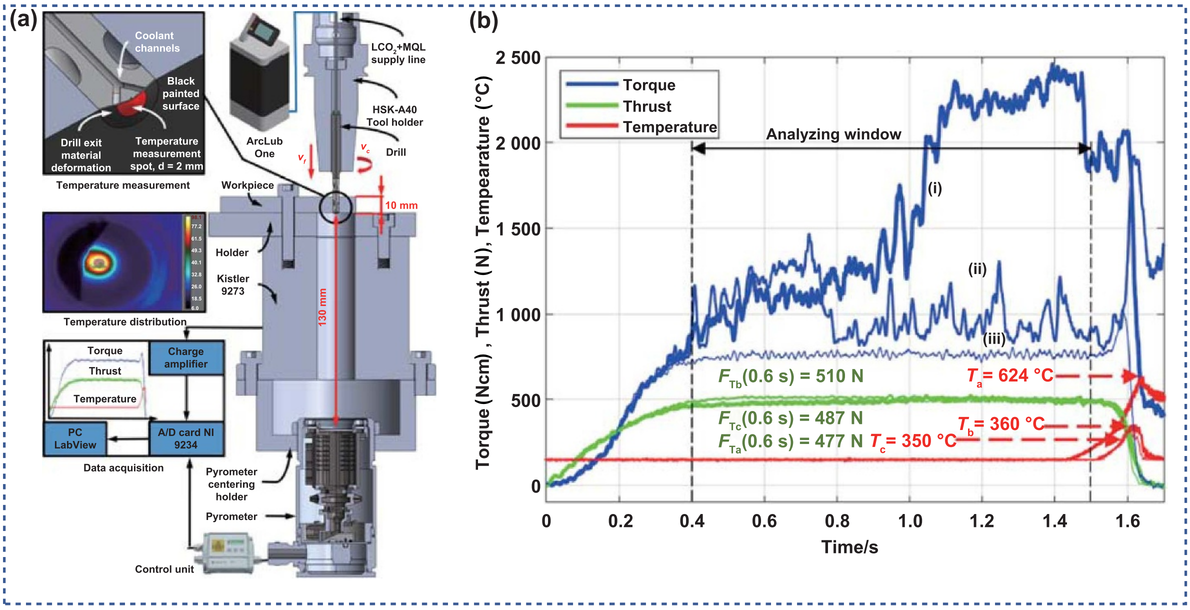

Figure 57. MQL-assisted drilling and its performance. (a) Illustration of the experimental setup [307]. (b) Comparisons of torque, thrust force, and temperature between dry, liquid CO_2, and liquid CO_2 + MQL-assisted drilling [307]. Reprinted from [307], © 2021 The Authors. Published by Elsevier Ltd on behalf of CIRP.

8.2.4. Minimum quantity lubrication-assisted grinding. Tawakoli *et al* [310] determined that MQL grinding substantially enhanced the cutting performance, leading to extended wheel longevity and elevated quality in machining of 100Cr6 and 42CrMo4. Notably, MQL grinding provided more advantages for high-hardness materials. Examination of the ground surfaces revealed that the predominant mechanism of metal removal was through shearing and fracturing in MQL grinding, as opposed to the prevalence of plastic deformation, grain pullout, and ploughing observed in conventional fluid and dry grinding methods. Furthermore, MQL grinding allowed higher removal rates while concurrently delivering improved surface quality and a reduced grinding friction coefficient compared to conventional methods (figure 58).

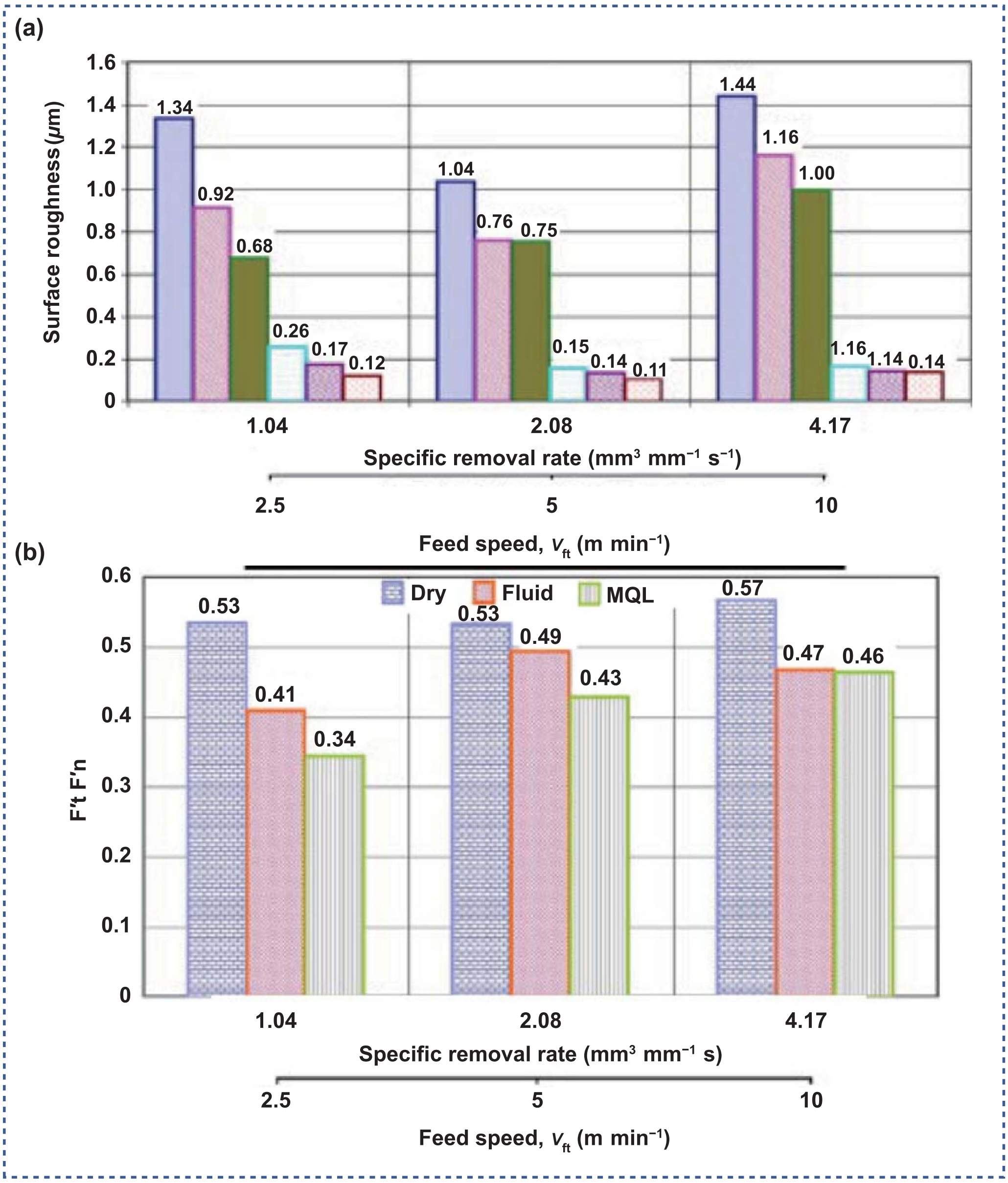

Figure 58. Generated surface roughness and force ratio in dry, fluid cooling, and MQL-assisted grinding at different feed speeds. (a) Comparison of surface roughness [310]. (b) Comparison of force ratios [310]. Reprinted from [310], Copyright © 2009 Elsevier Ltd. All rights reserved.

In addition, the implementation of CNMQL represents a pioneering methodology that capitalizes on the extraordinary heat transfer capabilities of cryogenic air in tandem with the exceptional anti-wear and anti-friction properties of nanolubricants. In the study conducted by Cui *et al* [311], calculation formulas were established to assess the grindability of Ti–6Al–4V, specifically focusing on the energy ratio coefficient of the cooling medium and defect ratio (D_r) of the workpiece surface. The schematic in figure 59 shows the underlying mechanism of material removal. The results revealed that the utilization of CNMQL yielded remarkable outcomes. The D_r value of CNMQL was 84.5% lower than that of cryogenic air cooling and 69.2% lower than that of nMQL. The cryogenic nanolubricant exhibited exceptional grinding performance, owing to its elevated viscosity and ability to augment convective heat transfer capacity.

8.3. High-pressure coolant-assisted mechanical machining

The utilization of a pressurized jet for augmented cooling dates back to 1952, which is credited to the pioneering efforts of Pigott and Colwell. Their experiments yielded seven to eight times augmentation in tool lifespan, eradication of BUEs, and improved machining precision. Pigott and Colwell [312], in a comprehensive assessment, expounded upon the transformative enhancements yielded by the application of cutting fluids through the hi-jet modality, juxtaposing these outcomes against the precedent approach. They elucidated the

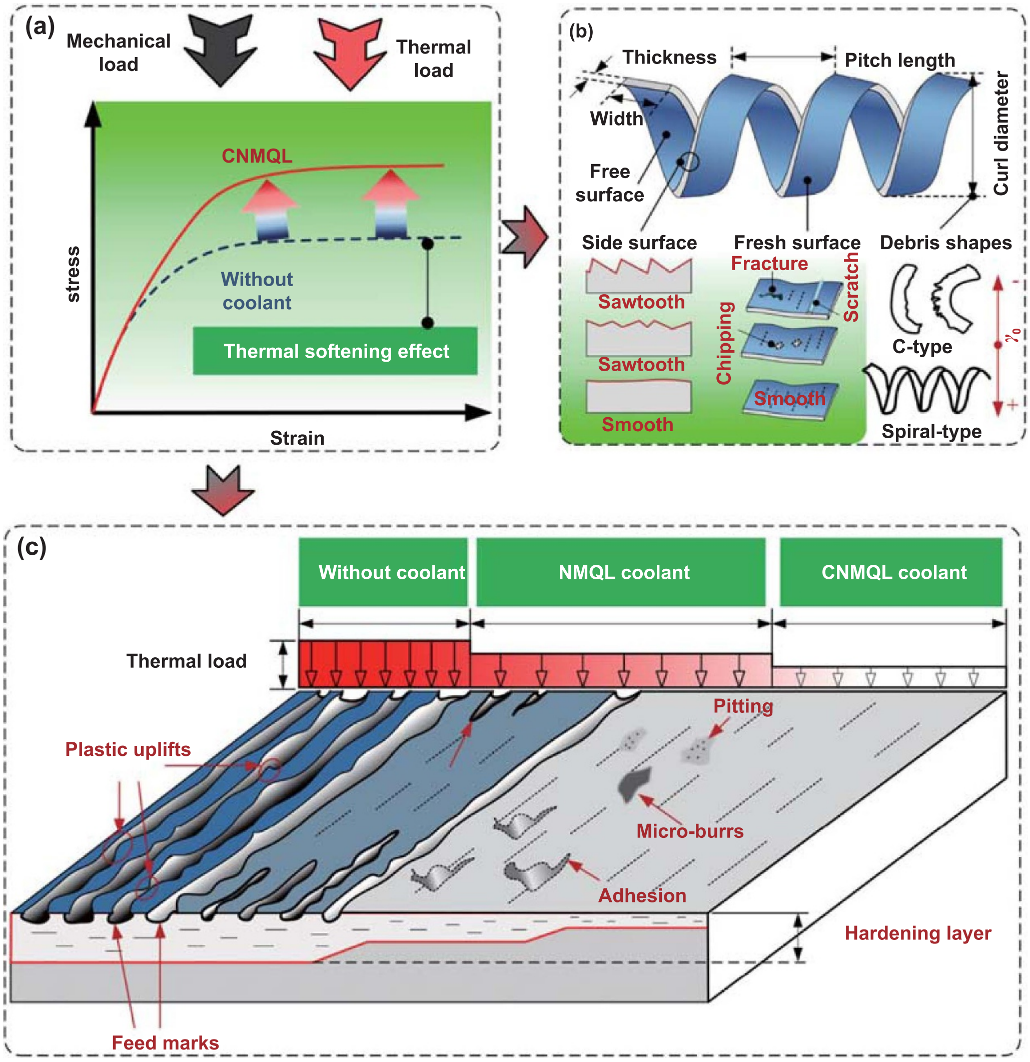

Figure 59. Schematic showing the (a) stress–strain curves, (b) debris shapes, and (c) surface defect patterns in grinding of Ti–6Al–4V under various cooling and lubrication conditions [311]. Reprinted from [311], © 2022 Published by Elsevier Ltd on behalf of The Society of Manufacturing Engineers.

adaptations of diverse recording instruments and the evolution of other refinements throughout the hi-jet testing phase. They also outlined numerous practical applications of the hi-jet approach. According to the reported assessment, this method represents a significant advancement in the field of mechanical machining.

8.3.1. High-pressure coolant-assisted turning. Wertheim *et al* [313] employed the forceful impetus of high-pressure flow to permeate along the expanse of rake face, thereby reducing the temperature within the cutting zone. This comprehensive investigation encompassed different cutting tool materials and workpiece compositions. The ensuing improvement in the thermal environment of the cutting zone induced a transformation in the chips, rendering them narrow and curly, thus enhancing the efficacy of chip removal. Ezugwu and Bonney [314, 315] investigated the effects of cooling pressure on the roughness of machined surfaces and longevity of tools in the context of single-point turning of Inconel 718. The results revealed the presence of a critical coolant pressure threshold, below which the performance of the cutting tools was significantly enhanced in terms of coolant supply. The operational lifespan of the tools was significantly extended by 740% (figure 60(a)) when the machining process was conducted with a coolant supply pressure of 20.3 MPa and cutting speed of 50 m min^{-1}. Kaminski and Alvelid [264] employed a high-pressure coolant jet directed into the interface between the tool and chip. They observed a significant reduction in the cutting temperature, even within the pressure range of 20–70 MPa. The cutting-edge temperature was lowered by an impressive 40%–45%. The variation in cutting temperature with jet pressure and cutting speed is shown in figure 60(b). In addition, the jet pressure had a substantial influence on the fracture of the chip and morphology of the resultant fragments. The reported investigations also revealed that increasing the water flow and jet pressure resulted in a reduction in tool–chip contact length, chip compression ratio, and cutting force.

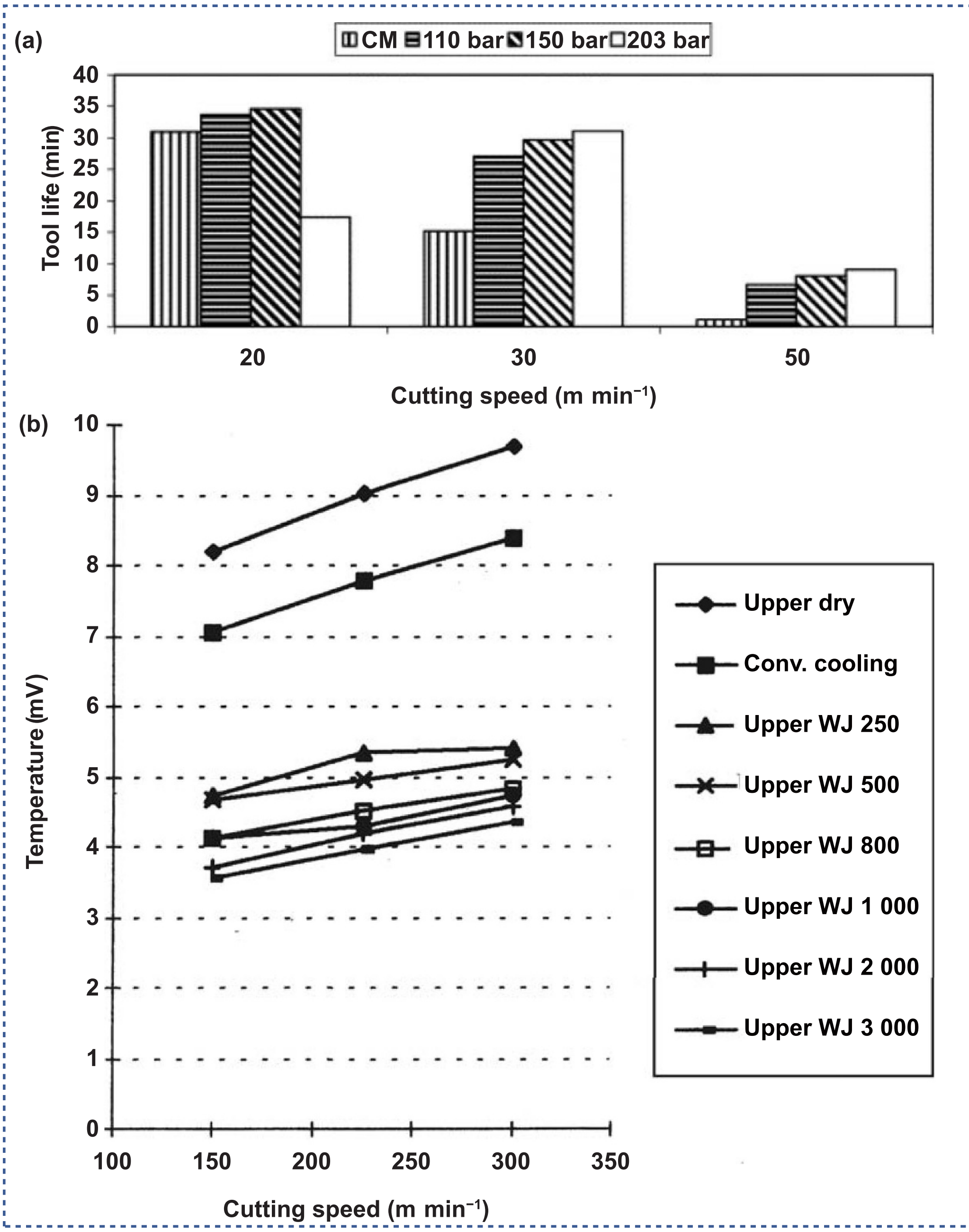

Figure 60. The variation in (a) tool life and (b) cutting temperature with cutting speed and jet pressure [264, 314]. Reprinted from [314], Copyright © 2004 Elsevier B.V. All rights reserved. Reprinted from [264], Copyright © 2000 Elsevier Science B.V. All rights reserved.

Klocke *et al* [316] investigated the effect of high-pressure lubricoolant jets on both the cutting temperature and tool wear in turning of Inconel 718 and Ti–6Al–4V. A solution comprising 7 vol% (ECOCOOL TN 2525 HP) was utilized as the cutting fluid. The results indicated that the cutting temperature was reduced by 25%. Under optimal processing parameters, the tool life was extended by 50%. Dahlman [317] explored the relationship between pressure and flow rate, which affects heat dissipation within the cutting zone. The workpiece materials were SS 2258, SS 2541, and Ti–6Al–4V. The findings revealed that the pressure–flow rate relationship exerted a significant influence on heat dissipation of steel materials. High-pressure cooling resulted in an approximately 50% reduction in temperature compared to conventional cooling, making it particularly advantageous for materials with lower ductility. Furthermore, achieving an optimal temperature reduction relied on precisely balancing the pressure and flow rate. Hosokawa *et al* [318] conducted an investigation into the influence of high-pressure cutting fluid on turning of Ti–6Al–4V alloy. Figure 61(a) presents the turning tool holders equipped with dual-sided outlets for dispensing high-pressure cutting fluid and the correlation between the fluid pressure (P_f) and the flow rate (Q_f) of the cutting fluid. They found that the cutting edge was subjected to abrasion or

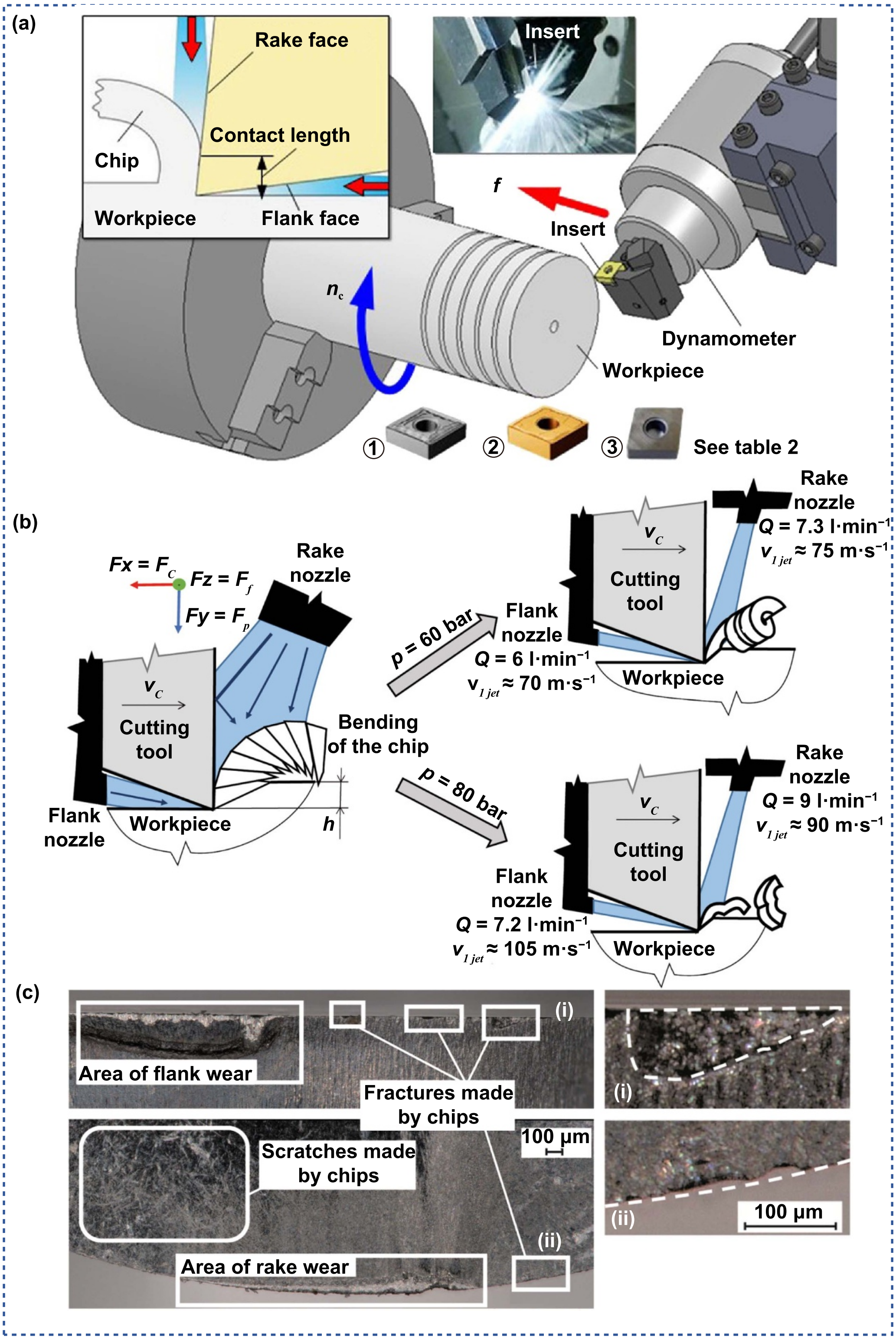

Figure 61. High-pressure coolant-assisted turning and its performance in machining titanium alloys. (a) Experimental setup of dual-sided outlets for dispensing a high-pressure cutting fluid [318]. (b) Schematic of the chip bending mechanism under different jet pressures [265]. (c) Tool wear morphology at a jet pressure of 140 bar [265]. Reprinted from [318], © 2022 The Author(s). Published by Elsevier Ltd on behalf of CIRP. Reprinted from [265], © 2022 The Authors. Published by Elsevier Ltd on behalf of The Society of Manufacturing Engineers.

deformation due to diffusion or adhesion wear at high temperatures. The application of a high-pressure cutting fluid significantly reduced tool wear. The cutting speed was increased to a maximum of 125 m min^{-1} when the cutting temperature was reduced by the high-pressure coolant equipment. In addition, when the coolant jet was directed toward the cutting zone on the rake face, it effectively lowered the cutting temperature due to the commensurate reduction in the length of the chip–tool

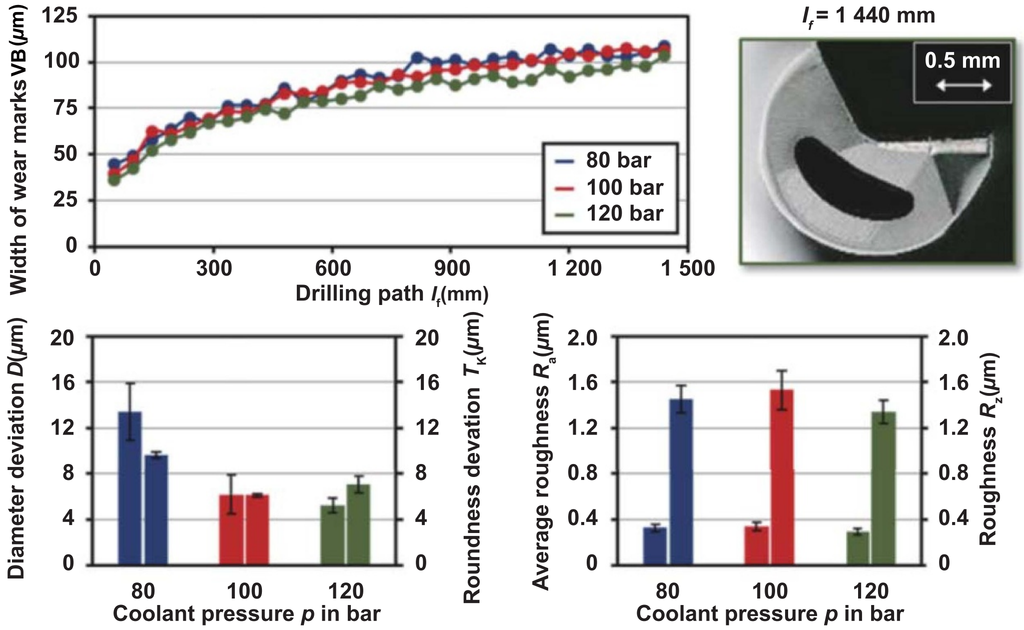

Figure 62. Evolution of tool wear, accuracy, and surface roughness with coolant pressure in high-pressure coolant-assisted drilling of Inconel 718 [323]. Reproduced from [323], with permission from Springer Nature.

contact. Masek *et al* [265] examined the optimal mode and intensity of a high-pressure coolant for mitigating tool wear during the turning of titanium alloys. The schematic of chip bending is shown in figure 61(b). Their findings indicated that an exceedingly high-pressure coolant (over 140 bars) could result in mechanical harm to the cutting edge (figure 61(c)) or unmachined surface due to chip blasting. However, the utilization of a 60 bar high-pressure coolant yielded a comparable reduction in tool wear without incurring additional damage to the cutting edge. In addition, the coolant pressure was observed to influence chip morphologies, with a pronounced increase in chips banding at high pressures.

8.3.2. High-pressure coolant-assisted milling. Kovacevic *et al* [319] devised an equipment for the application of high-pressure waterjet cooling at the tool–chip interface during the milling process. The milling experiments involving stainless-steel AISI 304 demonstrated that high-pressure waterjet-assisted milling yielded superior surface roughness compared to that achieved through flood cooling. This improvement resulted from the substantial reduction in friction at the tool–chip interface, leading to accelerated dissipation of heat from the cutting zone and extended tool lifespan. Furthermore, the cutting force exhibited a consistent decrease in response to the increase in both water pressure and orifice diameter. In a study by Rahman *et al* [320], the utilization of a high-pressure coolant within its effective zones was associated with the emergence of gradual flank wear. The investigation revealed that the application of a high-pressure coolant led to a reduction in cutting temperature (63%), enhancement of surface finish (up to 78%), narrowing of chip width, and an improved cooling effect. Lakner *et al* [321] analyzed the implementation of a high-pressure coolant in conjunction with a multiple-row shell milling tool. The investigation revealed potential cost savings of up to 20% when employing this technological approach for machining titanium alloys. Additionally, there was a significant reduction in the amount of waste filter material contaminated with cutting fluid during the process.

8.3.3. High-pressure coolant-assisted drilling. Lopez de Lacalle *et al* [322] conducted a comparison of tool lifespans between externally and internally cooled tools. In the context of drilling Ti–6Al–4V, the tool life of the internally cooled tool exceeded that of the externally cooled tool by over 100%. Oezkaya *et al* [323] investigated the tool wear and bore-hole quality in drilling of Inconel 718. Figure 62 illustrates the morphologies of the tool wear and the quality of the bore holes under different coolant pressures. The enhanced heat dissipation achieved at elevated coolant pressures resulted in reduced tool wear at a coolant pressure of 120 bar, concurrently leading to a diminished roundness deviation.

8.3.4. High-pressure coolant-assisted grinding. Very Impressive Performance Extreme Removal (VIPER) grinding was developed through a collaborative effort between Rolls-Royce and the Grinding Division of Makino-NCMT [324]. It serves as a substitute for the creep feed grinding of Inconel and other nickel-based alloys by utilizing cubic boron nitride (CBN) wheels. The methodology involves the utilization of a high-pressure coolant delivered through both the spindle and programmable coolant nozzle. The results demonstrated that VIPER grinding achieved a metal removal rate that was four times faster than that achieved through milling.

In today's industrial landscape, advanced coolant-assisted mechanical machining is a favorable processing technology due to its environmentally friendly nature. Table 7 presents a comparison of the output parameters of the

Table 7. Advanced coolant-assisted mechanical machining processes and output parameters. (↑: increased by.↓: decreased by)

Reference	Workpiece material	Hybrid process	Process parameters	Output parameters (compared with conventional)
Makhesana *et al* [262]	Inconel 625	MQL-assisted turning	Medium: vegetable oil and MoS_2 nanoparticles Cutting speed: 70 m min^{-1} Feed: 0.2 mm rev^{-1} Depth of cut: 0.5 mm Pressure: 3 bar	Cutting temperature: ↓ 35%
Klock *et al* [278]	Ti–6Al–4V and Inconel 718	Cryogenic cooling-assisted turning	Cryogenic medium: LN_2 and CO_2 Cutting speed: 150 m min^{-1} Depth of cut: 0.3 mm Feed: 0.13 mm rev^{-1}	Tool life: ↑ more than two times
Wang and Rajurkar [279]	Inconel 718	Cryogenic cooling-assisted turning	Cryogenic medium: LN_2 Cutting speed: 2.23 m s^{-1} Depth of cut: 0.5 mm Feed: 0.1 mm rev^{-1}	Surface roughness: ↓ up to 81% Tool life: ↑ more than two times
Pusavec *et al* [281]	Inconel 718	Cryogenic cooling-assisted turning	Cryogenic medium: LN_2 Cutting speed: 60 m min^{-1} Depth of cut: 0.5 mm Feed: 0.05 mm rev^{-1} Pressure: 1.5 MPa	Microhardness: ↑ 60% Surface roughness: ↓ 22% Compressive residual stresses ↑ 50%
Wang and Wang [283]	GH4169 alloy	Cryogenic cooling-assisted milling	Cryogenic medium: LN_2 Cutting speed: 75, 100, 150, 200, and 300 m min^{-1} LN_2 nozzle temperature: -30 °C, -80 °C, -130 °C, and -190 °C Depth of cut: 0.1, 0.3, 0.6, 0.9, and 1.2 mm Width of cut: 6 mm Feed: 0.01, 0.03, and 0.05 mm rev^{-1}	Surface roughness: ↓ up to 65% Tool life: ↑ more than two times
Huang *et al* [284]	7075-T6 aluminum alloy	Cryogenic cooling-assisted milling	Cryogenic medium: LN_2 Spindle speed: 12 240 rpm Axial depth of cut: 2–8 mm Radial depth of cut: 4 and 1.2 mm Feed: 0.05 mm/tooth	Stability limits: ↑ 50%–100%
Rodríguez *et al* [285]	CFRP–Ti–6Al–4V stacks	Cryogenic cooling-assisted drilling	Cryogenic medium: liquefied CO_2 Cutting speed: 15 and 70 m min^{-1} Feed: 0.025 mm/tooth	Cutting temperature was reduced to 350 °C Drilling accuracy: ↑ 0.5%
Mura *et al* [286]	CFRP	Cryogenic cooling-assisted drilling	Cryogenic medium: LN_2 Cutting speed: 56.5 m min^{-1} Feed: 0.01, 0.02, 0.03, and 0.04 mm rev^{-1}	Cutting force: ↓ 50% Delamination factor: ↓ up to 30%
Kumar *et al* [287]	Ti–6Al–4V	Cryogenic cooling-assisted drilling	Cryogenic medium: LN_2 Cutting speed: 65 and 95 m min^{-1} Feed: 0.1 and 0.2 mm rev^{-1} Exit coolant velocity: 2.91 m s^{-1}	Cutting temperature: ↓ up to 50%
Fredj and Sidhom [292]	AISI 304 stainless steel	Cryogenic cooling- and MQL-assisted grinding	Medium: Soluble oil (20%) and LN_2 Peripheral speed: 30 m s^{-1} Feed: 9 m min^{-1} Depth of cut: 53 μm Pressure: 0.3 MPa	Work harding: ↑ 86% and 137% Endurance limit: ↑ 15% in LN_2 cooling mode

(Continued.)

Table 7. (Continued.)

Khoran *et al* [293]	PEEK	CCAG	Cryogenic medium: CO_2 snow Peripheral speed: 5, 10, and 15 m s^{-1} Feed: 2000 mm min^{-1} Depth of cut: 30 μm	Surface roughness: ↓ up to 40% Tangential cutting force: ↓ 15.5% Normal cutting force: ↓ 28.5%
Abedrabbo *et al* [289]	27MnCr5 steel	CCAG	Cryogenic medium: LN_2 Peripheral speed: 40 and 53 m s^{-1} Feed: 10 mm min^{-1}	Compressive residual stresses: ↓ 10%–20%
Wang *et al* [297]	Tantalum–tungsten alloy Ta-2.5 W	Cryogenic cooling-assisted milling	Cryogenic medium: MQL + CO_2 Cutting speed: 60, 120, and 180 m min^{-1} Depth of cut: 0.1, 0.125, and 0.15 mm Feed: 0.1, 0.125, and 0.15 mm rev^{-1}	Tool life: ↑ 50% Chip thickness: ↓ 34.7%
Laghari *et al* [301]	65 vol% SiCp/Al	MQL and CO_2 snow coolant-assisted milling	Medium: CO_2 snow Cutting speed: 160 and 200 m min^{-1} Feed: 0.06, 0.12, and 0.24 mm/tooth Pressure: 0.6 and 5.5 MPa	Tool life: ↑ more than 13%
Sterle *et al* [307]	42CrMo4	Cryogenic cooling-assisted drilling	Cryogenic medium: MQL + CO_2 Cutting speeds: 30, 50, and 70 m min^{-1} Feed: 0.1 mm rev^{-1} Depth of cut: 10 mm $qLCO_2$: 0, 125, and 250 g min^{-1} qMQL: 0, 50, and 100 ml h^{-1}	Torque: ↓ up to 56% Thrust force: ↑ 18% Cutting temperature: ↓ up to 249%
Khunt *et al* [308]	6063 Aluminum alloy	MQL-assisted drilling	Medium: vegetable oil MQL supply rate: 50 ml h^{-1} Pressure: 2 bar Feed: 0.2 m rev^{-1} Spindle speed: 80, 122, 160, 244, 290, 445, 580, and 890 rpm	Surface roughness: ↓ up to 44% Torque: ↓ up to 52%
Pal *et al* [309]	AISI 321 stainless steel	MQL-assisted drilling	Medium: 1.5 wt% aluminum oxide nanoparticles with sunflower vegetable oil Cutting speed: 7.91 m min^{-1} Feed: 0.125 mm rev^{-1} Pressure: 6 bar	Thrust force: ↓ 44% Torque: 67% ↓ Surface roughness: ↓ 56% Drill tip temperature: ↓ 26%
Tawakoli *et al* [310]	100Cr6 and 42CrMo4	MQL-assisted grinding	Medium: LB8000 MQL oil Peripheral speed: 20, 25, and 30 m s^{-1} Feed: 2.5, 5, and 10 m min^{-1} Depth of cut: 5, 10, 15, and 25 μm Flow rate: 66 ml h^{-1} Pressure: 4 bar	Surface roughness: ↓ up to 51% and 40%
Cui *et al* [311]	Ti–6Al–4V	Cryogenic air cooling and nanolubricant-assisted grinding	Medium: Al_2O_3 nanofluids Peripheral speed: 24 m s^{-1} Feed: 4 m min^{-1} Depth of cut: 10 μm Flow rate: 50 ml h^{-1} Pressure: 0.6 MPa	Tangential force: ↓ 16.6% Normal force: ↓ 13.2% Grinding temperature: ↓ 29.4%

(Continued.)

Table 7. (Continued.)

Reference	Workpiece material	Hybrid process	Process parameters	Output parameters (compared with conventional)
Dahlman [317]	SS 2258, SS 2541, and Ti–6Al–4V	High-pressure coolant-assisted turning	Medium: Sintolin 86 Cutting speed: 300 m min^{-1} Feed: 0.3 mm rev^{-1} Depth of cut: 3 mm Pressure: 270 MPa Flow rate: 1.5 l min^{-1}	Tool–chip contact length: ↓ 50%
Hosokawa *et al* [318]	Ti–6Al–4V	High-pressure coolant-assisted turning	Medium: water soluble (1:30 in water) Cutting speed:100, 125, 150, and 200 m min^{-1} Feed: 0.1 mm rev^{-1} Depth of cut: 0.5 mm Pressure: 0.6 and 15 MPa	Cutting speed: ↑ up to 125 m min^{-1} Tool life: ↑ 50% Cutting temperature: ↓ 34.9%
Rahman *et al* [320]	ASSAB 718 mold steel	High-pressure coolant-assisted milling	Cutting speed: 150 m min^{-1} Depth of cut: 0.35 mm Feed: 0.05 mm/tooth Pressure: 17 bar	Surface roughness: ↓ up to 78% Machining temperature: ↓ 63%
Lakner *et al* [321]	Ti–6Al–4V	High-pressure coolant-assisted milling	Feed: 0.1 mm/tooth Depth of cut: 43 mm Width of cut: 10 mm Pressure: 70 bar	Tool life: ↑ 50% Cost: ↓ up to 20%
Venables [324]	Nickel-based alloys	High-pressure coolant-assisted grinding	Feed: 1.5 m min^{-1} Peripheral speed: 60 m s^{-1} Depth of cut: 4 mm Width of cut: 34 mm	MRR: ↑ 300%

advanced coolant-assisted mechanical machining and conventional mechanical machining. By utilizing the advanced coolant technologies mentioned previously, these methods can improve the surface integrity, enhance the machining efficiency, and reduce tool wear. Extensive research has been conducted by scholars, both domestically and internationally, on the material removal mechanisms associated with mechanical machining while utilizing advanced coolant techniques. However, the utilization of advanced coolant technology incurs high costs. Therefore, optimizing the tradeoff between machining efficiency, quality, and cost is crucial for maximizing the widespread adoption of this technique. The future research agenda include exploring strategies to lower the cost of advanced coolant-assisted mechanical machining while simultaneously enhancing machining quality. Furthermore, it is imperative to consider the impact of cryogenic coolants on both the workpiece and cutting tool materials, such as potential cryogenic-induced brittleness, during process design.

9. Conclusions and future perspectives

Difficult-to-cut materials with extremely high mechanical, thermal, tribological, and optical properties, as well as geometrically complex components, such as micro-features, low-stiffness structures, and honeycomb or laminated structures, are widely applied in the aerospace community. Mechanical machining of these materials and components has the characteristics of low process efficiency, rapid tool wear, poor surface integrity, high machining cost, or even incapable of being machined. To cope with these critical challenges, in-depth research has been conducted on nontraditional EAMM technologies, including processing principles, parameter optimization, material removal mechanisms, and other related areas. Numerous nontraditional EAMM processes have been developed. The primary principles, advantages, and limitations of each technology are summarized in table 8.

(1) Vibration-assisted machining involves the application of low-frequency or ultrasonic vibrations in various directions to a tool or workpiece, transforming conventional continuous contact machining into intermittent, instantaneous, and reciprocating intermittent contact machining. Vibration-assisted machining can reduce cutting forces and temperatures, mitigate tool wear, and enhance the surface quality. However, this method incurs additional costs to the machining system and imposes new and elevated demands on the tools employed. It is crucial to enhance the performance of vibration processing equipment, provide innovative tools compatible with ultrasonic vibrations, and strengthen fundamental theoretical research to meet increasingly stringent processing demands.

(2) Laser-assisted mechanical machining mainly uses a laser beam to soften the local material or induce material modification (forming a metamorphic layer) to enhance machinability. A laser is also used to ablate the local material directly. Thus, mechanical machining is only responsible for removing the heat-affected zone or recast layer resulting from the laser ablation. Laser-assisted

Table 8. Summary of nontraditional EAMM.

Processing method	Primary principles	Advantages	Limitations
Vibration	Intermittent machining	Suitable for difficult-to-cut materials, low machining force and temperature, and high machined surface quality	Complex equipment and high difficulty in application
Laser	Soften, ablate, or modify materials	Low cutting force, high controllability, easy integration, and high machining efficiency	Inapplicable for machining complex surfaces
Hybrid nontraditional energies	Coupling effects of several energy fields on a workpiece or tool	Combination of the advantages of several nontraditional EAMM technologies	Low machining efficiency, complex device, and high cost
Electric energy	Degrade the material or change the properties of machining fluids	Reduced tool wear, suitable for microstructures, and enhanced machining efficiency	Electrical conductivity requirement for workpiece and complex device
Magnetic energy	Reduce machining vibration or change the properties of machining fluids	Superior machining quality, suitable for complex structures, and eco-friendly machining	Magnetism requirement for workpiece or machining media, complex device, and high cost
Chemical	Modify and degrade the materials by a chemical reaction	Superior machining quality and reduced tool wear	Complex chemical solution formula, low machining efficiency, and environmental pollution
Advanced coolant	Reduce the machining temperature and friction and remove chips efficiently	Improved machining efficiency and eco-friendly machining	Difficult to control the temperature

mechanical machining can effectively reduce the cutting force and tool wear and improve the quality of the machined surface. In addition, larger mechanical machining parameters can be used because the material is much easier to remove, which contributes to an improved MRR. However, it remains difficult to apply laser-assisted mechanical machining to process geometrically complex structures. The designed laser path should not be blocked by the workpiece. Moreover, collaborative cooperation between laser scanning and cutting tool movement should be considered.

(3) Hybrid nontraditional energy-assisted mechanical machining is a hybrid machining technology in which two or more nontraditional energies are applied simultaneously, considering the processing characteristics of materials and the structural characteristics of parts. This method combines the advantages of several nontraditional energies. However, due to the requirement of exerting different types of energy on the workpiece or tool during machining, the equipment for this technology is very complex. In addition, the synergistic effects of these nontraditional energies on the material removal process have not yet been thoroughly investigated.

(4) In electric, magnetic, and chemical energy-assisted mechanical machining processes, nontraditional energy is applied to degrade the properties of the workpiece material, control the fluid behavior, or produce damping on either the workpiece or cutting tool. As a result, the machinability of the material and the stability of the process are improved. These hybrid processes can achieve an ultraprecision surface and stable process performance, particularly for the machining of freeform components and microparts. However, the integration of nontraditional energy sources with machine tools is a difficult task that requires consideration of the interaction between them. In addition, process design methods and process optimization considering the synergistic effects of nontraditional energies and mechanical processes need to be explored.

(5) Advanced coolants in terms of cryogenic medium, MQL, and high-pressure fluid-assisted mechanical machining can significantly reduce the cutting temperature and friction, especially in the machining of difficult-to-cut materials in the aerospace community, such as nickel-based superalloys and titanium alloys. Although numerous studies have demonstrated that machining performance can be improved substantially by optimizing coolant parameters, such as pressure, jet angle, and supply method (internal or external), some issues still need to be considered to promote their industrial applications. Specialized equipment for delivering cryogenic media, especially LN_2, is required because parts tend to be damaged at such a low temperature. It is not possible to supply LN_2 through the fluid supply system of the machine tool because LN_2 may damage some parts of the machine, and deformation of some precision parts may occur, resulting in a loss of accuracy and even fluid leakage. Attention should also be paid to handling the mist resulting from using MQL. Evaluating the sustainability of advanced coolant-assisted mechanical machining processes is also necessary in practice.

With the rapid development of the aerospace community, more and more difficult-to-cut materials and components with excellent comprehensive properties and the ability to operate

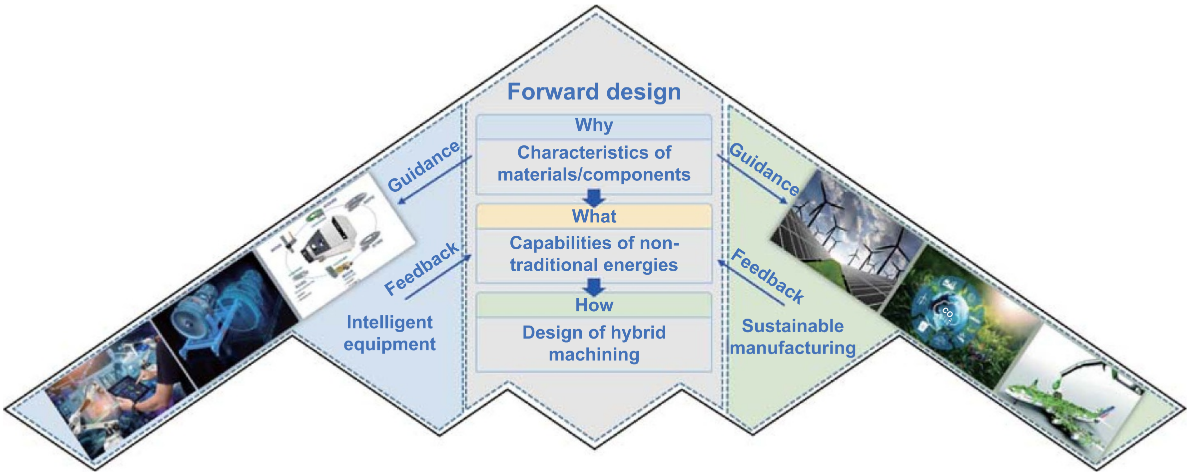

Figure 63. Prospects of future studies with regard to nontraditional EAMM in the aerospace community.

in extremely harsh environments are being invented and utilized. Remarkable progress in nontraditional EAMM technology has been made by researchers. Although some of the technologies listed in table 8 can achieve high efficiency and surface integrity in processing these materials and components, some specific challenges remain unaddressed. Future research should be conducted on forward design, intelligent equipment development, and sustainability of nontraditional EAMM, as shown in figure 63. The purpose of forward design is to achieve an optimal match between the technology and processing demands in terms of efficiency, quality, and cost. In forward design, the machining characteristics of materials or components should be first investigated and understood based on the properties of materials/components and fundamental knowledge on machining. This step of 'why' is the groundwork and the foundation of forward design. Subsequently, the capabilities of various nontraditional energies in machining or pretreating materials should be clearly revealed. The realization of forward design is only possible if it is accomplished with the help of this step of 'what'. The final step of 'how' relies highly on a solid understanding of the previous two steps. The development of intelligent equipment for nontraditional EAMM is mandatory to promote the wide application of these technologies. In addition, the sustainability of hybrid machining should be considered when designing hybrid processes.

Acknowledgments

This study was supported by the National Natural Science Foundation of China (Nos. 52075255, 92160301, 52175415, 52205475, and 92060203).

ORCID iDs

Guolong Zhao https://orcid.org/0000-0003-4126-2114
Wenfeng Ding https://orcid.org/0000-0001-7687-4319
Zhiwen Nian https://orcid.org/0009-0009-2194-9024
Jianhao Peng https://orcid.org/0009-0002-6582-5145

References

[1] Acanfora V, Sellitto A, Russo A, Zarrelli M and Riccio A 2023 Experimental investigation on 3D printed lightweight sandwich structures for energy absorption aerospace applications *Aerosp. Sci. Technol.* **137** 108276

[2] Fu Y Q, Zhang Y L, Chen H, Han L Y, Yin X M, Fu Q G and Sun J 2023 Ultra-high temperature performance of carbon fiber composite reinforced by HfC nanowires: a promising lightweight composites for aerospace engineering *Composites* B **250** 110453

[3] Ahmed F, Ko T J, Kurniawan R and Kwack Y 2021 Machinability analysis of difficult-to-cut material during ultrasonic vibration-assisted ball end milling *Mater. Manuf. Process.* **36** 1734–45

[4] Kishawy H A and Hosseini A 2019 *Machining Difficult-to-Cut Materials: Basic Principles and Challenges* (Springer)

[5] Li B K, Li C H, Zhang Y B, Wang Y G, Jia D Z, Yang M, Zhang N Q, Wu Q D, Han Z G and Sun K 2017 Heat transfer performance of MQL grinding with different nanofluids for Ni-based alloys using vegetable oil *J. Clean. Prod.* **154** 1–11

[6] Zhang J, Huang X F, Kang X Z, Yi H, Wang Q Y and Cao H J 2023 Energy field-assisted high-speed dry milling green machining technology for difficult-to-machine metal materials *Front. Mech. Eng.* **18** 28

[7] Gao G F, Wang Y, Fu Z X, Zhao C Y, Xiang D H and Zhao B 2023 Review of multi-dimensional ultrasonic vibration machining for aeronautical hard-to-cut materials *Int. J. Adv. Manuf. Technol.* **124** 681–707

[8] Zhang Y B, Li C H, Jia D Z, Zhang D K and Zhang X W 2015 Experimental evaluation of the lubrication performance of MoS_2/CNT nanofluid for minimal quantity lubrication in Ni-based alloy grinding *Int. J. Mach. Tools Manuf.* **99** 19–33

[9] Liu M Z *et al* 2021 Cryogenic minimum quantity lubrication machining: from mechanism to application *Front. Mech. Eng.* **16** 649–97

[10] Schlobohm J, Li Y N, Pösch A, Kästner M and Reithmeier E 2017 Multiscale measurement of air foils with data fusion of three optical inspection systems *CIRP J. Manuf. Sci. Technol.* **17** 32–41

[11] Golchin H, Ommi F and Saboohi Z 2020 Assessment of converting approach to efficient design of micro-turboprop engines *Chin. J. Aeronaut.* **33** 572–88

[12] Aschenbruck J, Adamczuk R and Seume J R 2014 Recent progress in turbine blade and compressor blisk regeneration *Proc. CIRP* **22** 256–62

[13] An Q L, Chen J, Ming W W and Chen M 2021 Machining of SiC ceramic matrix composites: a review *Chin. J. Aeronaut.* **34** 540–67

[14] Choi J P, Jeon B H and Kim B H 2007 Chemical-assisted ultrasonic machining of glass *J. Mater. Process. Technol.* **191** 153–6

[15] Pu Y Z, Zhao Y G, Zhang H Y, Zhao G Y, Meng J B and Song P P 2020 Study on the three-dimensional topography of the machined surface in laser-assisted machining of Si_3N_4 ceramics under different material removal modes *Ceram. Int.* **46** 5695–705

[16] Marousi M, Rimpault X, Turenne S and Balazinski M 2023 Initial tool wear and process monitoring during titanium metal matrix composite machining (TiMMC) *J. Manuf. Process.* **86** 208–20

[17] Zhao G L, Xin L J, Li L, Zhang Y, He N and Hansen H N 2023 Cutting force model and damage formation mechanism in milling of 70wt% Si/Al composite *Chin. J. Aeronaut.* **36** 114–28

[18] Diaz O G, Luna G G, Liao Z R and Axinte D 2019 The new challenges of machining ceramic matrix composites (CMCs): review of surface integrity *Int. J. Mach. Tools Manuf.* **139** 24–36

[19] Su Y L 2019 Effect of the cutting speed on the cutting mechanism in machining CFRP *Compos. Struct.* **220** 662–76

[20] Gao T *et al* 2022 Fiber-reinforced composites in milling and grinding: machining bottlenecks and advanced strategies *Front. Mech. Eng.* **17** 24

[21] Pahuja R and Ramulu M 2019 Abrasive water jet machining of titanium (Ti6Al4V)–CFRP stacks—a semi-analytical modeling approach in the prediction of kerf geometry *J. Manuf. Process.* **39** 327–37

[22] Cong W L, Pei Z J, Deines T W, Liu D F and Treadwell C 2013 Rotary ultrasonic machining of CFRP/Ti stacks using variable feedrate *Composites* B **52** 303–10

[23] Cheng H, Zhang K F, Wang N, Luo B and Meng Q X 2017 A novel six-state cutting force model for drilling-countersinking machining process of CFRP-Al stacks *Int. J. Adv. Manuf. Technol.* **89** 2063–76

[24] Wang G D, Melly S K, Li N, Peng T and Li Y C 2018 Research on milling strategies to reduce delamination damage during machining of holes in CFRP/Ti stack *Compos. Struct.* **200** 679–88

[25] Zhang Y B, Li C H, Ji H J, Yang X H, Yang M, Jia D Z, Zhang X P, Li R Z and Wang J 2017 Analysis of grinding mechanics and improved predictive force model based on material-removal and plastic-stacking mechanisms *Int. J. Mach. Tools Manuf.* **122** 81–97

[26] Ulutan D and Ozel T 2011 Machining induced surface integrity in titanium and nickel alloys: a review *Int. J. Mach. Tools Manuf.* **51** 250–80

[27] Gao T, Li C H, Yang M, Zhang Y B, Jia D Z, Ding W F, Debnath S, Yu T B, Said Z and Wang J 2021 Mechanics analysis and predictive force models for the single-diamond grain grinding of carbon fiber reinforced polymers using CNT nano-lubricant *J. Mater. Process. Technol.* **290** 116976

[28] Silvia R C, Lauro C H, Ana H and Davim J P 2022 Development of FEM-based digital twins for machining difficult-to-cut materials: a roadmap for sustainability *J. Manuf. Process.* **75** 739–66

[29] Liu M Z *et al* 2023 Analysis of grain tribology and improved grinding temperature model based on discrete heat source *Tribol. Int.* **180** 108196

[30] Bansal N P 2005 *Handbook of Ceramic Composites* (Springer)

[31] Li H S, Prinz S, Liu Y, Mattfeld P and Shih A J 2023 Experiment and smooth particle hydrodynamic modeling of single-grain diamond scribing of silicon carbide fiber reinforced silicon carbide (SiC_f/SiC) *CIRP Ann.-Manuf. Technol.* **72** 263–6

[32] Zhang B, Lu S X, Rabiey M, Axinte D and Bleicher F 2023 Grinding of composite materials *CIRP Ann.-Manuf. Technol.* **72** 645–71

[33] Wei C J, Zhao L, Hu D J and Ni J 2013 Electrical discharge machining of ceramic matrix composites with ceramic fiber reinforcements *Int. J. Adv. Manuf. Technol.* **64** 187–94

[34] Wang J J, Zhang J F and Feng P F 2017 Effects of tool vibration on fiber fracture in rotary ultrasonic machining of C/SiC ceramic matrix composites *Composites* B **129** 233–42

[35] Yang H J, Chen Y, Xu J H, Ladonne M, Lonfier J and Fu Y C 2019 Tool wear mechanism in low-frequency vibration–assisted drilling of CFRP/Ti stacks and its individual layer *Int. J. Adv. Manuf. Technol.* **104** 2539–51

[36] Xu J Y and El Mansori M 2016 Experimental study on drilling mechanisms and strategies of hybrid CFRP/Ti stacks *Compos. Struct.* **157** 461–82

[37] Jiao F, Li Y X, Niu Y, Zhang Z Q and Bie W B 2023 A review on the drilling of CFRP/Ti stacks: machining characteristics, damage mechanisms and suppression strategies at stack interface *Compos. Struct.* **305** 116489

[38] Xu J Y, Kolesnyk V, Li C P, Lysenko B, Peterka J and Gupta M K 2023 A critical review addressing conventional twist drilling mechanisms and quality of CFRP/Ti stacks *J. Mater. Res. Technol.* **24** 6614–51

[39] Yin Q G, Liu Z Q, Wang B, Song Q H and Cai Y K 2020 Recent progress of machinability and surface integrity for mechanical machining Inconel 718: a review *Int. J. Adv. Manuf. Technol.* **109** 215–45

[40] Zadafiya K, Kumari S, Chatterjee S and Abhishek K 2021 Recent trends in non-traditional machining of shape memory alloys (SMAs): a review *CIRP J. Manuf. Sci. Technol.* **32** 217–27

[41] Xu J Y and El Mansori M 2017 Wear characteristics of polycrystalline diamond tools in orthogonal cutting of CFRP/Ti stacks *Wear* **376–377** 91–106

[42] He Y L, Qing H N, Zhang S G, Wang D Z and Zhu S W 2017 The cutting force and defect analysis in milling of carbon fiber-reinforced polymer (CFRP) composite *Int. J. Adv. Manuf. Technol.* **93** 1829–42

[43] Lauwers B, Klocke F, Klink A, Tekkaya A E, Neugebauer R and Mcintosh D 2014 Hybrid processes in manufacturing *CIRP Ann.-Manuf. Technol.* **63** 561–83

[44] Wang X M *et al* 2023 Nanofluids application in machining: a comprehensive review *Int. J. Adv. Manuf. Technol.* (https://doi.org/10.1007/s00170-022-10767-2)

[45] Lu Y, Sun P Y, Yang X H, Guo X D, Li X K and Ming W Y 2023 Review of research progress in nontraditional machining of ultrahigh-temperature ceramic matrix composites *Coatings* **13** 187

[46] Wang X, Ding W F and Zhao B 2022 A review on machining technology of aero-engine casings *J. Adv. Manuf. Sci. Technol.* **2** 2022011

[47] Du J G, Tian B, Duan L Y, Ming W Y, Liu K and He W B 2022 Traditional and non-traditional machining technology of metallic glass *Int. J. Adv. Manuf. Technol.* **120** 2879–902

[48] Zhao B *et al* 2023 Collaborative manufacturing technologies of structure shape and surface integrity for complex

thin-walled components of aero-engine: status, challenge and tendency *Chin. J. Aeronaut.* **36** 1–24
[49] Cui X, Li C H, Yang M, Liu M Z, Gao T, Wang X M, Said Z, Sharma S and Zhang Y B 2023 Enhanced grindability and mechanism in the magnetic traction nanolubricant grinding of Ti-6Al-4V *Tribol. Int.* **186** 108603
[50] Liu M Z, Li C H, Yang M, Gao T, Wang X M, Cui X, Zhang Y B, Said Z and Sharma S 2023 Mechanism and enhanced grindability of cryogenic air combined with biolubricant grinding titanium alloy *Tribol. Int.* **187** 108704
[51] Xu W X and Zhang L C 2015 Ultrasonic vibration-assisted machining: principle, design and application *Adv. Manuf.* **3** 173–92
[52] Yang Z C, Zhu L D, Zhang G X, Ni C B and Lin B 2020 Review of ultrasonic vibration-assisted machining in advanced materials *Int. J. Mach. Tools Manuf.* **156** 103594
[53] Liu X F, Wu D B, Zhang J H, Hu X Y and Cui P 2019 Analysis of surface texturing in radial ultrasonic vibration-assisted turning *J. Mater. Process. Technol.* **267** 186–95
[54] Jing L, Niu Q L, Yue W H, Rong J, Gao H and Tang S W 2023 Groove bottom material removal mechanism and machinability evaluation for longitudinal ultrasonic vibration-assisted milling of Al–50wt% Si alloy *Int. J. Adv. Manuf. Technol.* **127** 365–80
[55] Lu H, Zhu L D, Yang Z C, Lu H, Yan B L, Hao Y P and Qin S Q 2021 Research on the generation mechanism and interference of surface texture in ultrasonic vibration assisted milling *Int. J. Mech. Sci.* **208** 106681
[56] Jamshidi H and Nategh M J 2013 Theoretical and experimental investigation of the frictional behavior of the tool–chip interface in ultrasonic-vibration assisted turning *Int. J. Mach. Tools Manuf.* **65** 1–7
[57] Peng Z L, Zhang D Y and Zhang X Y 2020 Chatter stability and precision during high-speed ultrasonic vibration cutting of a thin-walled titanium cylinder *Chin. J. Aeronaut.* **33** 3535–49
[58] Liu X F, Zhang J H and Li L 2021 Surface integrity and friction performance of brass H62 textured by one-dimensional ultrasonic vibration-assisted turning *Micromachines* **12** 1398
[59] Duan J W, Zou P, Wang A Q, Wei S Y and Fang R 2023 Research on three-dimensional ultrasonic vibration-assisted turning cutting force *J. Manuf. Process.* **91** 167–87
[60] Wang J T, Bai X L, Shen X H, Liu X F and Wang B L 2022 Effect of micro-texture on substrate surface on adhesion performance of electroless Ni-P coating *J. Manuf. Process.* **74** 296–307
[61] Lu M M, Zhou J K, Lin J Q, Gu Y, Han J G and Zhao D P 2017 Study on Ti-6Al-4V alloy machining applying the non-resonant three-dimensional elliptical vibration cutting *Micromachines* **8** 306
[62] Lin J Q, Han J G, Lu M M, Zhou J K, Gu Y, Jing X and Feng D 2017 Design and performance testing of a novel three-dimensional elliptical vibration turning device *Micromachines* **8** 305
[63] Wei S Y, Zou P, Zhang J H, Duan J W and Fang R 2022 Theoretical and experimental research on 3D ultrasonic vibration-assisted turning driven by a single actuator *Int. J. Adv. Manuf. Technol.* **121** 1173–90
[64] Júnior M G, França T V, Fortulan C A, da Silva R H L and Foschini C R 2022 Green ceramic machining benefits through ultrasonic-assisted turning: an experimental investigation *Int. J. Adv. Manuf. Technol.* **118** 3091–104
[65] Ni C B, Zhu L D and Yang Z C 2019 Comparative investigation of tool wear mechanism and corresponding machined surface characterization in feed-direction ultrasonic vibration assisted milling of Ti–6Al–4V from dynamic view *Wear* **436–437** 203006
[66] Sahoo A K, Sahoo S K, Pattanayak S and Moharana M K 2023 Ultrasonic vibration assisted turning of Inconel 825: an experimental analysis *Mater. Manuf. Process.* **38** 1600–14
[67] Liu J J, Jiang X G, Han X, Gao Z and Zhang D Y 2019 Effects of rotary ultrasonic elliptical machining for side milling on the surface integrity of Ti–6Al–4V *Int. J. Adv. Manuf. Technol.* **101** 1451–65
[68] Chen W Q, Teng X Y, Zheng L, Xie W K and Huo D H 2018 Burr reduction mechanism in vibration-assisted micro milling *Manuf. Lett.* **16** 6–9
[69] Liu X F, Wang W H, Jiang R S, Xiong Y F and Lin K Y 2020 Tool wear mechanisms in axial ultrasonic vibration assisted milling in-situ TiB_2/7050Al metal matrix composites *Adv. Manuf.* **8** 252–64
[70] Tong J L, Wei G, Zhao L, Wang X L and Ma J J 2019 Surface microstructure of titanium alloy thin-walled parts at ultrasonic vibration-assisted milling *Int. J. Adv. Manuf. Technol.* **101** 1007–21
[71] Gao G F, Xia Z W, Su T T, Xiang D H and Zhao B 2021 Cutting force model of longitudinal-torsional ultrasonic-assisted milling Ti–6Al–4V based on tool flank wear *J. Mater. Process. Technol.* **291** 117042
[72] Xiong Y F, Wang W H, Jiang R S, Huang B and Liu C 2022 Feasibility and tool performance of ultrasonic vibration-assisted milling-grinding SiC_f/SiC ceramic matrix composite *J. Mater. Res. Technol.* **19** 3018–33
[73] Yin X M, Yang S L, Li X and Zhang D Y 2023 Research on surface integrity of Inconel 718 with various ultrasonic ball-end milling times *Int. J. Adv. Manuf. Technol.* **128** 2187–97
[74] Xu M R, Chen S, Kurniawan R, Li C P, Kwak Y I, Ali S, Choo M K, Han P W and Ko T J 2023 Enhancement of machinability study in longitudinal ultrasonic vibration-assisted milling Inconel 718 using high-frequency-vibration spindle *Int. J. Adv. Manuf. Technol.* **126** 3523–42
[75] Zhang M L, Zhang D Y, Geng D X, Shao Z Y, Liu Y H and Jiang X G 2020 Effects of tool vibration on surface integrity in rotary ultrasonic elliptical end milling of Ti–6Al–4V *J. Alloys Compd.* **821** 153266
[76] Vasylyev M A, Mordyuk B N, Sidorenko S I, Voloshko S M and Burmak A P 2018 Influence of microstructural features and deformation-induced martensite on hardening of stainless steel by cryogenic ultrasonic impact treatment *Surf. Coat. Technol.* **343** 57–68
[77] Xie W B, Wang X K, Zhao B, Li G X and Xie Z J 2022 Surface and subsurface analysis of TC18 titanium alloy subject to longitudinal-torsional ultrasonic vibration-assisted end milling *J. Alloys Compd.* **929** 167259
[78] Chang B Q, Yi Z X, Cao X B and Duan J A 2023 Defect suppression and grain refinement during ultrasonic vibration-assisted side milling of GH4169 superalloy *J. Manuf. Process.* **85** 281–94
[79] Ding H, Ibrahim R, Cheng K and Chen S J 2010 Experimental study on machinability improvement of hardened tool steel using two dimensional vibration-assisted micro-end-milling *Int. J. Mach. Tools Manuf.* **50** 1115–8
[80] Elhami S, Razfar M R and Farahnakian M 2016 Experimental study of surface roughness and tool flank wear during hybrid milling *Mater. Manuf. Process.* **31** 933–40
[81] Fang B, Yuan Z H, Li D P and Gao L Y 2021 Effect of ultrasonic vibration on finished quality in ultrasonic vibration assisted micromilling of Inconel718 *Chin. J. Aeronaut.* **34** 209–19

[82] Shen X H and Xu G F 2018 Study of milling force variation in ultrasonic vibration-assisted end milling *Mater. Manuf. Process.* **33** 644–50

[83] Börner R, Winkler S, Junge T, Titsch C, Schubert A and Drossel W G 2018 Generation of functional surfaces by using a simulation tool for surface prediction and micro structuring of cold-working steel with ultrasonic vibration assisted face milling *J. Mater. Process. Technol.* **255** 749–59

[84] Ni C B, Zhu L D, Liu C F and Yang Z C 2018 Analytical modeling of tool-workpiece contact rate and experimental study in ultrasonic vibration-assisted milling of Ti–6Al–4V *Int. J. Mech. Sci.* **142–143** 97–111

[85] Maurotto A and Wickramarachchi C T 2016 Experimental investigations on effects of frequency in ultrasonically-assisted end-milling of AISI 316L: a feasibility study *Ultrasonics* **65** 113–20

[86] Ding K, Fu Y C, Su H H, Cui F F, Li Q L, Lei W N and Xu H X 2017 Study on surface/subsurface breakage in ultrasonic assisted grinding of C/SiC composites *Int. J. Adv. Manuf. Technol.* **91** 3095–105

[87] Li S C, Xiao G J, Chen B Q, Zhuo X Q, Xu J Y and Huang Y 2022 Surface formation modeling and surface integrity research of normal ultrasonic assisted flexible abrasive belt grinding *J. Manuf. Process.* **80** 232–46

[88] Qin S Q, Zhu L D, Hao Y P, Shi C L, Wang S F and Yang Z C 2023 Theoretical and experimental investigations of surface generation induced by ultrasonic assisted grinding *Tribol. Int.* **179** 108120

[89] Zhou W H, Tang J Y, Shao W and Wen J 2022 Towards understanding the ploughing friction mechanism in ultrasonic assisted grinding with single grain *Int. J. Mech. Sci.* **222** 107248

[90] Feng H R, Xiang D H, Wu B F and Zhao B 2019 Ultrasonic vibration-assisted grinding of blind holes and internal threads in cemented carbides *Int. J. Adv. Manuf. Technol.* **104** 1357–67

[91] Yang Y Y, Yang M, Li C H, Li R Z, Said Z, Ali H M and Sharma S 2023 Machinability of ultrasonic vibration-assisted micro-grinding in biological bone using nanolubricant *Front. Mech. Eng.* **18** 1

[92] Gao T *et al* 2020 Surface morphology evaluation of multi-angle 2D ultrasonic vibration integrated with nanofluid minimum quantity lubrication grinding *J. Manuf. Process.* **51** 44–61

[93] Yang Z C, Zhu L D, Ni C B and Ning J S 2019 Investigation of surface topography formation mechanism based on abrasive-workpiece contact rate model in tangential ultrasonic vibration-assisted CBN grinding of ZrO_2 ceramics *Int. J. Mech. Sci.* **155** 66–82

[94] Paknejad M, Abdullah A and Azarhoushang B 2017 Effects of high power ultrasonic vibration on temperature distribution of workpiece in dry creep feed up grinding *Ultrason. Sonochem.* **39** 392–402

[95] Cao Y, Zhu Y J, Ding W F, Qiu Y T, Wang L F and Xu J H 2022 Vibration coupling effects and machining behavior of ultrasonic vibration plate device for creep-feed grinding of Inconel 718 nickel-based superalloy *Chin. J. Aeronaut.* **35** 332–45

[96] Zhao B, Wu B F, Yue Y S, Ding W F, Xu J H and Guo G Q 2023 Developing a novel radial ultrasonic vibration-assisted grinding device and evaluating its performance in machining PTMCs *Chin. J. Aeronaut.* **36** 244–56

[97] Singh A K and Sharma V 2022 A comparative appraisal of sustainable strategy in ultrasonic assisted grinding of Nimonic 80A using novel green atomized cutting fluid *Sustain. Mater. Technol.* **32** e00423

[98] Wang H, Hu Y B, Cong W L and Burks A R 2019 Rotary ultrasonic machining of carbon fiber-reinforced plastic composites: effects of ultrasonic frequency *Int. J. Adv. Manuf. Technol.* **104** 3759–72

[99] Wang H, Hu Y B, Cong W L, Hu Z Y and Wang Y Q 2020 A novel investigation on horizontal and 3D elliptical ultrasonic vibrations in rotary ultrasonic surface machining of carbon fiber reinforced plastic composites *J. Manuf. Process.* **52** 12–25

[100] Maroju N K, Vamsi K P and Xiaoliang J 2017 Investigations on feasibility of low-frequency vibration-assisted turning *Int. J. Adv. Manuf. Technol.* **91** 3775–88

[101] Hussein R, Sadek A, Elbestawi M A and Attia M H 2018 Low-frequency vibration-assisted drilling of hybrid CFRP/Ti6Al4V stacked material *Int. J. Adv. Manuf. Technol.* **98** 2801–17

[102] Li C, Xu J Y, Chen M, An Q L, El Mansori M and Ren F 2019 Tool wear processes in low frequency vibration assisted drilling of CFRP/Ti6Al4V stacks with forced air-cooling *Wear* **426–427** 1616–23

[103] Hussein R, Sadek A, Elbestawi M A and Attia M H 2019 An investigation into tool wear and hole quality during low-frequency vibration-assisted drilling of CFRP/Ti6Al4V stack *J. Manuf. Mater. Process.* **3** 63

[104] Yan C R, Qian N, Chen Y, Wang Y Q, Guo N and Lin H 2022 Theoretical and experimental analyses of dynamic deformation in low-frequency vibration-assisted drilling of CFRP/Ti stacks *J. Manuf. Process.* **82** 818–28

[105] Zhou J K, Lu M M, Lin J Q and Wei W Q 2023 Influence of tool vibration and cutting speeds on removal mechanism of SiCp/Al composites during ultrasonic elliptical vibration-assisted turning *J. Manuf. Process.* **99** 445–55

[106] Kang R K, Zhang P N, Wei Z C, Dong Z G and Wang Y D 2023 Experimental study on ultrasonic assisted turning of GH4068 superalloy *Materials* **16** 3554

[107] Bertolini R, Andrea G, Alagan N T and Bruschi S 2023 Tool wear reduction in ultrasonic vibration-assisted turning of SiC-reinforced metal-matrix composite *Wear* **523** 204785

[108] Xu M R, Chen S, Kurniawan R, Li C P, Wei R, Teng H W, Kumaran T, Han P W and Ko T J 2023 Machinability study of cryogenic-ultrasonic vibration-assisted milling Inconel 718 alloy *Int. J. Adv. Manuf. Technol.* **127** 4887–901

[109] Li G X, Xie W B, Wang H T, Chai Y B, Zhang S L and Yang L Q 2023 Optimizing processing parameters and surface quality of TC18 via ultrasonic-assisted milling (UAM): an experimental study *Micromachines* **14** 1111

[110] Wang X W, Tang Y, Zhao B, Chen T, Ding W F and Xu J H 2023 Grindability of γ-TiAl intermetallic compounds during ultrasonic vibration-assisted high efficiency deep grinding process *Int. J. Adv. Manuf. Technol.* **128** 1127–38

[111] Huang Q, Zhao B, Qiu Y T, Cao Y, Fu Y C, Chen Q L, Tang M L, Deng M M, Liu G L and Ding W F 2023 MOPSO process parameter optimization in ultrasonic vibration-assisted grinding of hardened steel *Int. J. Adv. Manuf. Technol.* **128** 903–14

[112] Sun S, Brandt M and Dargusch M S 2010 Thermally enhanced machining of hard-to-machine materials–a review *Int. J. Mach. Tools Manuf.* **50** 663–80

[113] Parida A K and Maity K 2021 Study of machinability in heat-assisted machining of nickel-base alloy *Measurement* **170** 108682

[114] Pandey K and Datta S 2021 Hot machining of *difficult-to-cut* materials: a review *Mater. Today Proc.* **44** 2710–5

[115] Niu J C *et al* 2023 Machining water through laser cutting of nanoparticle-encased water pancakes *Nat. Commun.* **14** 3853

[116] Germain G, Dal Santo P and Lebrun J L 2011 Comprehension of chip formation in laser assisted machining *Int. J. Mach. Tools Manuf.* **51** 230–8

[117] Zhang H, Yan R, Deng B, Lin J Y, Yang M H and Peng F Y 2022 Investigation on surface integrity in laser-assisted machining of Inconel 718 based on in-situ observation *Proc. CIRP* **108** 129–34

[118] Bejjani R, Shi B, Attia H and Balazinski M 2011 Laser assisted turning of titanium metal matrix composite *CIRP Ann.-Manuf. Technol.* **60** 61–64

[119] Lei S T, Shin Y C and Incropera F P 2000 Deformation mechanisms and constitutive modeling for silicon nitride undergoing laser-assisted machining *Int. J. Mach. Tools Manuf.* **40** 2213–33

[120] Anderson M, Patwa R and Shin Y C 2006 Laser-assisted machining of Inconel 718 with an economic analysis *Int. J. Mach. Tools Manuf.* **46** 1879–91

[121] Habrat W, Krupa K, Markopoulos A P and Karkalos N E 2021 Thermo-mechanical aspects of cutting forces and tool wear in the laser-assisted turning of Ti–6Al–4V titanium alloy using AlTiN coated cutting tools *Int. J. Adv. Manuf. Technol.* **115** 759–75

[122] Sugioka K and Cheng Y 2013 *Ultrafast Laser Processing: From Micro- to Nanoscale* (Jenny Stanford Publishing)

[123] Sugioka K, Meunier M and Piqué A 2010 *Laser Precision Microfabrication* (Springer)

[124] Guo B S, Sun J Y, Lu Y F and Jiang L 2019 Ultrafast dynamics observation during femtosecond laser-material interaction *Int. J. Extrem. Manuf.* **1** 032004

[125] Navas V G, Arriola I, Gonzalo O and Leunda J 2013 Mechanisms involved in the improvement of Inconel 718 machinability by laser assisted machining (LAM) *Int. J. Mach. Tools Manuf.* **74** 19–28

[126] Wang Y, Yang L J and Wang N J 2002 An investigation of laser-assisted machining of Al_2O_3 particle reinforced aluminum matrix composite *J. Mater. Process. Technol.* **129** 268–72

[127] Rashid R R, Sun S, Wang G and Dargusch M S 2012 An investigation of cutting forces and cutting temperatures during laser-assisted machining of the Ti–6Cr–5Mo–5V–4Al beta titanium alloy *Int. J. Mach. Tools Manuf.* **63** 58–69

[128] Dandekar C R, Shin Y C and Barnes J 2010 Machinability improvement of titanium alloy (Ti–6Al–4V) via LAM and hybrid machining *Int. J. Mach. Tools Manuf.* **50** 174–82

[129] Bai W, Roy A, Sun R L and Silberschmidt V V 2019 Enhanced machinability of SiC-reinforced metal-matrix composite with hybrid turning *J. Mater. Process. Technol.* **268** 149–61

[130] Dandekar C R and Shin Y C 2013 Multi-scale modeling to predict sub-surface damage applied to laser-assisted machining of a particulate reinforced metal matrix composite *J. Mater. Process. Technol.* **213** 153–60

[131] Attia H, Tavakoli S, Vargas R and Thomson V 2010 Laser-assisted high-speed finish turning of superalloy Inconel 718 under dry conditions *CIRP Ann.-Manuf. Technol.* **59** 83–88

[132] Wei C, Guo W, Pratomo E S, Li Q, Wang D, Whitehead D and Li L 2020 High speed, high power density laser-assisted machining of Al-SiC metal matrix composite with significant increase in productivity and surface quality *J. Mater. Process. Technol.* **285** 116784

[133] Wei C, Guo W, Gao B, Wang Y W, Sun Z and Li L 2021 Understanding the behaviour of workpieces' bulk temperature during laser-assisted turning of Ti6Al4V alloy and heating of Al-SiC metal-matrix composite rods *Opt. Laser Technol.* **139** 106951

[134] Xu B B, Zhang J, Liu X, Liu H G and Zhao W H 2023 Fully coupled thermomechanical simulation of laser-assisted machining Ti6Al4V reveals the mechanism of morphological evolution during serrated chip formation *J. Mater. Process. Technol.* **315** 117925

[135] Przestacki D, Szymanski P and Wojciechowski S 2016 Formation of surface layer in metal matrix composite A359/20SiCP during laser assisted turning *Composites* A **91** 370–9

[136] Przestacki D 2014 Conventional and laser assisted machining of composite A359/20SiCp *Proc. CIRP* **14** 229–33

[137] Dong L 2006 *In-Situ Detection and Heating of High Pressure Metallic Phase of Silicon during Scratching* (University of North Carolina at Charlotte)

[138] You K Y, Fang F Z and Yan G P 2021 Surface generation of tungsten carbide in laser-assisted diamond turning *Int. J. Mach. Tools Manuf.* **168** 103770

[139] You K Y and Fang F Z 2022 High effective laser assisted diamond turning of binderless tungsten carbide *J. Mater. Process. Technol.* **302** 117505

[140] You K Y, Liu G Y and Fang F Z 2022 Investigation of surface integrity on laser pre-heat assisted diamond turning of binderless tungsten carbide *Proc. CIRP* **108** 566–70

[141] Zhang J G, Fu Y F, Chen X, Shen Z F, Zhang J J, Xiao J F and Xu J F 2023 Investigation of the material removal process in in-situ laser-assisted diamond cutting of reaction-bonded silicon carbide *J. Eur. Ceram. Soc.* **43** 2354–65

[142] Lin C T, Chen X, He W B, Xu G Q, Liu C L, Zhang J G and Xu J F 2022 Experimental investigation on the ductile machinability of fused silica during in-situ laser assisted diamond cutting *J. Manuf. Process.* **84** 383–93

[143] Park S S, Wei Y and Jin X L 2018 Direct laser assisted machining with a sapphire tool for bulk metallic glass *CIRP Ann.-Manuf. Technol.* **67** 193–6

[144] Hedberg G K, Shin Y C and Xu L 2015 Laser-assisted milling of Ti–6Al–4V with the consideration of surface integrity *Int. J. Adv. Manuf. Technol.* **79** 1645–58

[145] Yang B, Shen X and Lei S 2009 Mechanisms of edge chipping in laser-assisted milling of silicon nitride ceramics *Int. J. Mach. Tools Manuf.* **49** 344–50

[146] Muženič D, Kramar D and Pušavec F 2022 Advances in understanding of damage formation during laser-assisted milling of ZnO-based varistor ceramics *J. Manuf. Process.* **84** 1478–91

[147] Ding H T, Shen N G and Shin Y C 2012 Thermal and mechanical modeling analysis of laser-assisted micro-milling of difficult-to-machine alloys *J. Mater. Process. Technol.* **212** 601–13

[148] Shang Z D, Liao Z R, Sarasua J A, Billingham J and Axinte D 2019 On modelling of laser assisted machining: forward and inverse problems for heat placement control *Int. J. Mach. Tools Manuf.* **138** 36–50

[149] Kang D W and Lee C M 2014 A study on the development of the laser-assisted milling process and a related constitutive equation for silicon nitride *CIRP Ann.-Manuf. Technol.* **63** 109–12

[150] Xia H J, Zhao G L, Zhang Y, Li L, He N and Hansen H N 2022 Nanosecond laser-induced controllable oxidation of TiB_2–TiC ceramic composites for subsequent micro milling *Ceram. Int.* **48** 2470–81

[151] Xin L J, Zhang B, Zhao G L, Liu H L, Yang Y F and Li L 2021 Laser-induced oxidation-assisted micromilling of deep narrow microgroove on Inconel 718 *Int. J. Adv. Manuf. Technol.* **114** 173–84

[152] Xia H J, Zhao G L, Mao P C, Hao X Q, Li L and He N 2021 Improved machinability of TiB_2–TiC ceramic composites via laser-induced oxidation assisted micro-milling *Ceram. Int.* **47** 11514–25

[153] Zhao G L, Xia H J, Zhang Y, Li L, He N and Hansen H N 2021 Laser-induced oxidation assisted micro milling of high aspect ratio microgroove on WC-Co cemented carbide *Chin. J. Aeronaut.* **34** 465–75

[154] Zhao G L, Mao P C, Li L, Iqbal A and He N 2020 Micro-milling of 65 vol% SiC_p/Al composites with a novel laser-assisted hybrid process *Ceram. Int.* **46** 26121–8

[155] Zhao G L, Hu M S, Li L, Zhao C X, Zhang J B and Zhang X H 2020 Enhanced machinability of SiC_p/Al composites with laser-induced oxidation assisted milling *Ceram. Int.* **46** 18592–600

[156] Xia H J, Zhao G L, Hu M S, Li L, Khan A M and He N 2020 Investigation on laser-induced oxidation assisted micro-milling of Inconel 718 *Proc. Inst. Mech. Eng.* B **234** 1102–12

[157] Zhao G L, Xia H J, Li L, Mao P C, Du Y N and He N 2020 Study on laser-induced oxidation modification coupled with micro milling of WC-Co cemented carbide *Ceram. Int.* **46** 9554–66

[158] Xia H J, Zhao G L, Li L, Hu M S, He N and Ochengo D 2019 Fabrication of high aspect ratio microgroove on Ti6Al4V by laser-induced oxidation assisted micro milling *J. Manuf. Process.* **45** 419–28

[159] Yang Y F, Zhao G L, Hu M S, Li L and He N 2019 Laser-induced oxidation assisted micro milling of spark plasma sintered TiB_2-SiC ceramic *Ceram. Int.* **45** 12780–8

[160] Xia H J, Zhao G L, Yan J H, Li L, He N and Hao X Q 2019 Study on laser-induced oxidation assisted micro milling of Ti6Al4V alloy *Int. J. Adv. Manuf. Technol.* **103** 1579–91

[161] Zhao G L, Nian Z W, Zhang Z H, Li L and He N 2023 Enhancing the machinability of C_f/SiC composite with the assistance of laser-induced oxidation during milling *J. Mater. Res. Technol.* **22** 1651–63

[162] Chen J, An Q L, Ming W W and Chen M 2021 Investigations on continuous-wave laser and pulsed laser induced controllable ablation of SiC_f/SiC composites *J. Eur. Ceram. Soc.* **41** 5835–49

[163] Li C, Hu Y X, Zhang F H, Geng Y Q and Meng B B 2023 Molecular dynamics simulation of laser assisted grinding of GaN crystals *Int. J. Mech. Sci.* **239** 107856

[164] Guerrini G, Lutey A H A, Melkote S N and Fortunato A 2018 High throughput hybrid laser assisted machining of sintered reaction bonded silicon nitride *J. Mater. Process. Technol.* **252** 628–35

[165] Ma Z L, Wang Q H, Chen H, Chen L Y, Qu S, Wang Z X and Yu T B 2022 A grinding force predictive model and experimental validation for the laser-assisted grinding (LAG) process of zirconia ceramic *J. Mater. Process. Technol.* **302** 117492

[166] Ma Z L, Wang Q H, Chen H, Chen L Y, Meng F W, Chen X, Qu S, Wang Z X and Yu T B 2022 Surface prediction in laser-assisted grinding process considering temperature-dependent mechanical properties of zirconia ceramic *J. Manuf. Process.* **80** 491–503

[167] Fortunato A, Guerrini G, Melkote S N and Bruzzone A A G 2015 A laser assisted hybrid process chain for high removal rate machining of sintered silicon nitride *CIRP Ann. Manuf. Technol.* **64** 189–92

[168] He Y, Xiao G J, Zhu S W, Liu G, Liu Z Y and Deng Z C 2023 Surface formation in laser-assisted grinding high-strength alloys *Int. J. Mach. Tools Manuf.* **186** 104002

[169] Kumar M, Melkote S and Lahoti G 2011 Laser-assisted microgrinding of ceramics *CIRP Ann.-Manuf. Technol.* **60** 367–70

[170] Azarhoushang B, Soltani B and Daneshi A 2018 Study of the effects of laser micro structuring on grinding of silicon nitride ceramics *CIRP Ann.-Manuf. Technol.* **67** 329–32

[171] Zhou K, Xu J Y, Xiao G J and Huang Y 2022 A novel low-damage and low-abrasive wear processing method of C_f/SiC ceramic matrix composites: laser-induced ablation-assisted grinding *J. Mater. Process. Technol.* **302** 117503

[172] Chang C W and Kuo C P 2007 An investigation of laser-assisted machining of Al_2O_3 ceramics planing *Int. J. Mach. Tools Manuf.* **47** 452–61

[173] Chang C W and Kuo C P 2007 Evaluation of surface roughness in laser-assisted machining of aluminum oxide ceramics with Taguchi method *Int. J. Mach. Tools Manuf.* **47** 141–7

[174] Zhai C T, Xu J K, Hou Y G, Sun G B, Zhao B B and Yu H D 2022 Effect of fiber orientation on surface characteristics of C/SiC composites by laser-assisted machining *Ceram. Int.* **48** 6402–13

[175] Ding H T and Shin Y C 2010 Laser-assisted machining of hardened steel parts with surface integrity analysis *Int. J. Mach. Tools Manuf.* **50** 106–14

[176] Kim J, Zani L, Abdul-Kadir A, Jones L, Roy A, Zhao L G and Silberschmidt V V 2022 Hybrid-hybrid machining of SiC-reinforced aluminium metal matrix composite *Manuf. Lett.* **32** 63–66

[177] Wu H Q, Duan W H, Sun L H, Zeng J, Li S S, Wang Q, Wu Y B and Chen Y H 2023 Effect of ultrasonic vibration on the machining performance and mechanism of hybrid ultrasonic vibration/plasma oxidation assisted grinding *J. Manuf. Process.* **94** 466–78

[178] Yang X Z, Yang X, Gu H Y, Kawai K, Arima K and Yamamura K 2022 Efficient and slurryless ultrasonic vibration assisted electrochemical mechanical polishing for 4H–SiC wafers *Ceram. Int.* **48** 7570–83

[179] Kim J, Zani L, Abdul-Kadir A, Roy A, Baxevanakis K P, Jones L C R and Silberschmidt V V 2023 Hybrid-hybrid turning of micro-SiCp/AA2124 composites: a comparative study of laser-and-ultrasonic vibration-assisted machining *J. Manuf. Process.* **86** 109–25

[180] Li B, Xiang D H, Peng P C, Li Y Q, Liu G F, Gao G F and Zhao B 2023 Experimental and FEM study of surface formation and deformation mechanism of SiC_p/Al composites in laser-ultrasonic vibration assisted turning *Ceram. Int.* **49** 13510–9

[181] Dominguez-Caballero J, Ayvar-Soberanis S, Kim J, Roy A, Li L and Curtis D 2023 Hybrid simultaneous laser- and ultrasonic-assisted machining of Ti–6Al–4V alloy *Int. J. Adv. Manuf. Technol.* **125** 1903–16

[182] Deswal N and Kant R 2023 Hybrid turning process by interacting ultrasonic vibration and laser energies *Mater. Manuf. Process.* **38** 570–6

[183] Peng P C, Xiang D H, Li Y Q, Yuan Z J, Lei X F, Li B, Liu G F, Zhao B and Gao G F 2022 Experimental study on laser assisted ultrasonic elliptical vibration turning (LA-UEVT) of 70% SiC_p/Al composites *Ceram. Int.* **48** 33538–52

[184] Zhang C J and Jiao F 2020 Tool wear in laser ultrasonically combined turning of tungsten carbide with PCD tools *Int. J. Adv. Manuf. Technol.* **111** 2201–13

[185] Jiao F, Niu Y and Zhang M J 2018 Prediction of machining dimension in laser heating and ultrasonic vibration composite assisted cutting of tungsten carbide *J. Adv. Manuf. Syst.* **17** 35–45

[186] Wang Z Y, Rajurkar K P, Fan J, Lei S, Shin Y C and Petrescu G 2003 Hybrid machining of Inconel 718 *Int. J. Mach. Tools Manuf.* **43** 1391–6

[187] Sharma A, Jain V and Gupta D 2020 A novel investigation study on float glass hole surface integrity & tool wear using chemical assisted rotary ultrasonic machining *Mater. Today Proc.* **26** 632–7

[188] Zhang L, Kuriyagawa T, Kaku T and Zhao J 2005 Investigation into electrorheological fluid-assisted polishing *Int. J. Mach. Tools Manuf.* **45** 1461–7

[189] Zhang L, He X S, Yang H R and Zhang Y 2010 An integrated tool for five-axis electrorheological fluid-assisted polishing *Int. J. Mach. Tools Manuf.* **50** 737–40
[190] Zhang L, Zhao Y W, He X S and Kuriyagawa T 2008 An investigation of effective area in electrorheological fluid-assisted polishing of tungsten carbide *Int. J. Mach. Tools Manuf.* **48** 295–306
[191] Zhai K, He Q, Li L and Ren Y 2017 Study on chemical mechanical polishing of silicon wafer with megasonic vibration assisted *Ultrasonics* **80** 9–14
[192] Zhai Q, Zhai W J, Gao B, Shi Y Q and Cheng X 2021 Synthesis and characterization of nanocomposite Fe_3O_4/SiO_2 core–shell abrasives for high-efficiency ultrasound-assisted magneto-rheological polishing of sapphire *Ceram. Int.* **47** 31681–90
[193] Guo J, Feng W H, Jong H J H, Suzuki H and Kang R K 2020 Finishing of rectangular microfeatures by localized vibration-assisted magnetic abrasive polishing method *J. Manuf. Process.* **49** 204–13
[194] Kitamura T and Kunieda M 2014 Clarification of EDM gap phenomena using transparent electrodes *CIRP Ann.-Manuf. Technol.* **63** 213–6
[195] Kunieda M, Lauwers B, Rajurkar K P and Schumacher B M 2005 Advancing EDM through fundamental insight into the process *CIRP Ann.-Manuf. Technol.* **54** 64–87
[196] Shao B and Rajurkar K P 2015 Modelling of the crater formation in micro-EDM *Proc. CIRP* **33** 376–81
[197] Selvarajan L, Rajavel R, Venkataramanan K and Srinivasan V P 2023 Experimental investigation on surface morphology and recasting layer of Si_3N_4-TiN composites machined by die-sinking and rotary EDM *Ceram. Int.* **49** 8487–501
[198] Selvarajan L, Rajavel R, Yunus M and Alfattani R 2023 Die-sinking and rotary EDM surface and subsurface analysis of $MoSi_2$-SiC ceramic composites *Mater. Sci. Technol.* **39** 3150–66
[199] Alam M N, Siddiquee A N, Khan Z A and Khan N Z 2022 A comprehensive review on wire EDM performance evaluation *Proc. Inst. Mech. Eng.* E **236** 1724–46
[200] Fan C, Liu K X, Chen Y G, Xue Y C, Zhao J and Khudoley A 2022 A new modelling method of material removal profile for electrorheological polishing with a mini annular integrated electrode *J. Mater. Process. Technol.* **305** 117589
[201] Fan C, Wang X F, Liu K X, Chen Y G, Liang F S, Wang Z and Zhao J 2023 Material removal mechanism in and experiments of electrorheological polishing of foldable intraocular lenses at low temperatures *J. Manuf. Process.* **101** 1032–45
[202] Li C P, Huang L, Xu M R, Chen Y N, Chen J L, Li S J, Li P N, Choi Y S and Ko T J 2022 Processing mechanism of electrical discharge-assisted milling titanium alloy based on 3D thermal-mechanical coupling cutting model *J. Manuf. Process.* **78** 107–19
[203] Xu M R, Wei R, Li C P and Ko T J 2023 High-frequency electrical discharge assisted milling of Inconel 718 under copper-beryllium bundle electrodes *J. Manuf. Process.* **85** 1116–32
[204] Yan J W and Tan T H 2015 Sintered diamond as a hybrid EDM and grinding tool for the micromachining of single-crystal SiC *CIRP Ann.-Manuf. Technol.* **64** 221–4
[205] Rao X S, Zhang F H, Li C and Li Y J 2018 Experimental investigation on electrical discharge diamond grinding of RB-SiC ceramics *Int. J. Adv. Manuf. Technol.* **94** 2751–62
[206] Xu M R, Wei R, Li C P, Kurniawan R, Chen J L and Ko T J 2023 Comprehensive study on the cutting force modeling and machinability of high frequency electrical discharge assisted milling process using a novel tool *Int. J. Precis. Eng. Manuf. Green Technol.* **10** 381–408
[207] Li C P, Kim M Y, Islam M M and Ko T J 2016 Mechanism analysis of hybrid machining process comprising EDM and end milling *J. Mater. Process. Technol.* **237** 309–19
[208] Xu M R, Li C P, Kurniawan R, Park G, Chen J L and Ko T J 2022 Study on surface integrity of titanium alloy machined by electrical discharge-assisted milling *J. Mater. Process. Technol.* **299** 117334
[209] Xu M R, Li C P, Kurniawan R, Chen J L and Ko T J 2022 Influence of different dielectrics and machining parameters for electrical discharge-assisted milling of titanium alloy *Int. J. Precis. Eng. Manuf.* **23** 1095–112
[210] Li C P, Xu M R, Yu Z, Huang L, Li S J, Li P N, Niu Q L and Ko T J 2020 Electrical discharge-assisted milling for machining titanium alloy *J. Mater. Process. Technol.* **285** 116785
[211] Kim M Y, Li C P, Kurniawan R, Jung S T and Ko T J 2019 Experimental investigation of burr reduction during EDM end-milling hybrid process *J. Mech. Sci. Technol.* **33** 2847–53
[212] Satyarthi M K and Pandey P M 2013 Modeling of material removal rate in electric discharge grinding process *Int. J. Mach. Tools Manuf.* **74** 65–73
[213] Wei J Q, Zhang Y, Dong G J, Zhang L C and Zhang F H 2022 Surface integrity of Inconel 718 in electrical discharge grinding *Int. J. Adv. Manuf. Technol.* **123** 3275–83
[214] Koshy P, Jain V K and Lal G K 1996 Mechanism of material removal in electrical discharge diamond grinding *Int. J. Mach. Tools Manuf.* **36** 1173–85
[215] Shu K M and Tu G C 2003 Study of electrical discharge grinding using metal matrix composite electrodes *Int. J. Mach. Tools Manuf.* **43** 845–54
[216] Shrivastava P K and Dubey A K 2013 Intelligent modeling and optimization of material removal rate in electric discharge diamond grinding *Proc. ASME 2012 Int. Manufacturing Science and Engineering Conf. Collocated with the 40th North American Manufacturing Research Conf. and in Participation with the Int. Conf. on Tribology Materials and Processing* (ASME, Notre Dame) pp 431–8
[217] Rao X S, Zhang F H, Lu Y J, Luo X C and Chen F M 2020 Surface and subsurface damage of reaction-bonded silicon carbide induced by electrical discharge diamond grinding *Int. J. Mach. Tools Manuf.* **154** 103564
[218] Ji R J, Liu Y H, Yu L L and Li X P 2009 Research on mechanism of ultra-precision electrical discharge and mechanical grinding for nonconductive engineering ceramics *Proc. 2007 First Int. Conf. on Integration and Commercialization of Micro and Nanosystems* (ASME) pp 1445–7
[219] Kuriyagawa T, Saeki M and Syoji K 2002 Electrorheological fluid-assisted ultra-precision polishing for small three-dimensional parts *Precis. Eng.* **26** 370–80
[220] Feng J H, Yan Q S, Lu J B and Gao W Q 2009 A study of fine machining using instantaneous tiny grinding wheel based on electrorheological effect *Proc. 2007 First Int. Conf. on Integration and Commercialization of Micro and Nanosystems* (ASME) pp 985–7
[221] Fan C, Chen Y G, Xue Y C and Zhang L 2021 Study on the electrorheological ultra-precision polishing process with an annular integrated electrode *Micromachines* **12** 1235
[222] Su J S, Cheng H B, Wen Y F, Feng Y P and Tam H Y 2016 Investigation into the mechanism for ultra smooth electrorheological finishing using wheel-like finishing tool *J. Mater. Process. Technol.* **238** 124–31
[223] Suzuki H, Okada M, Lin W, Morita S, Yamagata Y, Hanada H, Araki H and Kashima S 2014 Fine finishing of ground DOE lens of synthetic silica by magnetic field-assisted polishing *CIRP Ann.-Manuf. Technol.* **63** 313–6

[224] Yamaguchi H, Fergani O and Wu P Y 2017 Modification using magnetic field-assisted finishing of the surface roughness and residual stress of additively manufactured components *CIRP Ann.-Manuf. Technol.* **66** 305–8
[225] Loh Y M, Gao R, Cheung C F, Cheng Y N, Li X, Li X G, Tsoi J K H and Wang C J 2023 A novel magnetic field assisted automatic batch polishing method for dental ceramic crowns *Ceram. Int.* **49** 26540–7
[226] Möhring H C and Werkle K T 2022 Lightweight semi-actively damped high performance milling tool *CIRP Ann.-Manuf. Technol.* **71** 353–6
[227] Yip W S and To S 2017 Reduction of material swelling and recovery of titanium alloys in diamond cutting by magnetic field assistance *J. Alloys Compd.* **722** 525–31
[228] Mei D Q, Kong T R, Shih A J and Chen Z C 2009 Magnetorheological fluid-controlled boring bar for chatter suppression *J. Mater. Process. Technol.* **209** 1861–70
[229] Yip W S and To S 2017 An application of eddy current damping effect on single point diamond turning of titanium alloys *J. Phys. D: Appl. Phys.* **50** 435002
[230] Chen F, Lu X D and Altintas Y 2014 A novel magnetic actuator design for active damping of machining tools *Int. J. Mach. Tools Manuf.* **85** 58–69
[231] Zhu W L and Beaucamp A 2020 Compliant grinding and polishing: a review *Int. J. Mach. Tools Manuf.* **158** 103634
[232] Xia Z B, Fang F Z, Ahearne E and Tao M R 2020 Advances in polishing of optical freeform surfaces: a review *J. Mater. Process. Technol.* **286** 116828
[233] Wu J Z, Zou Y H and Sugiyama H 2015 Study on ultra-precision magnetic abrasive finishing process using low frequency alternating magnetic field *J. Magn. Magn. Mater.* **386** 50–59
[234] Murata J, Ueno Y, Yodogawa K and Sugiura T 2016 Polymer/CeO_2–Fe_3O_4 multicomponent core–shell particles for high-efficiency magnetic-field-assisted polishing processes *Int. J. Mach. Tools Manuf.* **101** 28–34
[235] Wang C J, Cheung C F, Ho L T, Yung K L and Kong L B 2020 A novel magnetic field-assisted mass polishing of freeform surfaces *J. Mater. Process. Technol.* **279** 116552
[236] Yip W S and To S 2017 Tool life enhancement in dry diamond turning of titanium alloys using an eddy current damping and a magnetic field for sustainable manufacturing *J. Clean. Prod.* **168** 929–39
[237] Khalil A K, Yip W S and To S 2022 Theoretical and experimental investigations of magnetic field assisted ultra-precision machining of titanium alloys *J. Mater. Process. Technol.* **300** 117429
[238] Zhang K D, Li Z H, Wang S S, Wang P, Zhang Y P and Guo X H 2023 Study on the cooling and lubrication mechanism of magnetic field-assisted Fe_3O_4@CNTs nanofluid in micro-textured tool cutting *J. Manuf. Process.* **85** 556–68
[239] Chen F and Liu G Y 2017 Active damping of machine tool vibrations and cutting force measurement with a magnetic actuator *Int. J. Adv. Manuf. Technol.* **89** 691–700
[240] Lu X D, Chen F and Altintas Y 2014 Magnetic actuator for active damping of boring bars *CIRP Ann.-Manuf. Technol.* **63** 369–72
[241] Zhang Z L, Jin Z J and Guo J 2020 The effect of the interface reaction mode on chemical mechanical polishing *CIRP J. Manuf. Sci. Technol.* **31** 539–47
[242] Li Z Y, Deng Z H, Ge J M, Liu T and Wan L L 2022 Experimental and theoretical analysis of single-sided and double-sided chemical mechanical polishing of sapphire wafers *Int. J. Adv. Manuf. Technol.* **119** 5095–106
[243] Wang M L and Qu N S 2021 Investigation on material removal mechanism in mechano-electrochemical milling of TC4 titanium alloy *J. Mater. Process. Technol.* **295** 117206
[244] Li G Z, Xiao C, Zhang S B, Luo S Q, Chen Y H and Wu Y B 2023 Study of the humidity-controlled CeO_2 fixed-abrasive chemical mechanical polishing of a single crystal silicon wafer *Tribol. Int.* **178** 108087
[245] Tao H F, Zeng Q Y, Liu Y H, Zhao D W and Lu X C 2023 Effects of grinding-induced surface topography on the material removal mechanism of silicon chemical mechanical polishing *Appl. Surf. Sci.* **631** 157509
[246] Malik F and Hasan M 1995 Manufacturability of the CMP process *Thin Solid Films* **270** 612–5
[247] Xiong Q, Luo Z Y, Yan Q S, Lu J B and Pan J S 2023 Influences of process parameters on chemical mechanical polishing effect of $ZnGeP_2$ crystal *Mater. Sci. Semicond. Process.* **162** 107499
[248] Ding C, Liu M Y, Wan S Z, Cai Z Y, Yuan L J, Wang R and Zheng P 2023 The sustainable treatment of chemical polishing wastewater under low-carbon economy: pollutants removal, resource recovery and energy generation *J. Clean. Prod.* **414** 137469
[249] Wang W, Hua D P, Zhou Q, Li S, Eder S J, Shi J Q, Wang Z J, Wang H F and Liu W M 2023 Effect of a water film on the material removal behavior of Invar during chemical mechanical polishing *Appl. Surf. Sci.* **616** 156490
[250] Zhao D W and Lu X C 2013 Chemical mechanical polishing: theory and experiment *Friction* **1** 306–26
[251] Takaya Y, Kishida H, Hayashi T, Michihata M and Kokubo K 2011 Chemical mechanical polishing of patterned copper wafer surface using water-soluble fullerenol slurry *CIRP Ann.-Manuf. Technol.* **60** 567–70
[252] Takaya Y, Michihata M, Hayashi T, Murai R and Kano K 2013 Surface analysis of the chemical polishing process using a fullerenol slurry by Raman spectroscopy under surface plasmon excitation *CIRP Ann.-Manuf. Technol.* **62** 571–4
[253] Zhang Z Y, Cui J F, Zhang J B, Liu D D, Yu Z J and Guo D M 2019 Environment friendly chemical mechanical polishing of copper *Appl. Surf. Sci.* **467–468** 5–11
[254] Guo J, Shi H H, Tong Z and Li L 2023 A new chemo-mechanical slurry for close-to-atomic scale polishing of $LiNbO_3$ crystal *CIRP Ann.-Manuf. Technol.* **72** 293–6
[255] Zhang Z L, Jin Z J, Guo J, Han X L, Mu Q and Zhu X L 2019 A novel chemical mechanical polishing slurry for yttrium aluminum garnet crystal *Appl. Surf. Sci.* **496** 143601
[256] Byrne G, Mullany B and Young P 1999 The effect of pad wear on the chemical mechanical polishing of silicon wafers *CIRP Ann.-Manuf. Technol.* **48** 143–6
[257] Ryu H J, Kim D G, Kang S, Jeong J H and Kim S 2021 Mechanical abrasion by bi-layered pad micro-asperity in chemical mechanical polishing *CIRP Ann.-Manuf. Technol.* **70** 273–6
[258] Wang K, Li W H, Qu Q T and Wang Z S 2020 Chemical mechanical polishing of the narrow channel of a channel-cut crystal *Int. J. Adv. Manuf. Technol.* **108** 1691–700
[259] Wang M L, Liu T and Qu N S 2022 Interaction between electrochemical machining and conventional milling in mechano-electrochemical milling of TC4 titanium alloy *J. Electrochem. Soc.* **169** 053506
[260] Pei S H, Xue F, Zhou Y F, Pan C and Jia K 2023 Effects of cryogenic gas jet cooling on milling surface roughness and tool life for GH4169 alloy additive manufacturing parts *J. Manuf. Process.* **86** 266–81
[261] Augspurger T, Koch M, Lakner T, De Bartolomeis A, Shokrani A and Bergs T 2021 Development of a virtual sensor for the comparison of heat partitions in milling under cryogenic cooling lubrication and high-pressure

cutting fluid supply *CIRP J. Manuf. Sci. Technol.* **35** 118–31
[262] Makhesana M A, Patel K M, Krolczyk G M, Danish M, Singla A K and Khanna N 2023 Influence of MoS_2 and graphite-reinforced nanofluid-MQL on surface roughness, tool wear, cutting temperature and microhardness in machining of Inconel 625 *CIRP J. Manuf. Sci. Technol.* **41** 225–38
[263] Haq M A U, Hussain S, Ali M A, Farooq M U, Mufti N A, Pruncu C I and Wasim A 2021 Evaluating the effects of nano-fluids based MQL milling of IN718 associated to sustainable productions *J. Clean. Prod.* **310** 127463
[264] Kaminski J and Alvelid B 2000 Temperature reduction in the cutting zone in water-jet assisted turning *J. Mater. Process. Technol.* **106** 68–73
[265] Masek P, Maly J, Zeman P, Heinrich P and Alagan N T 2022 Turning of titanium alloy with PCD tool and high-pressure cooling *J. Manuf. Process.* **84** 871–85
[266] Jiang G, Jianguo Z, Yanan P, Renke R K, Yoshiharu N, Paul S, Xiaobin Y, Baorui W and Dongming G 2020 A critical review on the chemical wear and wear suppression of diamond tools in diamond cutting of ferrous metals *Int. J. Extrem. Manuf.* **2** 012001
[267] Xu W H *et al* 2022 Electrostatic atomization minimum quantity lubrication machining: from mechanism to application *Int. J. Extrem. Manuf.* **4** 042003
[268] Hohe J, Neubrand A, Fliegener S, Beckmann C, Schober M, Weiss K P and Appel S 2021 Performance of fiber reinforced materials under cryogenic conditions—a review *Composites* A **141** 106226
[269] Ni C B, Wang X Z, Zhu L D, Liu D J, Wang Y Q, Zheng Z P and Zhang P 2022 Machining performance and wear mechanism of PVD TiAlN/AlCrN coated carbide tool in precision machining of selective laser melted Ti6Al4V alloys under dry and MQL conditions *J. Manuf. Process.* **79** 975–89
[270] Shokrani A, Betts J and Jawahir I S 2022 Improved performance and surface integrity in finish machining of Inconel 718 with electrically charged tungsten disulphide MQL *CIRP Ann.-Manuf. Technol.* **71** 109–12
[271] Zhang F, Zhang Y B, Cheung C F, Shokrani A and Newman S T 2023 A low temperature nano-lubrication method for enhancing machinability in ultra-precision grinding of binderless tungsten carbide (WC) *CIRP Ann.-Manuf. Technol.* **72** 273–6
[272] Ibrahim A M M, Li W, Mourad A H I, Omer M A E, Essa F A, Abd El-Naby A M, Al Soufif M S, Ezzat M F and Elsheikh A 2023 Cooling and lubrication techniques in grinding: a state-of-the-art review, applications, and sustainability assessment *Chin. J. Aeronaut.* **36** 76–113
[273] Kaynak Y, Gharibi A, Yılmaz U, Köklü U and Aslantaş K 2018 A comparison of flood cooling, minimum quantity lubrication and high pressure coolant on machining and surface integrity of titanium Ti-5553 alloy *J. Manuf. Process.* **34** 503–12
[274] Alagan N T, Hoier P, Beno T, Klement U and Wretland A 2020 Coolant boiling and cavitation wear—a new tool wear mechanism on WC tools in machining alloy 718 with high-pressure coolant *Wear* **452–453** 203284
[275] Mia M and Dhar N R 2018 Effects of duplex jets high-pressure coolant on machining temperature and machinability of Ti–6Al–4V superalloy *J. Mater. Process. Technol.* **252** 688–96
[276] Wei W M, Robles-Linares J A, Liao Z R, Wang Z, Luna G G, Billingham J and Axinte D 2022 On modelling coolant penetration into the microchannels at the tool-workpiece interface *J. Manuf. Process.* **84** 43–54
[277] Stolf P, Paiva J M, Ahmed Y S, Endrino J L, Goel S and Veldhuis S C 2019 The role of high-pressure coolant in the wear characteristics of WC-Co tools during the cutting of Ti–6Al–4V *Wear* **440–441** 203090
[278] Klocke F, Krämer A, Sangermann H and Lung D 2012 Thermo-mechanical tool load during high performance cutting of hard-to-cut materials *Proc. CIRP* **1** 295–300
[279] Wang Z Y and Rajurkar K P 2000 Cryogenic machining of hard-to-cut materials *Wear* **239** 168–75
[280] Wang Z Y, Rajurkar K P and Murugappan M 1996 Cryogenic PCBN turning of ceramic (Si_3N_4) *Wear* **195** 1–6
[281] Pusavec F, Hamdi H, Kopac J and Jawahir I S 2011 Surface integrity in cryogenic machining of nickel based alloy—Inconel 718 *J. Mater. Process. Technol.* **211** 773–83
[282] Paul S, Dhar N R and Chattopadhyay A B 2001 Beneficial effects of cryogenic cooling over dry and wet machining on tool wear and surface finish in turning AISI 1060 steel *J. Mater. Process. Technol.* **116** 44–48
[283] Wang F B and Wang Y Q 2021 Comparison of cryogenic cooling strategy effects on machinability of milling nickel-based alloy *J. Manuf. Process.* **66** 623–35
[284] Huang X D, Zhang X M, Mou H K, Zhang X J and Ding H 2014 The influence of cryogenic cooling on milling stability *J. Mater. Process. Technol.* **214** 3169–78
[285] Rodríguez A, Calleja A, de Lacalle L N L, Pereira O, Rubio-Mateos A and Rodríguez G 2021 Drilling of CFRP-Ti6Al4V stacks using CO_2-cryogenic cooling *J. Manuf. Process.* **64** 58–66
[286] Mura M D and Dini G 2021 Drilling carbon fiber reinforced plastics with pre-cooling treatment by cryogenic fluid *J. Manuf. Process.* **68** 23–31
[287] Kumar A, Bhardwaj R and Joshi S S 2022 Thermal analysis of drilling in titanium under flood and cryogenic cooling using coupled CFD and FEM *J. Manuf. Process.* **81** 605–23
[288] Attanasio A, Ceretti E, Outeiro J and Poulachon G 2020 Numerical simulation of tool wear in drilling Inconel 718 under flood and cryogenic cooling conditions *Wear* **458–459** 203403
[289] Abedrabbo F, Madariaga A, Soriano D, Pérez M, Butano E, Fernández R, Abolghasem S and Arrazola P J 2023 Influence of cryogenic grinding surface on fatigue performance of carburised 27MnCr5 *J. Mater. Res. Technol.* **23** 1792–804
[290] Paul S and Chattopadhyay A B 1996 Determination and control of grinding zone temperature under cryogenic cooling *Int. J. Mach. Tools Manuf.* **36** 491–501
[291] Paul S and Chattopadhyay A B 1995 Effects of cryogenic cooling by liquid nitrogen jet on forces, temperature and surface residual stresses in grinding steels *Cryogenics* **35** 515–23
[292] Fredj N B and Sidhom H 2006 Effects of the cryogenic cooling on the fatigue strength of the AISI 304 stainless steel ground components *Cryogenics* **46** 439–48
[293] Khoran M, Amirabadi H and Azarhoushang B 2020 The effects of cryogenic cooling on the grinding process of polyether ether ketone (PEEK) *J. Manuf. Process.* **56** 1075–87
[294] Byrne G, Dornfeld D and Denkena B 2003 Advancing cutting technology *CIRP Ann.-Manuf. Technol.* **52** 483–507
[295] Klocke F and Eisenblätter G 1997 Dry cutting *CIRP Ann.-Manuf. Technol.* **46** 519–26
[296] Dhar N R, Islam M W, Islam S and Mithu M A H 2006 The influence of minimum quantity of lubrication (MQL) on cutting temperature, chip and dimensional accuracy in turning AISI-1040 steel *J. Mater. Process. Technol.* **171** 93–99
[297] Wang R B, Wang X B, Yan P, Zhou T F, Jiao L, Teng L L and Zhao B 2023 The effects of cryogenic cooling on tool

wear and chip morphology in turning of tantalum-tungsten alloys Ta-2.5W *J. Manuf. Process.* **86** 152–62
[298] Das A, Mundu A R S and Bajpai V 2023 Enhancing tribological performance of lead free brass in high speed micro turning via hybrid cryogenic cooling technique *Tribol. Int.* **179** 108090
[299] Rahman M, Kumar A S and Salam M U 2002 Experimental evaluation on the effect of minimal quantities of lubricant in milling *Int. J. Mach. Tools Manuf.* **42** 539–47
[300] Duan Z J, Yin Q G, Li C H, Dong L, Bai X F, Zhang Y B, Yang M, Jia D Z, Li R Z and Liu Z Q 2020 Milling force and surface morphology of 45 steel under different Al_2O_3 nanofluid concentrations *Int. J. Adv. Manuf. Technol.* **107** 1277–96
[301] Laghari R A, Mekid S, Akhtar S S, Laghari A A and Jamil M 2022 Investigating the tribological aspects of tool wear mechanism and tool life in sustainable lubri-cooling face milling process of particle reinforced SiC_p/Al metal matrix composites *Proc. ASME 2022 Int. Mechanical Engineering Congress and Exposition* (ASME) (https://doi.org/10.1115/IMECE2022-95183)
[302] Saha S, Deb S and Bandyopadhyay P P 2023 Tool wear induced burr formation and concomitant reduction in MQL wetting capability in micro-milling *Int. J. Mech. Sci.* **245** 108095
[303] Saha S, Deb S and Bandyopadhyay P P 2022 Shadow zone in MQL application and its influence on lubricant deficiency and machinability during micro-milling *Int. J. Mech. Sci.* **220** 107181
[304] Khosravi J, Azarhoushang B, Barmouz M, Bösinger R and Zahedi A 2022 High-speed milling of Ti6Al4V under a supercritical CO_2 + MQL hybrid cooling system *J. Manuf. Process.* **82** 1–14
[305] Li J H, Shi W T, Lin Y X, Li J, Liu S and Liu B 2023 Comparative study on MQL milling and hole making processes for laser beam powder bed fusion (L-PBF) of Ti–6Al–4V titanium alloy *J. Manuf. Process.* **94** 20–34
[306] Kim W Y, Senguttuvan S, Kim S H, Lee S W and Kim S M 2021 Numerical study of flow and thermal characteristics in titanium alloy milling with hybrid nanofluid minimum quantity lubrication and cryogenic nitrogen cooling *Int. J. Heat Mass Transfer* **170** 121005
[307] Sterle L, Krajnik P and Pušavec F 2021 The effects of liquid-CO_2 cooling, MQL and cutting parameters on drilling performance *CIRP Ann.-Manuf. Technol.* **70** 79–82
[308] Khunt C P, Makhesana M A, Patel K M and Mawandiya B K 2021 Performance assessment of vegetable oil-based minimum quantity lubrication (MQL) in drilling *Mater. Today Proc.* **44** 341–5
[309] Pal A, Chatha S S and Sidhu H S 2021 Performance evaluation of the minimum quantity lubrication with Al_2O_3- mixed vegetable-oil-based cutting fluid in drilling of AISI 321 stainless steel *J. Manuf. Process.* **66** 238–49
[310] Tawakoli T, Hadad M J, Sadeghi M H, Daneshi A, Stöckert S and Rasifard A 2009 An experimental investigation of the effects of workpiece and grinding parameters on minimum quantity lubrication—MQL grinding *Int. J. Mach. Tools Manuf.* **49** 924–32
[311] Cui X, Li C H, Zhang Y B, Said Z, Debnath S, Sharma S, Ali H M, Yang M, Gao T and Li R Z 2022 Grindability of titanium alloy using cryogenic nanolubricant minimum quantity lubrication *J. Manuf. Process.* **80** 273–86
[312] Pigott R J S and Colwell A T 1952 *Hi-Jet System for Increasing Tool Life* (SAE International) (https://doi.org/10.4271/520254)
[313] Wertheim R, Rotberg J and Ber A 1992 Influence of high-pressure flushing through the rake face of the cutting tool *CIRP Ann.-Manuf. Technol.* **41** 101–6
[314] Ezugwu E O and Bonney J 2004 Effect of high-pressure coolant supply when machining nickel-base, Inconel 718, alloy with coated carbide tools *J. Mater. Process. Technol.* **153–154** 1045–50
[315] Ezugwu E O and Bonney J 2005 Finish machining of nickel-base Inconel 718 alloy with coated carbide tool under conventional and high-pressure coolant supplies *Tribol. Trans.* **48** 76–81
[316] Klocke F, Sangermann H, Krämer A and Lung D 2011 Influence of a high-pressure lubricoolant supply on thermo-mechanical tool load and tool wear behaviour in the turning of aerospace materials *Proc. Inst. Mech. Eng.* B **225** 52–61
[317] Dahlman P 2002 A comparison of temperature reduction in high-pressure jet-assisted turning using high pressure versus high flowrate *Proc. Inst. Mech. Eng.* B **216** 467–73
[318] Hosokawa A, Kosugi K and Ueda T 2022 Turning characteristics of titanium alloy Ti–6Al–4V with high-pressure cutting fluid *CIRP Ann.-Manuf. Technol.* **71** 81–84
[319] Kovacevic R, Cherukuthota C and Mohan R 1995 Improving milling performance with high pressure waterjet assisted cooling/lubrication *J. Eng. Ind.* **117** 331–9
[320] Rahman M, Kumar A S and Choudhury M R 2000 Identification of effective zones for high pressure coolant in milling *CIRP Ann.-Manuf. Technol.* **49** 47–52
[321] Lakner T, Splettstoesser A, Schraknepper D and Bergs T 2021 Economic and ecological evaluation of high-pressure cutting fluid supply in milling of Ti–6Al–4V *Proc. CIRP* **101** 362–5
[322] López de Lacalle L N, Pérez-Bilbatua J, Sánchez J A, Llorente J I, Gutiérrez A and Albóniga J 2000 Using high pressure coolant in the drilling and turning of low machinability alloys *Int. J. Adv. Manuf. Technol.* **16** 85–91
[323] Oezkaya E, Michel S and Biermann D 2021 Chip formation simulation and analysis of the mechanical loads during micro single-lip deep hole drilling of Inconel 718 with varying cooling lubricant pressure *Prod. Eng.* **15** 299–309
[324] Venables M 2006 It's a grind [grinding technology] *Manuf. Eng.* **85** 42–45